WARWICK
THE UNIVERSITY OF WARWICK

A Thesis Submitted for the Degree of PhD at the University of Warwick

Permanent WRAP URL:
http://wrap.warwick.ac.uk/163218

Copyright and reuse:
This thesis is made available online and is protected by original copyright.
Please scroll down to view the document itself.
Please refer to the repository record for this item for information to help you to cite it.
Our policy information is available from the repository home page.

For more information, please contact the WRAP Team at: wrap@warwick.ac.uk

warwick.ac.uk/lib-publications

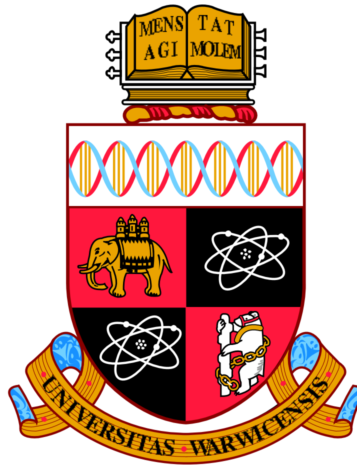

Large-Scale Computational Simulation and Theoretical Spectroscopy of 2D Metal Chalcogenides

by

Siow Mean Loh

Thesis

Submitted to the University of Warwick

for the degree of

Doctor of Philosophy

Department of Physics

June 2021

Contents

List of Tables iv

List of Figures vi

Acknowledgments xvi

Declarations xvii

Abstract xviii

Abbreviations xix

1 Introduction 1

2 Theory of electronic structure based on *ab initio* calculations 6

2.1 In a many-particle system . . . 6

2.2 Hohenberg-Kohn theorems . . . 9

2.2.1 Theorem I . . . 9

2.2.2 Theorem II . . . 10

2.3 Kohn-Sham density functional theory . . . 11

2.4 Exchange-correlation functionals . . . 13

2.4.1 Local density approximation (LDA) . . . 13

2.4.2 Generalised gradient approximation (GGA) . . . 14

2.4.3 Van der Waals (vdW) density functional . . . 14

2.5 Pseudopotentials . . . 16

2.5.1 Norm-conserving pseudopotentials (NCPPs) . . . 16

2.6 Projector augmented waves (PAWs) . . . 17

2.7 Basis functions used in DFT . . . 18

2.8 Force theorem . . . 20

3 Linear-scaling density functional theory **22**
3.1 Order-N electronic total energy package (ONETEP) . . . 22
3.1.1 Density kernel optimisation . . . 27
3.1.2 NGWF optimisation . . . 28
3.1.3 Projector augmented waves (PAWs) in ONETEP . . . 29
3.2 Spectral function unfolding method . . . 31

4 Two-dimensional transition metal dichalcogenide alloy-$Mo_{1-x}W_xS_2$ monolayer **35**
4.1 Introduction . . . 35
4.2 Computational methods . . . 38
4.3 Results and discussions . . . 40
4.3.1 Binding energy of $Mo_{1-x}W_xS_2$ monolayer . . . 41
4.3.2 Monte Carlo simulations . . . 43
4.3.3 Electronic properties of $Mo_{1-x}W_xS_2$ monolayer . . . 49
4.4 Conclusions . . . 59

5 Two-dimensional transition metal dichalcogenide alloy-$W_{1-x}Nb_xS_2$ monolayer **60**
5.1 Introduction . . . 60
5.2 Computational methods . . . 62
5.3 Results and discussions . . . 64
5.3.1 Binding energy of $W_{1-x}Nb_xS_2$ monolayer . . . 65
5.3.2 Electronic structure of $W_{1-x}Nb_xS_2$ monolayer . . . 72
5.3.3 Electrical conductivity of $W_{1-x}Nb_xS_2$ monolayer . . . 75
5.4 Conclusions . . . 77

6 Twistronics in two-dimensional InSe bilayer **79**
6.1 Introduction . . . 79
6.2 Computational methods . . . 82
6.3 Results and discussions . . . 84
6.3.1 Electronic structures of InSe monolayer and InSe bilayer with different stacking configurations . . . 84
6.3.2 Residual force in twisted InSe bilayer . . . 93
6.3.3 Electronic structure of twisted InSe bilayer . . . 99
6.3.4 Exciton binding energy of twisted InSe bilayer and twisted InSe/hBN/InSe heterostructure . . . 113

6.4 Conclusions 115

7 Conclusions **117**

Bibliography **120**

List of Tables

4.1 Binding energies for the atomic configurations in figure 4.4. The binding energy (E_B) $\simeq$ 7.57 meV, calculated based on eq. (4.5). The predicted binding energy is defined to estimate the binding energy of a cluster with m W atoms considering only the interaction between the first nearest-neighbour W-W pairs. It is calculated by the binding energy (7.57 meV) including only one W-W bond ($m = 2$) multiplying by the number of W-W bonds. Δ = Binding energy-Predicted binding energy. 43

5.1 Binding energies for the atomic configurations in figure 4.4. A binding energy of -125.79 meV/bond is obtained based on eq. (5.5). The predicted binding energy is defined to estimate the binding energy of a cluster with m Nb atoms considering only the interaction between the first nearest-neighbour Nb-Nb pairs. It is calculated by the binding energy (-125.79 meV) including only one Nb-Nb bond ($m = 2$) multiplying by the number of Nb-Nb bonds. Δ = Binding energy-Predicted binding energy. 66

6.1 Lattice constant (a), interlayer distance (d) between two InSe layers (In_{tt}-In_{tb}), binding energy (E_B), band gap (E_g) and effective mass for holes (m_h) of InSe monolayer and InSe bilayers with different stacking configurations. 86

6.2 Projected density of states (PDOS) for the VBM in InSe monolayer at different kpoints along Γ to $\mathbf{K}$. 89

6.3 Projected density of states (PDOS) for the CBM in InSe monolayer at different kpoints along Γ to $\mathbf{K}$. 90

6.4 Intralayer and interlayer exciton binding energies of twisted InSe bilayer in the environment of vacuum. The parameter settings are effective mass for electrons $m_e = 0.16\ m_0$ from InSe bilayer in [224], screening length $r_* = 7.7 * \epsilon_{\rm hBN} \simeq 38.9$ Å (where $\epsilon_{\rm hBN} = \sqrt{\epsilon_\parallel * \epsilon_\perp} = \sqrt{6.9 * 3.7} \simeq 5.1$ [225]) [226, 227, 228], effective dielectric constant $\tilde{\epsilon} = \epsilon_{\rm vacuum} = 1$. The effective mass for holes and interlayer distances obtained in this work are used, $m_h = [1.39, 1.75]\ m_0$ and $d = [8.81, 8.89]$ Å. 114

6.5 Intralayer and interlayer exciton binding energies of twisted InSe bilayer in the environment of hBN. The parameter settings are effective mass for electrons $m_e = 0.16\ m_0$ from InSe bilayer in [224], screening length $r_* = 7.7$ Å [226, 227, 228], effective dielectric constant $\tilde{\epsilon} = \epsilon_{\rm hBN} = \sqrt{\epsilon_\parallel * \epsilon_\perp} = \sqrt{6.9 * 3.7} \simeq 5.1$ [225]. The effective mass for holes and interlayer distances obtained in this work are used, $m_h = [1.39, 1.75]\ m_0$ and $d = [8.81, 8.89]$ Å. 114

6.6 Intralayer exciton binding energies of twisted InSe/hBN/InSe heterostructure. The parameter settings are effective mass for electrons $m_e = 0.18\ m_0$ from InSe monolayer in [224], screening length $r_* = 7.7 {*} \epsilon_{\rm hBN}/\tilde{\epsilon} \simeq 12.86$ Å [225, 226, 227, 228], where $\epsilon_{\rm hBN} = \sqrt{\epsilon_\parallel * \epsilon_\perp} = \sqrt{6.9 * 3.7} \simeq 5.1$ [225], effective dielectric constant $\tilde{\epsilon} = (\epsilon_{\rm vacuum} + \epsilon_{\rm hBN})/2 = (1.0 + 5.1)/2 \simeq 3.0$ for the environment of vacuum and $\tilde{\epsilon} = \epsilon_{\rm hBN}$ for the environment of hBN. The effective mass for holes of InSe monolayer obtained in this work is used: $m_h = 2.22\ m_0$. 115

List of Figures

4.1 Electronic structures of MoS_2 and WS_2 monolayers calculated with a plane wave basis set and the GGA-PBE pseudopotential through Quantum Espresso [61, 62]. 36

4.2 (a) Top view (b) Side view of a $Mo_{1-x}W_xS_2$ monolayer. Red, blue and yellow colours refer to Mo, W and S atoms, respectively. Nth-nearest-neighbour pair is labelled as NN_i, where $i = 1, ..., 8$. 40

4.3 Total energy versus lattice constant of (a) MoS_2 (b) WS_2 monolayer. 41

4.4 Atomic structures of $Mo_{1-x}W_xS_2$ monolayers involved clusters with m W atoms ($m = 1, ..., 6$) within 4×4×1 supercells. Red, blue and yellow colours represent molybdenum, tungsten and sulphur atoms, respectively. 42

4.5 (a) Binding energy/bond (b) Δ versus the number of W-W bonds from twenty $Mo_{0.8}W_{0.2}S_2$ monolayers with different random configurations within 12×12×1 supercells. Δ = Binding energy-Predicted binding energy. 43

4.6 Monte Carlo simulations for $Mo_{0.78}W_{0.22}S_2$ monolayers with interaction energy (a) J = -50 meV (b) J = 0 meV (c) J = 7.6 meV (d) J = 50 meV at T = 800 K. Pink and blue dots refer to Mo and W atoms, respectively. 45

4.7 (a) ADF-STEM image of $Mo_{0.78}W_{0.22}S_2$ monolayer (dark dots: Mo atoms, bright dots: W atoms). Experiments performed by X. Xia, N. C. Teutsch, A. J. Graham, V. Kandyba, A. Barinov, A. M. Sanchez and N. R. Wilson. Reproduced from [142]. (b) Ratio of W-W pairs versus nth-nearest-neighbour pair for ADF-STEM images of $Mo_{0.78}W_{0.22}S_2$ monolayer and the corresponding Monte Carlo simulations with J = 7.6 meV at T = 800 K. The error bars are based on the standard deviations calculated from ten regions within 40×40×1 supercells in the same ADF-STEM image. Ratio of W-W pairs versus nth-nearest-neighbour pair for $Mo_{0.78}W_{0.22}S_2$ monolayer with interaction energy (c) J = -50 meV (d) J = 0 meV (e) J = 7.6 meV (f) J = 50 meV at T = 800 K. Ratio of W-W pairs = number of W-W pairs/ ($x\times$ number of $M - M$ pairs), where M refers to Mo or W atom and x refers to the W composition. Nth-nearest-neighbour pair is labelled in figure 4.2. 46
4.8 Monte Carlo simulations for $Mo_{0.37}W_{0.63}S_2$ monolayer with interaction energy (a) J = -50 meV (b) J = 0 meV (c) J = 7.6 meV (d) J = 50 meV at T = 800 K. Pink and blue dots refer to Mo and W atoms, respectively. Ratio of W-W pairs versus nth-nearest-neighbour pair for $Mo_{0.37}W_{0.63}S_2$ monolayer with interaction energy (e) J = -50 meV (f) J = 0 meV (g) J = 7.6 meV (h) J = 50 meV at T = 800 K. Ratio of W-W pairs = number of W-W pairs/ ($x\times$ number of $M-M$ pairs), where M refers to Mo or W atom and x refers to the W composition. Nth-nearest-neighbour pair is labelled in figure 4.2. 48
4.9 Ratio of W-W pairs versus nth-nearest-neighbour pair with J = 7.6 meV at T = 0 K to T = 8000 K for $Mo_{0.41}W_{0.59}S_2$ monolayer. Ratio of W-W pairs = number of W-W pairs/ ($x\times$ number of $M-M$ pairs), where M refers to Mo or W atom and x refers to the W composition. Nth-nearest-neighbour pair is labelled in figure 4.2. 49
4.10 The effective band structure of (a) $Mo_{0.750}W_{0.250}S_2$ (b) $Mo_{0.625}W_{0.375}S_2$ (c) $Mo_{0.500}W_{0.500}S_2$ (d) $Mo_{0.375}W_{0.625}S_2$ (e) $Mo_{0.250}W_{0.750}S_2$ (f) $Mo_{0.125}W_{0.875}S_2$ monolayer. A Lorentzian broadening of 0.02 eV was employed in the effective band structures. Note that SOC was included in all effective band structures. 50

4.11 ARPES measurement along Γ to **K** for $Mo_{1-x}W_xS_2$ monolayers ($x =$ 0.37, 0.50, 0.71). Experiments performed by X. Xia, N. C. Teutsch, A. J. Graham, V. Kandyba, A. Barinov, A. M. Sanchez and N. R. Wilson. Reproduced from [142] 51
4.12 (a) Definition of the band gap (E_g) and the bandwidth of the VB (D_{vb}) are indicated in an effective band structure of $Mo_{1-x}W_xS_2$ monolayer with SOC included. (b) Valence and conduction band splittings around the Fermi level (SOC_{VBM} and SOC_{CBM}) at **K** for MoS_2, $Mo_{1-x}W_xS_2$ and WS_2 monolayers. Red and black colours refer to two different spin states. The ordering of energy level of the conduction bands in red and black colours in WS_2 monolayer around the Fermi level at **K** are opposite to MoS_2 monolayer, leading to the overlap of these two bands at intermediate W composition x. 52
4.13 (a) Band gap and PL emission peak energy (b) Valence band splitting around the Fermi level (SOC_{VBM}) at **K** (c) Bandwidth of the VBM (D_{vb}) (d) Effective mass for holes (m_h) around **K** (e) Conduction band splitting around the Fermi level (SOC_{CBM}) at **K** as a function of W composition x. Black, red and blue data points refer to the results of LS-DFT calculations, VCA calculations and experiments. Green data points are the results of LS-DFT calculations based on the atomic configuration derived from an ADF-STEM image within a 8×8×1 supercell. 55
4.14 Energy versus W composition x for conduction band splitting around the Fermi level at **K** and disorder potential. 56

4.15 (a) Optical microscopy image (top) and schematic cross section (bottom) of the hBN-encapsulated $Mo_{0.5}W_{0.5}S_2$ monolayer flake. (b) Fractional intensity of polarisation-resolved PL spectra versus energy for the heterostructure in (a) at $T = 4$ K. σ^+ and σ^- refer to the right-handed and left-handed circularly polarised light, respectively. V refers to a vertical and linear polarised light with a spin state of $(\sigma^+ + \sigma^-)/\sqrt{2}$. Fractional intensity for each incident polarisation was obtained through its intensity divided by the sum of the intensities for each incident polarisation at 1.92 eV. The sharp peaks within an energy range between 1.92 eV and 1.975 eV originated from Raman scattering. (c) Circularity of the PL versus energy. The circularity is defined as $\frac{\sigma^+\sigma^+ - \sigma^+\sigma^-}{\sigma^+\sigma^+ + \sigma^+\sigma^-}$ under σ^+ excitation. (d) Differential reflectivity versus energy for the heterostructure in (a) at $T = 4$ K. The fitting (red curve) is based on a T-matrix model with layer thickness included. A Lorentzian oscillator is used to model the A1s exciton, where its centre energy was fitted to 1.954 ± 0.001 eV and the width is 41 ± 1 meV. Experiments performed by J. Viner and D. C. Smith. Reproduced from [142]. 58

5.1 (a) ADF-STEM image of $W_{0.9}Nb_{0.1}S_2$ monolayer, where bright and dark colours refer to W and Nb atoms, repectively. Experiments performed by X. Xia and N. R. Wilson. Reproduced from [180]. (b) Top view (c) side view of a region in (a). Red, blue and yellow colours refer to Nb, W and S atoms, respectively. (d) First Brillouin zone of the atomic structure within a hexagonal lattice in (b). Some specified kpoints: three equivalent **K** and one **M**, are indicated. The directions of parallel and perpendicular to the line in (a) are also indicated for later discussions. 64

5.2 $W_{1-x}Nb_xS_2$ monolayers with different dopant distributions within 4×4×1 supercells. The corresponding binding energies are indicated. Red, blue and yellow colours refer to Nb, W and S atoms, respectively. 67

5.3 $W_{1-x}Nb_xS_2$ monolayers with different dopant distributions based on the combinations of prototypes in figure 5.2 within 4×12×1 supercells. The correponding binding energies are indicated. Red, blue and yellow colours refer to Nb, W and S atoms, respectively. 68

5.4 $W_{1-x}Nb_xS_2$ monolayers with different dopant distributions within 6×6×1 supercells. (a)(b) An additional Nb atom is inclined to occupy the atomic site near the line. (c)(d) An additional Nb atom is inclined to occupy the atomic site near the isolated Nb. (e)(f) An additional Nb atom is inclined to occupy the atomic site near the isolated Nb although occupying the atomic site near the line will form a perfect line in the whole simulation cell. Red, blue and yellow colours refer to Nb, W and S atoms, respectively. 69

5.5 $W_{1-x}Nb_xS_2$ monolayers with different dopant distributions within 4×4×1 supercells. The corresponding binding energies are indicated. Red, blue and yellow colours refer to Nb, W and S atoms, respectively. 71

5.6 Atomic structures of $W_{1-x}Nb_xS_2$ monolayers with dopant distributions named as (a) "random" (b) "half line" (c) "real" (d) "perfect line" within 12×12×1 supercells and their corresponding effective band structures along Γ to **M**. The "real" distribution is based on a region of ADF-STEM image in figure 5.1(a). A Lorentzian broadening of 0.02 eV was employed in the effective band structures. Dashed line represents the Fermi level. Red, blue and yellow colours refer to Nb, W and S atoms, respectively. 72

5.7 Effective band structures of $W_{1-x}Nb_xS_2$ monolayers with different dopant distributions are the same as figure 5.6 along Γ to **K1**, **K2** and **K3**. The "real" is based on a region of ADF-STEM image in figure 5.1(a). A Lorentzian broadening of 0.02 eV was employed in the effective band structures. Dashed line represents the Fermi level. Red, blue and yellow colours refer to Nb, W and S atoms, respectively. 74

5.8 Charge density distributions of chosen eigenstates for the "real" distribution in figure 5.6. The *d* orbital contribution of Nb atom predominated the VBM and flat bands, whereas the *d* orbital contribution of W atom predominated the CBM. The two eigenstates associated with the flat bands have well-separated charge densities both in space and energy. The isosurfaces of charge densities for VBM, CBM and flat bands are around energy ranges of [-0.15, 0.03] eV, [2.06, 2.10] eV and [0.26, 0.28] eV, respectively. The charge densities were calculated via ONETEP by setting the parameters "homo_plot" and "lumo_plot" to the numbers of bands below and above the Fermi level desired to plot, respectively. Red, blue and yellow colours refer to Nb, W and S atoms, respectively. 75

5.9 Normalised electrical conductivity (σ/τ) as a function of extrinsic doping for $W_{1-x}Nb_xS_2$ monolayers with dopant distributions named as "random" ($x = 0.219$), "real (isolated Nb)" ($x = 0.125$), "half line" ($x = 0.063$), "real (line Nb)" ($x = 0.141$) and "perfect line" ($x = 0.125$) along the direction parallel to the line and perpendicular to the line at $T = 300$ K. The "real (isolated Nb)" and "real (line Nb)" are based on two representative regions of the ADF-STEM image in figure 5.1(a). The ratio is the conductivity along the direction of parallel to the line divided by the conductivity along the direction perpendicular to the line. For the atomic structures: red, blue and yellow colours refer to Nb, W and S atoms, respectively. 77

6.1 Schematic diagrams of InSe bilayers with different stacking arrangements, denoted as (a) A-1 (b) A-2 (c) B-1 (d) B-2 (e) B-3. Grey: In, yellow: Se. All In and Se atoms (In_{ij} and Se_{ij}) in (a) are labelled for later discussions, where i refers to the vertical position of In or Se atom (t: top atom, b: bottom atom) in the top or bottom layers, whereas j refers to the top or bottom layer (t: top layer, b: bottom layer). 81

6.2 Top view of the (a) A-type (b) B-type twisted InSe bilayer with a twist angle of 4.4°. Grey: In, yellow: Se. 85

6.3 Band structures of InSe monolayer and InSe bilayers with different stacking configurations. 87

6.4 Projected band structures for InSe monolayer. In_t and Se_t refer to In and Se atoms in the top layer, respectively. In_b and Se_b refer to In and Se atoms in the bottom layer, respectively. 88

6.5 Projected band structures for InSe bilayers with different stacking configurations. Black, red and magenta refer to the s, p_z and p_y (or p_x) orbitals of In atoms, whereas blue and green refer to the p_z, p_y (or p_x) orbitals of Se atoms. 88

6.6 The contribution from p_z orbitals of each Se atom for the VBM in InSe bilayers with different stacking configurations. 92

6.7 Band structures of InSe monolayer with different twist angles (0°, 4.4°, 10°, 20°, 30°, 40° and 50°) along Γ to $\mathbf{K}$ of an untwisted (0°) InSe monolayer. 93

6.8 Total energy as a function of (a) interlayer distance without considering the out-of-plane corrugation (b) averaged corrugation for the A-type twisted InSe bilayer ($\theta = 4.4^o$). 94
6.9 Distribution of the corrugation of each atom with considering the interlayer distance in each region for the A-type twisted InSe bilayer ($\theta = 4.4^o$). The x and y axes refer to the atomic position in x and y direction. 95
6.10 Distribution of the residual total force for the A-type twisted InSe bilayer ($\theta = 4.4^o$, $d = 8.89$ Å, corrugation $\simeq 0.1$ Å). (a)-(d) Before the structural relaxation (e)-(h) After the structural relaxation. The x and y axes refer to the atomic position in x and y direction. 96
6.11 Distribution of the residual force for the A-type twisted InSe bilayer ($\theta = 4.4^o$, $d = 8.89$ Å, corrugation $\simeq 0.1$ Å) after the structural relaxation. (a)-(d) Residual forces along z direction (e)-(h) Residual forces in xy plane. The x and y axes refer to the atomic position in x and y direction. 98
6.12 Effective band structure along Γ to $\mathbf{K}$ of (a) InSe monolayer (without SOC) (b) InSe monolayer (with SOC) (c) A-type twisted InSe bilayer (without SOC) (d) A-type twisted InSe bilayer (with SOC) (e) A-type twisted InSe/hBN/InSe heterostructure (without SOC) (f) A-type twisted InSe/hBN/InSe heterostructure (with SOC). A Lorentzian broadening of 0.02 eV was employed in the effective band structures. 100
6.13 Effective band structure along Γ to $\mathbf{K}$ of the B-type twisted InSe bilayer with a twist angle of (a) 4.4^o (without SOC) (b) 4.4^o (with SOC) (c) 17.9^o (without SOC) (d) 17.9^o (with SOC) (e) 27.8^o (without SOC) (f) 27.8^o (with SOC). A Lorentzian broadening of 0.02 eV was employed in the effective band structures. 101
6.14 Top view of the (a) A-type (b) B-type twisted InSe/hBN/InSe heterostructure with a twist angle of $\theta = 4.4^o$. $\phi = 32.2^o$ is the twist angle between InSe and hBN layers. Grey: In, yellow: Se, blue: B and green: N. The moiré pattern can be clearly seen when repeating the unit cell. 102

6.15 (a) Effective band structure along Γ to **K** of the A-type twisted InSe/hBN/InSe heterostructure with a twist angle of 4.4° projected on the hBN layer. A Lorentzian broadening of 0.02 eV was employed in the effective band structures. (b) Projected density of states of the A-type twisted InSe/hBN/InSe heterostructure. In_{Bottom} and In_{Top} refer to In atoms in the bottom and the top InSe layers, respectively. Se_{Bottom} and Se_{Top} refer to Se atoms in the bottom and the top InSe layers, respectively. SOC was not included in the calculations. 103
6.16 Effective band structure of the A-type twisted InSe bilayer ($\theta = 4.4^o$) (a) without (b) with considering the corrugation. A Lorentzian broadening of 0.02 eV was employed in the effective band structures. Some increases of the separations between neighbouring bands are indicated by the double-headed arrows. SOC was not included in the band structure calculations. 104
6.17 Effective band structure along Γ to **K** of the A-type twisted InSe bilayer projected on the (a)(c) bottom (b)(d) top InSe layer with a twist angle of (a)(b) $\theta = 4.4^o$ (c)(d) $\theta = 17.9^o$. Effective band structure of the A-type twisted InSe/hBN/InSe heterostructure projected on the (e) bottom (f) top InSe layer with a twist angle of $\theta = 4.4^o$. A Lorentzian broadening of 0.02 eV was employed in the effective band structures. SOC was not included in the band structure calculations. 105
6.18 Effective band structure along Γ to **K** of the B-type twisted InSe bilayer projected on the (a)(c)(e) bottom (b)(d)(f) top InSe layer with a twist angle of (a)(b) $\theta = 4.4^o$ (c)(d) $\theta = 17.9^o$ (e)(f) $\theta = 27.8^o$. A Lorentzian broadening of 0.02 eV was employed in the effective band structures. SOC was not included in the band structure calculations. 106

6.19 (a) Effective band structure along Γ to **K** of the A-type twisted InSe bilayer with a twist angle of 4.4°. (a) Without SOC (b) With SOC. The green and yellow curves refer to the two different spin states for the same band in the A-1, whereas the blue and pink curves refer to the two different spin states for the same band in the A-2. These bands were all calculated by Quantum Espresso in the primitive cells with the same interlayer distance as twisted InSe bilayer. A Lorentzian broadening of 0.02 eV was employed in the effective band structures. Isosurface of the charge density corresponds to the (c) A-1 around an energy range of [-0.03, 0.00] eV (d) A-2 around an energy range of [-0.20, -0.17] eV without considering SOC. The charge densities were calculated via ONETEP by setting the parameter "homo_plot" to the number of bands below the Fermi level desired to plot. 108

6.20 Effective band structure along Γ to **K** of the A-type and B-type twisted InSe bilayers with different twist angles. (a) A type with θ= 4.4° (b) B type with θ= 4.4° (c) A type with θ= 17.9° (d) B type with θ= 17.9° (e) A type with θ= 27.8° (f) B type with θ=27.8°. Green (A-1 or B-1), blue (A-2 or B-2) and purple (B-3) curves are the bands corresponding to the bottom InSe layer, whereas yellow (A-1 or B-1), pink (A-2 or B-2) and cyan (B-3) are the bands corresponding to the top InSe layer. All these colour curves were calculated by Quantum Espresso in the primitive cells with the same interlayer distance as twisted InSe bilayers. A Lorentzian broadening of 0.02 eV was employed in the effective band structures. SOC was not included in the band structure calculations. 109

6.21 (a) Topmost valence band and the band below it along Γ to **K** for the A-2 at two different lattice constants. Black: 4.059 Å (lattice constant of InSe monolayer and twisted InSe bilayer), red: 4.067 Å (lattice constant of the A-2). (b) Topmost valence band and the band below it for InSe bilayers with different stacking configurations at two different interlayer distances. 8.89 Å and 8.82 Å are the optimised interlayer distances (without considering the corrugation) for the A-type and B-type twisted InSe bilayers with a twist angle of 4.4°, respectively. Another interlayer distance in each stacking configuration is the optimised interlayer distance of InSe bilayer with each stacking configuration (see table 6.1). 110

6.22 Effective band structure along Γ to $\mathbf{K}$ of the (a) A-type (b) B-type InSe/hBN/InSe heterostructure with a twist angle of 4.4°. Bands of InSe monolayer calculated by Quantum Espresso in the primitive cells was shown in purple colours. A Lorentzian broadening of 0.02 eV was employed in the effective band structures. 111
6.23 Interlayer distance as a function of twist angle for the A-type (black) and B-type (red) twisted InSe bilayers. Corrugation was not considered here. 112
6.24 Topmost valence band and the band below it along Γ to $\mathbf{K}$ for InSe bilayers with different stacking configurations at different twist angles and interlayer distances. Solid and dashed curves refer to the bands for the bottom InSe layer and top InSe layer, respectively. The kpoint path (Γ to $\mathbf{K}$) shown here is according to the kpoint path of the bottom InSe layer. 113
6.25 Intralayer and interlayer exciton binding energies of twisted InSe bilayer in the environment of (a) vacuum corresponding to table 6.4 (b) hBN corresponding to table 6.5. 114

Acknowledgments

My supervisor, Dr. Nicholas Hine, has given me a lot of help and support over the years when I am studying my PhD. Thank you for giving me lots of advice on my research, academic and computational knowledge. Without his help, I would not be able to get the Chancellor's International Scholarship and study in the University of Warwick. I really thank University of Warwick for providing me this scholarship, otherwise, I may not have the chance to pursue my PhD degree.

I would also like to thank Dr. Nelson Yeung, Dr. Joly Aarons and Dr. Kenming Lin in providing me various academic advices. Furthermore, I must thank Wanting Gao and Ming-Hung Wu in sharing the happy and sad moments of life with me.

Finally, I am deeply thankful to my beloved family for always supporting me in my life.

All works shown in this thesis used the High Performance Computing Service, the Scientific Computing Research Technology Platform of the Univeristy of Warwick, ARCHER UK National Supercomputing Service (http://www.archer.ac.uk), via the UKCP consortium (EP/P022561/1), ARCHER2 UK National Supercomputing Service (http://www.archer2.ac.uk). We acknowledge the use of Athena at HPC Midlands+ ,which was funded by the EPSRC on grant EP/P020232/1.

Declarations

This thesis is submitted to the University of Warwick in support of my application for the degree of Doctor of Philosophy. It has been composed by myself and has not been submitted in any previous application for any degree.

The work presented (including data generated and data analysis) was carried out by the author except for chapter 4 and 5, the experimental results (including synthesis and measurements of the transition metal dichalcogenide alloys) were provided by our collaborators led by Dr. Neil R. Wilson, from the University of Warwick.

Parts of this thesis have been published in the following papers:

1. Chapter 4: Two-dimensional transition metal dichalcogenide alloy-$Mo_{1-x}W_xS_2$ monolayer

- X. Xia, S. M. Loh, J. Viner, N. C. Teutsch, A. J. Graham, V. Kandyba, A. Barinov, A. M. Sanchez, D. C. Smith, N. D. M. Hine, and N. R. Wilson. Atomic and electronic structure of two-dimensional $Mo_{(1-x)}W_xS_2$ alloys. *J. Phys. Mater.*, 4:025004, 2021.

2. Chapter 5: Two-dimensional transition metal dichalcogenide alloy-$W_{1-x}Nb_xS_2$ monolayer

- S. M. Loh, X. Xia, N. R. Wilson, and N. D. M. Hine. Strong in-plane anisotropy in the electronic properties of doped transition metal dichalcogenides exhibited in $W_{1-x}Nb_xS_2$. *Phys. Rev. B*, 103:245410, 2021.

Abstract

The effects of alloying and twisting on the atomic and electronic structures of two-dimensional metal chalcogenides which are current interests of scientific community have been studied in this thesis. Monte Carlo simulations and statistical analysis of the atomic configurations of the as-grown crystal of $Mo_{1-x}W_xS_2$ monolayers synthesised by our experimental collaborators both consistently suggest a random distribution. The results calculated by using the ONETEP linear-scaling density functional theory package and the angle-resolved photoemission spectroscopy measurements give consistent results for the bandwidth and the band splitting due to spin-orbit coupling near the topmost valence band at $\mathbf{K}$. The spin-valley locking is proved to be maintained at $x = 0.5$ through polarisation-resolved photoluminence measurements. In contrast, a striking dopant distribution with striped pattern was observed in the as-grown crystal of $W_{1-x}Nb_xS_2$ monolayer synthesised by our experimental collaborators, different from the random distribution of $Mo_{1-x}W_xS_2$ monolayer. Through the analysis of the binding energy of various dopant distributions, the kinetic processes and the energetics both play roles in forming this kind of dopant distribution. A highly anisotropic conductivity is predicted by our calculations in this alloy. The twistronics in InSe is discussed in the final part of the thesis. We show that the calculations on the InSe bilayer within the primitive cell can be used to efficiently obtain the topmost valence band of twisted InSe bilayer. The effective mass for holes remains approximately a constant as twist angle varies. It is estimated to be ~ 441.1 meV and ~ 183.2 meV for A1s intralayer and interlayer exciton binding energies in twisted InSe bilayer regardless of the twist angle. The encapsulated hBN layer in the twisted InSe bilayer is regarded as a spacer to weaken the interaction between two InSe layers. The band structure of the hBN-spaced system can also be well-described by InSe monolayer within the primitive cell calculation. The A1s intralayer exciton binding energy of this system is calculated to be 232.9 meV by using the effective mass for holes of InSe monolayer.

Abbreviations

ADF Annular Dark-Field

ADF-STEM Annular Dark-Field Scanning Transmission Electron Microscopy

AFM Atomic Force Miscroscopy

ARPES Angle-Resolved Photoemission Spectroscopy

ASE Atomic Simulation Environment

B88 Becke

BSE Bethe-Salpeter Equation

CBM Conduction Band Minimum

CDW Charge Density Wave

C/M Chalcogen to Metal

CVD Chemical Vapor Deposition

CPA Coherent Potential Approximation

CVT Chemical Vapor Transport

DFT Density Functional Theory

DOS Density Of States

EBS Effective Band Structure

EDX Energy Dispersive X-ray analysis

FET Field Effect Transistor

FFT Fast Fourier Transform

GBRV Garrity, Bennett, Rabe, Vanderbilt

GGA Generalised Gradient Approximation

hBN Hexagonal Boron Nitride

JTH Jollet, Torrent, Holzwarth

LDA Local Density Approximation

LNV Li, Nunes and Vanderbilt

LS-DFT Linear-Scaling Density Functional Theory

NCPP Norm-Conserving Pseudopotential

NGWF Nonorthogonal Generalised Wannier Function

PAW Projected augmented wave

PBE Perdew, Burke and Enzerhof

PC Primitive Cell

PDOS Projected Density Of States

PL Photoluminescence

PTMC Post-Transition Metal Monochalcogenide

PW91 Perdew and Wang

ONETEP Order-N Electronic Total Energy Package

QSGW Quasiparticle Self-consistent GW approximation

SC Supercell

SDW Spin Density Wave

SL Semilocal

SOC Spin-Orbit Coupling

STEM Scanning Transmission Electron Microscopy

TMDC Transition Metal Dichalcogenide

VBM Valence Band Maximum

vdW van der Waals

VCA Virtual Crystal Approximation

XC Exchange Correlation [functional]

XPS X-ray Photoelectron Spectroscopy

Chapter 1

Introduction

Many novel phenomena emerge when a well-known 3D system is thinned down to a lower dimension [1, 2, 3, 4, 5]. Graphene [6, 7], as one of the most typical two-dimensional materials, exhibit several superior properties. For example, the mobility of charge carriers is very high (2×10^5 cm^{2}V^{-1}s^{-1}) [8, 9] because there is no scattering for a propagation distance of charge carrier of micrometres [10], high thermal conductivity near room temperature [11], no rest mass [12] and quantum Hall effect [12] in graphene. However, it is hard for graphene to be applied in field effect transistors (FETs) because the ratio between "on" current and "off" current ($I_{\text{on}}/I_{\text{off}}$) is small [13] and optoelectronics because the band gap is zero [14]. Other two-dimensional materials, such as hexagonal boron nitride (hBN) [15, 16], black phosphorus [17, 18], transition metal dichalcogenides (TMDCs) [1, 4, 19] and post-transition metal monochalcogenides (PTMCs) [20, 21] have similar honeycomb lattice structures, except that the vertical positions of atoms may be different. These materials are regarded as very promising materials in optoelectronics [22, 23, 24, 25, 26], electronic devices [26, 27, 28, 29], electrocatalysis [30] and superconductors [31, 32]. This thesis aims to provide inspiration for how the atomic and electronic properties of the promising TMDCs and PTMCs change by alloying and twisting. WS_2 as one of the most typical TMDCs was adopted as a prototype. We were interested to know what phenemena will be seen when it is alloyed with a similar material (MoS_2) and a different material (NbS_2). Furthermore, InSe as one of the promising PTMCs was also adopted to study the variation of atomic and electronic structures when twisting. Generalising from the four prototypical materials investigated here, the knowledge obtained from these methods (alloying and twisting) is expected to extend to other similar materials, such as $MoSe_2$, WSe_2, $NbSe_2$, InS and etc.

Radisavljevic et al. [28] have shown that MoS_2 monolayer possesses high carrier mobility (at least 200 $cm^2V^{-1}s^{-1}$) and high current on/off ratio (1×10^8) in transistors at room temperature, along with negligible standby power dissipation. In the bulk form, the valence band maximum (VBM) is at Γ, whereas the conduction band minimum (CBM) is at a position between Γ and $\mathbf{K}$ [33, 34]. In contrast, the VBM and the CBM are at $\mathbf{K}$ for MoS_2 monolayer [33, 34]. Thus, the resulting band gaps are direct and indirect for the monolayer and bulk forms, respectively [33, 34]. An indirect-direct band gap transition occurs when thinning down MoS_2 from bulk to monolayer [35]. The band gap of MoS_2 is 1.287 eV for bulk and 2.759 eV for monolayer based on a quasiparticle self-consistent GW approximation (QSGW) [35], whereas the band gap is 1.23 eV for bulk and 1.9 eV for monolayer from experiments [27, 36]. This large deviation of the band gap between the QSGW and the experiment in MoS_2 monolayer is related to the significant excitonic effect (2D Wannier-Mott excitons recombination) in the 2D system [33, 35, 37]. The option of using both GW approximation and Bethe-Salpeter equation (BSE) [38, 39] can produce consistent results with absorption and photoluminescence (PL) [40]. Furthermore, the band splitting owing to the spin-orbit coupling (SOC) are pronounced in MoS_2 monolayer (especially near the VBM with $\sim$ 150 meV at $\mathbf{K}$) owing to the lack of inversion symmetry [33, 41]. A WS_2 monolayer has a greater valence band splitting near the Fermi level at $\mathbf{K}$ ($\sim$ 400 meV) than MoS_2 monolayer due to its larger atomic number [41, 42, 43]. The atomic and electronic structures of WS_2 are similar to MoS_2, there is also an indirect-direct band gap transition from WS_2 bulk to WS_2 monolyers [44, 45]. WS_2 based FET gives $\sim 1 \times 10^6$ and $\sim$ 140 cm^2 V^{-1} s^{-1} of current on/off ratio at high room temperature and mobility at low temperature, respectively [46]. The mixing of these two materials can be realised from a few synthetic approaches, for examples, chemical vapor transport (CVT) [42], chemical vapor deposition (CVD) [47, 48] and co-sputtering technique [49] with the composition determined by the ratio of the raw materials of MoS_2 to WS_2. The resulting alloys were shown to be highly homogenous from Raman spectroscopy with no phase segregation in the samples [50].

NbS_2 has been proposed to give an open-circuit voltage as good as gold in perovskite solar cell and 8.3% for power conversion efficiency as a counter electrode [51]. It was also calculated to be good in application of lithium-ion batteries at room temperature, where Li^+ adsorption is highly stable and Li diffused with high speed, thus it is promising to be the negative electrode of lithium-ion batteries [52]. Furthermore, the decrease of the density of mobile holes leads to the superconducting transition temperature of NbS_2 decreases as the thickness decreases [53]. The

photoresponse and response time were measured to be 34.7 mA/W and 488 μs in few-layer InSe, respectively, which is sufficiently promising to be applied in optoelectronics [54]. In addition, the quantum Hall effect can be observed in the hexagonal boron nitride (hBN) encapsulated InSe, which displays a carrier Hall mobility of 5000 cm^2 V^{-1} s^{-1} at 1.5 K [55].

Density functional theory (DFT) has been widely adopted as a tool to provide predictions and explanations of experimental results in investigating various properties of different materials for decades. However, the computational effort increases with the cube of the system size [56]. Linear-scaling density functional theory (LS-DFT) [57, 58, 59] has been proposed to ease the difficulty of studying large-scale system. In this thesis, both traditional DFT with plane wave basis and LS-DFT with highly localised basis were adopted for different purposes. Highly accurate traditional DFT package such as CASTEP [60] and Quantum Espresso [61, 62] were used to calculate the atomic parameters (e.g. lattice constant and interlayer distance), total energy of the system and geometry optimisation of smaller system. The LS-DFT package used in this thesis, ONETEP [59, 63], was adopted to do structural relaxation and study the effective band structures as well as the electronic properties of large-scale systems (more than hundred atoms). The results of LS-DFT can be tuned to approach the accuracy of traditional DFT package (e.g. CASTEP), by improving a parameter similar to the kinetic energy cut-off of the plane waves [56, 64]. The spectral function unfolding method implemented in ONETEP [42, 65, 66] facilitates us to efficiently simulate the electronic structure in large-scale system, even it is an disordered material. Furthermore, a non-empirical Monte Carlo [67] simulation based on the binding energy calculated via CASTEP was also used to simulate the dopant distributions of alloys purely from the perspective of energetics. In addition, a post-processing package based on semi-classical Boltzmann transport equations, BoltzTrap [68], was used to study the macroscopic electrical conductivity of the alloy (instead of the microscopic ballistic carrier transport).

In Chapter 4, the alloys composed of MoS_2 and WS_2 monolayers (denoted as $Mo_{1-x}W_xS_2$ monolayer, where $0 \leq x \leq 1$) were studied. A plane-wave (CASTEP [60]) and a linear-scaling (ONETEP [59, 63]) density-functional theory packages were adopted to study the $Mo_{1-x}W_xS_2$ monolayer. It is suggested a random distribution of tungsten dopants in MoS_2 monolayer from the Monte Carlo simulations [67] based on the binding energy calculated via CASTEP. This result is consistent with the experiments provided by our collaborators as well as the previous studies on this alloy [69]. Various electronic properties studied such as bandwidth, effective mass for holes and valence band splitting at **K** as a function of W composition are

consistent with the results of angle-resolved photoemission spectroscopy (ARPES). As expected, the band gaps of $Mo_{1-x}W_xS_2$ monolayer significantly deviate from PL measurement due to the inaccuracy of conduction band in DFT calculation, absence of excitonic effect and absence of intrinsic carriers of the as-grown crystals in the DFT calculations. In addition, the polarisation-resolved low-temperature PL measurement performed by our experimental collaborators showed that there is spin-valley locking in $Mo_{1-x}W_xS_2$ monolayer.

Unlike the situation of alloys formed by MoS_2 and WS_2 monolayers, a different combination of TMDCs (WS_2 and NbS_2 monolayers) was studied in Chapter 5, performing with the same simulation packages. WS_2 is a kind of semiconductor type TMDC, whereas NbS_2 is a metal [70]. The dopant (Nb atoms) distribution in the WS_2 monolayer is significantly different from $Mo_{1-x}W_xS_2$ monolayer. The scanning transmission electron microscopy (STEM) images provided by our collaborators as well as the analysis of our DFT calculations both showed that Nb atoms prefer to align along a specific direction. A lot of line segments were seen in the STEM images. Kinetic processes are suggested to be important factors to form this kind of dopant distributions. After analysing the effective band structure and the calculated electrical conductivity (through BoltzTrap [68]), it is suggested that superior and highly anisotropic electrical conductity can be realised.

Inspired by the novel properties of the recently emerging twisted graphene bilayer, twisted InSe bilayer was discussed in Chapter 6. In the previous literature, many novel phenomena appear when the relative angle between two graphene layers was tuned to some "magic angles". The zero Fermi velocity and the flattening of moiré Bloch bands at magic angles in twisted graphene bilayer have been analysed by utilizing a fundamental continuum model [71, 72, 73, 74, 75]. Superconducting and correlated insulating phases have been demonstrated in graphene bilayer at a twist angle of $\sim 1.1^o$ owing to the flat bands associated with the strong correlations [76]. The appearance of flat bands can occur without the need for magic angles if we switch from graphene to other 2D materials. From the work of Xian et al. [77], n-fold ($n = 2, 4, 6$) degenerate flat bands appear at twist angles which are not close to magic angles in twisted boron nitride bilayer, thus providing a new way to tune their optical and excitonic properties. Kang et al. [78] showed flat bands, indirect-direct band gap transition and localisation of charge density in twisted InSe bilayer as the twist angle decreases. In this thesis, the atomic and electronic properties of InSe monolayer, InSe bilayers with different stacking configurations, twisted InSe bilayer and hBN-encapsulated twisted InSe bilayer were studied. The band structures of InSe bilayers with different stacking configurations can be explained by their orbital contributions

and the stacking configuration. The effective band structure of twisted InSe bilayer is strongly related to InSe bilayers with different stacking configurations appeared within some regions of twisted InSe bilayer from the analysis of both the band structure and the localisation of charge density. Furthermore, the encapsulation of hBN layer in twisted InSe bilayer has the effect of weakening the interaction between two InSe layers. Twistronics is proved to be an efficient method to tune the electronic properties including the band gap and effective mass for holes of InSe from this study, thus widening its applications in optoelectronics and semiconductor devices.

Through these different manipulation techniques, the knowledge of the atomic structure and electronic properties of these kind of materials were deepened and thus benefit their future applications.

Chapter 2

Theory of electronic structure based on *ab initio* calculations

Most of the contents in this chapter are based on “Electronic structure : basic theory and practical methods” written by R. M. Martin [79].

2.1 In a many-particle system

The Schrödinger equations are the fundamental equations of quantum mechanics and are classified to be used in time-independent and time-dependent situations. In this thesis, the time-independent form is adopted because time-dependent interactions among atoms were not considered. The time-independent Schrödinger equation is

$$\hat{H}\Psi = E\Psi, \tag{2.1}$$

where $\hat{H}$ is the Hamiltonian operator, Ψ and E are the eigenfunction and energy eigenvalue of the Hamiltonian operator, respectively. In a material, all information about the positions of electrons and nuclei are described by a many-body wave function. Importantly, the Hamiltonian operator needs to include all the pairwise interactions among electrons and atomic nuclei [79],

$$\begin{aligned}\hat{H} = &-\frac{\hbar^2}{2m}\sum_{i=1}^{n}\nabla_i^2 - \sum_{i=1}^{n}\sum_{I=1}^{N}\frac{Z_I e^2}{|\mathbf{r}_i - \mathbf{R}_I|} + \frac{1}{2}\sum_{i\neq j}^{n}\frac{e^2}{|\mathbf{r}_i - \mathbf{r}_j|} \\ &-\sum_{I}^{N}\frac{\hbar^2}{2M_I}\nabla_I^2 + \frac{1}{2}\sum_{I\neq J}^{N}\frac{Z_I Z_J e^2}{|\mathbf{R}_I - \mathbf{R}_J|},\end{aligned} \tag{2.2}$$

where $\hbar = h/2\pi$ (h is the Planck constant), e is the elementary charge, Z_I is the charge of atomic nucleus I. Here lowercase letters are used to denote electrons, whereas uppercase letters are used to denote atomic nuclei. Thus, m and M_I are the masses of electron and atomic nucleus, respectively. Similarly, $\mathbf{r}_i$ and $\mathbf{R}_I$ are the positions of electron and atomic nucleus, respectively. The first and fourth terms are the sum of kinetic energy of each electron and atomic nucleus, respectively. The second, third and fifth terms are the sum of the Coulomb interactions between an electron and an atomic nucleus, an electron and an electron and an atomic nucleus and an atomic nucleus, respectively. According to the Born-Oppenheimer or adiabatic approximation [80], the motion of electrons and atomic nuclei can be treated separately. This is because of the large difference of mass between an atomic nucleus and an electron, thus the motion of electron is instantaneous compared to the atomic nucleus. The kinetic term of the atomic nuclei (fourth term) can be treated separately because its inverse mass is far smaller than electrons. Thus the Hamiltonian in eq. (2.2) can be simplified to only concern about the motion of electrons with the terms related to the atomic nuclei are approximated as parameters in the Hamiltonian [79]. This makes calculation of the many-body system feasible after adopting this approximation.

The Hamiltonian operator for the electrons after adopting the Born-Oppenheimer approximation, in which the nuclear coordinates were represented by a set of parameters R, is written as [79]

$$\begin{aligned}\hat{H} &= \sum_{i=1}^{n} -\frac{1}{2}\nabla_i^2 + \sum_{i=1}^{n}\sum_{I=1}^{N} \frac{Z_I}{|\mathbf{r}_i - \mathbf{R}_I|} + \frac{1}{2}\sum_{i \neq j}^{n} \frac{1}{|\mathbf{r}_i - \mathbf{r}_j|} + \frac{1}{2}\sum_{I \neq J}^{N} \frac{Z_I Z_J}{|\mathbf{R}_I - \mathbf{R}_J|} \\ &= \hat{T} + \hat{V}_{\text{ext}} + \hat{V}_{\text{int}} + E_{\text{II}},\end{aligned} \tag{2.3}$$

where $\hat{T}$ is the kinetic term of the electrons, $\hat{V}_{\text{ext}}$ and $\hat{V}_{\text{int}}$ are the classical Coulomb potential terms associated with the electron-nucleus interaction and electron-electron interaction, respectively. More terms will be added into $\hat{V}_{\text{ext}}$ if the system is under an external field such as electric field or magnetic field. Lastly, E_{II} is the electrostatic nucleus-nucleus interaction which can be regarded as a parametric constant in this Hamiltonian operator. It is noted here that the Hartree atomic units have been used, so that $\hbar = m = e = 4\pi\epsilon_0 = 1$.

The Hartree potential was introduced by Hartree [81] to approximate the potential of the self-interaction term of electrons (the third term in eq. (2.3)) for further reducing the computational effort. This is a Coulomb potential determined

by the electron charge density $n(\mathbf{r}')$ [79],

$$V_{\mathrm{H}}(\mathbf{r}) = \int\int \frac{n(\mathbf{r}')}{|\mathbf{r}-\mathbf{r}'|}\, d\mathbf{r}'. \tag{2.4}$$

The many-body wave function can be expressed by an antisymmetric Slater determinant (without considering the spin-orbit interaction) [79, 82],

$$\Psi = \frac{1}{(N!)^{\frac{1}{2}}} \begin{vmatrix} \psi_1(\mathbf{r}_1,\sigma_1) & \psi_1(\mathbf{r}_2,\sigma_2) & \psi_1(\mathbf{r}_3,\sigma_3) & \dots \\ \psi_2(\mathbf{r}_1,\sigma_1) & \psi_2(\mathbf{r}_2,\sigma_2) & \psi_2(\mathbf{r}_3,\sigma_3) & \dots \\ \psi_3(\mathbf{r}_1,\sigma_1) & \psi_3(\mathbf{r}_2,\sigma_2) & \psi_3(\mathbf{r}_3,\sigma_3) & \dots \\ . & . & . & \dots \\ . & . & . & \dots \end{vmatrix}, \tag{2.5}$$

where the $\psi_i(\mathbf{r}_j,\sigma_j)$ is a single-particle wave function with state i. The $\psi_i(\mathbf{r}_j,\sigma_j)$ is linearly independent with any other single-particle wave function in this determinant. This kind of wave function implicitly implies that the electrons satisfy the Pauli exclusion principle. Each $\psi_i(\mathbf{r}_j,\sigma_j)$ in eq. (2.5) satisfies the one-electron Schrödinger equation [83]

$$-\frac{\hbar^2}{2m}\nabla^2\psi_i(\mathbf{r}) - \sum_I \frac{Ze^2}{|\mathbf{r}-\mathbf{R}_I|}\psi_i(\mathbf{r}) + \sum_k \int d\mathbf{r}'\,\frac{|\psi_k(\mathbf{r}')|^2 e^2}{|\mathbf{r}-\mathbf{r}'|}\psi_i(\mathbf{r}) = \epsilon_i\psi_i(\mathbf{r}) \tag{2.6}$$

The expectation value of an operator $\hat{O}$ can be expressed as [79]

$$\langle\hat{O}\rangle = \sum_i^{\sigma} f_i^{\sigma}\langle\psi_i^{\sigma}|\hat{O}|\psi_i^{\sigma}\rangle, \tag{2.7}$$

where ψ_i^{σ} is a spin-dependent one-electron wave function with state i and spin σ, whereas f_i^{σ} is its corresponding occupation number,

$$f_i^{\sigma} = \frac{1}{e^{\beta(\epsilon_i^{\sigma}-\mu)}+1}. \tag{2.8}$$

This is the Fermi-Dirac distribution with chemical potential μ. Therefore, the total energy of the non-interacting electrons can be written as [79]

$$E = \langle\hat{H}\rangle = \sum_i^{\sigma} f_i^{\sigma}\epsilon_i^{\sigma}, \tag{2.9}$$

and the total electron density can be expressed as the sum of each electron density

in state i

$$N^{\sigma}(\mathbf{r}) = \sum_i n_i^{\sigma} = \sum_i f_i^{\sigma} |\psi_i^{\sigma}(\mathbf{r})|^2. \tag{2.10}$$

In addition, the total electron density can also be obtained when the density matrix operator acts on the many-body wave function. The density matrix operator is written as [79]

$$\hat{\rho} = \sum_i |\psi_i^{\sigma}\rangle f_i^{\sigma} \langle \psi_i^{\sigma}|. \tag{2.11}$$

There is a more accurate approximation referred to as the Hartree-Fock approximation [84] which includes the exchange interaction among electrons. The expectation value of the Hamiltonian operator when the basis function of spin is diagonal [79],

$$\begin{aligned}\langle \Psi|\hat{H}|\Psi\rangle =& \sum_{i,\sigma} \int d\mathbf{r}\, \psi_i^{\sigma *}(\mathbf{r}) \left[-\frac{1}{2}\nabla^2 + V_{\text{ext}}(\mathbf{r})\right] \psi_i^{\sigma} + E_{\text{II}} \\ &+ \frac{1}{2} \sum_{i,j,\sigma_i,\sigma_j} \int\int d\mathbf{r}d\mathbf{r}'\, \psi_i^{\sigma_i^*}(\mathbf{r})\psi_j^{\sigma_j^*}(\mathbf{r}') \frac{1}{|\mathbf{r}-\mathbf{r}'|} \psi_i^{\sigma_i}(\mathbf{r})\psi_i^{\sigma_j}(\mathbf{r}') \\ &- \frac{1}{2} \sum_{i,j,\sigma} \int\int d\mathbf{r}d\mathbf{r}'\, \psi_i^{\sigma^*}(\mathbf{r})\psi_j^{\sigma^*}(\mathbf{r}') \frac{1}{|\mathbf{r}-\mathbf{r}'|} \psi_i^{\sigma}(\mathbf{r})\psi_i^{\sigma}(\mathbf{r}'),\end{aligned} \tag{2.12}$$

where the third term is the direct interaction, whereas the fourth term is the exchange interactions among the same-spin electrons. The unphysical terms for $i = j$ in direct and exchange terms are eliminated when adding them up in the equation. Thus, the effective potential can also be expressed as $\hat{V}_{\text{eff}}^{i,\sigma}(\mathbf{r}) = V_{\text{ext}}(\mathbf{r}) + V_{\text{H}}(\mathbf{r}) + \hat{V}_{\text{x}}^{i,\sigma}(\mathbf{r})$, where $V_{\text{H}}(\mathbf{r})$ and $\hat{V}_{\text{x}}^{i,\sigma}(\mathbf{r})$ correspond to the third and fourth terms in eq. (2.12), respectively [79]. It is not an easy task to solve the Hartree-Fock equations and it is still not accurate for some materials (e.g. solids) since the correlations among electrons are not considered.

2.2 Hohenberg-Kohn theorems

Density functional theory (DFT) is based on two theorems proposed by Hohenberg and Kohn [85]. It provides a feasible way different from Hartree-Fock approximation, to solve the many-body system of interacting particles.

2.2.1 Theorem I

There is a one-to-one correspondence between the external potential V_{ext} defined to within an unknown constant shift and the ground state particle density $n_0(\mathbf{r})$ in an interacting particle system [79, 85].

Proof

Suppose $V_{\text{ext}}^{(1)}(\mathbf{r})$ is a unique external potential in a Hamiltonian operator $\hat{H}^{(1)}$ with ground state wave function $\Psi^{(1)}$ and ground state density $n_0(\mathbf{r})$. $V_{\text{ext}}^{(2)}(\mathbf{r})$ is another external potential different from $V_{\text{ext}}^{(1)}(\mathbf{r})$ (not just by a constant) in a Hamiltonian operator $\hat{H}^{(2)}$ with ground state wave function $\Psi^{(2)}$ and the same ground state density $n_0(\mathbf{r})$. This gives the following inequality:

$$E^{(1)} = \langle \Psi^{(1)} | \hat{H}^{(1)} | \Psi^{(1)} \rangle < \langle \Psi^{(2)} | \hat{H}^{(1)} | \Psi^{(2)} \rangle. \tag{2.13}$$

The last term in eq. (2.13) can be reformulated as

$$\begin{aligned} \langle \Psi^{(2)} | \hat{H}^{(1)} | \Psi^{(2)} \rangle =& \langle \Psi^{(2)} | \hat{H}^{(2)} | \Psi^{(2)} \rangle + \langle \Psi^{(2)} | \hat{H}^{(1)} - \hat{H}^{(2)} | \Psi^{(2)} \rangle \\ =& E^{(2)} + \int d^3r \left[V_{\text{ext}}^{(1)}(\mathbf{r}) - V_{\text{ext}}^{(2)}(\mathbf{r}) \right] n_0(\mathbf{r}). \end{aligned} \tag{2.14}$$

From eq. (2.13) and eq. (2.14), the inequality now is written as

$$E^{(1)} < E^{(2)} + \int d^3r \left[V_{\text{ext}}^{(1)}(\mathbf{r}) - V_{\text{ext}}^{(2)}(\mathbf{r}) \right] n_0(\mathbf{r}). \tag{2.15}$$

The inequality for superscript (2) is written in a similar way,

$$E^{(2)} < E^{(1)} + \int d^3r \left[V_{\text{ext}}^{(2)}(\mathbf{r}) - V_{\text{ext}}^{(1)}(\mathbf{r}) \right] n_0(\mathbf{r}). \tag{2.16}$$

Adding up eq. (2.15) and eq. (2.16) gives a contradictory result,

$$E^{(1)} + E^{(2)} < E^{(1)} + E^{(2)}. \tag{2.17}$$

This contradictory result means that there is a one-to-one correspondence between the non-degenerate ground state charge density $n_0(\mathbf{r})$ and an external potential $V_{\text{ext}}(\mathbf{r})$ (another external potential with a constant shift is regarded as the same external potential).

2.2.2 Theorem II

The global minimum of an energy functional $E[n]$ including an external potential $\mathrm{V}_{\text{ext}}(\mathbf{r})$ is the exact ground state energy with the exact ground state density $n_0(\mathbf{r})$ [79, 85].

Proof

The total energy of the system is uniquely determined by a particular charge density $n(\mathbf{r})$. The terms inside the total energy which are related to the electrons are all uniquely determined by this density, for example, the external energy is expressed as $\int d^3r V_{\text{ext}}(\mathbf{r})n(\mathbf{r})$, where $V_{\text{ext}}(\mathbf{r})$ is the external potential. Thus, the total energy eq. (2.3) can be expressed as a functional of the charge density,

$$\begin{aligned} E_{\text{HK}}[n] =& T[n] + E_{\text{int}}[n] + \int d^3r V_{\text{ext}}(\mathbf{r})n(\mathbf{r}) + E_{\text{II}} \\ \equiv& F_{\text{HK}}[n] + \int d^3r V_{\text{ext}}(\mathbf{r})n(\mathbf{r}) + E_{\text{II}}. \end{aligned} \tag{2.18}$$

$F_{\text{HK}}[n]$ is a universal functional because the terms included are both functionals of the density $n(\mathbf{r})$ only,

$$F_{\text{HK}}[n] = T[n] + E_{\text{int}}[n]. \tag{2.19}$$

Now, the same assumption as theorem I is applied that there are two ground state densities $n_0^{(1)}(\mathbf{r})$ with wave function $\Psi^{(1)}$ and $n_0^{(2)}(\mathbf{r})$ with wave function $\Psi^{(2)}$ corresponding to external potential $V_{\text{ext}}^{(1)}(\mathbf{r})$ and $V_{\text{ext}}^{(2)}(\mathbf{r})$, respectively. The total energy is the expectation value of the Hamiltonian operator

$$E^{(1)} = E_{\text{HK}}[n^{(1)}] = \langle \Psi^{(1)} | \hat{H}^{(1)} | \Psi^{(1)} \rangle, \tag{2.20}$$

and the same inequality as eq. (2.13),

$$E^{(1)} = \langle \Psi^{(1)} | \hat{H}^{(1)} | \Psi^{(1)} \rangle < \langle \Psi^{(2)} | \hat{H}^{(1)} | \Psi^{(2)} \rangle = E^{(2)}. \tag{2.21}$$

This means that the total energy from the expectation value of the Hamiltonian operator $\hat{H}^{(1)}$ with ground state density $n_0^{(1)}(\mathbf{r})$ is lower than the total energy from the same Hamiltonian operator with the other density $n(\mathbf{r})$. The exact ground state density and energy are obtained by minimising the total energy in eq. (2.18) with respect to the charge density $n(\mathbf{r})$. It is worth noting that the excited state properties cannot be determined by this variational method.

2.3 Kohn-Sham density functional theory

According to the Hohenberg-Kohn theorems, the ground state density uniquely determine all of the properties of many-body systems. However, it is very difficult to solve the problem since the exact universal functionals of the systems are not known. Kohn and Sham proposed an approach in 1965 [86] to solve the many-

body interacting particles problems by introducing independent-particle methods with interacting density. All of the many-body terms are included in the exchange-correlation functional term [79].

The Hamiltonian operator of an independent-particle system is written as (in atomic units) [79],

$$\hat{H}^{\sigma}_{\mathrm{KS}}(\mathbf{r}) = -\frac{1}{2}\nabla^2 + V^{\sigma}_{\mathrm{KS}}(\mathbf{r}). \tag{2.22}$$

The charge density is the sum of each orbital contribution with the spins explicitly counted,

$$n(\mathbf{r}) = \sum_{\sigma} n(\mathbf{r},\sigma) = \sum_{\sigma}\sum_{i=1}^{N^{\sigma}} |\psi_i^{\sigma}(\mathbf{r})|^2. \tag{2.23}$$

The interaction between two electrons is handled via the Hartree approximation introduced above, whereas all the exchange and correlation terms are put into an unknown term, referred to as the exchange-correlation functional. The Kohn-Sham reformulation of eq. (2.18) is [79, 86]

$$E_{\mathrm{KS}} = T_{\mathrm{s}}[n] + \int d\mathbf{r} V_{\mathrm{ext}}(\mathbf{r})n(\mathbf{r}) + E_{\mathrm{H}}[n] + E_{\mathrm{II}} + E_{\mathrm{xc}}[n], \tag{2.24}$$

where T_{s} $(= \int n(\mathbf{r}')d\mathbf{r}' \int -\frac{1}{2}\nabla^2 n(\mathbf{r})d\mathbf{r})$ is the kinetic energy functional for independent particles and E_{H} is the Hartree energy (see the Hartree potential in eq. (2.4)). The Hartree energy is written as

$$E_{\mathrm{H}}[n] = \frac{1}{2}\int d^3r d^3r' \, \frac{n(\mathbf{r})n(\mathbf{r}')}{|\mathbf{r}-\mathbf{r}'|}. \tag{2.25}$$

The exchange-correlation functional $E_{\mathrm{xc}}[n]$ is obtained by comparing eq. (2.18) and eq. (2.24),

$$E_{\mathrm{xc}}[n] = (T[n] - (T_{\mathrm{s}}[n]) + (E_{\mathrm{int}}[n] - E_{\mathrm{H}}[n]). \tag{2.26}$$

Eq. (2.26) shows that the exchange-correlation energy functional is the combination of the differences in the kinetic and internal interaction terms between the interacting-particle and the independent-particle systems.

The ground state of Kohn-Sham equation can be obtained by using the method of Lagrange multipliers [79],

$$\delta[\langle\Psi|\hat{H}|\Psi\rangle - E(\langle\Psi|\Psi\rangle - 1)] = 0, \tag{2.27}$$

where the Hamiltonian operator is from eq. (2.22) and the minimisation is with respect to the density $n(\mathbf{r},\sigma)$ along with the constraint of orthonormality $(\langle\Psi_i|\Psi_j\rangle =$

δ_{ij}). Here the Kohn-Sham effective potential is written as [79]

$$\begin{aligned} V_{\mathrm{KS}}^{\sigma}(\mathbf{r}) &= V_{\mathrm{ext}}(\mathbf{r}) + \frac{\delta E_{\mathrm{H}}}{\delta n(\mathbf{r},\sigma)} + \frac{\delta E_{\mathrm{xc}}}{\delta n(\mathbf{r},\sigma)} \\ &= V_{\mathrm{ext}}(\mathbf{r}) + V_{\mathrm{H}}(\mathbf{r}) + V_{\mathrm{xc}}^{\sigma}(\mathbf{r}). \end{aligned} \tag{2.28}$$

where V_{H} is the Hartree potential mentioned in eq. (2.4) which satisfies eq. (2.6). Because the relationship between charge density and effective potential is a one-to-one correspondence, the Kohn-Sham equation can be solved self-consistently by introducing a trial charge density first and then varying the charge density until it satisfies the convergence criterion. The exact ground-state properties of the interacting many-body system can in principle be obtained from the Kohn-Sham equations if the exact exchange-correlation functional $E_{\mathrm{xc}}[n]$ can be determined, since all many-body effects are in principle included in $E_{\mathrm{xc}}[n]$ [79].

2.4 Exchange-correlation functionals

In practice, the accuracy of the Kohn-Sham DFT depends heavily on the accuracy of the exchange-correlation functional $E_{\mathrm{xc}}[n]$ used. Two kinds of the most widely used approximations will be introduced below.

2.4.1 Local density approximation (LDA)

In the original seminal paper of Kohn and Sham [86], the local density approximation (LDA) was proposed. In this approximation, it is assumed that there is no difference between the exchange-correlation energy density of a real system and that of a homogeneous electron gas of the same density. If the density $n(\mathbf{r})$ is varying slowly enough, it is reasonable to express the exchange-correlation functional as [79, 86]

$$\begin{aligned} E_{\mathrm{xc}}^{\mathrm{LDA}}[n] &= \int d^3r\, n(\mathbf{r})\epsilon_{\mathrm{xc}}^{\mathrm{hom}}(n) \\ &= \int d^3r\, n(\mathbf{r})[\epsilon_{x}^{\mathrm{hom}}(n)) + \epsilon_{c}^{\mathrm{hom}}(n)], \end{aligned} \tag{2.29}$$

where the exchange-correlation energy density is expressed as exchange and correlation terms separately in the second term of eq. (2.29). The exchange energy density has an analytical form [87],

$$\epsilon_{\mathrm{x}}^{\mathrm{hom}}(n(\mathbf{r})) = -\frac{3}{4}\left(\frac{3n(\mathbf{r})}{\pi}\right)^{1/3}. \tag{2.30}$$

There is no a simple analytic function can be used to express the density of correlation energy [79]. Wigner [88, 89] proposed a quantitative form to interpolate the situation between low- and high-density limits in a homogeneous gas. However, it was found that this expression was not correct due to the error in the low-density limit [79]. The correct expression of correlation energy in the high-density limit was proposed by Gell-mann and Brueckner [90].

2.4.2 Generalised gradient approximation (GGA)

Unlike the LDA which is at its best when used to describe the materials with slowly varying charge density, the generalised-gradient approximation (GGA) considers both the charge density and its gradients. Similarly, it has a generalised form for spin-unpolarised case [79, 91],

$$\begin{aligned} E_{\mathrm{xc}}^{\mathrm{GGA}}[n] &= \int d^3r\, n(\mathbf{r})\epsilon_{\mathrm{xc}}^{\mathrm{GGA}}(n, |\nabla n|) \\ &\equiv \int d^3r\, n(\mathbf{r})\epsilon_{\mathrm{x}}^{\mathrm{hom}}(n)F_{\mathrm{xc}}(n, |\nabla n|), \end{aligned} \tag{2.31}$$

where the exchange energy density $\epsilon_{\mathrm{x}}^{\mathrm{hom}}$ is the same as eq. (2.30) and F_{xc} refers to the enhancement factor over local exchange. F_{xc} can naturally be discussed in terms of the reduced density gradient. For the first dimensionless reduced density gradients,

$$s = \frac{|\nabla n|}{2k_{\mathrm{F}}n}, \tag{2.32}$$

where the local Fermi wave vector $k_{\mathrm{F}} = (3\pi^2 n)^{1/3}$. Becke (B88) [92], Perdew and Wang (PW91) [93] and Perdew, Burke and Enzerhof (PBE) [94] are three kinds of GGA with different forms of $F_{\mathrm{x}}(n, s)$ which are widely used nowadays [79]. For example, the F_{x} of PBE is [79, 94]

$$F_{\mathrm{x}}(s) = 1 + \kappa - \frac{\kappa}{1 + \mu s^2/\kappa}, \tag{2.33}$$

where $\kappa = 0.804$ and $\mu \simeq 0.21951$.

2.4.3 Van der Waals (vdW) density functional

Van der Waals (vdW) interactions are relatively weak but are essential to accurately describe processes such as biological reactions [95] and interaction in layered systems [96]. Dion et al. [97] proposed to rewrite the exchange-correlation functional by adding the nonlocal dispersion correlations into the original exchange-correlation

energy functional [96, 98],

$$E_{\rm xc}[n] = E_{\rm x}^{\rm GGA}[n] + E_{\rm c}^{\rm LDA}[n] + E_{\rm c}^{\rm nl}[n]. \tag{2.34}$$

Here the exchange-correlation energy functional is described by the exchange energy functional of semilocal GGA (various types of van der Waals density functional were obtained by considering different types of $E_{\rm x}^{\rm GGA}[n]$ [99]), the correlation energy functional of local LDA and a universal nonlocal correlation energy functional, where $E_{\rm c}^{\rm nl}[n]$ can be expressed as [98]

$$E_{\rm c}^{\rm nl}[n] = \frac{1}{2}\iint d^3r_1\, d^3r_2\, n(\mathbf{r}_1)n(\mathbf{r}_2)\phi(q_1, q_2, r_{12}), \tag{2.35}$$

where $r_{12} = |\mathbf{r}_1 - \mathbf{r}_2|$, $q_1 = q_0[n(\mathbf{r}_1), |\nabla n(\mathbf{r}_1)|)]$ and $q_2 = q_0[n(\mathbf{r}_2), |\nabla n(\mathbf{r}_2)|)]$. There are two conditions that ϕ has to obey: (i) In the system with constant density, the nonlocal exchange energy functional is zero; (ii) A form of r^{-6} dependence (r is large) appropriately describes the interaction between two molecules. The computational cost can be reduced by considering the case of fixed q_i ($i = 1, 2$). Then the kernel ϕ can be expanded as [98]

$$\phi(q_1, q_2, r_{12}) \simeq \sum_{\alpha\beta} \phi(q_\alpha, q_\beta, r_{12}) p_\alpha(q_1) p_\beta(q_2), \tag{2.36}$$

where q_α are fixed values for each r_{12} for interpolating well the kernel ϕ. This means that a set of interpolating polynomials $p_\alpha(q)$ (cubic spline functions) are used to represent the kernel. Eq. (2.35) can be evaluated now by utilising Fourier methods owing to the expression of eq. (2.36). The nonlocal energy functional $E_{\rm c}^{\rm nl}[n]$ is rewritten as [98]

$$\begin{aligned} E_{\rm c}^{\rm nl} &= \frac{1}{2}\sum_{\alpha\beta}\iint d^3r_1\, d^3r_2\, \theta_\alpha(\mathbf{r}_1)\theta_\beta(\mathbf{r}_2)\phi_{\alpha\beta}(r_{12}) \\ &= \frac{1}{2}\sum_{\alpha\beta}\int d^3\mathbf{k}\, \theta_\alpha^*(\mathbf{k})\theta_\beta(\mathbf{k})\phi_{\alpha\beta}(k), \end{aligned} \tag{2.37}$$

where $\theta_\alpha(\mathbf{r}_i) = n(\mathbf{r}_i)p_\alpha[(q_0(n(\mathbf{r}_i), \nabla n(\mathbf{r}_i)]$ ($i = 1, 2$) and $\phi_{\alpha\beta}(r) \equiv \phi(q_\alpha, q_\beta, r)$. $\theta(\mathbf{k})$ and $\phi_{\alpha\beta}(k)$ (can be precalculated) are the corresponding Fourier transforms of $\theta(\mathbf{r})$ and $\phi_{\alpha\beta}(r)$, respectively. In chapter 6 for the calculations of twisted InSe bilayer, the optB88-vdW functional [99] was adopted to incorporate the vdW interaction between layers.

2.5 Pseudopotentials

Due to the large Coulomb potential near atomic nucleus, the wave functions of the core electrons vary rapidly (with more nodes) and need many Fourier coefficients with plane wave basis set to describe it. For implementing the calculations more efficiently and reducing the computational cost, "pseudopotentials" (an effective ionic potential) are usually adopted. The valence electrons are acted on by the pseudopotential. The explicit representation of core electron states is removed, and the potential has the same functional form as an original full Coulomb potential outside a given radius R_c [79]. This method is practical because most chemical reactions only involve the valence electrons. There is a trade-off between cost-saving and transferability in choosing the pseudopotential. If a pseudopotential is a "hard" potential with a small R_c, it may describe the wave function more accurately near the core region and is more transferable to other materials. In contrast, if the pseudopotential is a "soft" potential with large R_c, it may describe the wave function less accurately, however, fewer basis functions are needed [79]. In general, the valence electrons are chosen from the outermost shell of an atom, however, this is not a strict rule. More electrons may be included from deeper electron shells as the valence electrons to improve the accuracy of a calculation, but this will also increase the computational cost [79].

2.5.1 Norm-conserving pseudopotentials (NCPPs)

Norm-conserving pseudopotentials are the most widely used type of pseudopotential. They are developed to be highly accurate and transferable, however, high computational costs are often required. It provides the same properties related to the valence states as the all-electron calculation. The orthonormality condition is also satisfied for these kind of pseudopotentials [79],

$$\langle \psi_i^{\sigma,\mathrm{PS}} | \psi_j^{\sigma',\mathrm{PS}} \rangle = \delta_{i,j}\delta_{\sigma,\sigma'}. \tag{2.38}$$

Furthermore, the pseudo wave functions and eigenvalues are required to be consistent with the all-electron calculations outside a core radius R_c, their logarithmic derivatives $D_l(\epsilon, r) \equiv r\frac{d}{dr}\ln\psi_l(\epsilon, r)$ needs to be equivalent at R_c and the consistency is also required for $\frac{dD_l(\epsilon,r)}{d\epsilon}$ all $r \geq R_c$. "Norm-conservation" means that the charge from pseudo wave functions and all-electron wave functions for valence state inside

a given radius R_c are integrated to be equivalent [79, 100],

$$Q = \int_0^{R_c} |\psi(\mathbf{r})|^2 d\mathbf{r} = \int_0^{R_c} |\psi_{\mathrm{PS}}(\mathbf{r})|^2 d\mathbf{r}. \tag{2.39}$$

The orbital-dependent (l-dependent) ionic pseudopotential V_l can be expressed in terms of its local and non-local parts separately. When the special relativity in the calculations is considered, scalar relativistic effects and spin-orbit interactions need to be included in the potential V_l [79, 101, 102],

$$V_l = \frac{l}{2l+1}[(l+1)V_{l+1/2} + lV_{l-1/2}], \tag{2.40}$$

$$\delta V_l^{\mathrm{SO}} = \frac{2}{2l+1}[V_{l+1/2} - V_{l-1/2}]. \tag{2.41}$$

Eq. (2.40) and eq. (2.41) are for scalar relativistic and spin-orbit effects, respectively. The short-range non-local operator with "semilocal (SL)" form (local in the radial part, non-local in the angular part) is related to δV_l^{SO} as [79]

$$\delta\hat{V}_{\mathrm{SL}}^{\mathrm{SO}} = \sum_{lm} |Y_{lm}\rangle \delta V_l^{\mathrm{SO}}(r)\mathbf{L}\cdot\mathbf{S}\langle Y_{lm}|, \tag{2.42}$$

where $Y_{lm}(\theta,\phi) = P_l(cos(\theta))e^{im\phi}$ are the spherical harmonics.

Ultrasoft pseudopotentials [103] are another type of pseudopotential which are written as a combination of a smooth function and an auxiliary function (for rapidly varying density near the core region). It is still valid to use the Hartree potential with ultrasoft pseudopotentials outside of the core because the multipole moment of the charge density is reproduced. These kinds of pseudopotentials are smoother (less expensive) than the norm-conserving pseudopotential and achieve the desired accuracy at the same time [79].

2.6 Projector augmented waves (PAWs)

In real materials, the wave functions consist of a relatively smooth part in the bonding region as well as a rapidly oscillating part near the nucleus. The projector augmented wave (PAW) method [104, 105, 106] was inspired from the ideas of the ultrasoft pseudopotential and augmented wave methods, it also includes smooth functions and auxiliary localised functions (for representing the core states) to express the wave functions [79]. The PAW sphere is an atom-centred sphere with the inside and outside consisting of a partial wave expansion and plane waves, re-

spectively. The full all-electron wave functions are more efficiently maintained and calculated with the PAW method. Therefore, PAW method provides an accurate, transferable and efficient way to perform calculations [79, 104].

In PAW method, all-electron wave function $|\psi\rangle$ is transformed into a pseudo wave function $|\tilde{\psi}\rangle$ by linear transformation $\mathcal{T}$ [79, 104],

$$|\psi\rangle = \mathcal{T}|\tilde{\psi}\rangle, \tag{2.43}$$

and

$$|\psi\rangle = \sum_m c_m|\psi_m\rangle, \quad |\tilde{\psi}\rangle = \sum_m c_m|\tilde{\psi}_m\rangle, \tag{2.44}$$

where $|\psi_m\rangle$ ($|\tilde{\psi}_m\rangle$) is the partial wave of the all-electron (pseudo) wave function and $c_m = \langle\tilde{p}_m|\tilde{\psi}\rangle$ ($\{\tilde{p}_m\}$ are a set of projection operators) is the corresponding expansion coefficient. The linear transformation $\mathcal{T}$ is written as

$$\mathcal{T} = 1 + \sum_R \hat{\mathcal{T}}_R, \tag{2.45}$$

where each $\hat{\mathcal{T}}_R$ is an atom-centred contribution only from some augmentation regions (referred to as the core region in the pseudopotential method). Thus, the all-electron and the pseudo wave functions are the same outside those regions. From eq. (2.43) and eq. (2.44), we get

$$\begin{aligned} |\psi\rangle =& |\tilde{\psi}\rangle + \sum_m c_m\{|\psi_m\rangle - |\tilde{\psi_m}\rangle\} \\ =& \left(1 + \sum_m \{|\psi_m\rangle - |\tilde{\psi_m}\rangle\}\langle\tilde{p}_m|\right)|\tilde{\psi}\rangle. \end{aligned} \tag{2.46}$$

Thus,

$$\mathcal{T} = \mathbf{1} + \sum_m \{|\psi_m\rangle - |\tilde{\psi}_m\rangle\}\langle\tilde{p}_m|, \tag{2.47}$$

In the augmentation region, if $\sum_m |\tilde{\psi}_m\rangle\,\langle\tilde{p}_m| = 1$ is satisfied, then $\sum_m |\tilde{\psi}_m\rangle\,\langle\tilde{p}_m|\tilde{\psi}\rangle = |\tilde{\psi}\rangle$. This means that $\langle\tilde{p}_m|\tilde{\psi}_{m'}\rangle = \delta_{mm'}$.

2.7 Basis functions used in DFT

The wave function ψ_i is usually expressed as

$$\psi_i(\mathbf{r}) = \sum_\lambda c_\lambda \phi_\lambda(\mathbf{r}), \tag{2.48}$$

where $\{\phi_\lambda\}$ is a set of basis functions and $\{c_\lambda\}$ is a set of corresponding expansion coefficients. The lattice vector $\mathbf{R}$ of a unit cell is defined as [79, 107]

$$\mathbf{R} = n_1\mathbf{a}_1 + n_2\mathbf{a}_2 + n_3\mathbf{a}_3, \tag{2.49}$$

where a_i $(i = 1, 2, 3)$ are the primitive lattice vectors and n_i is an integer coefficient for the corresponding $\mathbf{a}_i$. On the other hand, the effective potential in the Kohn-Sham Hamiltonian also has the same property for the periodic system [79, 107],

$$V_{\text{eff}}(\mathbf{r} + \mathbf{R}) = V_{\text{eff}}(\mathbf{r}). \tag{2.50}$$

Due to the periodicity of the effective potential, by applying Fourier transform,

$$V_{\text{eff}}(\mathbf{r}) = \sum_m V_{\text{eff}}(\mathbf{G}_m)e^{i\mathbf{G}_m\cdot\mathbf{r}}, \tag{2.51}$$

where $\mathbf{G}_m$ is the reciprocal lattice vector,

$$\mathbf{G}_m = m_1\mathbf{b}_1 + m_2\mathbf{b}_2 + m_3\mathbf{b}_3, \tag{2.52}$$

where $\{m_i\}$ $(i = 1, 2, 3)$ are integers and $\{\mathbf{b}_i\}$ are the primitive reciprocal lattice vectors which has relations with the primitive lattice vector in real space,

$$\mathbf{b}_i \cdot \mathbf{a}_j = 2\pi\delta_{ij}. \tag{2.53}$$

A plane wave basis set is naturally used for periodic systems since it satisfies the requirement in eq. (2.50) ($e^{i\mathbf{G}\cdot(\mathbf{r}+\mathbf{R})} = e^{i\mathbf{G}\cdot\mathbf{r}}$). The wave function can be rewritten as a form of Bloch's theorem: $\psi_{i\mathbf{k}}(\mathbf{r}) = e^{i\mathbf{k}\cdot\mathbf{r}}u_{i\mathbf{k}}(\mathbf{r})$ [79, 107],

$$\psi_{i\mathbf{k}} = \sum_m \frac{1}{\sqrt{\Omega}} c_{i,\mathbf{m}}(\mathbf{k})e^{i(\mathbf{k}+\mathbf{G}_m)\cdot\mathbf{r}} = \frac{1}{\sqrt{N_{cell}}} u_{i,\mathbf{k}}(\mathbf{r})e^{i\mathbf{k}\cdot\mathbf{r}}, \tag{2.54}$$

where $\Omega = N_{cell}\Omega_{cell}$ and $u_{i,\mathbf{k}}(\mathbf{r})$ is a periodic function with periodicity identical to the crystal $(u_\mathbf{k}(\mathbf{r} + \mathbf{R}_n) = u_\mathbf{k}(\mathbf{r}))$,

$$u_{i,\mathbf{k}}(\mathbf{r}) = \frac{1}{\sqrt{\Omega_{cell}}} \sum_m c_{i,m}(\mathbf{k})e^{i\mathbf{G}_m\cdot\mathbf{r}}. \tag{2.55}$$

The computational cost can be reduced by limiting the calculation within a cut-off energy E_{cut} which satisfies the desired convergence tolerance. The kinetic energy

($\frac{1}{2}|\mathbf{k}+\mathbf{G}|^2$) cut-off of the plane wave is

$$E_{\text{cut}} = \frac{1}{2}|\mathbf{G}_{\text{max}}|^2, \tag{2.56}$$

where $\mathbf{G}_{\text{max}}$ is chosen as the largest value in eq. (2.52) (corresponding to E_{cut}) in the calculation. The accuracy is improved as the magnitude of E_{cut} increases (so the basis functions increase) to include short-wavelength behaviour in the wave function.

2.8 Force theorem

All forces acting on each atom are required to be smaller than some chosen convergence criteria in the calculation of geometry optimisation, otherwise the optimised structure is not acceptable. Based on the contributions of Hellmann [108] and Feynman [109], a theorem now referred to as the "Hellmann-Feynman theorem" can be used to calculate the force which acts on an atomic nucleus I with position $\mathbf{R}_I$,

$$\mathbf{F}_I = -\frac{\partial E}{\partial \mathbf{R}_I}. \tag{2.57}$$

The orthonormality of wave function $\langle\Psi|\Psi\rangle = 1$ is assumed. The expectation value of the Hamiltonian operator gives the total energy [79, 109],

$$E_{\text{tot}} = \frac{\langle\Psi|\hat{H}|\Psi\rangle}{\langle\Psi|\Psi\rangle} = \langle\Psi|\hat{H}|\Psi\rangle, \tag{2.58}$$

$$\begin{aligned}
-\frac{\partial E}{\partial \mathbf{R}_I} =& -\langle\frac{\partial \Psi}{\partial \mathbf{R}_I}|\hat{H}|\Psi\rangle - \langle\Psi|\frac{\partial \hat{H}}{\partial \mathbf{R}_I}|\Psi\rangle - \langle\Psi|\hat{H}|\frac{\partial \Psi}{\partial \mathbf{R}_I}\rangle \\
=& -E\left[\langle\frac{\partial \Psi}{\partial \mathbf{R}_I}|\Psi\rangle + \langle\Psi|\frac{\partial \Psi}{\partial \mathbf{R}_I}\rangle\right] - \langle\Psi|\frac{\partial \hat{H}}{\partial \mathbf{R}_I}|\Psi\rangle \\
=& -\langle\Psi|\frac{\partial \hat{H}}{\partial \mathbf{R}_I}|\Psi\rangle.
\end{aligned} \tag{2.59}$$

In eq. (2.59), the terms inside the square bracket add up to zero,

$$\langle\frac{\partial \Psi}{\partial \mathbf{R}_I}|\Psi\rangle + \langle\Psi|\frac{\partial \Psi}{\partial \mathbf{R}_I}\rangle = \frac{d}{d\mathbf{R}_I}\langle\Psi|\Psi\rangle = 0. \tag{2.60}$$

From eq. (2.59) and eq. (2.3), only terms which explicitly dependent on the position of atomic nucleus I will survive, thus

$$\mathbf{F}_I = -\frac{\partial E}{\partial \mathbf{R}_I} = -\int d^3r\, n(\mathbf{r})\frac{\partial V_{\text{ext}}}{\partial \mathbf{R}_I} - \frac{\partial E_{\text{II}}}{\partial \mathbf{R}_I}. \tag{2.61}$$

In fact, the Hellman-Feynman theorem provides a more generalised expression which is the derivative of the total energy with respect to any parameter λ, so that

$$\frac{\partial E}{\partial \lambda} = \langle \Psi(\lambda) | \frac{\partial \hat{H}}{\partial \lambda} | \Psi(\lambda) \rangle. \tag{2.62}$$

It is worth mentioning that the Hellmann-Feynman theorem is valid to be used for getting the information of the ionic forces at the ground state and the wave functions are required to be expressed in a complete basis set in self-consistent calculations. Incomplete basis set functions are adopted in some computational simulation packages, so in that case the Pulay forces [110] need to be included in the calculations to correct the forces if the incomplete basis set functions have explicit dependence on the position of nuclei [79].

Chapter 3

Linear-scaling density functional theory

3.1 Order-N electronic total energy package (ONETEP)

In this thesis, a linear-scaling density functional theory (LS-DFT) package called ONETEP [59, 63] was also adopted to simulate large-scale systems, such as the transition metal dichalcogenide alloys and twisted bilayer InSe in later chapters. In the linear-scaling density functional theory, the computational cost increases linearly as the number of atoms in the simulated cell and the number of processor increase. This benefits research studies in fields such as biophysics and nanoscience which involve thousands of atoms [63]. Otherwise, a big difficulty will be faced when dealing with large scale systems because the computational cost and time are proportional to the cube of the number of atoms ($\propto N^3$). The Kohn-Sham orbitals are restricted to satisfy the orthonormality condition [56],

$$\int d^3r\, \psi_m^*(\mathbf{r})\psi_n(\mathbf{r}) = \delta_{mn}. \tag{3.1}$$

This imposes a N^2-scaling number of constraints. In addition, a Kohn-Sham orbital spreads over the whole system ($\propto N$). Thus, the computational cost is proportional to N^3. In contrast, ONETEP utilises a minimal number of highly localised functions called nonorthogonal generalised Wannier functions (NGWFs) [111] as basis functions which largely reduces the computational cost because NGWFs are confined around each atom and can be truncated to be non-vanishing only within a fixed radius [56, 63].

The spinless single-particle density matrix eq. (2.11) can also be written in terms of position coordinates [56, 63]

$$\rho(\mathbf{r}, \mathbf{r}') = \sum_n f_n \psi_n^*(\mathbf{r}) \psi_n(\mathbf{r}'), \tag{3.2}$$

where f_n is the occupancy of state $\psi_n(\mathbf{r})$ and its value is within an interval of 0 and 1. For an insulating system at zero temperature, it has unity and zero occupancy below and above the Fermi level, respectively. In addition, the property of idempotency applies

$$\rho^2(\mathbf{r}, \mathbf{r}') = \int d^3r'' \rho(\mathbf{r}, \mathbf{r}'') \rho(\mathbf{r}'', \mathbf{r}') = \rho(\mathbf{r}, \mathbf{r}'). \tag{3.3}$$

This means that the orthonormality condition eq. (3.1) and the Aufbau principle (as well as the Pauli exclusion principle) need to be satisfied. The diagonal elements form the charge density $n(\mathbf{r})$

$$n(\mathbf{r}) = 2\rho(\mathbf{r}, \mathbf{r}), \tag{3.4}$$

where the factor of 2 is based on spin-unpolarised assumption (spin degeneracy). The total energy can also be written as

$$E = 2\,\mathrm{Tr}[\hat{\rho}\hat{H}], \tag{3.5}$$

where Tr refers to the operator trace. From Chapter 2, the Kohn-Sham equation can be written as

$$\begin{aligned} \hat{H}\psi_n(\mathbf{r}) &= \left[-\frac{1}{2}\nabla^2 + V_{\text{eff}}[n](\mathbf{r})\right]\psi_n(\mathbf{r}) \\ &= \epsilon_n \psi_n(\mathbf{r}). \end{aligned} \tag{3.6}$$

The properties of the ground state are obtained by applying $\frac{\partial E}{\partial n(\mathbf{r})} = 0$, along with the idempotency constraint eq. (3.3) and the integral of eq. (3.4) (or the trace of the density matrix) is confined to be the total number of electrons in the system [56, 63],

$$N_e = 2\int d^3r \rho(\mathbf{r}, \mathbf{r}) = 2\,\mathrm{Tr}[\hat{\rho}]. \tag{3.7}$$

To reduce the computational cost to be just proportional to N, the “nearsightedness" [112, 113] of quantum many-particle systems needs to be considered in the calculations. “Nearsightedness" means that the local density is increasingly less affected by the potential at increasing distance. The combination of the “nearsightedness” and the matrix truncation reduces the computational cost but at the same time sacrificing the accuracy of the calculation. For systematically improving the accuracy until the standard of the plane wave, a basis set which can be adjusted

through a single parameter is desired. In a system which possesses a band gap, its density matrix eq. (3.2) behaves as [56, 114, 115, 116, 117]

$$\rho(\mathbf{r},\mathbf{r}') \sim \exp(-\gamma|\mathbf{r}-\mathbf{r}'|) \rightarrow 0 \text{ as } |\mathbf{r}-\mathbf{r}'| \rightarrow \infty, \tag{3.8}$$

where γ is the decay rate determined by the band gap of the system. The density matrix preserves values only if the distance between $\mathbf{r}$ and $\mathbf{r}'$ remains finite. Now the density matrix can be truncated to be a sparse matrix whose information scales as N, instead of N^2. In practice, the density matrix is rewritten as [56]

$$\rho(\mathbf{r},\mathbf{r}') = \sum_{\alpha\beta} \phi_\alpha(\mathbf{r}) K^{\alpha\beta} \phi^*_\beta(\mathbf{r}'), \tag{3.9}$$

where the $\{\phi_\alpha(\mathbf{r})\}$ are a set of basis functions which are spatially localised and nonorthogonal, called support functions [118] or NGWFs [111]. The Kohn-Sham orbitals $\{\psi_i\}$ are now expressed by the NGWFs $\{\phi_\alpha\}$ [119],

$$\psi_i(\mathbf{r}) = \sum_{\alpha=1}^{N_\phi} \phi_\alpha(\mathbf{r}) M^\alpha_i = \sum_{\alpha=1}^{N_\phi} \phi^\alpha(\mathbf{r}) M_{\alpha i}, \tag{3.10}$$

where M^α_i and $M_{\alpha i}$ are the transformation matrices between the representation of Kohn-Sham orbitals $\{\psi_i\}$ and NGWFs $\{\phi_\alpha\}$,

$$M^\alpha_i = \sum_{\beta=1}^{N_\phi} S^{\alpha\beta} M_{\beta i}, \tag{3.11}$$

$$M_{\alpha i} = \sum_{\beta=1}^{N_\phi} S_{\alpha\beta} M^\beta_i. \tag{3.12}$$

Here $S^{\alpha\beta}$ and $S_{\alpha\beta}$ are the overlap matrices,

$$S^{\alpha\beta} = \langle \phi^\alpha | \phi^\beta \rangle, \tag{3.13}$$

$$S_{\alpha\beta} = \langle \phi_\alpha | \phi_\beta \rangle. \tag{3.14}$$

Therefore from eq. (3.9) and eq. (3.10), the matrix of density kernel $K^{\alpha\beta}$ [120] is defined as

$$K^{\alpha\beta} = \sum_{i=1} M^\alpha_i f_i M^{\dagger\beta}_i. \tag{3.15}$$

The relation between transformation matrices $\{M_{\alpha i}\}$ and overlap matrices $\{S_{\alpha\beta}\}$

are

$$S^{\alpha\beta} = \sum_{i=1} M_i^{\alpha} M_i^{\dagger\beta}, \tag{3.16}$$

$$S_{\alpha\beta} = \sum_{i=1} M_{\alpha i} M_{i\beta}^{\dagger}, \tag{3.17}$$

where $(M^{-1})_{\alpha i} = M_i^{\dagger\alpha}$ was implied. In addition, the biorthonormality condition applies to a set of duals of the NGWFs $\{\phi_\alpha(\mathbf{r})\}$ [119],

$$\langle\phi_\beta|\phi^\alpha\rangle = \int d^3r\, \phi_\beta^*(\mathbf{r})\phi^\alpha(\mathbf{r}) = \delta_\beta^\alpha. \tag{3.18}$$

The dual functions $\{\phi_\alpha\}$ can be transformed to each other via

$$\phi^\alpha(\mathbf{r}) = \sum_{\beta=1}^{N_\phi} \phi_\beta(\mathbf{r}) S^{\beta\alpha}, \tag{3.19}$$

$$\phi_\alpha(\mathbf{r}) = \sum_{\beta=1}^{N_\phi} \phi^\beta(\mathbf{r}) S_{\beta\alpha}. \tag{3.20}$$

From eq. (3.13), eq. (3.14) and eq. (3.18),

$$\sum_{\beta=1}^{N_\phi} S^{\alpha\beta} S_{\beta\gamma} = \sum_{\beta}^{N_\phi} \langle\phi^\alpha|\phi^\beta\rangle\langle\phi_\beta|\phi_\gamma\rangle = \delta_\gamma^\alpha. \tag{3.21}$$

Although eq. (3.9) is still proportional to N^2, this form of density matrix can use spatial cut-offs by considering “nearsightedness" mentioned above. The NGWFs $\{\phi_\alpha\}$ can be expanded in terms of a basis of periodic sinc [121, 122] or psinsc functions $\{D_k(\mathbf{r})\}$ [123],

$$\phi_\alpha(\mathbf{r}) = \sum_k D_k(\mathbf{r}) c_{k,\alpha}, \tag{3.22}$$

$$\phi^\alpha(\mathbf{r}) = \sum_k D_k(\mathbf{r}) c_k^\alpha, \tag{3.23}$$

where $\{D_k(\mathbf{r})\}$ are a set of orthogonal and highly localised spike-like functions which centred on each grid point in the simulation cell (zero everywhere except at the centre grid point and oscillating between grid points [56]), whereas the $\{c_{k,\alpha}\}$ are the set of corresponding expansion coefficients. The NGWFs of each atom in the system with centre points at $\{\mathbf{R}_\alpha\}$ can be truncated owing to their exponentially localised forms, so that they vanish beyond a spherical region of fixed radii $\{r_\alpha\}$.

The fixed radii $\{r_\alpha\}$ are related to the atomic species [56]. One of the advantages of utilising psinc functions is that it can be transformed to plane waves by Fourier transform. The accuracy of the psinc functions can be improved by only increasing its grid spacing, like the kinetic energy cut-off of the plane waves [56, 64]. Therefore, the accuracy can be adjusted from the standard of minimal atomic-type basis set (NGWF optimisation is not performed) to a basis set of full plane-waves in ONETEP calculation [56]. Furthermore, the density kernel can also be truncated to be a sparse matrix by imposing condition below [63],

$$K^{\alpha\beta} = 0 \text{ as } |\mathbf{R}_\alpha - \mathbf{R}_\beta| > r_K, \tag{3.24}$$

where $\mathbf{R}_\alpha$ ($\mathbf{R}_\beta$) refers to the centre of the localisation region of $\phi_\alpha(\mathbf{r})$ ($\phi_\beta(\mathbf{r})$). According to eq. (3.11) and eq. (3.15) for the duals of the NGWFs, $r_K \neq r_\alpha + r_\beta$ because the NGWFs are nonorthogonal [56]. The spatial cut-offs $\{r_\alpha\}$ and $\{r_K\}$ are normally tested and increased until satisfying the desired accuracy criteria for the system.

The idempotency condition eq. (3.3) can now be reformulated in terms of the NGWFs and density kernel $\mathbf{K}$ [122],

$$\begin{aligned} \rho^2(\mathbf{r},\mathbf{r}') &= \left[\sum_{\alpha,\mu}\langle\mathbf{r}|\phi_\alpha\rangle K^{\alpha\mu}\langle\phi_\mu|\mathbf{r}''\rangle\right]\left[\sum_{\nu,\beta}\langle\mathbf{r}''|\phi_\nu\rangle K^{\nu\beta}\langle\phi_\beta|\mathbf{r}'\rangle\right] \\ &= \sum_{\alpha,\nu}\langle\mathbf{r}|\phi_\alpha\rangle\left[\sum_{\beta,\mu}K^{\alpha\mu}S_{\mu\nu}K^{\nu\beta}\right]\langle\phi_\beta|\mathbf{r}'\rangle, \\ \rho(\mathbf{r},\mathbf{r}') &= \sum_{\alpha,\beta}\langle\mathbf{r}|\phi_\alpha\rangle K^{\alpha\beta}\langle\phi_\beta|\mathbf{r}'\rangle. \end{aligned} \tag{3.25}$$

The overlap matrix in eq. (3.14) was substituted in the equation. This implies that

$$K^{\alpha\mu}S_{\mu\nu}K^{\nu\beta} = K^{\alpha\beta}. \tag{3.26}$$

In addition, the normalisation condition eq. (3.7) in terms of NGWFs and density kernel $\mathbf{K}$ can also be written as [122]

$$\begin{aligned} N_e =& 2\,\mathrm{Tr}[\hat{\rho}] = 2\sum_{\alpha,\beta,\gamma}\langle\phi_\alpha|\phi_\gamma\rangle K^{\gamma\beta}\langle\phi_\beta|\phi^\alpha\rangle \\ =& 2\sum_{\alpha,\beta,\gamma}S_{\alpha\gamma}K^{\gamma\beta}\delta^\alpha_\beta = 2\,\mathrm{Tr}[\mathbf{KS}]. \end{aligned} \tag{3.27}$$

The ground state energy is obtained by minimising the energy calculated

from eq. (3.6) with respect to NGWFs $\{\phi_\alpha\}$ and density kernel $K^{\alpha\beta}$ self-consistently, subject to the constraints in eq. (3.26) and eq. (3.27). This is implemented in two nested loops [124, 125]:

$$E_{\text{min}} = \min_{\{\phi_\alpha\}} L(\{\phi_\alpha\}) \Rightarrow \frac{\delta E}{\delta \phi_\alpha} = 0 \ \forall \ k, \alpha, \tag{3.28}$$

$$L(\{\phi_\alpha\}) = \min_{\{K^{\alpha\beta}\}} E(\{K^{\alpha\beta}\}; \{\phi_\alpha\}) \Rightarrow \frac{\delta E}{\delta K^{\alpha\beta}} = 0 \ \forall \ \alpha, \beta. \tag{3.29}$$

Eq. (3.28) and eq. (3.29) are implemented in the outer loop and the inner loop (with a given set of NGWFs $\{\phi_\alpha\}$), respectively.

3.1.1 Density kernel optimisation

In ONETEP, a penalty-functional approach of Haynes and Payne [126] and the method of Li, Nunes and Vanderbilt (LNV) [127] variational approach based on McWeeny's purification transformation [120] are utilised to impose the idempotency constraint [56].

In LNV approach, an auxiliary kernel $\mathbf{L}$ is adopted to define an auxiliary matrix σ, such that [56, 128]

$$\sigma(\mathbf{r}, \mathbf{r}') = \sum_{\alpha\beta} \phi_\alpha(\mathbf{r}) L^{\alpha\beta} \phi^*_\beta(\mathbf{r}'), \tag{3.30}$$

where $\{L^{\alpha\beta}\}$ represents a set of matrix elements of the auxiliary kernel $\mathbf{L}$. The density kernel is expressed by the auxiliary kernel as [56, 128]

$$\mathbf{K} = 3\mathbf{LSL} - 2\mathbf{LSLSL}. \tag{3.31}$$

The density matrix ρ can be related to an auxiliary matrix σ through the purification transformation,

$$\rho(\mathbf{r}, \mathbf{r}') = 3\sigma^2(\mathbf{r}, \mathbf{r}') - 2\sigma^3(\mathbf{r}, \mathbf{r}'), \tag{3.32}$$

where $\rho(\mathbf{r}, \mathbf{r}')$ and $\sigma(\mathbf{r}, \mathbf{r}')$ commute with each other. The idempotency of the density matrix ρ is naturally obtained in the energy minimisation process of $\frac{\delta E[\rho]}{\delta \sigma}$ through the optimisation of $L^{\alpha\beta}$. Multiple minima do not appear in this method due to the nature of the cubic functional of $\mathbf{L}$. However, the same reason causes the instability of this method if any of the eigenvalues of $\mathbf{L}$ is not within the range of convergence for the purification transformation. The purification transformation is stabilised by restricting the occupation numbers $\{f_n\}$ within an interval of $\left[\frac{1-\sqrt{5}}{2}, \frac{1+\sqrt{5}}{2}\right]$.

The globally convergent penalty-functional method is applied if the calculation is unstable [56, 128].

Another method for imposing the idempotency of density matrix is through the minimisation of the positive definite functional $P[\rho]$ by using a steepest descents method [56, 128],

$$\begin{aligned} P[\rho] =& \int\int d^3r\, d^3r' \,[\rho^2(\mathbf{r},\mathbf{r}') - \rho(\mathbf{r},\mathbf{r}')][\rho^2(\mathbf{r}',\mathbf{r}) - \rho(\mathbf{r}',\mathbf{r})] \\ =& \mathrm{Tr}\left[(\rho^2-\rho)^2\right] = \sum_n (f_n^2 - f_n)^2. \end{aligned} \tag{3.33}$$

This quantitatively measures how much $\rho(\mathbf{r},\mathbf{r}')$ deviates from idempotency. $P[\rho]$ may be regarded as a penalty functional to enforce idempotency. This is realised by minimising a generalised energy functional $Q[\rho] = E[\rho] + \alpha P[\rho]$, where $E[\rho]$ is the energy functional (energy calculated from eq. (3.5)) and the strength of the penalty functional $P[\rho]$ is adjusted by α. One of the weaknesses for using penalty functionals is that may suffer from multiple local minima. Fortunately, this is observed empirically not to cause a problem if the density matrix is prepared properly in the beginning because the normalisation constraint will remove most of the local minima and the density matrix will be driven towards the global ground state minimum in the process of energy minimisation [128].

3.1.2 NGWF optimisation

The adoption of NGWFs in ONETEP benefits its transferability because the size of the orbital set does not need to be increased to satisfy the convergence criterion. Although extra computational effort is needed in the process of optimisation, the cost is partly reduced while at the same time maintaining the accuracy owing to the minimal size of the orbital set used [56]. From the previous section, the NGWFs are expanded in terms of psinc functions in eq. (3.22) and eq. (3.23) where $D_k(\mathbf{r})$ is written as [123]

$$D_k(\mathbf{r}) = \frac{1}{N}\sum_p e^{i\mathbf{k}_p\cdot(\mathbf{r}-\mathbf{r}_k)}, \tag{3.34}$$

where $\mathbf{k}_p$ refers to a grid point in reciprocal space and $\mathbf{r}_k$ refers to a grid point of the simulation cell and the total number of grid points in a three-dimensional simulation cell is $N = N_1N_2N_3$.

Fast Fourier transforms (FFTs) are adopted to calculate the kinetic energy accurately and efficiently benefiting from the relation between psinc functions and plane waves. However, the calculation time by adopting FFTs would be $O(N^2)$

in overall and $O(N\log N)$ for the computational cost when calculating the kinetic energy of a single NGWF [56]. The FFT box technique [129] is then used to solve this problem. FFT box is centred on each NGWF and all the overlapping neighbours of centred NGWF are also included in the same FFT box. It is designed to have universal and appropriate shape and size for all FFT boxes with different NGWFs. In reciprocal space, the sampling can be coarser than the simulation cell because the localisation of NGWFs in real space broaden its Fourier transforms [56]. Furthermore, the $O(N)$ effort is maintained because the volume of the FFT box is only determined by the cut-off radii of the NGWFs. The FFTs are performed over the whole simulation cell in traditional cubic-scaling methods, however, the FFT box is only performed in the position of NGWFs (or position of atoms) and ignore the vacuum. The computation time of performing FFTs are substantial in both cubic-scaling and linear-scaling methods. The cross-over when the efficiency of linear-scaling method is higher than the traditional cubic-scaling methods can be estimated when the volume of the FFT box is comparable to the simulation cell because both methods perform a comparable number and size of FFTs. The number of atoms where cross-over occurs is lower in low-dimensional systems than solids because larger vacuum regions are included in low-dimensional systems [56].

3.1.3 Projector augmented waves (PAWs) in ONETEP

In section 2.6, PAW was introduced as based on a transformation between all-electron wave function and pseudo wave function. In linear-scaling methods, PAW needs to be reformulated as a function of the density matrix before it can be used because the eigenstates cannot be accessed directly. Eq. (2.46) is rewritten below based on [130],

$$|\psi_n\rangle = |\tilde{\psi}_n\rangle + \sum_{\nu} \left(|\varphi_\nu\rangle - |\tilde{\varphi}_\nu\rangle\right) \langle \tilde{p}^\nu | \tilde{\psi}_n\rangle \,, \tag{3.35}$$

where $|\tilde{p^\nu}\rangle$ is a predefined projector ($|\tilde{p_m}\rangle$ in eq. (2.46)), $|\tilde{\varphi_\nu}\rangle$ is the partial wave function and $|\varphi_\nu\rangle$ is the all-electron wave function. According to eq. (3.2) and eq.

(3.35), the density matrix is now reformulated as

$$
\begin{aligned}
\rho =& \sum_n |\psi_n\rangle f_n \langle\psi_n| \\
=& \sum_n \left(|\tilde{\psi}_n\rangle + \sum_\nu (|\varphi_\nu\rangle - |\tilde{\varphi}_\nu\rangle) \langle\tilde{p}^\nu|\tilde{\psi}_n\rangle \right) f_n \left(\langle\tilde{\psi}_n| + \sum_\mu (\langle\varphi_\mu| - \langle\tilde{\varphi}_\mu|) \langle\tilde{\psi}_n|\tilde{p}^\mu\rangle \right) \\
=& \sum_n |\tilde{\psi}_n\rangle f_n \langle\tilde{\psi}_n| + \sum_{\nu\mu} (|\varphi_\nu\rangle - |\tilde{\varphi}_\nu\rangle)(\langle\varphi_\mu| - \langle\tilde{\varphi}_\mu|) \sum_n \langle\tilde{p}^\nu|\tilde{\psi}_n\rangle f_n \langle\tilde{\psi}_n|\tilde{p}^\mu\rangle \\
&+ \sum_\nu (|\varphi_\nu\rangle - |\tilde{\varphi}_\nu\rangle) \langle\tilde{p}^\nu| \sum_n |\tilde{\psi}_n\rangle f_n \langle\tilde{\psi}_n| + \sum_n |\tilde{\psi}_n\rangle f_n \langle\tilde{\psi}_n|\tilde{p}^\mu\rangle \sum_\mu (\langle\varphi_\mu| - \langle\tilde{\varphi}_\mu|),
\end{aligned}
\tag{3.36}
$$

where the pseudo density matrix $\tilde{\rho} = \sum_n |\tilde{\psi}_n\rangle f_n \langle\tilde{\psi}_n|$ can be substituted into all terms in eq. (3.36). Assuming the partial waves form a complete set within the augmentation region, thus $\sum_\nu |\tilde{\varphi}_\nu\rangle \langle\tilde{p}^\nu| = 1$ and $\sum_\mu |\tilde{p}^\mu\rangle \langle\tilde{\varphi}_\mu| = 1$, these two expressions can be inserted into third and fourth terms, respectively. Then,

$$
\begin{aligned}
\rho =& \tilde{\rho} + \sum_{\nu\mu} (|\varphi_\nu\rangle - |\tilde{\varphi}_\nu\rangle) \langle\tilde{p}^\nu|\tilde{\rho}|\tilde{p}^\mu\rangle (\langle\varphi_\mu| - \langle\tilde{\varphi}_\mu|) + \sum_{\nu\mu} (|\varphi_\nu\rangle - |\tilde{\varphi}_\nu\rangle) \langle\tilde{p}^\nu|\tilde{\rho}|\tilde{p}^\mu\rangle \langle\tilde{\psi}_\mu| \\
&+ \sum_{\nu\mu} |\tilde{\psi}_\nu\rangle \langle\tilde{p}^\nu|\tilde{\rho}|\tilde{p}^\mu\rangle (\langle\varphi_\mu| - \langle\tilde{\varphi}_\mu|) \\
=& \tilde{\rho} + \sum_{\nu\mu} \left(|\varphi_\nu\rangle \langle\varphi_\mu| - |\tilde{\psi}_\nu\rangle \langle\tilde{\psi}_\mu| \right) \langle\tilde{p}^\nu|\tilde{\rho}|\tilde{p}^\mu\rangle .
\end{aligned}
\tag{3.37}
$$

It is noted that any nonlocal operators are assumed not to act between the regions of different PAW spheres. Radial grids and uniform grids are presumed to be treated in the region inside (“atomic" part) and outside (“soft" part) PAW sphere, respectively, when calculating energies with PAW method. According to eq. (3.37), the total all-electron density of valence states is the sum of the pseudo electron density (on uniform grids) $\tilde{n}(\mathbf{r})$ and atomic part of all-electron $n^1(\mathbf{r})$, subtracting an atomic part of pseudo electron $\tilde{n}^1(\mathbf{r})$ [130],

$$
n_v(\mathbf{r}) = \rho(\mathbf{r}, \mathbf{r}) = \tilde{n}(\mathbf{r}) + n^1(\mathbf{r}) - \tilde{n}^1(\mathbf{r}). \tag{3.38}
$$

According to the density matrix based on NGWF formalism eq. (3.9),

$$
\tilde{n}(\mathbf{r}) = \sum_{\alpha\beta} \phi_\alpha(\mathbf{r}) K^{\alpha\beta} \phi^*_\beta(\mathbf{r}), \tag{3.39}
$$

$$
n^1(\mathbf{r}) = \sum_{\nu\mu} \varphi_\nu(\mathbf{r}) \rho^{\nu\mu} \varphi^*_\mu(\mathbf{r}), \tag{3.40}
$$

$$\tilde{n}^1(\mathbf{r}) = \sum_{\nu\mu} \tilde{\varphi}_\nu(\mathbf{r})\rho^{\nu\mu}\tilde{\varphi}^*_\mu(\mathbf{r}), \tag{3.41}$$

where $\rho^{\nu\mu}$ refers to the projection of the density matrix within the PAW spheres,

$$\rho^{\nu\mu} = \sum_{\alpha\beta} \langle \tilde{p}^\nu|\phi_\alpha\rangle K^{\alpha\beta} \langle \phi_\beta|\tilde{p}^\mu\rangle . \tag{3.42}$$

$\langle \phi_\alpha|\tilde{p}^\nu\rangle$ is a sparse matrix in large systems due to the localisation of ϕ_α and $\tilde{p}^\nu$. Therefore, $\rho^{\nu\mu}$ can be efficiently obtained with efficient sparse matrix algebra [124, 130, 131] when evaluating $K^{\alpha\beta}$. Nonzero blocks only exist when ν and μ are on the same atom, thus forming a "block-diagonal" matrix [130].

3.2 Spectral function unfolding method

The spectral function unfolding method below is based on the paper of Popsecu et al. [65]. Some of the research presented in this thesis involves the study of electronic properties of large-scale systems with ordered and disordered structures, thus an efficient method for calculating band structures is necessary. For disordered structures with no long-range periodicity, the concept of band structure (E versus $\mathbf{k}$ dispersion) and the quantities derived from it, for example, effective mass ($m^* = \hbar^2 \left[\frac{\partial^2 E}{\partial k_\alpha \partial k_\beta}\right]^{-1}$) and band-velocity ($v_\mathbf{k} = \hbar^{-1}\frac{\partial E}{\partial \mathbf{k}}$) no longer truly exist. Instead, an effective band structure (EBS) can be generated through the spectral function unfolding method where the information of band structure is mapped from supercell to primitive cell. It gives a better result than effective medium approximations with the assumption of the same potential in all atoms [65]. The local atomic relaxations can be explicitly considered in the spectral function unfolding method, whereas the structure is artificially enforced to have a high symmetry in effective medium approximations [65]. The dispersion relation in the primitive cell (PC) is reconstructed from a supercell (SC) calculation through a band unfolding technique [132, 133, 134, 135, 136]. For disordered structures, virtual crystal approximation (VCA) [137] or the single-site coherent potential approximation (CPA) [138, 139] may be used to calculate the band structure by forcing a PC periodicity. "Broadened bands" are obtained in the CPA [139]. Therefore, the polymorphic nature of disordered structures leads to an EBS with "broadened band complex" [65].

The derivation of the spectral function is according to the following procedure. A given SC wave vector $\mathbf{K}$ can be obtained by folding a given PC wave vector

$\mathbf{k}$ into a wave vector $\mathbf{K}$ through a reciprocal lattice vector $\mathbf{G}_0$ [65],

$$\mathbf{K} = \mathbf{k} - \mathbf{G}_0. \tag{3.43}$$

In contrast, a set of PC wave vectors $\{\mathbf{k}_i\}$ can be obtained by unfolding a given SC wave vector $\mathbf{K}$ through a reciprocal lattice vector set $\{\mathbf{G}_i\}$,

$$\mathbf{k}_i = \mathbf{K} + \mathbf{G}_i, \quad i = 1, ..., N_{\mathbf{K}}, \tag{3.44}$$

where $N_{\mathbf{k}} = \det(M) = v_{\text{pbz}}/V_{\text{SBZ}}$ (pbz and SBZ are the Brillouin zones of primitive cell and supercell, respectively). In periodic solids, $\mathbf{k} \in$ pbz and $\mathbf{K} \in$ SBZ are both good quantum numbers to obtain the dispersion relation.

A linear combination of PC eigenvectors $|\mathbf{k}_i n\rangle$ ($i = 1, ..., N_{\mathbf{K}}$) can be used to represent any SC eigenvector $|\mathbf{K}m\rangle$ through the zone folding and unfolding relations mentioned above [65, 133, 140],

$$|\mathbf{K}m\rangle = \sum_{i=1}^{N_{\mathbf{K}}} \sum_{n} F(\mathbf{k}_i, n; \mathbf{K}, m) \, |\mathbf{k}_i n\rangle \, . \tag{3.45}$$

$\{F(\mathbf{k}_i, n; \mathbf{K}, m)\}$ is a set of parameters to recover a SC eigenvector from a set of PC eigenvectors. It is expressed as the spectral weight [132, 133] shown below,

$$P_{\mathbf{K}m}(\mathbf{k}_i) = \sum_{n} |\langle \mathbf{K}m|\mathbf{k}_i n\rangle|^2. \tag{3.46}$$

A spectral function (SF) with continuous variable is defined as [65]

$$A(\mathbf{k}_i, E) = \sum_{m} P_{\mathbf{K}m}(\mathbf{k}_i)\delta(E_m - E). \tag{3.47}$$

The symmetry of PC is not required to be identical to the SC, so that the eigenstates $|\mathbf{k}_i n\rangle$ may be different in the SC representation when considering different symmetries. In that case, the spectral weights in eq. (3.46) may not have integer values even in ordered compounds. The spectral weights are not δ functions in disordered alloys due to the different local environments and the inelastic scattering in the alloy, thus forming a spectral function, $A(\mathbf{k}, E)$ with finite width [65].

It is worth noting that the final expression of $P_{\mathbf{K}m}(\mathbf{k}_j)$ is not written in terms of $|\mathbf{k}n\rangle$, thus these do not need to be explicitly calculated. However, the orthonormality condition needs to be satisfied [65],

$$\langle \mathbf{k}n|\mathbf{k}n'\rangle = \delta_{nn'}. \tag{3.48}$$

The polymorphic nature of a disordered structure is implicitly included in the dispersion relation. Furthermore, the cumulative sum of $\mathbf{A}(\mathbf{k}_i, E)$ [134] can help estimating the positions and widths of bands [65],

$$S_{\mathbf{k}_i}(\varepsilon_n) = \int^{\varepsilon_n} \mathbf{A}(\mathbf{k}_i, E) dE. \tag{3.49}$$

The spectral function unfolding method implemented in ONETEP below is based on the paper of Constantinescu et al. [66]. They adapted the work of Lee et al. [141] with the basis of local orbitals to PAW and NGWF formalism. The spectral function operator is defined as

$$\hat{A}(\omega) = -\frac{1}{\pi} \mathrm{Im} \sum_{\mathbf{K},J} \frac{|\Psi_{\mathbf{K}J}\rangle \langle \Psi_{\mathbf{K}J}|}{\omega + i\eta - \epsilon_{\mathbf{K}J}} = \frac{\eta}{\pi} \sum_{\mathbf{K},J} \frac{|\Psi_{\mathbf{K}J}\rangle \langle \Psi_{\mathbf{K}J}|}{(\omega - \epsilon_{\mathbf{K}J})^2 + \eta^2}, \tag{3.50}$$

where $|\Psi_{\mathbf{K}J}\rangle$ is the all-electron Bloch state in a SC calculation with corresponding eigenvalue $\epsilon_{\mathbf{K}J}$. $\mathbf{K}$ is the wave vector in SBZ, J is the band index and η is an infinitesimal positive broadening factor for keeping away from the singularity at $\omega = \epsilon_{\mathbf{K}J}$. A broadening factor of 0.02 eV was used for all effective band structures shown in this thesis. This is different from the disordered broadening which is related to the polymorphic nature of disordered structures mentioned above. The effect of disordered broadening can be seen from the difference of width for any given band along the kpoint path in the effective band structure.

The desired spectral function is represented by a wave function in the PC. It is written as the trace of the spectral function operator,

$$A = \sum_{\mathbf{k}j} A_{\mathbf{k}j,\mathbf{k}j} = \sum_{\mathbf{k}j} \langle \Psi_{\mathbf{k}j} | \hat{A} | \Psi_{\mathbf{k}j} \rangle = \sum_{\mathbf{k},\alpha} A_{\mathbf{k}\alpha,\mathbf{k}^\alpha} = \sum_{\mathbf{k},\alpha} \langle \psi_{\mathbf{k},\alpha} | \hat{A} | \psi^{\alpha}_{\mathbf{k}} \rangle. \tag{3.51}$$

The spectral function in terms of the PC wave functions is expressed as

$$A^{I}_{\mathbf{k}j,\mathbf{k}j}(\omega) = \frac{L}{l} \sum_{\mathbf{K}} \delta_{\mathbf{k}-\mathbf{G},\mathbf{K}} \cdot A_{\mathbf{K}J,\mathbf{K}J}(\omega) \sum_{\mu,\nu,\mathbf{r}} e^{i\mathbf{k}\cdot(\mathbf{r}-\mathbf{r}'(\mu))} M^{\mu}_{\mathbf{K}J} M^{\nu^*}_{\mathbf{K}J} S_{\mathbf{0}\nu,\mathbf{r}\gamma(\mu)}, \tag{3.52}$$

with $\mathbf{r}\gamma(\mu) \in I$, so that $\mu \in I$. The l and L refer to the number of PC and SC duplicates, respectively. $M^{\mu}_{\mathbf{K}J}$ is the molecular orbital coefficient and μ refers to the index of the NGWF in the SC with its range between 1 and the total number of NGWFs in the simulation cell. The augmented overlap matrix element $\mathrm{S}_{\mathbf{0}\nu,\mathbf{r}\gamma(\mu)}$ is denoted as $\langle \phi_{\mathbf{0}\nu} | \phi_{\mathbf{r}\gamma(\mu)} \rangle$, where $\{|\phi\rangle\}$ is the NGWF basis set. $\mathbf{0}$ refers to the original SC lattice vector because only its influence is concerned. $\gamma = \mu\% N_{\mathrm{PC}}$ (N_{PC} is the total number of NGWFs in the unit cell) is an index of the considered NGWF in

the SC from the perspective of the PC. $\mathrm{A}_{\mathbf{K}J,\mathbf{K}J}$ is a broadened Lorentzian function according to eq. (3.50). The sum of each $\mathrm{A}^{I}_{\mathbf{k}j,\mathbf{k}j}$ in subsystem I gives the total spectral function in the representation of PC eigenstates. The calculated spectral function $A_{\mathbf{k}j,\mathbf{k}j}$ is often compared with the experimental results from ARPES.

Chapter 4

Two-dimensional transition metal dichalcogenide alloy-$Mo_{1-x}W_xS_2$ monolayer

This chapter is mainly related to the theoretical and computational simulations of $Mo_{1-x}W_xS_2$ monolayers. All the experimental results shown in this chapter were provided by our collaborators led by Dr. Neil R. Wilson, from the University of Warwick. This work has been published in the Journal of Physics: Materials in 2021 [142], licenced under CC BY 4.0: X. Xia, S. M. Loh, J. Viner, N. C. Teutsch, A. J. Graham, V. Kandyba, A. Barinov, A. M. Sanchez, D. C. Smith, N. D. M. Hine and N. R. Wilson. Atomic and electronic structure of two-dimensional $Mo_{(1-x)}W_xS_2$ alloys. *J. Phys. Mater.*, 4:025004, 2021. URL:`https://doi.org/10.1088/2515-7639/abdc6e`.

4.1 Introduction

The atomic and electronic structures of an alloy composed of 2H-MoS_2 and 2H-WS_2 monolayers were studied in this chapter. Through studying this alloy and comparing our theoretical results with the experimental results, the conclusions obtained here can be expanded to similar materials (e.g. $Mo_{1-x}W_xSe_2$) prior to an actual experiment. Furthermore, some properties which cannot be performed or measured in the experiment can even be predicted through theoretical studies.

MoS_2 and WS_2 are two typical transition metal dichalcogenides with wide range of applications in optoelectronic [22, 143] and semiconductor devices [27, 34, 46]. The alloy $Mo_{1-x}W_xS_2$ has been synthesised by several methods, such

as CVD and CVT [42, 47]. The quality of the crystal was then confirmed by multiple forms of experimental measurements such as atomic force microscopy (AFM) imaging, STEM, X-ray photoelectron spectroscopy (XPS) analysis, PL and Raman spectroscopies. The similarity in the atomic and electronic structures (see figure 4.1) of MoS_2 and WS_2 monolayers suggests that homogeneous alloys are expected to be formed. Zhang et al. [50] have proved this by showing highly homogeneous and non-phase-segregated crystals in their studies. Dumcenco et al. [69] have also displayed $Mo_{1-x}W_xS_2$ ($x = 0, ..., 1$) monolayers with random distribution. However, the kinetic driven process also needs to be considered. Dopant distribution with stripe patterns was formed in the work of Azizi et al. [144]. Their calculations showed that there is no difference in binding energy between striped and random distribution. The formation of stripes in the alloys is due to the fluctuations of the local chemical potentials of molybdenum, tungsten and sulphur atoms at the growth edge. Thus, they find the alloy is isotropic in the electronic property and anisotropic in the vibrational property due to the similarity of their electronic structure and the difference of their atomic masses, respectively. Furthermore, entropy was suggested to play a role in generating disordered distributions in this alloy by Tan et al. [145]. They showed that the ordered phase is less stable than the disordered phase as the temperature increases.

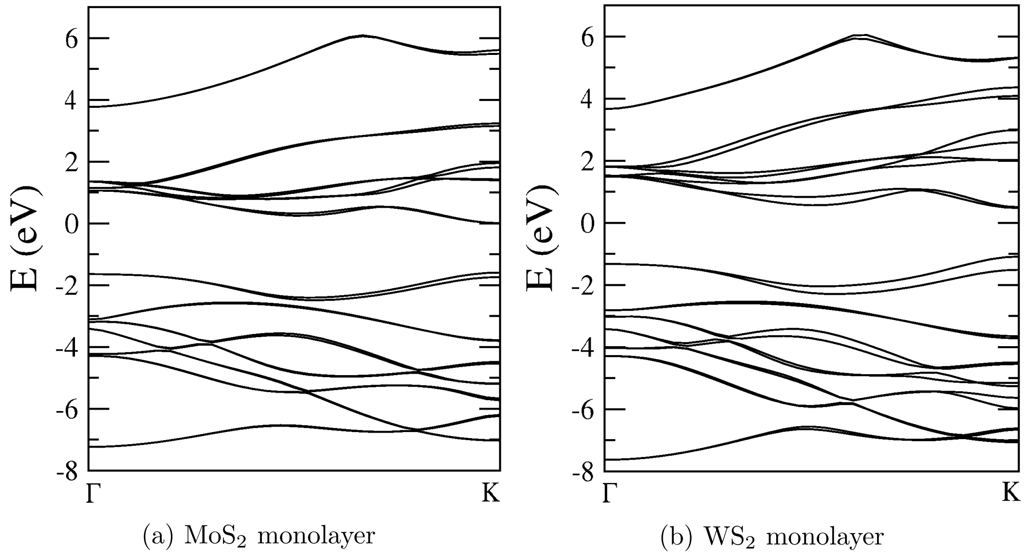

(a) MoS_2 monolayer

(b) WS_2 monolayer

Figure 4.1: Electronic structures of MoS_2 and WS_2 monolayers calculated with a plane wave basis set and the GGA-PBE pseudopotential through Quantum Espresso [61, 62].

Physical properties of an alloy $A_xB_{1-x}C$ composed of semiconductors AC

and BC (where A and B are required to be isovalent atoms) can normally be expressed by a simple equation according to the composition stoichiometry [146, 147],

$$F_x = xF_{AC} + (1-x)F_{BC} + kx(1-x), \tag{4.1}$$

where F_x, F_{AC} and F_{BC} are physical properties of the alloy, AC and BC, respectively. k is a general bowing parameter independent of the composition x of the alloy. For example, $k \simeq 0$ if F refers to the lattice constant for a system with negligible lattice mismatch between AC and BC (Vegard's law [148]). In contrast, the bowing effect is significant for electronic properties such as band gaps and band edges, The bowing parameters are 0.25 ± 0.04 eV and 0.28 ± 0.04 eV for the experimental and the theoretical band gaps, respectively [42].

Chen et al. [42] explained that the bowing of the band gap originated from the CBM. Orbitals d_{xy} and $d_{x^2-y^2}$ from MoS_2 and WS_2 contribute equally to the VBM of the alloy, while there are different orbitals contributed from MoS_2 and WS_2 for the CBM: orbitals d_{z^2} from MoS_2 and $\{d_{xy}, d_{x^2-y^2}, d_{z^2}\}$ from WS_2. Thus, the bowing for the VBM is not obvious due to the same orbital contributions from both MoS_2 and WS_2 monolayers. The contribution from WS_2 monolayer for the CBM with higher energy level increases as W composition x increases leading to the bowing in the CBM [42]. Furthermore, Tan et al. [145] suggested that the atomic distribution of the alloy also needs to be considered. Ordered atomic distributions generate a smaller band gap than disordered phases, due to the difference of the conduction band splitting around the Fermi level at **K** between ordered and disordered phases. For example, the conduction band splitting around the Fermi level at **K** are 20 meV and 220 meV for disordered and ordered phase at $x = 1/3$, respectively [145].

In this work, the atomic and electronic structures of $Mo_{1-x}W_xS_2$ monolayers were studied. The atomic distribution of W dopants in MoS_2 monolayer was analysed via Monte Carlo simulations. The electronic properties of $Mo_{1-x}W_xS_2$ monolayers including the band gap, band splitting due to SOC, bandwidth of the VBM and effective mass for holes were compared with the VCA [149] and experimental results provided by our collaborators led by Dr. Neil R. Wilson from the University of Warwick. The $Mo_{1-x}W_xS_2$ monolayers were synthesised via CVT [150] and determined by optical contrast, Raman spectra, PL emission, XPS and energy dispersive X-ray analysis (EDX). The experimental data were measured through PL spectroscopy and ARPES. A polarisation-resolved low-temperature PL spectroscopy was also performed by Dr. David C. Smith from the University of Southampton for determining the maintenance of the spin-valley locking in $Mo_{1-x}W_xS_2$ monolayer.

4.2 Computational methods

The lattice constant of MoS_2 and WS_2 monolayers and the binding energy of $Mo_{1-x}W_xS_2$ monolayers were calculated using CASTEP [60] (a plane-wave density functional theory package). The GGA-PBE [94] with ultrasoft pseudopotentials generated from on-the-fly [103] in CASTEP was used. The cut-off energy was set to 424.5 eV. The lattice constants of MoS_2 and WS_2 monolayers were calculated within primitive cells with a 10×10×1 of kpoint grids, whereas the binding energy was calculated within 4×4×1 supercells with a kpoint grid of 3×3×1. Furthermore, twenty $Mo_{0.8}W_{0.2}S_2$ monolayers within 12×12×1 supercells with a kpoint grid of 1×1×1 were also calculated to verify the validation of binding energy. The spurious interaction between two isolated cells is eliminated by increasing the vacuum spacing to 10 Å.

The distribution of W atoms within MoS_2 monolayers was analysed through Monte Carlo simulations [67] on a hexagonal lattice. The observation of the short-ranged W-W pairs inspires us to apply a model based on the Ising model [151] with only nearest-neighbour pairs of transition metal atoms (Mo and W atoms) being considered. The Hamiltonian is expressed as

$$H = -\sum_{ij} J_{ij}\sigma_i\sigma_j, \tag{4.2}$$

where J_{ij} is the interaction energy between the nearest-neighbour pairs. It is zero except for the nearest neighbours (in that case $J_{ij} = J$). In the simulation, proposed site swaps between Mo and W atoms were randomly generated. Whether a site swap is accepted depends on whether another random number generated in each site swap is smaller than $e^{-k_B T(E_{new}-E_{old})}$, where k_B is the Boltzmann constant, T is the temperature considered, E_{new} and E_{old} are the total energies after and before the site swap, respectively. Initially, a number of atoms of 14400 were randomly distributed within a 120×120 2D layer. The ratio of Mo and W atoms were determined by the W composition x considered. It was verified that equilibrium was achieved after 2×10^4 cycles at $T = 800$ K. The pairwise interaction energy J was based on the binding energy calculated via CASTEP (see later). Furthermore, the atomic configuration of a STEM with annular dark-field (ADF) image was also compared with the results of Monte Carlo simulations.

Lastly, the electronic properties of $Mo_{1-x}W_xS_2$ monolayers were calculated by ONETEP [59, 63] (a linear-scaling density functional theory (LS-DFT) package). Benefiting from the $O(N)$ computational effort of this LS-DFT package, large-scale systems can be more effectively simulated. Here, $Mo_{1-x}W_xS_2$ monolayers with

a random distribution within an 8×8×1 supercell (figure 4.2) were used in the calculations. The cut-off energy and NGWF cut-off radius were set to 1200 eV and 10 a_0, respectively. Projector-augmented wave (PAW) [104, 105, 130] from the JTH library [152] with the PBE pseudopotential functional was adopted. Only Gamma point was considered in the Brillouin zone sampling for all calculations in ONETEP, owing to the relatively large supercells. The spurious interaction between two isolated cells is eliminated by increasing the vacuum spacing to 15 Å. The force and enthalpy were converged within 0.1 eV/Å and 3×10^{-5} eV/atom, respectively, in geometry optimisation calculations. The effective band structures projected on the primitive cell for $Mo_{1-x}W_xS_2$ monolayers within 8×8×1 supercells were calculated through the spectral function unfolding method implemented in ONETEP [66] with the SOC included as a perturbation. A Lorentzian broadening of 0.02 eV was tested and employed for getting clear bands in the effective band structure. The bands in the effective band structure become more discontinuous or vague if the broadening factor is smaller or larger than 0.02 eV, respectively. The band gap, bandwidth, and band splitting due to SOC near the VBM and the CBM for various W compositions x were directly obtained from the spectral function unfolding calculations, whereas the effective masses for holes were obtained through a fitting around **K**.

The results from VCA [149] calculations via Quantum Espresso code [61, 62] are also shown to compare with the results from LS-DFT and the experiment. The GGA-PBE of optimised norm-conserving Vanderbilt pseudopotentials (fully-relativistic) [153] obtained from PseudoDojo [154] with a kpoint grid of 18×18×1 was used in the calculations for various W compositions x were generated via the "virtual" tool (upftools/virtual_v2.o) within the Quantum Espresso package. SOC [155, 156, 157] was considered in the calculations. The mixed pseudopotential is written as [158]

$$\begin{aligned} V^{\text{ps}}_{\text{VCA}}[x] =& xV^{\text{ps}}_{\text{W}} + (1-x)V^{\text{ps}}_{\text{Mo}} \\ &= \left[xV^{\text{loc}}_{\text{W}} + (1-x)V^{\text{loc}}_{\text{Mo}}\right] + \sum_{lm}\sum_{q} \frac{xV^{\text{ps}}_{\text{W},l}\,|\phi^{\text{W}}_{lm,q}\rangle\langle\phi^{\text{W}}_{lm,q}|\,xV^{\text{ps}}_{\text{W},l}}{\langle\phi^{\text{W}}_{lm,q}|xV^{\text{ps}}_{\text{W},l}|\phi^{\text{W}}_{lm,q}\rangle}, \\ &+ \sum_{lm}\sum_{q} \frac{(1-x)V^{\text{ps}}_{\text{Mo},l}\,|\phi^{\text{Mo}}_{lm,q}\rangle\langle\phi^{\text{Mo}}_{lm,q}|\,(1-x)V^{\text{ps}}_{\text{Mo},l}}{\langle\phi^{\text{Mo}}_{lm,q}|(1-x)V^{\text{ps}}_{\text{Mo},l}|\phi^{\text{Mo}}_{lm,q}\rangle} \end{aligned} \tag{4.3}$$

where $V^{\text{ps}}_{\text{Mo}}$ and V^{ps}_{W} are the pseudopotentials of molybdenum and tungsten atoms, respectively. The terms inside the square bracket represent the local contributions, whereas the second and third terms represent the short-range non-local corrections.

All atomic structures were generated and displayed via the atomic simulation environment (ASE) [159], NumPy [160] and visualisation for electronic and structural analysis (VESTA) [161].

4.3 Results and discussions

Figure 4.2 shows the top and side views of $Mo_{1-x}W_xS_2$ monolayers. Each Nth-nearest-neighbour pair is illustrated for later discussions.

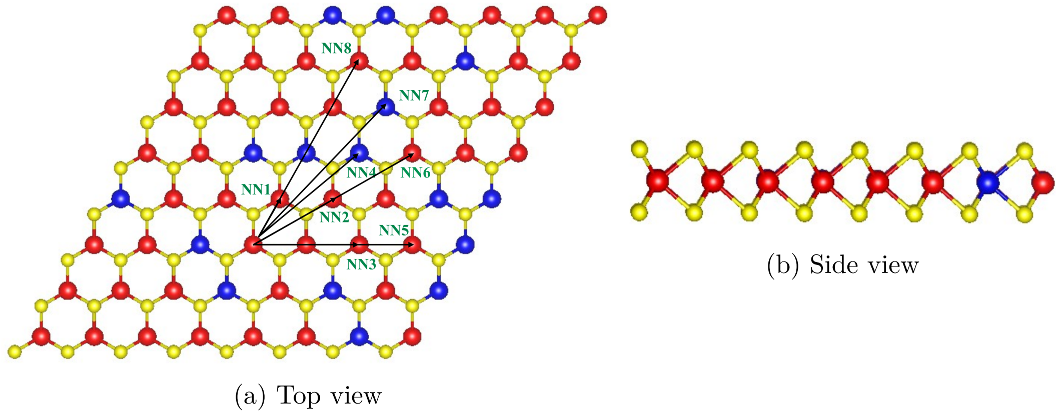

(a) Top view

(b) Side view

Figure 4.2: (a) Top view (b) Side view of a $Mo_{1-x}W_xS_2$ monolayer. Red, blue and yellow colours refer to Mo, W and S atoms, respectively. Nth-nearest-neighbour pair is labelled as NN_i, where $i = 1, ..., 8$.

In this work, the lattice constants of MoS_2 and WS_2 monolayers calculated by CASTEP are 3.18 Å and 3.19 Å, respectively, consistent with the lattice constant in [162] with the same pseudopotential (see figure 4.3). The difference of lattice constant between MoS_2 and WS_2 monolayers is only 0.3%. Thus 3.18 Å was used as the lattice constant for all calculations with different W compositions x, where x spans a range between 0 and 1.

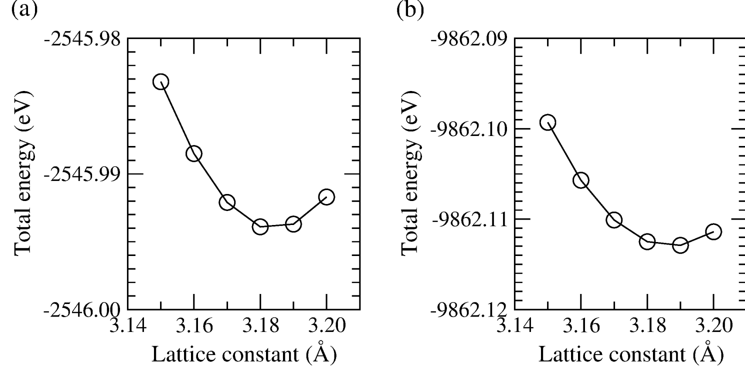

Figure 4.3: Total energy versus lattice constant of (a) MoS_2 (b) WS_2 monolayer.

4.3.1 Binding energy of $Mo_{1-x}W_xS_2$ monolayer

The energetics of various atomic configurations including isolated W atoms or W clusters in MoS_2 are considered in this section. The formation energy of substituting m tungsten atoms for the same number of molybdenum atoms in MoS_2 monolayer can be written as [163]

$$E_{\mathrm{F}} = E_{\mathrm{T}}^{\mathrm{alloy}} - E_{\mathrm{T}}^{\mathrm{MoS_2}} + m\mu_{\mathrm{W}} - m\mu_{\mathrm{Mo}}, \tag{4.4}$$

where $E_{\mathrm{T}}^{\mathrm{alloy}}$ is the total energy of $Mo_{1-x}W_xS_2$ monolayer, $E_{\mathrm{T}}^{\mathrm{MoS_2}}$ is the total energy of MoS_2 monolayer, μ_{Mo} and μ_{W} refers to the chemical potential of molybdenum and tungsten atoms, respectively. The binding energy for the atomic configuration involved m W atoms on adjacent lattice sites is then written as

$$\begin{aligned} E_{\mathrm{B}} &= E_{\mathrm{F}}^{m\mathrm{W}} - mE_{\mathrm{F}}^{1\mathrm{W}} \\ &= \left[E_{\mathrm{T}}^{m\mathrm{W}} - E_{\mathrm{T}}^{\mathrm{MoS_2}} + m\mu_{\mathrm{W}} - m\mu_{\mathrm{Mo}}\right] - m\left[E_{\mathrm{T}}^{1\mathrm{W}} - E_{\mathrm{T}}^{\mathrm{MoS_2}} + \mu_{\mathrm{W}} - \mu_{\mathrm{Mo}}\right] \\ &= E_{\mathrm{T}}^{m\mathrm{W}} - mE_{\mathrm{T}}^{1\mathrm{W}} + (m-1)E_{\mathrm{T}}^{\mathrm{MoS_2}}, \end{aligned} \tag{4.5}$$

where $E_{\mathrm{T}}^{m\mathrm{W}}$ and $mE_{\mathrm{T}}^{1\mathrm{W}}$ are the total energies of $Mo_{1-x}W_xS_2$ monolayers involved m W atoms in a cluster and m isolated W atoms, respectively.

The binding energy based on eq. (4.5) for various atomic configurations are shown in figure 4.4 and table 4.1. The binding energy $E_{\mathrm{B}} \simeq 7.6$ meV when $m = 2$ is obtained ($E_B \simeq 7.0$ meV if Mo atom is the substitutional dopant in WS_2 monolayer). The positive binding energy suggests that W and Mo atoms prefer not to form clusters in MoS_2 and WS_2 monolayers, respectively. Roughly, the difference of binding energy (Δ) between atomic configurations in figure 4.4 and their

corresponding predicted values calculated by the product of 7.57 meV and number of W-W bonds increases as the number of W-W bonds increases (table 4.1). The relationship between the binding energy and the number of W-W bonds was further studied in twenty $Mo_{0.8}W_{0.2}S_2$ monolayers with different random configurations within 12×12×1 supercells. In figure 4.5(b), it seems like Δ does not in fact simply increase monotonically with the number of W-W bonds. Different Δ values corresponding to the same number of W-W bonds can be seen, for example, in the atomic configuration with the number of W-W bonds = 13, 15, 17 and 20. The binding energies in figure 4.5(a) are in a range from 5 meV to 6.5 meV. This energy range slightly deviates from 7.6 meV due to the interactions beyond pairwise terms in large clusters. In fact, the binding energy is higher than 7.6 meV in larger supercell with the same atomic configurations as in figure 4.4. The density of W atoms is lower in a larger supercell. For example, the binding energies are 7.62 meV and 7.72 meV for 8×8×1 and 12×12×1 supercells, respectively. Because the difference of binding energy of $Mo_{1-x}W_xS_2$ monolayers with different atomic configurations and supercell sizes is relatively small, 7.6 meV is adopted as the pairwise interaction energy in Monte Carlo simulation to give a phenomenological description.

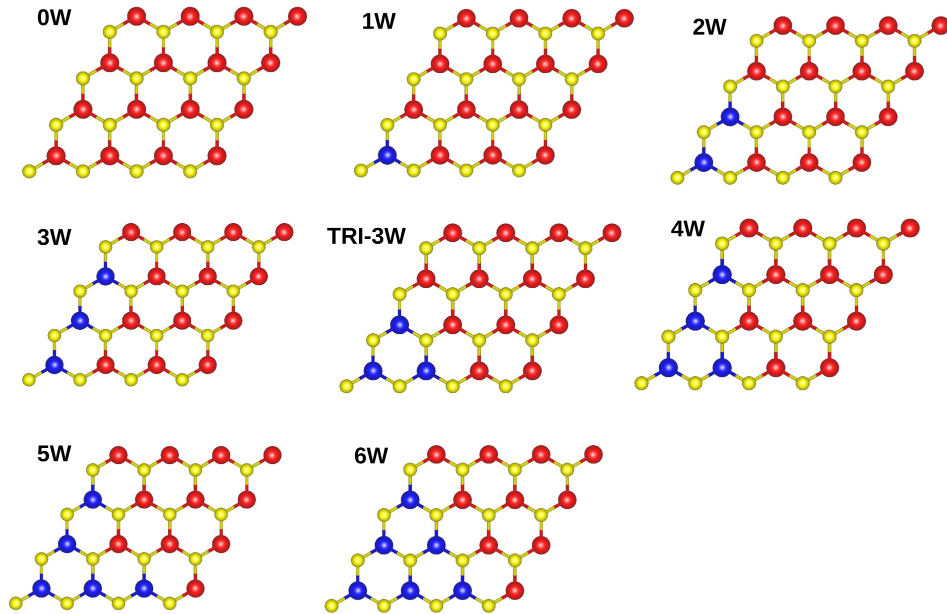

Figure 4.4: Atomic structures of $Mo_{1-x}W_xS_2$ monolayers involved clusters with m W atoms ($m = 1, ..., 6$) within 4×4×1 supercells. Red, blue and yellow colours represent molybdenum, tungsten and sulphur atoms, respectively.

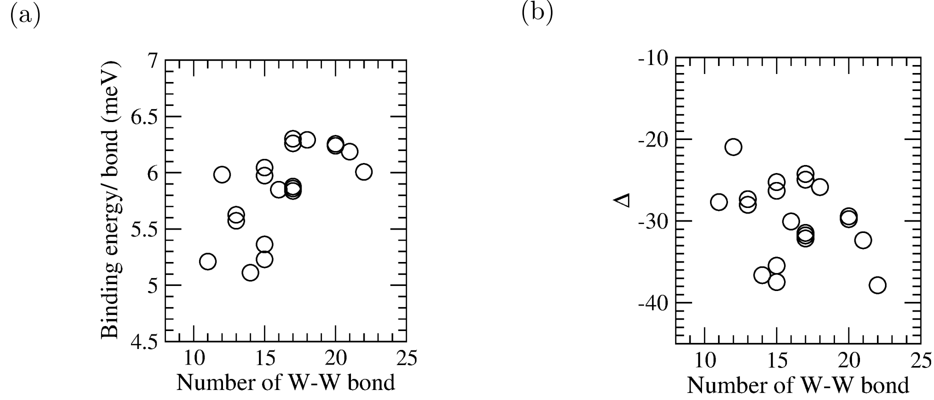

Figure 4.5: (a) Binding energy/bond (b) Δ versus the number of W-W bonds from twenty $Mo_{0.8}W_{0.2}S_2$ monolayers with different random configurations within 12×12×1 supercells. Δ = Binding energy-Predicted binding energy.

	Number of W-W bonds	Binding energy (meV)	Predicted binding energy (meV)	Δ (meV)
0W	0	0.00		
1W	0	0.00		
2W	1	7.57	7.57	0.00
3W	2	13.37	15.14	-1.78
TRI-3W	3	22.88	22.71	0.17
4W	4	26.60	30.28	-3.68
5W	5	29.41	37.85	-8.44
6W	9	58.17	68.13	-9.97

Table 4.1: Binding energies for the atomic configurations in figure 4.4. The binding energy (E_B) ≃ 7.57 meV, calculated based on eq. (4.5). The predicted binding energy is defined to estimate the binding energy of a cluster with m W atoms considering only the interaction between the first nearest-neighbour W-W pairs. It is calculated by the binding energy (7.57 meV) including only one W-W bond ($m = 2$) multiplying by the number of W-W bonds. Δ = Binding energy-Predicted binding energy.

4.3.2 Monte Carlo simulations

Figures 4.6 (a)-(d) show the atomic configurations of $Mo_{0.78}W_{0.22}S_2$ monolayers at T = 800 K (around the growth temperature of the alloy), calculated from Monte Carlo simulations based on different W-W pairwise interaction energy. A parameter is defined for easily comparing the atomic configurations with different interaction

energies:

$$\text{Ratio of W} - \text{W pairs} = \frac{\text{number of W} - \text{W pairs}}{x \times \text{number of } M - M \text{ pairs}}, \tag{4.6}$$

where M refers to the cations and x refers to the W composition. The atomic distribution calculated via Monte Carlo simulation is more clearly seen with a large interaction energy. Clusters are formed for a large negative interaction energy ($J =$ -50 meV) in figure 4.6(a), whereas W atoms spread over MoS_2 monolayer for a large positive interaction energy ($J = 50$ meV) in figure 4.6(d). The first nearest-neighbour W-W pair is higher and lower than other nth-nearest-neighbour W-W pairs ($n \neq 1$) in figure 4.7(c) and (f) for $J =$ -50 meV and 50 meV, respectively. This result is consistent with the implication of positive and negative binding energies defined in eq. (4.5). Figure 4.6(b) and (c) show the atomic configurations with $J = 0$ meV (no interaction between W-W pair) and 7.6 meV (the binding energy obtained from DFT calculations in section 4.3.1), respectively. The atomic distributions with $J = 0$ meV and $J = 7.6$ meV are very similar. The similarity can also be seen in figure 4.7(d) and (e).

The ratio of W-W pairs for nth-nearest-neighbour pairs ($n = 1, ..., 8$) are all close to the W composition x considered, suggesting a random distribution in the alloy. The annular dark-field scanning transmission electron miscroscopy (ADF-STEM) image in figure 4.7(a) is visually indistinguishable from figure 4.6(b) for $J =$ 0 meV and figure 4.6(c) for $J = 7.6$ meV. Furthermore, the first nearest-neighbour W-W pair is slightly lower than other nth-nearest-neighbour W-W pairs ($n \neq 1$) with $J = 7.6$ meV, corresponding to the feature of positive binding energy.

The variation of ratio with various nth-nearest-neighbour W-W pairs with $J = 7.6$ meV is similar to $J = 50$ meV: the first nearest-neighbour W-W pair depleted, second nearest-neighbour W-W pair enhanced and third nearest-neighbour W-W pair depleted, etc. In figure 4.7(b), the real atomic distribution based on the ADF-STEM images in figure 4.7(a) looks like figure 4.7(e): a slightly lower ratio for the first nearest-neighbour W-W pair compared to other nth-nearest-neighbour W-W pairs ($n \neq 1$). The predicted and observed statistical behaviour are comparable because all nth-nearest-neighbour W-W pairs from the Monte Carlo simulations are within the error bars of ADF-STEM images. The small positive interaction energy ($J = 7.6$ meV) also suggests $Mo_{1-x}W_xS_2$ monolayer can be regarded as a very-nearly-random distribution. It is worth noting that an almost identical ratio of W-W pairs are seen from $n = 4$ to $n = 8$ for all interaction energies considered in figure 4.7(c)-(f). This indicates that the long-ranged order is absent for all interaction strengths considered.

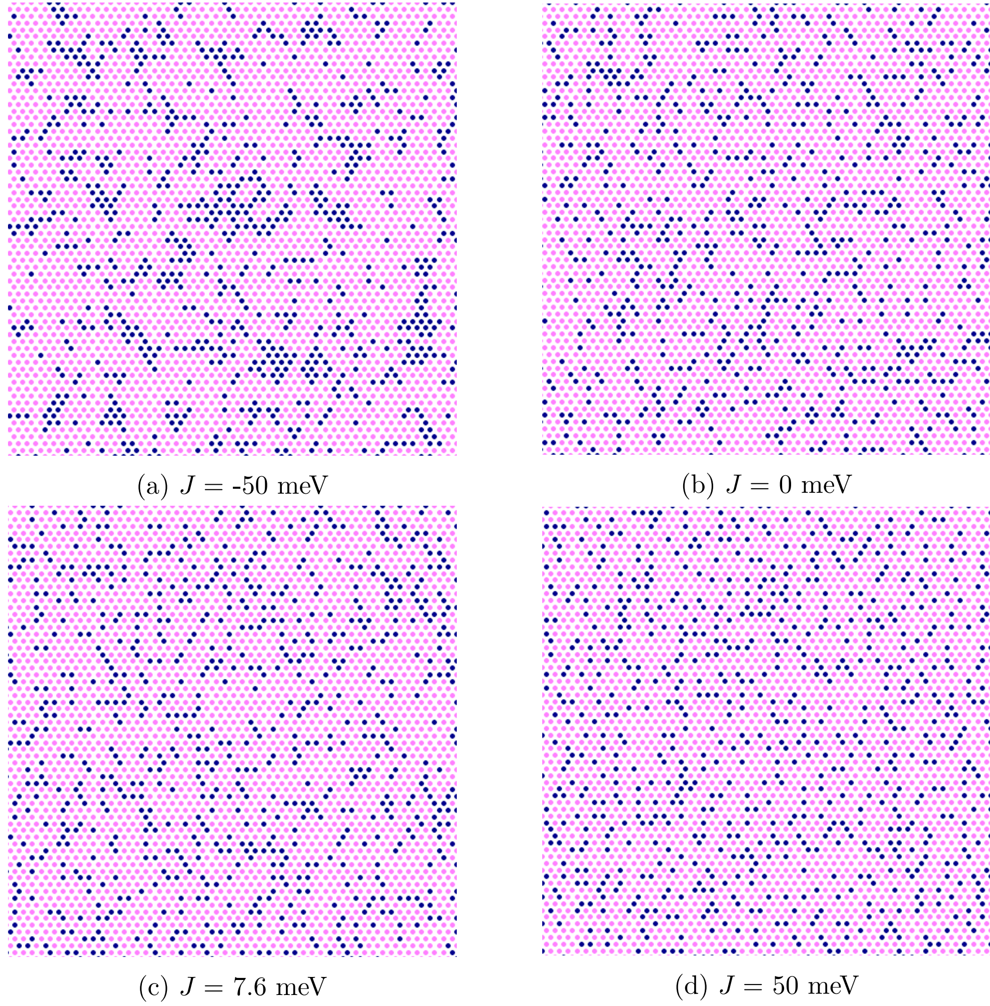

(a) J = -50 meV

(b) J = 0 meV

(c) J = 7.6 meV

(d) J = 50 meV

Figure 4.6: Monte Carlo simulations for $Mo_{0.78}W_{0.22}S_2$ monolayers with interaction energy (a) J = -50 meV (b) J = 0 meV (c) J = 7.6 meV (d) J = 50 meV at T = 800 K. Pink and blue dots refer to Mo and W atoms, respectively.

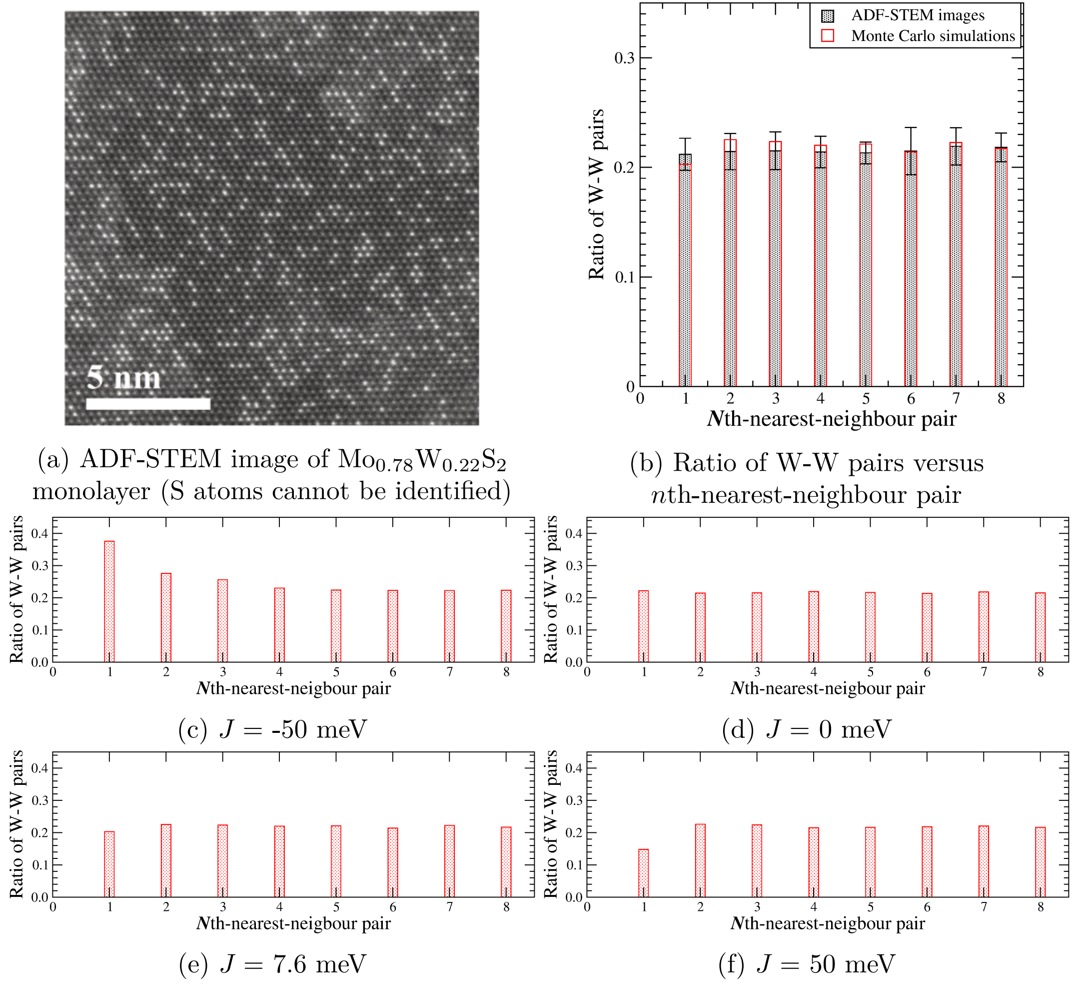

(a) ADF-STEM image of $Mo_{0.78}W_{0.22}S_2$ monolayer (S atoms cannot be identified)

(b) Ratio of W-W pairs versus nth-nearest-neighbour pair

(c) J = -50 meV

(d) J = 0 meV

(e) J = 7.6 meV

(f) J = 50 meV

Figure 4.7: (a) ADF-STEM image of $Mo_{0.78}W_{0.22}S_2$ monolayer (dark dots: Mo atoms, bright dots: W atoms). Experiments performed by X. Xia, N. C. Teutsch, A. J. Graham, V. Kandyba, A. Barinov, A. M. Sanchez and N. R. Wilson. Reproduced from [142]. (b) Ratio of W-W pairs versus nth-nearest-neighbour pair for ADF-STEM images of $Mo_{0.78}W_{0.22}S_2$ monolayer and the corresponding Monte Carlo simulations with J = 7.6 meV at T = 800 K. The error bars are based on the standard deviations calculated from ten regions within 40×40×1 supercells in the same ADF-STEM image. Ratio of W-W pairs versus nth-nearest-neighbour pair for $Mo_{0.78}W_{0.22}S_2$ monolayer with interaction energy (c) J = -50 meV (d) J = 0 meV (e) J = 7.6 meV (f) J = 50 meV at T = 800 K. Ratio of W-W pairs = number of W-W pairs/ ($x\times$ number of $M-M$ pairs), where M refers to Mo or W atom and x refers to the W composition. Nth-nearest-neighbour pair is labelled in figure 4.2.

Figure 4.8 shows similar atomic configurations and variation for the ratio of W-W pairs with J = -50 meV, 0 meV, 7.6 meV and 50 meV in $Mo_{0.37}W_{0.63}S_2$ monolayer. This implies that the arguments mentioned above can also be applied to other W compositions x. In a previous study [69], the distribution of W in $Mo_{1-x}W_xS_2$ monolayer has already been suggested to be random. In addition, clusters (or stripes seen in [144]) are suggested to be formed due to the small binding energy by technically adjusting the experimental parameters during the growth process. Furthermore, figure 4.9 shows the ratio of W-W pairs versus nth-nearest-neighbour pair for various temperatures with J = 7.6 meV in $Mo_{0.41}W_{0.59}S_2$ monolayer. The result at T = 0 K with clearly long-range order significantly deviates from other temperatures and decays very slowly indeed as the index of nearest neighbouring pair increases. The saturation can be seen when $T > 600$ K. The strong ordering in T = 0 K is eliminated by temperature, thus no long-ranged ordering can be seen in the as-grown $Mo_{1-x}W_xS_2$ with the growth temperature much higher than 50 K.

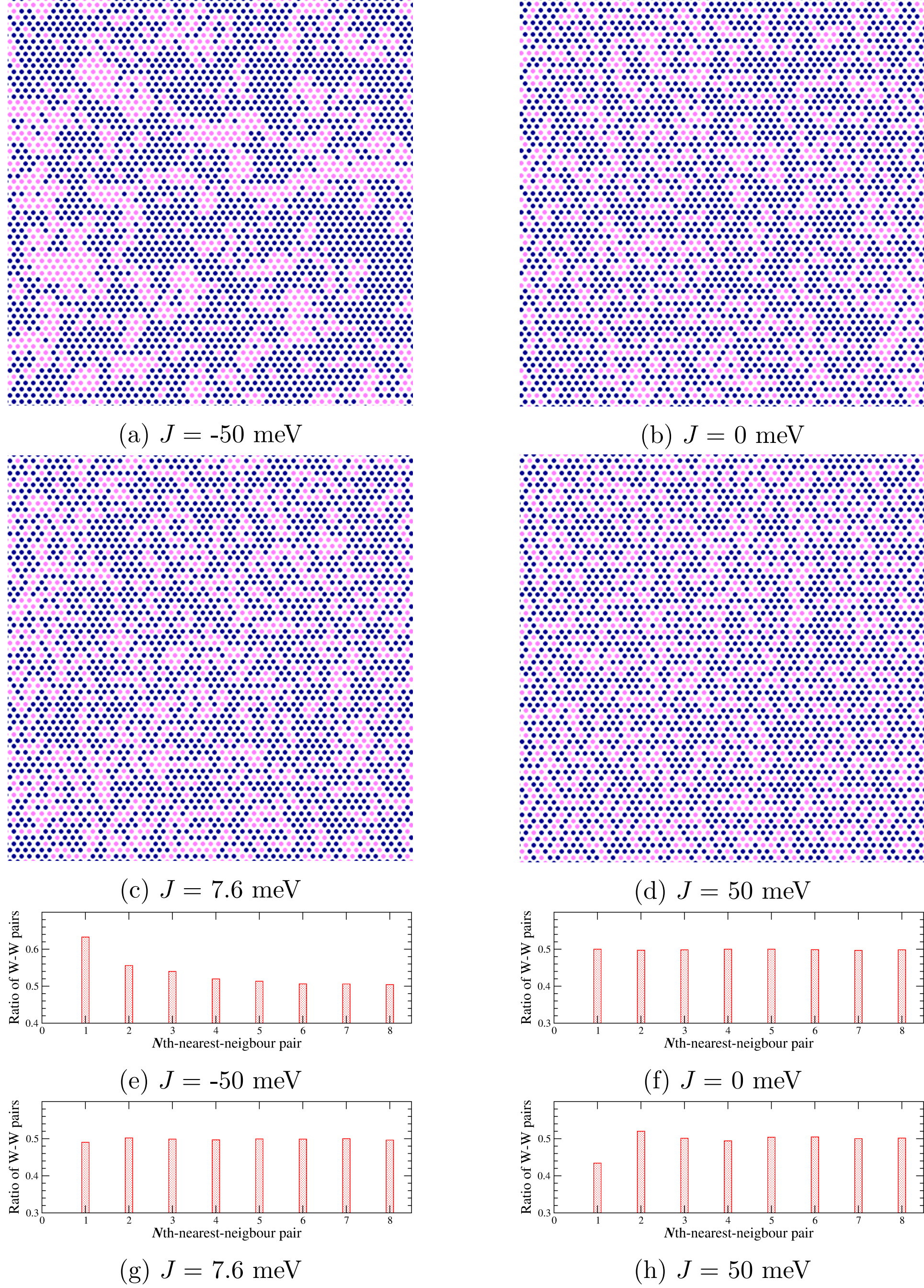

(a) J = -50 meV (b) J = 0 meV (c) J = 7.6 meV (d) J = 50 meV (e) J = -50 meV (f) J = 0 meV (g) J = 7.6 meV (h) J = 50 meV

Figure 4.8: Monte Carlo simulations for $Mo_{0.37}W_{0.63}S_2$ monolayer with interaction energy (a) J = -50 meV (b) J = 0 meV (c) J = 7.6 meV (d) J = 50 meV at T = 800 K. Pink and blue dots refer to Mo and W atoms, respectively. Ratio of W-W pairs versus nth-nearest-neighbour pair for $Mo_{0.37}W_{0.63}S_2$ monolayer with interaction energy (e) J = -50 meV (f) J = 0 meV (g) J = 7.6 meV (h) J = 50 meV at T = 800 K. Ratio of W-W pairs = number of W-W pairs/ ($x\times$ number of $M-M$ pairs), where M refers to Mo or W atom and x refers to the W composition. Nth-nearest-neighbour pair is labelled in figure 4.2.

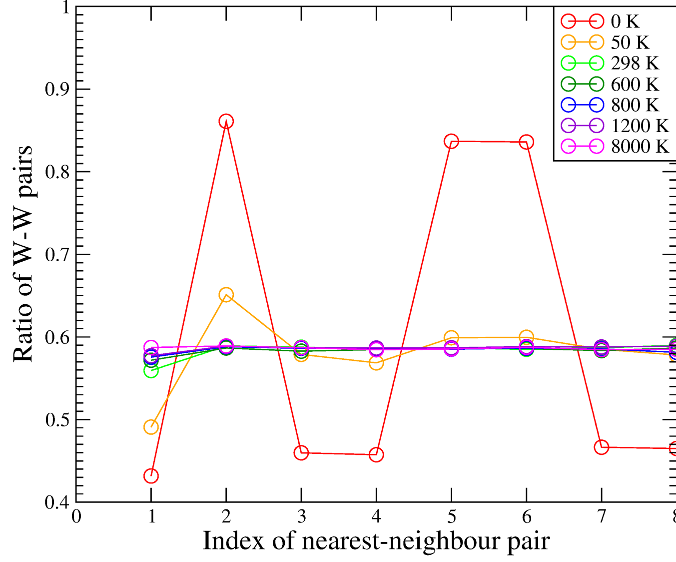

Figure 4.9: Ratio of W-W pairs versus nth-nearest-neighbour pair with $J = 7.6$ meV at $T = 0$ K to $T = 8000$ K for $Mo_{0.41}W_{0.59}S_2$ monolayer. Ratio of W-W pairs = number of W-W pairs/ ($x\times$ number of $M - M$ pairs), where M refers to Mo or W atom and x refers to the W composition. Nth-nearest-neighbour pair is labelled in figure 4.2.

4.3.3 Electronic properties of $Mo_{1-x}W_xS_2$ monolayer

Figure 4.10 shows the effective band structure of $Mo_{1-x}W_xS_2$ monolayers at $x =$ 0.250, 0.375, 0.500, 0.625, 0.750 and 0.875. SOC was included in all effective band structures at different W compositions x. The character of the band structure does not change significantly as W composition x increases. The band gap changes with W composition x due to the variation of valence band splitting around the Fermi level at **K**. The $E - k$ dispersion relation of $Mo_{1-x}W_xS_2$ monolayers at $x = 0.37$, 0.50 and 0.71 measured by ARPES are shown in figure 4.11. Direct comparison of the band structure can be made between figure 4.11 and 4.10(b), (c) and (e) when ignoring the energy offset.

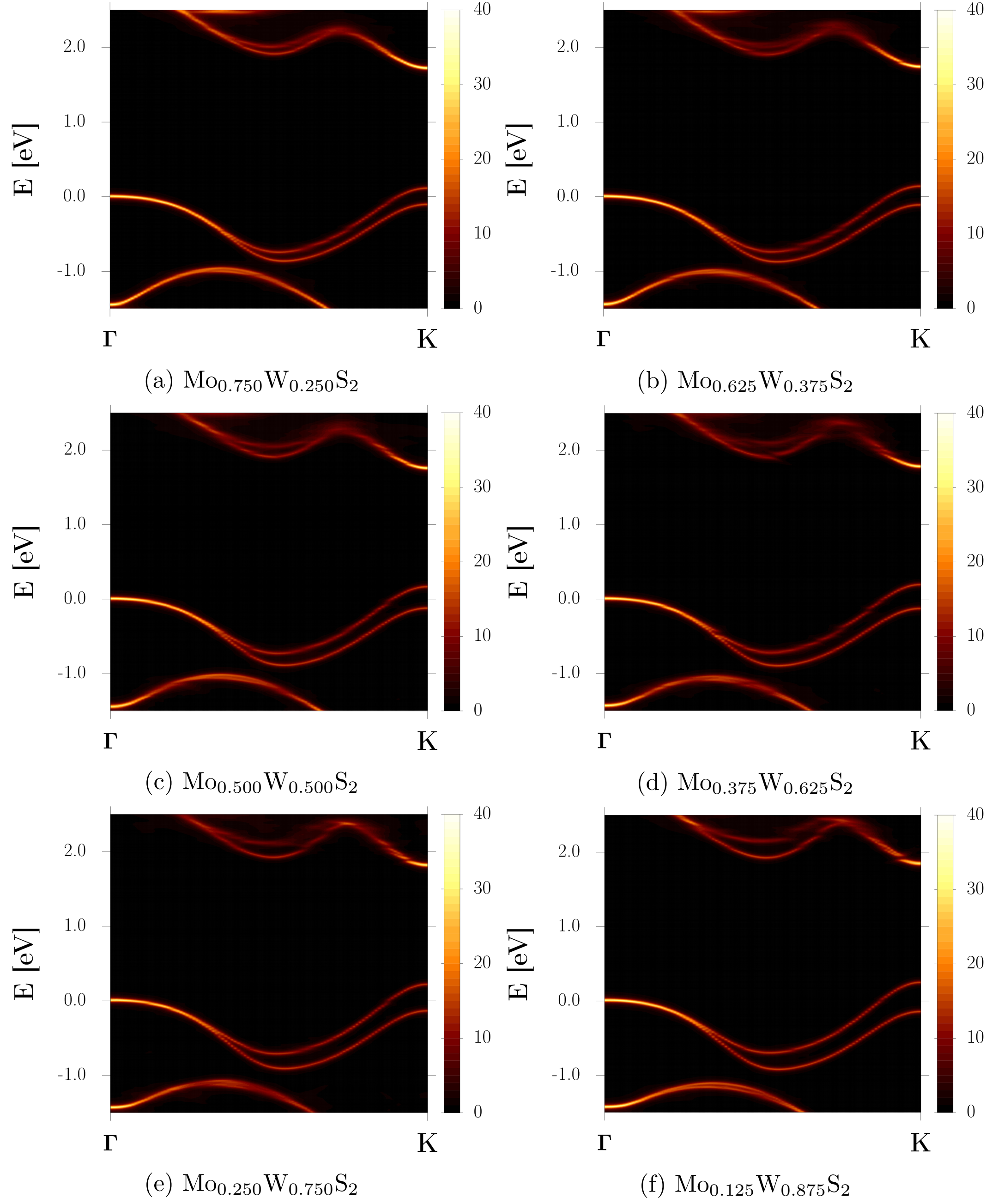

(a) $Mo_{0.750}W_{0.250}S_2$ (b) $Mo_{0.625}W_{0.375}S_2$

(c) $Mo_{0.500}W_{0.500}S_2$ (d) $Mo_{0.375}W_{0.625}S_2$

(e) $Mo_{0.250}W_{0.750}S_2$ (f) $Mo_{0.125}W_{0.875}S_2$

Figure 4.10: The effective band structure of (a) $Mo_{0.750}W_{0.250}S_2$ (b) $Mo_{0.625}W_{0.375}S_2$ (c) $Mo_{0.500}W_{0.500}S_2$ (d) $Mo_{0.375}W_{0.625}S_2$ (e) $Mo_{0.250}W_{0.750}S_2$ (f) $Mo_{0.125}W_{0.875}S_2$ monolayer. A Lorentzian broadening of 0.02 eV was employed in the effective band structures. Note that SOC was included in all effective band structures.

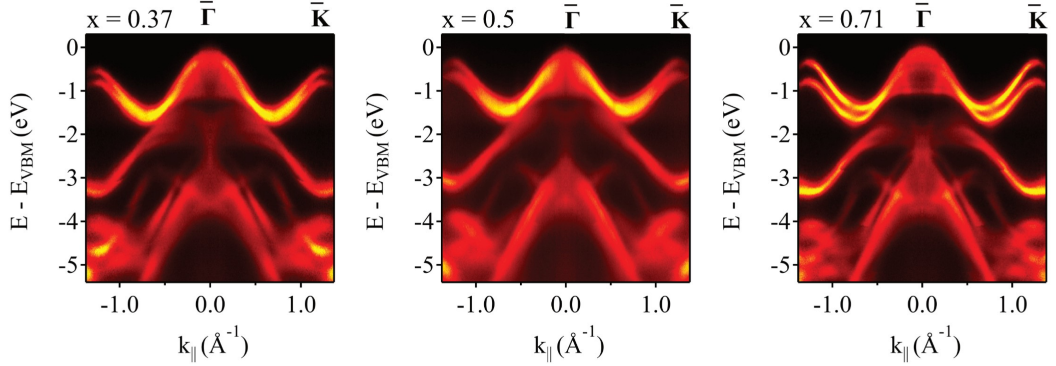

Figure 4.11: ARPES measurement along Γ to **K** for $Mo_{1-x}W_xS_2$ monolayers ($x =$ 0.37, 0.50, 0.71). Experiments performed by X. Xia, N. C. Teutsch, A. J. Graham, V. Kandyba, A. Barinov, A. M. Sanchez and N. R. Wilson. Reproduced from [142]

.

Definitions of the band parameters are shown schematically in figure 4.12. Band gap ($E_{\rm g}$) is the energy difference between the CBM and the VBM. A direct band gap can be seen for MoS_2, WS_2 and $Mo_{1-x}W_xS_2$ monolayers where the VBM and CBM are both located at **K**. The bandwidth of the VB ($D_{\rm vb}$) is the energy difference between the highest and lowest energy levels of the VB within the Brillouin zone. The Γ-**K** kpath where both the VBM and CBM occur is sufficient to calculate $D_{\rm vb}$. Figure 4.12(b) shows the band splitting caused by the SOC for MoS_2, $Mo_{1-x}W_xS_2$ and WS_2 monolayers and the corresponding spin states for each band at **K** valley. The magnitude of band splitting near the VBM and the CBM are denoted as $SOC_{\rm VBM}$ and $SOC_{\rm CBM}$, respectively. Bands in red and black colours shift up and down as W composition x increases from 0 (MoS_2) to 1 (WS_2). The ordering of energy level of the conduction bands in red and black colours at **K** are in reverse for MoS_2 and WS_2 monolayers, resulting in the overlap of conduction bands at intermediate W composition x.

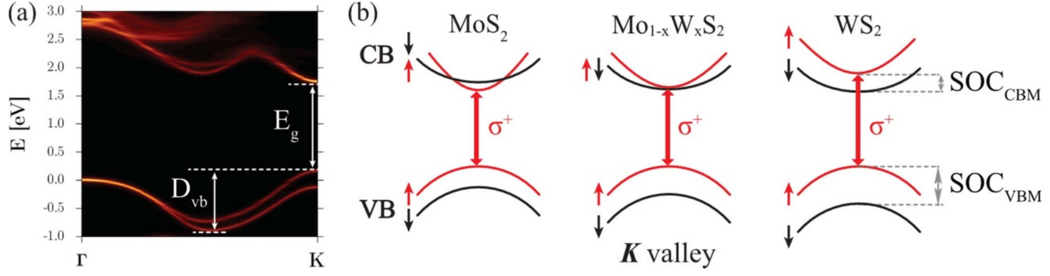

Figure 4.12: (a) Definition of the band gap (E_g) and the bandwidth of the VB (D_{vb}) are indicated in an effective band structure of $Mo_{1-x}W_xS_2$ monolayer with SOC included. (b) Valence and conduction band splittings around the Fermi level (SOC_{VBM} and SOC_{CBM}) at **K** for MoS_2, $Mo_{1-x}W_xS_2$ and WS_2 monolayers. Red and black colours refer to two different spin states. The ordering of energy level of the conduction bands in red and black colours in WS_2 monolayer around the Fermi level at **K** are opposite to MoS_2 monolayer, leading to the overlap of these two bands at intermediate W composition x.

Figure 4.13(a) shows the band gap obtained from the LS-DFT calculations (black data points), plane-wave DFT calculations with pseudopotential based on VCA (red data points) and the PL spectra (blue data points) as a function of W composition x. The PL emission is an electron transition between the VBM and the conduction band with the same spin state around the Fermi level at **K**. Therefore, it corresponds to the energy difference between the CBM or the band above CBM and VBM in figure 4.12(b) for MoS_2 or WS_2 monolayers, respectively. Band gap calculated by LS-DFT calculations and the PL emissions both possess bowing features, however, the variation of band gap with W composition x is completely different: the PL emission increases monotonically as W composition x increases, while the band gap calculated by LS-DFT decreases to around $x = 0.625$ and then increases as W composition x increases. This leads to different magnitudes of bowing parameters b: they are 0.12 ± 0.01 eV for LS-DFT calculations and 0.17 ± 0.01 eV for the PL emissions, neither being consistent with 0.28 ± 0.04 eV and 0.25 ± 0.04 eV for the theoretical and experimental bowing parameters in [42].

The band gaps are 1.63 eV and 1.85 eV for MoS_2, whereas the band gaps are 1.62 eV and 1.98 eV for WS_2 monolayers, obtained from LS-DFT calculations and the PL emissions, respectively. The band gap calculated by DFT with semilocal functionals give a smaller band gap than the quasiparticle band gap because $\frac{\partial E_{xc}}{\partial N}$ is not a continuous derivative [164, 165, 166, 167]. In addition, the PL emissions show the optical band gap relating to the excitonic effects [168, 169]. Defects and the intrinsic carriers in the as-grown crystals may also lead to unknown degree of band

gap renormalisation. The small difference of the band gap between MoS_2 (2.07 $\pm$ 0.05 eV) and WS_2 (2.03 $\pm$ 0.05 eV) monolayers from prior ARPES measurements [170] indicates a similar trend to LS-DFT calculations. Although the band gaps calculated with VCA at intermediate W compositions are close to LS-DFT calculations, the variation of the band gap with W composition x for VCA is linear (b = -0.02, no obvious bowing observed).

The experimental band parameters of the conduction band in figure 4.13(c)-(e) are not available because only the occupied states in valence bands can be probed in the ARPES measurements. Figure 4.13(b) shows the spin-orbit splitting of the VBM (SOC_{VBM}) versus W composition x. Both LS-DFT calculations (black data points) and the experimental results (blue data points) increase linearly as W composition x increases, but the SOC_{VBM} of LS-DFT calculations are smaller than the experiments. The valence band splittings around the Fermi level in MoS_2 and WS_2 monolayers calculated by LS-DFT calculations are approximately 145 meV and 426 meV, respectively (consistent with the results of [171] with LDA functional). The experimental SOC_{VBM} in WS_2 monolayer (458 $\pm$ 10 meV) is also consistent with a prior study [170]. The SOC_{VBM} calculated by VCA (red data points) calculation at $x = 0$ and $x = 1$ have similar values to LS-DFT, however, it does not increase linearly as W composition x increases.

The bandwidths (D_{vb}) calculated by LS-DFT (black data points) and the experimental results (blue data points) are very similar: the bandwidth increases linearly as the W composition x increases to around $x = 0.90$, followed by a slight decrease from around $x = 0.90$ to $x = 1.00$. There is a 0.1 eV systematic difference between LS-DFT calculations and the experiments. This deviation may be due to the slight difference of the lattice constant between theory and experiment (the experimental lattice constant of MoS_2 is 3.16 Å [172] and WS_2 is 3.15 Å [173]), since the magnitude of the bandwidth related to the interatomic distance. The largest difference between LS-DFT and VCA (red data points) is about 0.05 eV at $x = 0.00$ and they are very consistent in a range between $x = 0.40$ and $x = 0.60$.

The effective mass for holes (m_h) around $\mathbf{K}$ (figure 4.13(d)) has an opposite trend with respect to the SOC_{VBM} and the bandwidth of the VBM: it decreases monotonically as W composition x increases. This means that the curvature of the VBM around $\mathbf{K}$ increases as W composition x increases ($m_{\text{eff}} \propto [\frac{\partial^2 E}{\partial k^2}]^{-1}$). The largest difference of the effective mass for holes between LS-DFT (black data points) and VCA calculations (red data points) is about 0.05 m_0 (m_0: electron mass) at intermediate W composition x and decreases as x approaches 0 and 1. The error bars are large and no obvious trend is seen for the experimental effective mass for

holes (blue data points) due to the difficulty in extracting data from the ARPES spectra. Therefore, the effective masses for holes based on LS-DFT calculations and the experiments at various W compositions x cannot be compared. The effective masses for holes based on LS-DFT calculations are consistent with a previous study with LDA pseudopotential [171]. It is a 0.05 m_0 of systematic deviation between this work and [171].

It is worth mentioning that the green data points in figure 4.13(a)-(e) represent the results of LS-DFT calculations based on the atomic configuration from a ADF-STEM image within a 8×8×1 supercell. They are all consistent with the results of LS-DFT based on random distribution for different band parameters. This further confirms the random alloying in $Mo_{1-x}W_xS_2$ monolayers. The results of VCA calculations within primitive cells are less consistent with experiment than LS-DFT calculations within large supercells. It is reasonable to assume this is because the pseudopotential generated based on VCA is a stoichiometric mixture of two pseudopotentials, which implies that local atomic interaction is not considered.

Figure 4.13(e) displays the conduction band splitting around the Fermi level (SOC_{CBM}) as a function of W composition x. No experimental results can be shown due to the limitation of ARPES measurement to probe the unoccupied states. Bowing features can be observed for both LS-DFT and VCA calculations. Unlike the full SOC treatment in VCA calculation, SOC is a perturbation in the LS-DFT calculation. This leads to small differences of SOC_{CBM} between LS-DFT and VCA calculations at $x = 0$ and $x = 1$. The magnitude of the SOC_{CBM} is very small compared to the SOC_{VBM}. SOC_{CBM} are 48 and 15 times smaller than the SOC_{VBM} at $x = 0$ (MoS_2) and $x = 1$ (WS_2), respectively. The overlap of the conduction bands around the Fermi level at **K** at intermediate W composition x in figure 4.12(b) corresponds to zero SOC_{CBM}. This happens around $x \simeq 0.250$ and $x \simeq 0.063$ for LS-DFT and VCA calculations, respectively. The difference of the SOC_{CBM} between LS-DFT and VCA calculations is more apparent than the SOC_{VBM} due to the small magnitude of SOC_{CBM}.

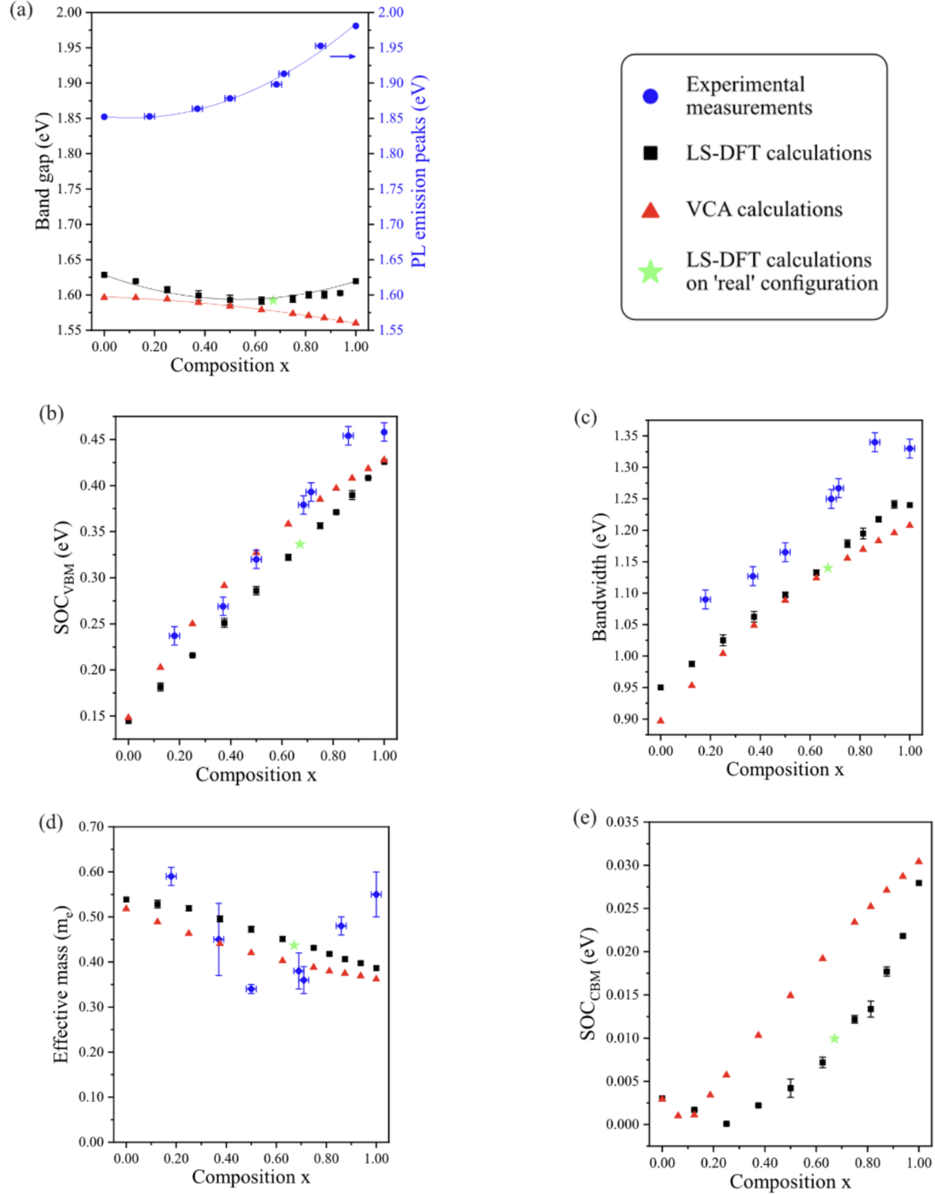

Figure 4.13: (a) Band gap and PL emission peak energy (b) Valence band splitting around the Fermi level (SOC_{VBM}) at **K** (c) Bandwidth of the VBM (D_{vb}) (d) Effective mass for holes (m_h) around **K** (e) Conduction band splitting around the Fermi level (SOC_{CBM}) at **K** as a function of W composition x. Black, red and blue data points refer to the results of LS-DFT calculations, VCA calculations and experiments. Green data points are the results of LS-DFT calculations based on the atomic configuration derived from an ADF-STEM image within a 8×8×1 supercell.

The change of the CBM position in $Mo_{1-x}W_xS_2$ monolayers with different random configurations within the length scale of exciton radius can be used to roughly estimate the disorder potential. $Mo_{1-x}W_xS_2$ monolayers with three different random configurations for various W compositions x were considered in LS-DFT calculations. The conduction band splitting around the Fermi level at **K** is smaller than the disorder potential around $0.125 < x < 0.428$ (figure 4.14). A previous study [145] showed that the band parameters related to the CBM are not only susceptible to W composition x but also ordering of the atomic configuration. It is therefore unclear whether spin-valley locking is retained in $Mo_{1-x}W_xS_2$ monolayer from LS-DFT calculations.

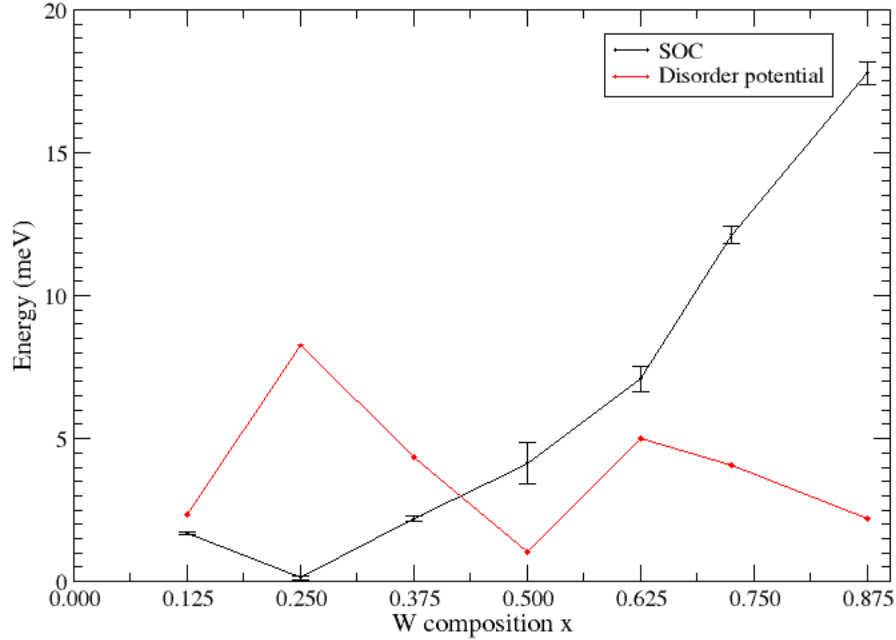

Figure 4.14: Energy versus W composition x for conduction band splitting around the Fermi level at **K** and disorder potential.

For studying the spin-valley locking in $Mo_{1-x}W_xS_2$ monolayer, optical microscopy measurements of the hBN-encapsulated $Mo_{0.5}W_{0.5}S_2$ monolayer flake are shown in figure 4.15(a). Figure 4.15(b) shows the fractional intensity as a function of energy. A right-handed (σ^+) and left-handed (σ^-) circularly polarised light emission are mainly generated through the excitation of the same polarised light. Fractional intensity for each polarisation was obtained through its intensity divided by the sum of the intensities for each polarisation at 1.92 eV. The sharp peaks within an energy range of 1.92 eV and 1.975 eV originated from Raman scattering. The spin-valley locking is suggested to be maintained because the valley polarisation $\eta > 0.4$ (obvious circular polarisation) ($\eta = \frac{\mathrm{PL}(\sigma^+)-\mathrm{PL}(\sigma^-)}{\mathrm{PL}(\sigma^+)+\mathrm{PL}(\sigma^-)}$, where $\mathrm{PL}(\sigma^+)$ and $\mathrm{PL}(\sigma^-)$ refer to the intensity of the right-handed and left-handed circularly polarised light emission, respectively) in figure 4.15(c) for most of the polarised lights within an energy range between 1.87 eV and 1.97 eV. In figure 4.15(d), the differential reflectivity shows a peak at 1.954 ± 0.001 eV (corresponding to the free A1s exciton). This energy is within the energy range of free A1s exciton from reflectivity for encapsulated MoS_2 ($\simeq$ 1.94 eV [174]) and WS_2 ($\simeq$ 2.09 eV [175]) monolayers. Spin-valley locking is shown to be maintained in $Mo_{1-x}W_xS_2$ monolayer by both PL and reflectivity measurements. This phenomenon satisfies the optical selection rules and consistent with previous studies for transition metal dichalcogenide monolayers [176, 177, 178, 179].

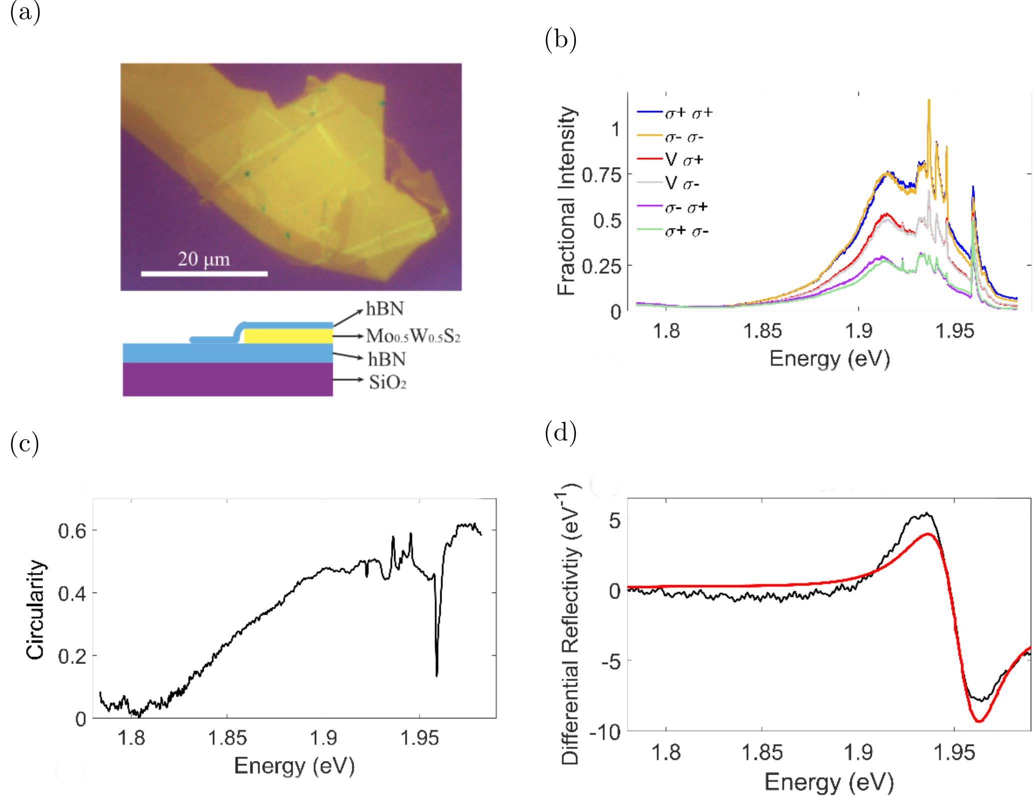

Figure 4.15: (a) Optical microscopy image (top) and schematic cross section (bottom) of the hBN-encapsulated $Mo_{0.5}W_{0.5}S_2$ monolayer flake. (b) Fractional intensity of polarisation-resolved PL spectra versus energy for the heterostructure in (a) at $T = 4$ K. σ^+ and σ^- refer to the right-handed and left-handed circularly polarised light, respectively. V refers to a vertical and linear polarised light with a spin state of $(\sigma^+ + \sigma^-)/\sqrt{2}$. Fractional intensity for each incident polarisation was obtained through its intensity divided by the sum of the intensities for each incident polarisation at 1.92 eV. The sharp peaks within an energy range between 1.92 eV and 1.975 eV originated from Raman scattering. (c) Circularity of the PL versus energy. The circularity is defined as $\frac{\sigma^+\sigma^+ - \sigma^+\sigma-}{\sigma^+\sigma^+ + \sigma^+\sigma-}$ under σ^+ excitation. (d) Differential reflectivity versus energy for the heterostructure in (a) at $T = 4$ K. The fitting (red curve) is based on a T-matrix model with layer thickness included. A Lorentzian oscillator is used to model the A1s exciton, where its centre energy was fitted to 1.954 ± 0.001 eV and the width is 41 ± 1 meV. Experiments performed by J. Viner and D. C. Smith. Reproduced from [142].

4.4 Conclusions

$Mo_{1-x}W_xS_2$ monolayers are suggested to exhibit essentially random alloying for various W composition x through the comparison between Monte Carlo simulations with W-W pairwise interaction energy obtained via plane-wave DFT calculations and STEM image. The results of LS-DFT calculations are more consistent with the experiments when comparing with VCA calculations because the local atomic interactions among Mo and W atoms are eliminated in VCA calculations. Therefore, there are significant differences between LS-DFT calculations and VCA calculations for properties which are affected by local interactions. Although bowing features can be seen for the band gap in both LS-DFT calculations and the experiments, their results cannot be compared due to the underestimation of the band gap obtained from DFT calculations with semilocal potential, not including excitonic effect and intrinsic carriers in the DFT calculations. Thus, the bowing parameters of the band gap are different for LS-DFT calculations and the experiments. The valence band splitting around the Fermi level at **K** and the bandwidth of the VBM increase linearly, whereas the effective mass for holes decreases linearly as W composition x increases for both LS-DFT calculations and the experiments. The valence band splitting and the bandwidth of the VBM obtained from LS-DFT calculations are systematically 50 meV and 100 meV smaller than the experimental results, respectively. The conduction band splitting around the Fermi level at **K** is smaller than the disorder potential at $0.125 < x < 0.428$ obtained from LS-DFT calculations. Spin-valley locking was observed in the hBN encapsulated $Mo_{0.5}W_{0.5}S_2$ monolayer through the polarisation-resolved PL and reflectivity measurements. These findings prove that alloying is a promising means by which to tune the electronic properties of transition metal dichalcogenides, thus widening their applications in future semiconductor devices, optoelectronics, valleytronics and spintronics.

Chapter 5

Two-dimensional transition metal dichalcogenide alloy-$W_{1-x}Nb_xS_2$ monolayer

This chapter mainly relates to the theoretical and computational simulations of $W_{1-x}Nb_xS_2$ monolayers. Only the ADF-STEM image shown in figure 5.1(a) was provided by our experimental collaborators led by Dr. Neil R. Wilson, from the University of Warwick. This work has been published in the Physical Review B in 2021 [180]: S. M. Loh, X. Xia, N. R. Wilson and N. D. M. Hine. Strong in-plane anisotropy in the electronic properties of doped transition metal dichalcogenides exhibited in $W_{1-x}Nb_xS_2$. *Phys. Rev. B*, 103:245410, 2021. URL:https://doi.org/10.1103/PhysRevB.103.245410. Copyright © 2021 American Physical Society.

5.1 Introduction

In chapter 4, the atomic and electronic structures of alloy composed of 2H-MoS_2 and 2H-WS_2 monolayers has been discussed. A similar topic is discussed in this chapter: the alloy composed of 2H-NbS_2 and 2H-WS_2 was studied. The alloy is expected to be quite different from the $Mo_{1-x}W_xS_2$ monolayer in chapter 4 because NbS_2 is a metal, whereas WS_2 is a semiconductor.

NbS_2 is a material belonging to group VB TMDCs which possesses superconductivity but no charge density wave (CDW) order because of anharmonic effects [181]. It has significant spin fluctuations and magnetic susceptibility [182]. The spin density wave (SDW) can be realised by adopting approaches such as doping, defects,

impurities or ribbon edges [182]. In addition, NbS_2 monolayer provides good p-type Ohmic contacts with two-dimensional materials such as WSe_2 and BP due to its large work function, which compensates the reduction of work function owing to the asymmetric interface dipole. The VBM is then fixed above the Fermi level leading to a good Ohmic contact even in a very large electric field [183].

CVD growth of $W_{1-x}Nb_xS_2$ monolayer has been proposed in [184, 185]. From the work of Feng et al. [186], the doping of Nb atoms in WS_2 leads to the shift of the Fermi level towards the valence bands. Thus, the band gap decreases from 1.82 eV to 1.64 eV as x increases from 0.03 to 0.15. From the projected density of states (PDOS), the valence bands near the Fermi level are dominated by the d orbitals of Nb atoms instead of W atoms, whereas the conduction bands are still dominated by the d orbitals of W atoms (similar to WS_2 monolayer) at $x = 0.15$ [186]. The electrode based on this alloy has a higher performance than WS_2-based electrodes since the Schottky barriers are reduced owing to the hybridisation among $5d$ orbitals of W atom, $4d$ orbitals of Nb atom and $3p$ orbitals of S atom near the Fermi level [186]. The effective hole mobility and the I_{on}/I_{off} are high and up to about 146 $cm^2V^{-1}s^{-1}$ and 10^7, respectively [186]. In a range of x between 0 and 0.25, 15% doping of Nb atoms gives the highest electrical conductivity [186]. The ambipolarity can also be eliminated in the $W_{1-x}Nb_xS_2$ monolayer-based FET [186].

Jin et al. [184] showed that the substitution of Nb atom at the position of W atom is the most stable when compared with other types of doping such as the substitution of Nb atom at the position of S atom and the absorption of Nb adatom above the positions of W or S atoms. Atomic configuration with Nb clustering in WS_2 monolayer has the lowest formation energy, compared to the isolated Nb or Nb in a row [184]. Furthermore, kinetic processes can significantly affect the dopant distribution. Azizi et al. [144] displayed a dopant distribution with stripe pattern in $Mo_{1-x}W_xS_2$ monolayer, different from the random alloying in chapter 4. The fluctuations of the chemical potential of Mo, W and S atoms at each atomic site determine jointly this atomic configuration. In fact, it was suggested from previous literature [187, 188, 189] that the growth of TMDC flakes is influenced by the competition among several non-equilibrium dynamic processes, for example, the adsorption and desorption of the constituent atoms of the TMDC, several different diffusions including flake edge, vacancy defects (metals and chalcogens) and surface diffusions. There are extrinsic and intrinsic parameters that influence the growth of the TMDC flake. The extrinsic parameters such as temperature, adsorption rate of adatom, chalcogen to metal (C/M) ratio of the precursors, can be controlled in the experiment. The intrinsic parameters cannot be altered as the synthesised materials

and substrate are determined initially.

In this work, $W_{1-x}Nb_xS_2$ monolayers were synthesised via CVT [142, 190] method, performed by our experimental collaborators led by Dr. Neil R. Wilson from the University of Warwick and analysed via *ab initio* calculations. An anisotropic atomic configuration in the as-grown sample was seen in the ADF-STEM image. This can be explained partly from the perspective of energetics. Kinetic processes need to be taken into account in forming this symmetry-breaking dopant distribution. The effective band structures and electrical conductivity of several designed atomic configurations were compared with the real atomic configuration in ADF-STEM image. It is found that the electrical conductivity is also strongly anisotropic for this dopant distribution. The conductivity can be improved by forming stripes with longer length, increasing the spacing between line segments and increasing the Nb composition.

5.2 Computational methods

CASTEP [60] was used as the simulation package in calculations to find the lattice constant of NbS_2 monolayer, the binding energies for various dopant distributions and the geometry optimisations of the atomic structures. On-the-fly generated ultrasoft pseudopotentials [103] with the GGA-PBE [94] was adopted along with a cut-off energy of 500 eV. A lattice constant of 3.345 Å was obtained for NbS_2 monolayer within a primitive cell with a kpoint grid of 21×21×1. The lattice constant of NbS_2 monolayer is consistent with the theoretical lattice constant (3.332 Å) in [191] and the experimental lattice constant (3.310 Å) in [192]. Several different sizes of supercells with the kpoint spacings not exceeding 0.11 $Å^{-1}$ were used in this work. The spurious interaction between two isolated cells is eliminated by setting the vacuum spacing to 20 Å. The convergence criteria were 1×10^{-5} eV/atom for total energy in an electronic minimisation task and 2×10^{-5} eV/atom for the free energy in a geometry optimisation task.

ONETEP [59, 63] was used for the effective band structure calculations. A cut-off energy of 1600 eV and a NGWF radius of 13 a_0 were set. GGA-PBE pseudopotentials with PAW datasets [104, 105, 130] from the GBRV library [193] were used. The spurious interaction between two isolated cells is eliminated by setting the vacuum spacing to 20 Å. The effective band structures within the Brillouin zone of primitive cell were projected from a 12×12×1 supercell by using spectral function unfolding method implemented in ONETEP (section 3.2). SOC was included as a perturbation in ONETEP in all effective band structure calculations. A Lorentzian

broadening of 0.02 eV was employed in the effective band structure.

The electrical conductivity of $W_{1-x}Nb_xS_2$ monolayer was further investigated through a post-processing package, BoltzTrap [68], with the initial input of atomic and electronic structures calculated from CASTEP. The j-dependent pseudopotentials obtained from CCPForge based on [156] were used in the calculations in CASTEP for including SOC. Semiclassical transport coefficients are generated by the smooth Fourier interpolation of the bands calculated from CASTEP. The conductivity tensor is written as [68]

$$\sigma_{\alpha\beta}(i,\mathbf{k}) = e^2\tau_{i,\mathbf{k}}v_\alpha(i,\mathbf{k})v_\beta(i,\mathbf{k}), \tag{5.1}$$

where e is the electron charge, τ is the relaxation time and $v_\beta(i,\mathbf{k})$ is the group velocity

$$v_\beta(i,\mathbf{k}) = \frac{1}{\hbar}\frac{\partial\varepsilon_{i,\mathbf{k}}}{\partial k_\beta}. \tag{5.2}$$

FFTs are useful in efficiently calculating the group velocity in eq. (5.2). If the conductivity is written in terms of density of states by applying a delta function, eq. (5.1) can be rewritten as

$$\sigma_{\alpha\beta}(\varepsilon) = \frac{1}{N}\sum_{i,\mathbf{k}}\sigma_{\alpha\beta}(i,\mathbf{k})\delta(\varepsilon-\varepsilon_{i,\mathbf{k}}), \tag{5.3}$$

where N represents the number of kpoints. In terms of the Fermi-Dirac distribution f, the conductivity tensor is

$$\sigma_{\alpha\beta}(T;\mu) = \frac{1}{\Omega}\int\sigma_{\alpha\beta}(\varepsilon)\left[-\frac{\partial f_\mu(T;\varepsilon)}{\partial\varepsilon}\right]d\varepsilon. \tag{5.4}$$

where Ω is the cell volume and μ is the chemical potential. In 2D systems, the calculated conductivity through BoltzTrap needs to be multiplied by the magnitude of the simulation cell along the z direction. This is because the calculated conductivity through BoltzTrap is divided by the volume of the simulation cell (eq. (5.4)) which includes sufficiently large vacuum spacing in the z direction for 2D systems. An energy grid (dϵ) of 0.0068 eV (0.0005 Ry) for the integration was set. The ratio of number of lattice points to kpoints is 5. A spectral kpoint sampling mesh of 6×6×1 within 8×8×1 supercells was used in CASTEP. A scheme of histogram sampling was used for obtaining the density of states (DOS). Note that a constant relaxation time τ was assumed in all calculations in this code.

All the atomic structures and the isosurfaces of charge densities were generated and exhibited via the atomic simulation environment (ASE) [159], NumPy

[160] and the visualisation for electronic and structural analysis (VESTA) [161].

5.3 Results and discussions

Figure 5.1(a) shows an ADF-STEM image of $W_{0.9}Nb_{0.1}S_2$ monolayer. Some stripes (lines), clusters and isolated Nb atoms are seen in the image (similar to $Re_{0.5}Nb_{0.5}S_2$ monolayer [194]). This kind of anisotropic dopant distribution is not commonly seen in the TMDC alloys. The spacing includes about 4-5 W atoms between two stripes. Clear schematic top and side views from a region of figure 5.1(a) are shown in figure 5.1(b) and (c), where the lines are parallel to the lattice vector **b**. The first Brillouin zone of the atomic structure is also shown in figure 5.1(d), where some specified kpoints and the directions parallel and perpendicular to the line are indicated. This anisotropic dopant distribution raises the question of which kind of dopant distribution is the most energetically favourable in $W_{1-x}Nb_xS_2$ monolayer.

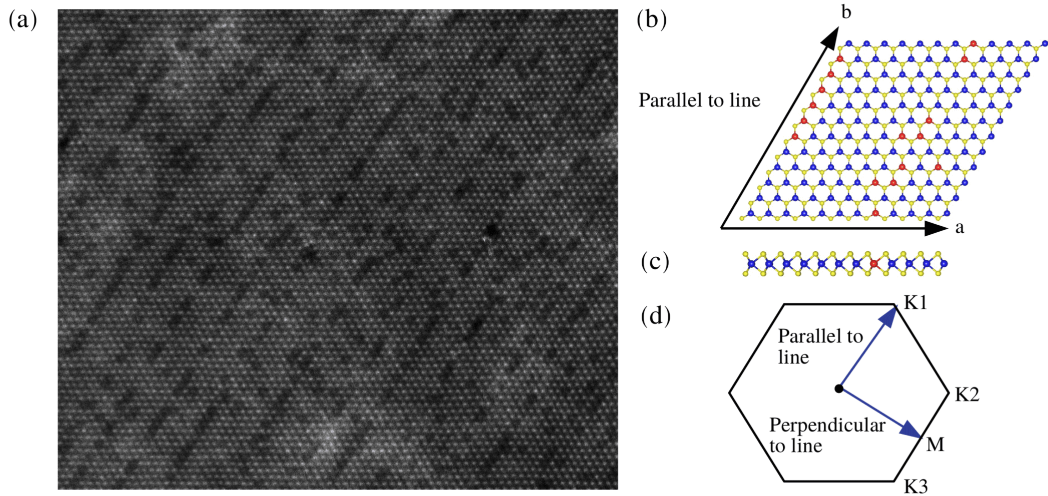

Figure 5.1: (a) ADF-STEM image of $W_{0.9}Nb_{0.1}S_2$ monolayer, where bright and dark colours refer to W and Nb atoms, repectively. Experiments performed by X. Xia and N. R. Wilson. Reproduced from [180]. (b) Top view (c) side view of a region in (a). Red, blue and yellow colours refer to Nb, W and S atoms, respectively. (d) First Brillouin zone of the atomic structure within a hexagonal lattice in (b). Some specified kpoints: three equivalent **K** and one **M**, are indicated. The directions of parallel and perpendicular to the line in (a) are also indicated for later discussions.

5.3.1 Binding energy of $W_{1-x}Nb_xS_2$ monolayer

Similar to eq. (4.5) in chapter 4, the binding energy for forming atomic configuration with m Nb atoms on neighbouring sites is written as

$$E_B = E_T^{m\text{Nb}} - mE_T^{1\text{Nb}} + (m-1)E_T^{\text{WS}_2}, \tag{5.5}$$

where $E_T^{m\text{Nb}}$ refers to the total energy of atomic configuration with m Nb atoms at adjacent sites and $mE_T^{1\text{Nb}}$ refers to the total energy of atomic configuration with m isolated Nb atoms. Similar to the atomic configurations shown in figure 4.4, the binding energies for various dopant distributions are discussed in table 5.1. A binding energy of about -125.8 meV was obtained, this means that Nb atoms prefer to form clusters in WS_2 monolayer. However, it is still unknown what kind of cluster is inclined to be formed. It is worth noting that a binding energy of about 20.76 meV was obtained for NbS_2 monolayer doped with W atoms. This positive binding energy suggests W atoms do not tend to form clusters, similar to MoS_2 monolayer doped with W atoms ($\simeq$ 7.6 meV) and WS_2 doped with Mo atoms ($\simeq$ 7.0 meV). The absolute value of the difference between the calculated and predicted binding energies (Δ) for different sizes of dopant clusters increases to $\simeq$ 270 meV as the number of Nb-Nb bonds increases to 9. The absolute value of Δ are also significantly larger than $Mo_{1-x}W_xS_2$ monolayer with the same dopant distributions when the number of Nb-Nb bonds larger than 2 in table 4.1. Interestingly, if sulphur is replaced by selenium, the binding energies are about -53.56 meV and 35.82 meV for WSe_2 monolayer doped with Nb atoms and $NbSe_2$ monolayer doped with W atoms, respectively. The sign of binding energies for $W_{1-x}Nb_xS_2$ and $W_{1-x}Nb_xSe_2$ monolayers are the same, but it is lower in sulphur cases. For example, binding energies in the WS_2 monolayer doped with Nb atoms are more than 2× lower than WSe_2 monolayer doped with Nb atoms.

Various dopant distributions are compared to investigate the most stable atomic configuration from the point of view of energetics. In figure 5.2(a) and (b) with $m = 3$, the dopant distribution with a triangular cluster has lower binding energy than the line. For $m = 4$ in figure 5.2(c)-(f), the "L" cluster has the lowest binding energy among the "line", "parallelogram" and "isolated" patterns. The ordering of binding energy is "L" < "parallelogram" < "line" < "isolated" (same as reference [184]). The "isolated" pattern with the highest binding energy seems to be the energetically least favourable pattern, consistent with the implication of negative binding energy mentioned above. Two types of "L" with different lengths along lattice vector **b** (figure 5.1) are compared in figure 5.2(g)-(h). It is seen that

	Number of Nb-Nb bonds	Binding energy (meV)	Predicted binding energy (meV)	Δ (meV)
0Nb	0	0.00		
1Nb	0	0.00		
2Nb	1	-125.79	-125.79	0.00
3Nb	2	-253.79	-251.59	-2.20
TRI-3Nb	3	-373.69	-377.38	3.69
4Nb	4	-480.02	-503.18	23.16
5Nb	5	-594.95	-628.97	34.02
6Nb	9	-862.03	-1132.15	270.12

Table 5.1: Binding energies for the atomic configurations in figure 4.4. A binding energy of -125.79 meV/bond is obtained based on eq. (5.5). The predicted binding energy is defined to estimate the binding energy of a cluster with m Nb atoms considering only the interaction between the first nearest-neighbour Nb-Nb pairs. It is calculated by the binding energy (-125.79 meV) including only one Nb-Nb bond ($m = 2$) multiplying by the number of Nb-Nb bonds. $\Delta =$ Binding energy-Predicted binding energy.

the “L” with longer length (figure 5.2(g)) is more inclined to be formed in the $W_{1-x}Nb_2S_2$ monolayer. The conclusions obtained here can be extended to larger supercells. In figure 5.3, the ordering of binding energy with different combinations of prototypes is the same as figure 5.2: “L-L” < “L-parallelogram” < “parallelogram-parallelogram” < “L-line” < “parallelogram-line” < “line-line” < “line-isolated”.

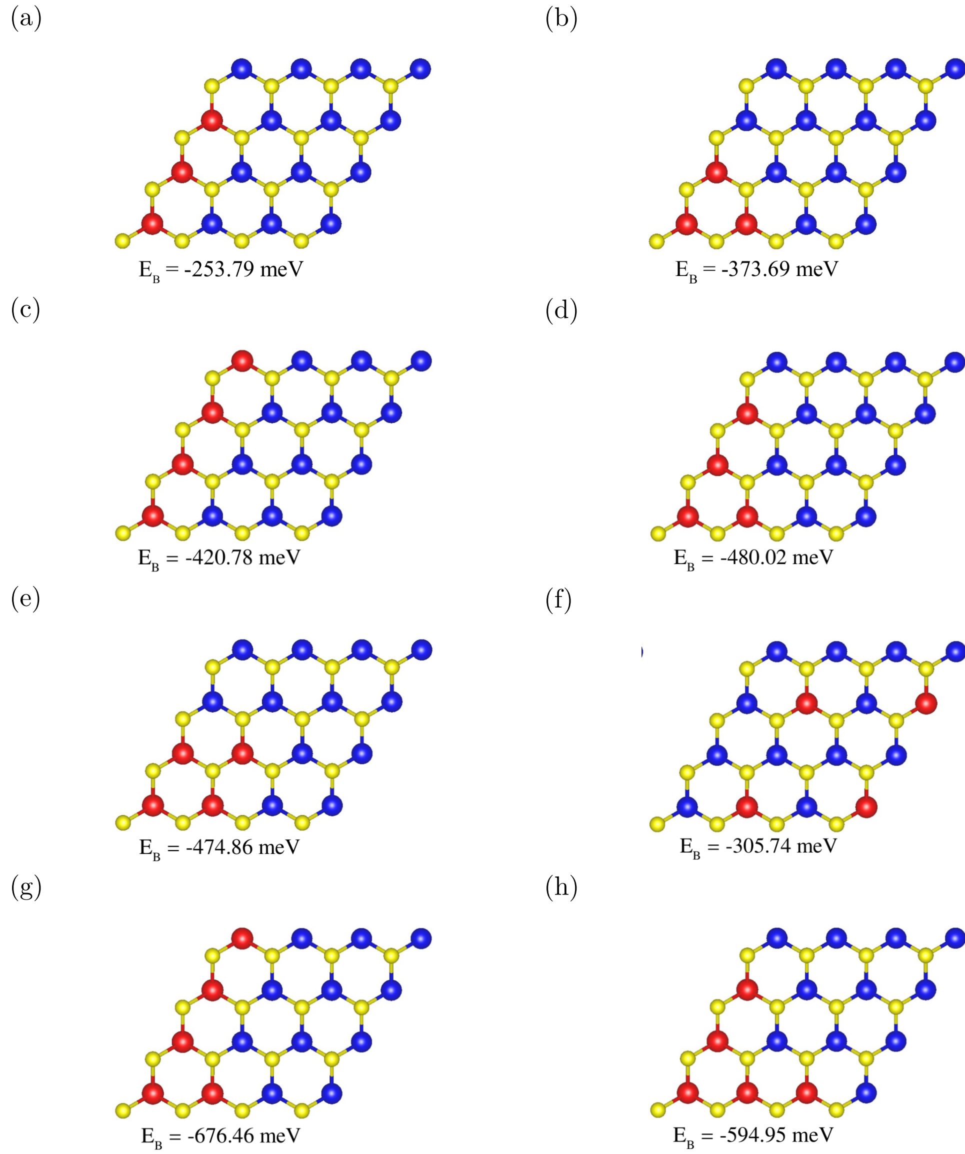

Figure 5.2: $W_{1-x}Nb_xS_2$ monolayers with different dopant distributions within 4×4×1 supercells. The corresponding binding energies are indicated. Red, blue and yellow colours refer to Nb, W and S atoms, respectively.

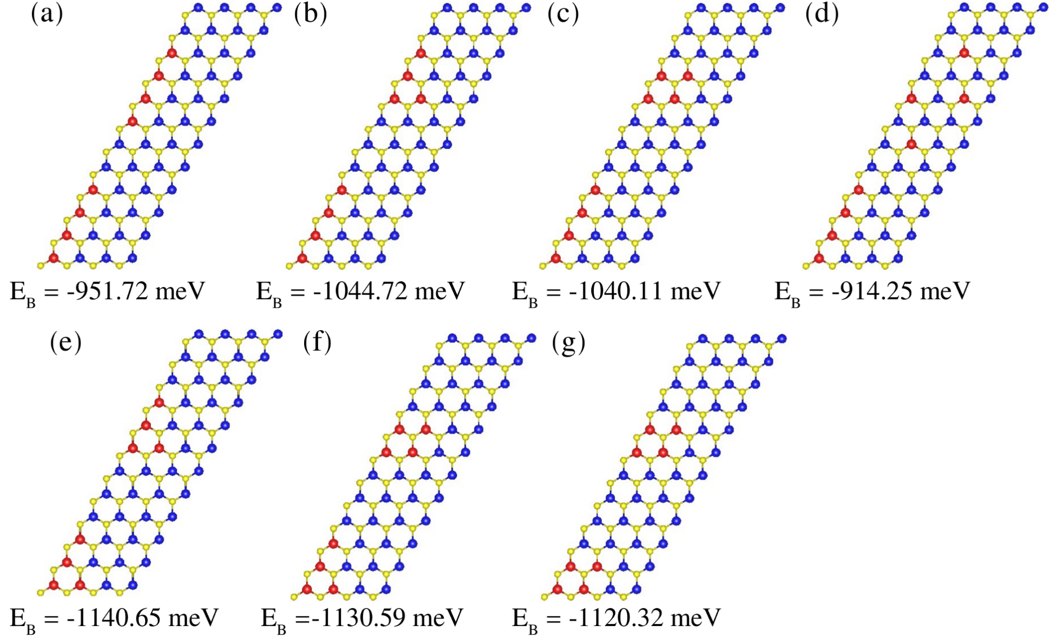

Figure 5.3: $W_{1-x}Nb_xS_2$ monolayers with different dopant distributions based on the combinations of prototypes in figure 5.2 within 4×12×1 supercells. The corresponding binding energies are indicated. Red, blue and yellow colours refer to Nb, W and S atoms, respectively.

The "line" instead of "L" pattern is considered as the initial configuration for simplicity in discussing the formation of dopant distribution seen in the ADF-STEM image in figure 5.1(a) and (b). An additional Nb atom is attracted to occupy the atomic site near the line (m = 5) to form a perfect line without a gap in the whole simulation cell (figure 5.4(a)), rather than becoming an isolated Nb at other atomic sites (figure 5.4(b)). However, an additional Nb atom is attracted to occupy the atomic site near the isolated Nb (figure 5.4(d)) rather than the atomic site near the line (m = 4) in figure 5.4(c). This is also true for a longer line (m = 5) in figure 5.4(f), even it has a chance to form a perfect line (figure 5.4(e)). This result is consistent with the dopant distribution seen in the ADF-STEM image in figure 5.1(a): there are many self-limited line segments (rather than the perfect lines) and isolated Nb atoms. Note that the binding energy is not only related to the number of Nb-Nb bonds, but also the dopant distribution. For example, the binding energy in figure 5.4(b) is different from figure 5.4(c) although they have the same number of Nb atoms and Nb-Nb bonds.

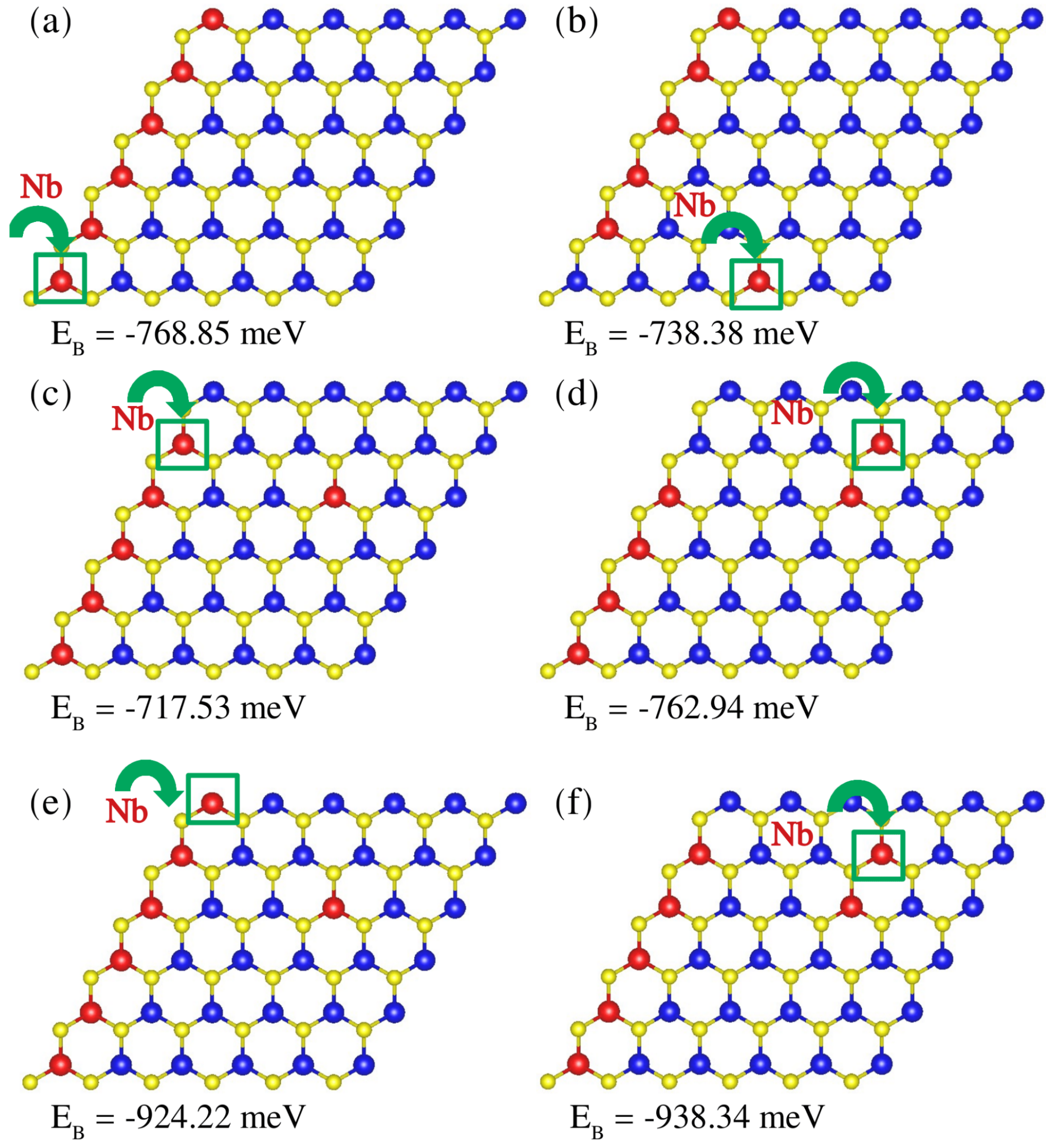

Figure 5.4: $W_{1-x}Nb_xS_2$ monolayers with different dopant distributions within 6×6×1 supercells. (a)(b) An additional Nb atom is inclined to occupy the atomic site near the line. (c)(d) An additional Nb atom is inclined to occupy the atomic site near the isolated Nb. (e)(f) An additional Nb atom is inclined to occupy the atomic site near the isolated Nb although occupying the atomic site near the line will form a perfect line in the whole simulation cell. Red, blue and yellow colours refer to Nb, W and S atoms, respectively.

It is interesting to know whether large Nb clusters tend to be formed in the WS_2 monolayer. In figure 5.5(a)-(d) with $m = 6$, the distributions comprising two small triangular clusters and two types of bigger clusters are shown. Figure 5.5(b) has the lowest binding energy among other three dopant distributions. It seems like the dopant distributions in figure 5.5(a) and (b) are the same, however, the number of Nb-Nb bonds is different. There are 6 for figure 5.5(a) and 8 for figure 5.5(b). The number of Nb-Nb bonds are 9 for both figure 5.5(c) and (d). It is suggested that Nb dopants are likely to be formed according to the following rules, in which the difference of number of Nb-Nb bonds is denoted as $\Delta N_{\mathrm{Nb-Nb}}$ below:

(i) Investigate whether larger number of clusters is more favourable: if $\Delta N_{\mathrm{Nb-Nb}} \leq 3$ between two dopant distributions, the dopant distribution with a higher number of Nb clusters is favourable (compare figure 5.5(b) with (c) and (d) or compare figure 5.5(a) with (d)). This can also be seen when comparing figure 5.4(c) with (d) or figure 5.4(e) with (f). This is consistent with the atomic configuration in the ADF-STEM image in figure 5.1(a), where many line segments are seen; If $\Delta N_{\mathrm{Nb-Nb}} > 3$ between two dopant distributions, the dopant distribution with higher number of Nb-Nb bonds is favourable. This can be seen when comparing figure 5.5(a) with (c). This implies that the inclination of one more Nb cluster is higher than three more Nb-Nb bonds but lower than four or more Nb-Nb bonds in a dopant distribution.

(ii) Investigate the favourable pattern in only one cluster: if $\Delta N_{\mathrm{Nb-Nb}} \leq 1$ between two dopant distributions, the dopant distribution with Nb cluster extends along both directions of lattice vectors ($\mathbf{a}$ and $\mathbf{b}$ in figure 5.1(b)) with longer Nb atoms is favourable. For example, the binding energy of $2\mathbf{a} - 2\mathbf{b} < 2\mathbf{a} - 1\mathbf{b}$ (compare figure 5.5(c) with (d)), $1\mathbf{a} - 1\mathbf{b} < 0\mathbf{a} - 2\mathbf{b}$ (compare figure 5.2(b) with (a)), $1\mathbf{a} - 2\mathbf{b} < 0\mathbf{a} - 3\mathbf{b}$ (figure 5.2(d) with (c)), $1\mathbf{a} - 1\mathbf{b} < 0\mathbf{a} - 3\mathbf{b}$ (figure 5.2(e) with (c)) and $1\mathbf{a} - 2\mathbf{b} < 1\mathbf{a} - 1\mathbf{b}$ (figure 5.2(d) with (e)). In the situation of two dopant distributions with $m\mathbf{a} - n\mathbf{b}$ and $p\mathbf{a} - q\mathbf{b}$ ($m + n = p + q$, where $m, n, p, s \neq 0$), the less symmetric dopant distribution is favourable. This can be seen when comparing figure 5.2(g) with (h) (where $1\mathbf{a} - 3\mathbf{b} < 2\mathbf{a} - 2\mathbf{b}$). If $\Delta N_{\mathrm{Nb-Nb}} > 1$, the dopant distribution with higher number of Nb-Nb bonds is favourable (compare figure 5.4 (a) with figure 5.4(b)).

These arguments also apply to dopant distributions with different Nb compositions, for example, figure 5.6 and figure 5.9 (binding energies are not shown). In figure 5.5(e) and (f), the atomic configuration with two adjacent lines has lower binding energy than two isolated lines, because two adjacent lines has larger number of Nb-Nb bonds (see argument (i) mentioned above). However, this is not seen in

the as-grown crystal in figure 5.1(a). In addition, the “L” is also not seen in the ADF-STEM image in figure 5.1(a). This suggests that the kinetic effects tend to prevent the diffused Nb atoms from occupying the adjacent positions of the existing line segments on any direction other than along the lines (although it has a chance to absorb and diffuse at these positions in the intermediate states [187, 188, 189]). This may be caused by the joint effect of the local availability of transition metal and chalcogenide atoms determined by the kinetic process [144] and the activation energy determined by the binding energy that influences the diffusion rate [187, 188, 189]. This implies that both the kinetic effects and the energetics needs to be considered to describe the dopant distribution seen in the as-grown $W_{1-x}Nb_xS_2$ monolayer.

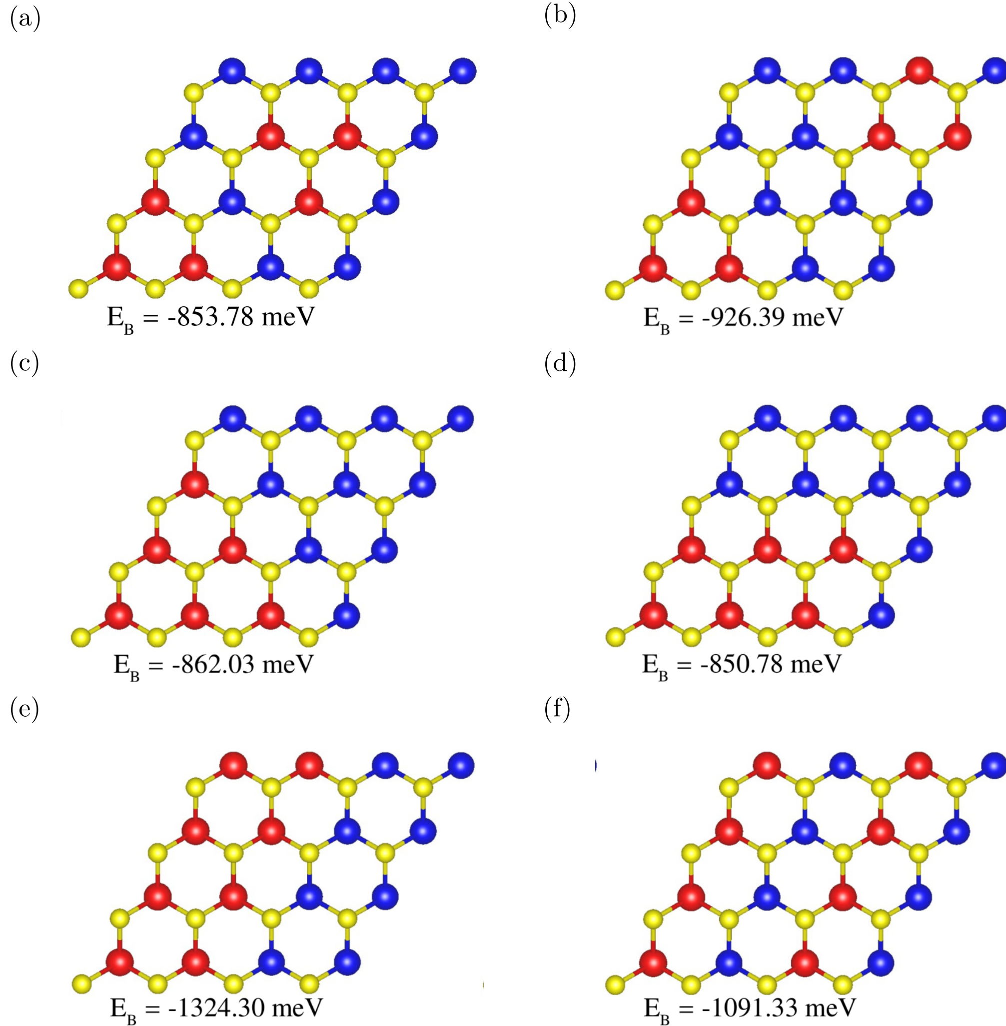

Figure 5.5: $W_{1-x}Nb_xS_2$ monolayers with different dopant distributions within 4×4×1 supercells. The corresponding binding energies are indicated. Red, blue and yellow colours refer to Nb, W and S atoms, respectively.

5.3.2 Electronic structure of $W_{1-x}Nb_xS_2$ monolayer

The anisotropic dopant distribution in the $W_{1-x}Nb_xS_2$ monolayer seen in figure 5.1(a) motivates us to investigate how the electronic structure is influenced by the dopant distribution. Some specially designed dopant distributions are also shown for comparison with a real dopant distribution taken from the as-grown crystal. For the effective band structure along Γ to **M**, there is a flat band appears above the Fermi level for the "perfect line" and the "real" in figure 5.6. Although there is also a flat band that appears above the Fermi level for the "half line", it is not as pronounced as the other two cases mentioned above. For the "random", two flat bands can be seen in the effective band structure. It seems like a more obvious flat band is generated in dopant distribution with longer "line" such as the "perfect line" and the "real" or larger Nb composition such as the "random". This is consistent with the argument in [195]: the flat band does not appear in $W_{1-x}Nb_xS_2$ with dopant distribution of isolated Nb. The effective band structures with the dopant distributions considered here do not change significantly except the appearance of the flat band.

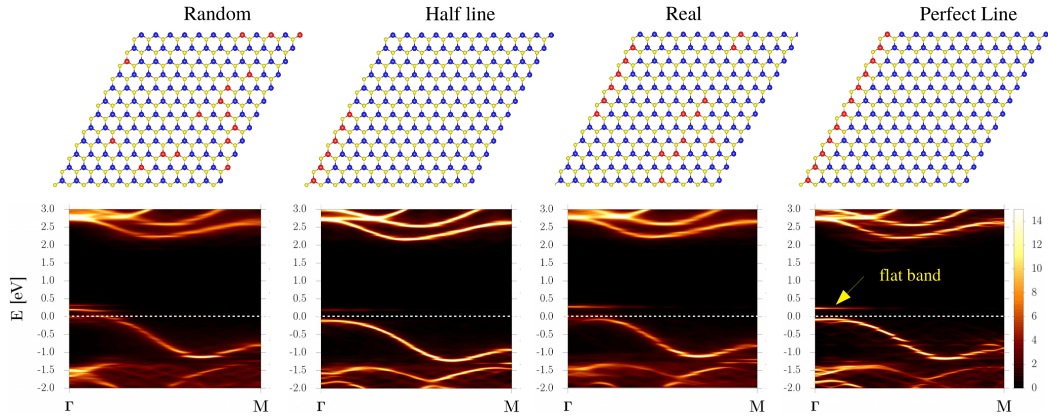

Figure 5.6: Atomic structures of $W_{1-x}Nb_xS_2$ monolayers with dopant distributions named as (a) "random" (b) "half line" (c) "real" (d) "perfect line" within 12×12×1 supercells and their corresponding effective band structures along Γ to **M**. The "real" distribution is based on a region of ADF-STEM image in figure 5.1(a). A Lorentzian broadening of 0.02 eV was employed in the effective band structures. Dashed line represents the Fermi level. Red, blue and yellow colours refer to Nb, W and S atoms, respectively.

The arguments mentioned above are also true for the effective band structures along Γ to **K1**, **K2** and **K3** in figure 5.7. $W_{1-x}Nb_xS_2$ monolayers with different dopant distributions display metallic behaviour because the VBM crosses the Fermi

level. The valence band splitting resulting from the spin-orbit coupling is obvious in these four cases. At first sight, the metallic behaviour contrasts with the band structure of $W_{0.9375}Nb_{0.0625}S_2$ monolayer in [195] in which a direct band gap of 1.95 eV is reported. Although the Nb composition for the "half line" ($x \simeq 0.04$) is lower than 0.0625, the separation between Nb dopant atoms in their case is much larger than the "half line" because WS_2 monolayer only doped with one Nb atom within a 4×4×1 supercell in [195]. The dopant distribution of the line facilitates the flowing of charge carriers, thus leading to the metallic behaviour in our cases. This means the relative position of each Nb dopant atom plays a more important role than the Nb composition. The obvious flat band can be obtained by simply increasing the Nb composition. The relative position of Nb atoms and the Nb composition are the major and minor factors in affecting the appearance of the flat band.

Interestingly, a normal band can be seen for the "perfect line" along Γ to **K1** instead of a flat band for other directions. The direction of Γ to **K1** is parallel to the line in our models of the $W_{1-x}Nb_xS_2$ monolayer. The band structure of the "real" distribution is a result of the combination of the isolated Nb atoms, lines and clusters, thus it has features between the "random" and the "perfect line". The transport properties are then expected to be superior in this dopant distribution.

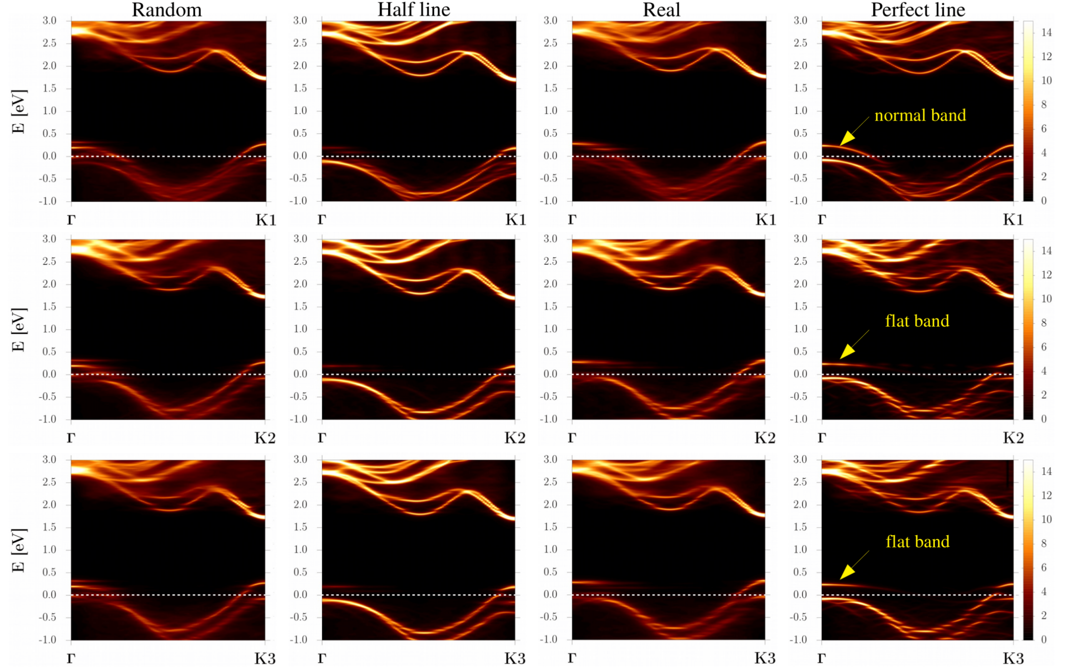

Figure 5.7: Effective band structures of $W_{1-x}Nb_xS_2$ monolayers with different dopant distributions are the same as figure 5.6 along Γ to **K1**, **K2** and **K3**. The "real" is based on a region of ADF-STEM image in figure 5.1(a). A Lorentzian broadening of 0.02 eV was employed in the effective band structures. Dashed line represents the Fermi level. Red, blue and yellow colours refer to Nb, W and S atoms, respectively.

Furthermore, the charge density shown in figure 5.8 is mainly contributed by the *d* orbitals of Nb and W atoms for the VBM and CBM, respectively, similar with the description in [186]. The flat band appears in the effective band structure in figure 5.6 and figure 5.7 is mainly contributed by the *d* orbitals of Nb atoms (the localisation of charge density around Nb atoms). Furthermore, the two eigenstates associated with the flat bands shown in figure 5.8 show well-separated charge densities both in space and energy.

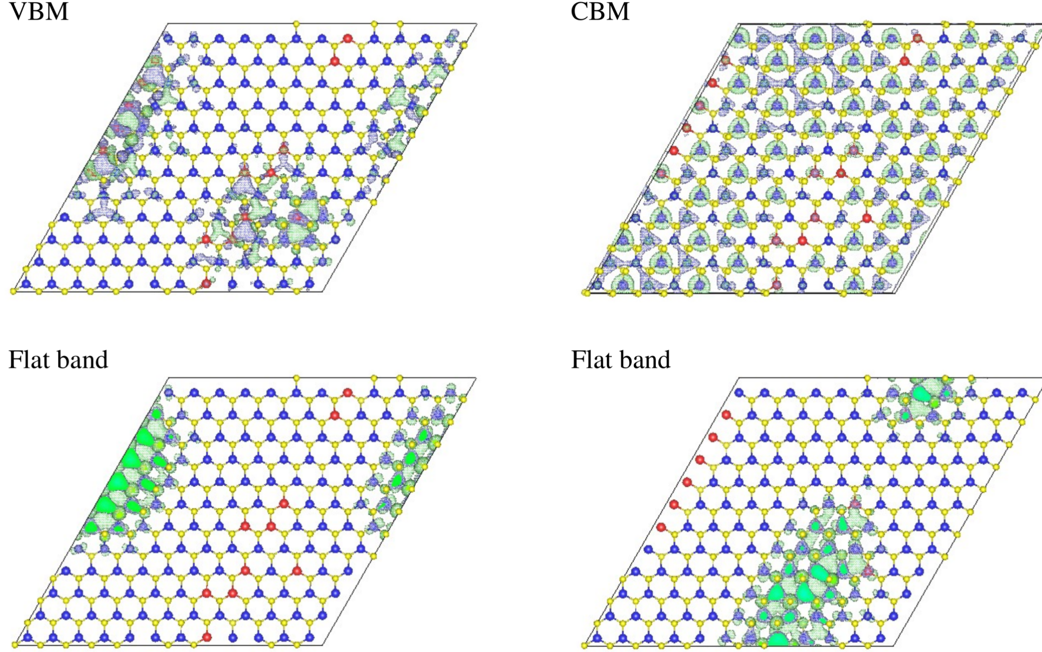

Figure 5.8: Charge density distributions of chosen eigenstates for the "real" distribution in figure 5.6. The d orbital contribution of Nb atom predominated the VBM and flat bands, whereas the d orbital contribution of W atom predominated the CBM. The two eigenstates associated with the flat bands have well-separated charge densities both in space and energy. The isosurfaces of charge densities for VBM, CBM and flat bands are around energy ranges of [-0.15, 0.03] eV, [2.06, 2.10] eV and [0.26, 0.28] eV, respectively. The charge densities were calculated via ONETEP by setting the parameters "homo_plot" and "lumo_plot" to the numbers of bands below and above the Fermi level desired to plot, respectively. Red, blue and yellow colours refer to Nb, W and S atoms, respectively.

5.3.3 Electrical conductivity of $W_{1-x}Nb_xS_2$ monolayer

The normalised conductivities (σ/τ) along the direction of parallel to the line and perpendicular to the line for various dopant distributions are displayed in figure 5.9, for systems which we have named as "random ($x = 0.219$)", "real (isolated Nb)" ($x = 0.125$), "half line" ($x = 0.063$), "real (line Nb)" ($x = 0.141$) and "perfect line" ($x = 0.125$). The purpose of considering various dopant distributions is to compare the electrical conductivity and the degree of anisotropy in the actual ("real") dopant distribution with other modelled dopant distributions for investigating the relation between the conductivity and dopant distribution. The "real (isolated Nb)" and the "real (line Nb)" are both copied from the regions of ADF-STEM image. The conductivities in units of the relaxation time (σ/τ) for all atomic configurations

considered here are all around 10^{18} $\Omega^{-1}m^{-1}s^{-1}$ and the doping level are around 10^{14} cm^{-2} at T = 300 K. The anisotropic conductivity can be easily seen in the "real (isolated Nb)", "half line", "real (line Nb)" and the "perfect line" with a range of ratio between around 1.6 ("real (isolated Nb)") to 17.2 ("perfect line") at zero extrinsic doping.

The conductivity for the "perfect line" along the direction of parallel to the line (black curve) has the highest value at zero extrinsic doping although its Nb composition is not the highest among the atomic configurations considered here. It also has the highest ratio of the conductivity ($\simeq$ 17.2) at the zero extrinsic doping. This is about 3.4× and 25.1× larger than the second highest in the "real (line Nb)" ($\simeq$ 5.0) and the lowest in the "random" ($\simeq$ 0.7). Although the lengths of the line segments in the "real (line Nb)" are shorter than the "half line" distribution, the conductivity along the direction of parallel to the line of "real (line Nb)" (1.89×10^{18} Ω^{-1} m^{-1} s^{-1}) is about 10× higher than the "half line" (0.17×10^{18} Ω^{-1} m^{-1} s^{-1}) at zero extrinsic doping, due to the tunneling of holes between line segments in the "real (line Nb)". It is about 4× higher conductivity in the "real (line)" (0.38×10^{18} Ω^{-1} m^{-1} s^{-1}) than the "half line" (0.09×10^{18} Ω^{-1} m^{-1} s^{-1}) along the direction of perpendicular to the line. It is worth noting that the conductivity of the "perfect line" (3.72×10^{18} Ω^{-1} m^{-1} s^{-1}) along the direction of parallel to the line is about twice as large as the "real (line Nb)" at zero extrinsic doping. This means that the hopping effect is still weaker than the bonding of Nb atoms although the "real (line)" (x = 0.141) has slightly larger Nb composition than the "perfect line" (x = 0.125). Thus, the conductivity along the direction of parallel to the line and the degree of anisotropy in conductivity can be improved by forming a longer length of the line segment and increasing the number of the lines. However, the conductivity of "half line" (0.17×10^{18} Ω^{-1} m^{-1} s^{-1}) is lower than the "real (isolated Nb)" (0.66×10^{18} Ω^{-1} m^{-1} s^{-1}) along the direction of parallel to the line at zero extrinsic doping (the Nb composition of "real (isolated Nb)" (x = 0.125) is twice as large as the "half line" (x = 0.063)). This means the Nb composition also needs to be considered.

The conductivity of the "half line" along the direction perpendicular to the line (red curve) is the lowest and the "perfect line" is the second lowest, whereas "random" is the highest (13.1× higher than the "half line"). It is worth noting that the relative position of each Nb dopant atom and the Nb composition are the major and minor factors in influencing the conductivity along the direction of parallel to the line, respectively. This is consistent with the discussion in the previous section about the electronic structures for various atomic configurations.

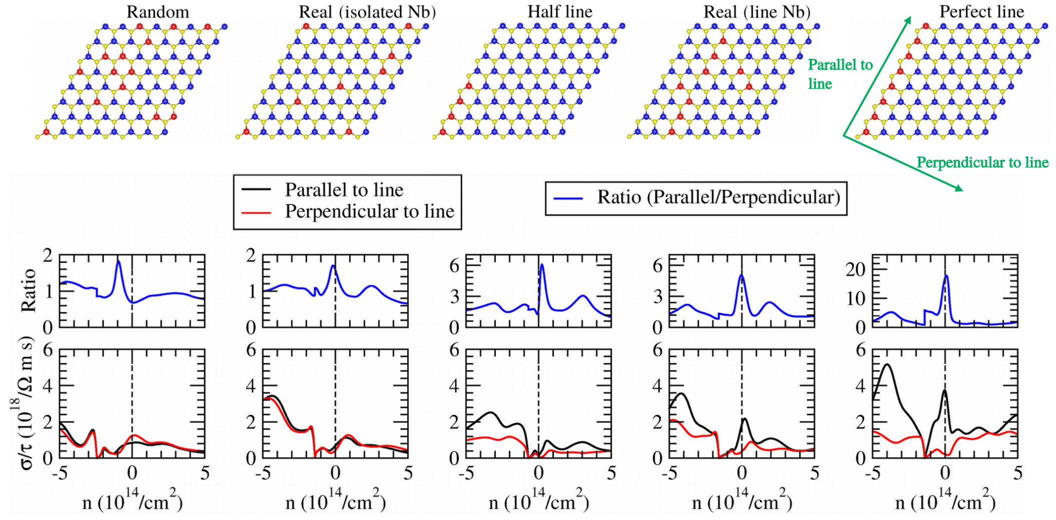

Figure 5.9: Normalised electrical conductivity (σ/τ) as a function of extrinsic doping for $W_{1-x}Nb_xS_2$ monolayers with dopant distributions named as "random" ($x = 0.219$), "real (isolated Nb)" ($x = 0.125$), "half line" ($x = 0.063$), "real (line Nb)" ($x = 0.141$) and "perfect line" ($x = 0.125$) along the direction parallel to the line and perpendicular to the line at $T = 300$ K. The "real (isolated Nb)" and "real (line Nb)" are based on two representative regions of the ADF-STEM image in figure 5.1(a). The ratio is the conductivity along the direction of parallel to the line divided by the conductivity along the direction perpendicular to the line. For the atomic structures: red, blue and yellow colours refer to Nb, W and S atoms, respectively.

5.4 Conclusions

A highly anisotropic dopant distribution was seen in the as-grown $W_{1-x}Nb_xS_2$ monolayer. It is suggested that energetics and kinetic processes both play important roles in forming this kind of symmetry-breaking dopant distribution. From the analysis of the binding energies from some particular dopant distributions (e.g. line, "L", triangle cluster, etc.) and the STEM image of the as-grown crystals, it is sufficient to express that the local availability of W, Nb and S atoms cause the inclination of Nb atoms to align in a specific direction in WS_2 monolayer. The formation of line segments in other places is due to the following Nb atom prefers to combine with the isolated Nb which is initially formed by chance and this 2-Nb cluster further combines with other following Nb atoms until forming a new line segment. The self-limitation of the length of the line segment is a mutual competition between energetics and kinetic processes, where the Nb atoms prefer to form Nb-Nb pairs (according to the negative binding energy) from the perspective of energetics.

From this analysis, it can be expected that dopant clusters which do not line along a specific direction (e.g. 5.5(c) and (d)) can possibly be seen if the binding energy of dopant pair is much larger than the kinetic effects. In contrast, we can expect to see a similar dopant distribution as the as-grown crystal in this work (even if the binding energy is positive) by tuning the kinetic processes (e.g. fluctuation of local availability of metals and chalcogenides [144]) to exceed the effect of energetics. This can be seen from the comparison between our previous work about $Mo_{1-x}W_xS_2$ monolayer [142] with a small positive binding energy (~7.6 meV) showed a random dopant distribution, and the work of Azizi et al. [144] showed striped pattern in the $Mo_{1-x}W_xS_2$ monolayer. From this work we have obtained an inspiration of growing different kinds of dopant distributions, we expect to observe a similar dopant distribution in other similar alloys, such as $W_{1-x}Nb_xSe_2$ with a binding energy of -53.56 meV, in appropriate growth conditions. In contrast, we can also intentionally grow striped pattern (or other clusters) in other kinds of alloys with a positive binding energy for the dopant pair, or forming a random distribution with a negative binding energy for the dopant pair, by controlling the experimental process.

The flat band appearing above the Fermi level in the effective band structure is related to the line seen in the dopant distribution. Although it can be surmised that an extended "perfect line" is not likely to be be realised in the growth process from energetic considerations, the real atomic configuration displays a high conductivity along the direction of parallel to the line and a high level of anisotropy in conductivity at zero extrinsic doping (even including realistic impurities in the samples). The conductivity along the direction parallel to the line can be improved by increasing the number and the lengths of the lines or the Nb composition. The degree of anisotropy in conductivity can also be improved by the factors mentioned above and increasing the spacing between two line segments. $W_{1-x}Nb_xS_2$ monolayer with anisotropic dopant distribution shown in this work is an exemplar of aliovalent TMDC alloys for realising superior anisotropic conductivity in the electronic devices.

Chapter 6

Twistronics in two-dimensional InSe bilayer

6.1 Introduction

The emerging research field focussing on the properties of materials composed of two or more 2D layers with relative rotation angles has attracted a great deal of scientific attention. Recent studies on twisted 2D materials have widened and deepened our knowledge about this novel topic in condensed matter physics. Twisted graphene bilayer must inevitably to be mentioned when introducing twistronics. Flat bands associated with Mott insulating and superconducting behaviours have been observed at the "magic angle" ($\sim 1.1^{o}$) in twisted graphene bilayer [71, 72, 76]. Tarnopolsky et al. [71] has proposed a periodicity of $\Delta\alpha \simeq 3/2$ ($\alpha \sim 1/\theta$) for the occurence of magic angles, at which the band gap becomes maximum and the bandwidth becomes zero within each period by setting the interlayer coupling parameter for AA stacking equals to zero (chiral symmentry) in the continuum model. The moiré pattern resulting from the relative rotation between two graphene layers leads to the localisation of Dirac electrons in the AA stacking, especially at small twist angles [196]. The wave functions associated with the flat bands localised in the same regions has also been shown in the twisted MoS_2 bilayer [197].

"Magic angles" are not always necessary in forming flat bands in twisted 2D materials. Zhao et al. [198] has proposed that flat bands can occur at any small twist angles (not "magic angles") for two-dimensional polar semiconductors with broken sublattice symmetry, concluded from the study of twisted hBN bilayer. For the band structure of twisted TMDC bilayers in a tight-binding model, the apperances of ultraflat bands have been predicted at any small twist angles [199]. Furthermore,

the long period moiré pattern resulted by the relative rotation between two TMDC layers changes the optical absorption spectrum with satellite excitonic peaks [200].

Liu et al. [201] showed that there is a sinusoidal relationship between the twist angle and the cohesive energy in twisted black phosphorene bilayer. It is suggested that the cohesive energy is related to the interlayer coupling strength because the periodicities of their sine relationships are very similar. In their studies, anisotropic transport of holes and electrons in twisted black phosphorene bilayer can be realised by arranging the two layers to specific stacking types or twist angles. They also showed that for some twist angles associated with weak interlayer coupling, a spontaneous electric polarisation may be induced by the symmetry-breaking in the atomic structure. This leads to a linear Stark effect, which means the band gap becomes linearly dependent on the external electric field. In addition, a rigid-lattice moiré pattern has been observed at large twist angles via transmission electron miscroscopy, whereas atomic reconstruction happens at small twist angles in the small lattice-mismatched twisted $MoSe_2/WSe_2$ heterobilayer [202].

InSe is a 2D material which possesses carrier mobility of more than 10^3 cm^2 V^{-1} s^{-1} in the few-layer form at room temperature and the effective mass of electrons in the conduction bands is small [203]. Furthermore, the I_{on}/I_{off} (1×10^8) is high and the dissipation of standby power is low in InSe based FET [204]. It was shown in previous studies [78, 205] that five different stacking arrangements can be formed when two InSe monolayers are put together. If the lattice vectors are $\mathbf{a} = [a\;0\;0]$ and $\mathbf{b} = [-\frac{a}{2}\;\;\frac{\sqrt{3}a}{2}\;\;0]$ as in this work, they can be categorised into two types according to whether one layer is mirrored (A type) or rotated (B type) with respect to the other layer: the A-2 is formed by translating the A-1 with a vector $\mathbf{T}= \frac{1}{3}\mathbf{a} - \frac{1}{3}\mathbf{b}$, whereas the B-2 and B-3 are formed by translating the B-1 with a vector $\mathbf{T}$ and $2\mathbf{T}$, respectively (figure 6.1). Kang et al. [78] showed that these stacking arrangments still can be seen in limited regions of the atomic structure when one of the layers is twisted. For example, the A-1 and A-2 are seen in figure 6.2(a), whereas the B-1, B-2 and B-3 are seen in figure 6.2(b). The out-of-plane corrugation was considered in their work owing to the different high-symmetry stacking configurations with different interlayer distances in the entire structure. They showed that although the B-3 stacking exhibits the lowest formation energy, the difference of the formation energy between the A-type and the B-type is very small ($\simeq$ 7.14 meV/atom) within a range of twist angle from 1.48° to 3.00°. The fluctuation of the formation energy as a function of twist angle is negligible. In addition, the VBM moves to Γ as the twist angle decreases from 3.00° to 1.48°, thus the indirect band gap changes to the direct band gap, where the band gap increases at the same time. From the analysis

of the spatial charge distribution, they showed that the degree of localisation for the VBM increases and the VBM becomes flatter as the twist angle decreases, whereas the CBM is delocalised for all twist angles between 1.48° and 3.00° [78].

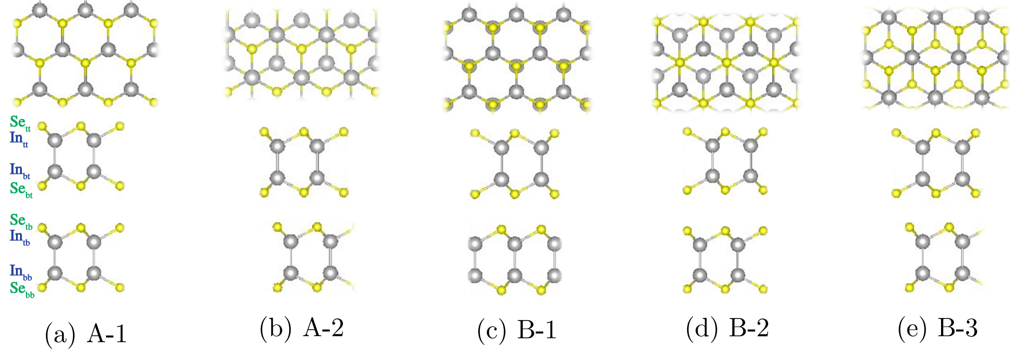

Figure 6.1: Schematic diagrams of InSe bilayers with different stacking arrangements, denoted as (a) A-1 (b) A-2 (c) B-1 (d) B-2 (e) B-3. Grey: In, yellow: Se. All In and Se atoms (In_{ij} and Se_{ij}) in (a) are labelled for later discussions, where i refers to the vertical position of In or Se atom (t: top atom, b: bottom atom) in the top or bottom layers, whereas j refers to the top or bottom layer (t: top layer, b: bottom layer).

In this chapter, we aim to get a deeper knowledge about InSe in original forms (monolayer and bilayer) and when considering twist angle for the bilayer. We are interested to know the variation of the atomic and electronic structures of InSe bilayer with different interlayer distances and twist angles. Understanding the relations among InSe monolayer, bilayer and twisted bilayer can give us a deeper knowledge about this material and help us choose different methods to tune its properties. The orbital contributions of the bands and the aligned InSe bilayer are expected to have effects on the electronic properties of twisted InSe bilayer. Furthermore, the purpose of separating InSe bilayer by the hBN layer is to modify the electronic properties of twisted InSe bilayer. From our studies, the stacking configuration plays an important role to influence the band structure of InSe bilayer and twisted InSe bilayer. The mapping of the bands of InSe bilayer with different stacking configurations within the primitive cell into the effective band structure of twisted InSe bilayer within the supercell is proposed. The hBN layer is shown to act effectively as a spacer to separate the InSe layers in twisted InSe/hBN/InSe heterostructure from the analysis of both the effective band structure and the projected density of states. The resulting effective band structure also matches the bands of InSe monolayer within the primitive cell. The exciton binding energy of twisted InSe bilayer and twisted InSe/hBN/InSe heterostructure were also calculated to

give an estimation of the length scale of the exciton binding energy to experiments. The computational effort required to study the electronic properties such as band gap and effective mass for holes of twisted InSe bilayer can thus be eased because only calculation within the primitive cell is needed. This is useful because different tests can be done before the implementation of the actual experiments and it also provides theoretical bases to explain the experimental results.

6.2 Computational methods

The calculations required to optimise geometric parameters such as lattice constant and interlayer distance of InSe bilayer with these five types of stacking configurations within the primitive cells were performed in Quantum Espresso simulation package [61, 62]. The GGA-PBE versions of the ultrasoft Vanderbilt pseudopotentials (scalar-relativistic) obtained from the GBRV library [193] were used. The optB88-vdW functional [99] was included to incorporate the van der Waals (vdW) interaction between two layers. A kinetic cut-off energy of 1632.7 eV (120 Ry) was employed. A Monkhorst-Pack [206] kpoint grids of 10×10×1 was set. The spurious interaction between two isolated cells is eliminated by increasing the vacuum spacing to 20 Å. The force and total energy in the ionic minimisation task were converged to within 5×10^{-5} eV/Å and 3×10^{-7} eV for all atoms, respectively. The GGA-PBE versions of the optimised norm-conserving Vanderbilt pseudopotentials (fully-relativistic) [153] obtained from PseudoDojo [154] (without vdW correction) was used in the calculations with considering SOC. Other parameter settings were the same as mentioned above.

ONETEP [59, 63] was used to simulate the twisted InSe bilayer within the large-scale supercell. The GGA-PBE versions of PAW [104, 105, 130] potentials from the GBRV library [193] were used. The optB88-vdW exchange-correlation functional [99] was included to correct the van der Waals (vdW) interaction between two layers. The cut-off energy and NGWF radius are 1200 eV and 12 a_0, respectively. For geometry optimisation of the atomic structure, the force and enthalpy tolerance are 0.12 eV/Å and 3×10^{-5} eV/atom, respectively. The spurious interaction between two isolated cells is eliminated by setting the vacuum spacing to 20 Å. A Lorentzian broadening of 0.02 eV was employed in the effective band structure. The lattice constant of InSe monolayer (4.059 Å) is adopted as the lattice constant for all twisted InSe bilayer.

The construction of the twisted InSe bilayer followed the work of Stradi et al. [207] and implemented with the atomic simulation environment (ASE) [159]. The

scripts used were developed by N. D. M. Hine with input from S. Coppola and C. Damour [208]. The twisted bilayer is normally constructed within a large supercell, especially when the twist angle is small ($\propto 1/\theta$) [78]. The supercell lattice vector of the layer A is obtained via a transformation matrix $\mathbf{S}$ applied on the primitive cell lattice vector $\mathbf{a}$ [207],

$$\begin{bmatrix} \mathbf{A}_1 \\ \mathbf{A}_2 \end{bmatrix} = \mathbf{S} \begin{bmatrix} \mathbf{a}_1 \\ \mathbf{a}_2 \end{bmatrix}, \tag{6.1}$$

where $\mathbf{A}_i$ and $\mathbf{a}_i$ $(i = 1, 2)$ represent the matrix elements of $\mathbf{A}$ and $\mathbf{a}$, respectively. The transformation matrix $\mathbf{S}$ is written as

$$\mathbf{S} = \begin{bmatrix} S_{11} & S_{12} \\ S_{21} & S_{22} \end{bmatrix}, \tag{6.2}$$

where S_{ij} $(i, j = 1, 2)$ are integers. Similarly, the supercell of the twisted layer B with a lattice vector $\mathbf{B}_{\mathrm{R}}$ is written as

$$\begin{bmatrix} \mathbf{B}_{\mathrm{R}1} \\ \mathbf{B}_{\mathrm{R}2} \end{bmatrix} = \mathbf{PR} \begin{bmatrix} \mathbf{b}_1 \\ \mathbf{b}_2 \end{bmatrix}, \tag{6.3}$$

where $\mathbf{P}$ is the transformation matrix for the layer B. The rotation matrix $\mathbf{R}$ is written as

$$\mathbf{R} = \begin{bmatrix} \cos\theta & -\sin\theta \\ \sin\theta & \cos\theta \end{bmatrix}, \tag{6.4}$$

where θ refers to the twist angle. To form a twisted bilayer, we require that

$$\begin{bmatrix} \mathbf{A}_1 \\ \mathbf{A}_2 \end{bmatrix} = \begin{bmatrix} \mathbf{B}_{\mathrm{R}1} \\ \mathbf{B}_{\mathrm{R}2} \end{bmatrix}. \tag{6.5}$$

According to this requirement, the matrix elements of $\mathbf{P}$ may not be integers. In order to ensure the matrix elements of $\mathbf{P}$ are integers, the closest integer values are considered. Thus, the twisted layer B is under strain. The expression is then written as

$$\begin{bmatrix} \mathbf{A}_1 \\ \mathbf{A}_2 \end{bmatrix} = \begin{bmatrix} \sigma_1 & \lambda_1 \\ \lambda_2 & \sigma_2 \end{bmatrix} \begin{bmatrix} p & q \\ r & s \end{bmatrix} \begin{bmatrix} \cos\theta & -\sin\theta \\ \sin\theta & \cos\theta \end{bmatrix} \begin{bmatrix} \mathbf{b}_1 \\ \mathbf{b}_2 \end{bmatrix}, \tag{6.6}$$

where p, q, r and s are integers. σ_i and λ_i $(i = 1, 2)$ are around 1 and 0, respectively. Searching for a given range of twist angle and supercell size, the integers (p, q, r, s) were chosen to most-closely satisfy the requirement in eq. (6.5) at a given twist angle, where σ_i and λ_i are required to below the chosen thresholds. If the match cannot be obtained, the search for the next twist angle within the given range of twist angle will

begin. For the twisted InSe/hBN/InSe heterostructure, the atomic structure was generated by implementing the procedure above again with the coincident supercell of twisted InSe bilayer and the hBN layer as inputs. Even if there is strain on the hBN layer, it will not affect the result significantly because the separation between the band edges of twisted InSe bilayer and the hBN layer is large. The bottom InSe layer is unstrained, whereas the strain (σ) in the top InSe layer and the hBN layer were smaller than 0.8%.

Furthermore, the exciton binding energy E_b can be estimated according to methods presented in recent works by the group of V. I. Fal'ko [209, 210, 211] if we know the required input parameters. The results of calculated exciton binding energies for the twisted InSe bilayers and the twisted InSe/hBN/InSe heterostructure are shown in section 6.3.4 with the interlayer distances and effective masses for holes for various twist angles obtained in this chapter as inputs. The details for calculating the exciton binding energy can be referred back to their original work [209, 210, 211].

All the atomic structures, isosurfaces of charge densities and the analysis of the residual force distribution were generated and exhibited via the atomic simulation environment (ASE) [159], NumPy [160], SciPy [212], Matplotlib [213] and the visualisation for electronic and structural analysis (VESTA) [161].

6.3 Results and discussions

6.3.1 Electronic structures of InSe monolayer and InSe bilayer with different stacking configurations

The atomic structures of the A-type and the B-type twisted InSe bilayers studied in this work are shown in figure 6.2.

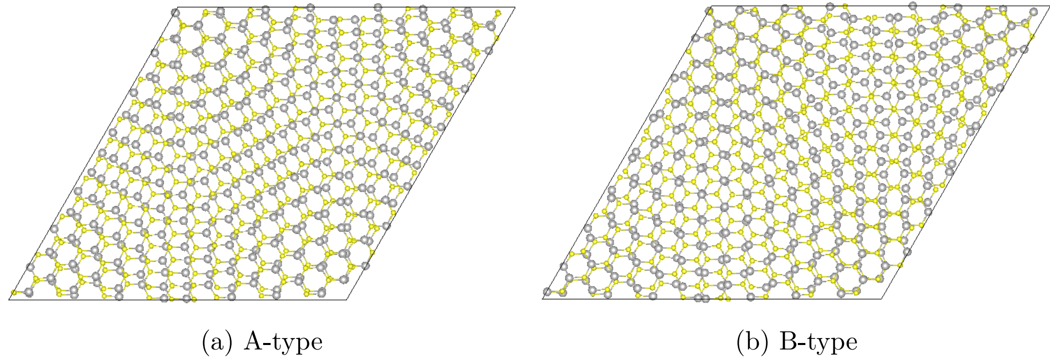

(a) A-type (b) B-type

Figure 6.2: Top view of the (a) A-type (b) B-type twisted InSe bilayer with a twist angle of 4.4°. Grey: In, yellow: Se.

Table 6.1 shows the calculated parameters of InSe monolayer and InSe bilayers with different stacking configurations. The lattice constant, band gap and effective mass for holes of InSe monolayer are consistent with previous studies [214, 215, 216]. For InSe bilayer with these five stacking configurations, their relative magnitudes of the lattice constant are similar to the previous studies with different pseudopotentials [78, 205]. The difference of the lattice constant among these five stacking configurations is smaller than 0.32% in this work. Furthermore, the interlayer distances are also similar to the previous studies with different pseudopotentials [78, 205] (except [205] with GGA-PBE pseudopotential).

The binding energy E_{B} is defined as the difference of the total energy between InSe bilayer and two InSe monolayers [205]: $E_{\mathrm{B}} = E_{\mathrm{bilayer}}$ - $2E_{\mathrm{monolayer}}$. The indirect band gap and the binding energy are consistent with the results in [205] with optB88-vdW pseudopotential. The deviation between this work and [205] is smaller than 0.04 eV for the band gap and 9 meV for the binding energy. It seems like the stacking configuration with the smallest interlayer distance corresponds to the lowest binding energy, thus the B-3 are the most stable stacking configurations among all InSe bilayers. This may because the repulsion is the smallest when two In atoms in two different InSe layers aligned. In contrast, the binding energy is the largest for the A-1 with two Se atoms in two diferent InSe layers aligned.

In addition, Yang et al. have explained that the interlayer vdW bonding for the stacking configuration with a smaller interlayer distance is stronger than the stacking configuration with a larger interlayer distance [205]. Yang et al. [205] and Shang et al. [217] have also shown that a larger interlayer distance gives a larger band gap, this is consistent with the results in this work for both indirect and direct (at Γ) band gap. The effective masses for holes at both the highest energy point and Γ of the VBM for the B-3 (the most stable stacking configuration

among these five types of stacking configurations) are consistent with [216]. From table 6.1, it is suggested that the band gaps and the binding energy increase as the interlayer distance increases when comparing InSe bilayers with different stacking configurations. Furthermore, the effective masses for holes also generally increases as the interlayer distance increases. The ordering of interlayer distance is B-3→A-2→B-1→B-2→A-1. The InSe monolayer possesses a larger band gap and effective mass for holes than the InSe bilayer due to the absence of interlayer hybridisation.

	monolayer	A-1	A-2	B-1	B-2	B-3
a (Å)	4.059	4.058	4.067	4.059	4.058	4.071
d (Å)		9.180	8.449	8.514	9.178	8.389
E_{B} (meV)		-179.52	-269.74	-264.23	-179.84	-274.22
E_{g} (eV)	1.42	1.02	0.87	0.92	1.02	0.82
E_{g} (eV) (at Γ)	1.50	1.08	0.94	0.99	1.08	0.90
m_{h} ($\mathrm{m_0}$)	2.22	1.99	1.03	1.10	1.93	1.05
m_{h} ($\mathrm{m_0}$) (at Γ)	-0.83	-0.96	-0.70	-0.74	-0.94	-0.66

Table 6.1: Lattice constant (a), interlayer distance (d) between two InSe layers ($\mathrm{In_{tt}}$-$\mathrm{In_{tb}}$), binding energy (E_{B}), band gap (E_{g}) and effective mass for holes (m_{h}) of InSe monolayer and InSe bilayers with different stacking configurations.

The band structures of InSe monolayer and InSe bilayers with different stacking configurations are shown in figure 6.3. The number of bands is doubled when two InSe monolayers are put together. For example, the VBM and the band below the VBM (denoted as VBM-1) of InSe bilayer originate from the two VBMs of the two different InSe monolayers. This also applies to the CBM and the band above the CBM. Basically, the band structures for different stacking configurations look similar without considering the detailed features. Because we are only interested in the bands near the Fermi level, only the differences related to these bands among different stacking configurations will be discussed. There are band intersections for the two valence and conduction bands near the Fermi level for the A-2 and B-1. This corresponds to a stacking type with the alignment between In and Se atoms in the two different layers. In contrast, the A-1 and B-2 do not show the band intersections in their band structures. This corresponds to a stacking type with the alignment between two Se atoms in the two different layers. The B-3 stacking type has intermediate features compared to these two extreme cases. For example, the two valence bands near the Fermi level almost intersects after half of the Γ-**K** path.

This corresponds to a stacking type with the alignment between two In atoms in the two different layers. The distance is the smallest when two atoms in two different layers are aligned, thus the larger repulsion between two Se atoms leads to there being no band intersection in band structures for the A-1 and B-2.

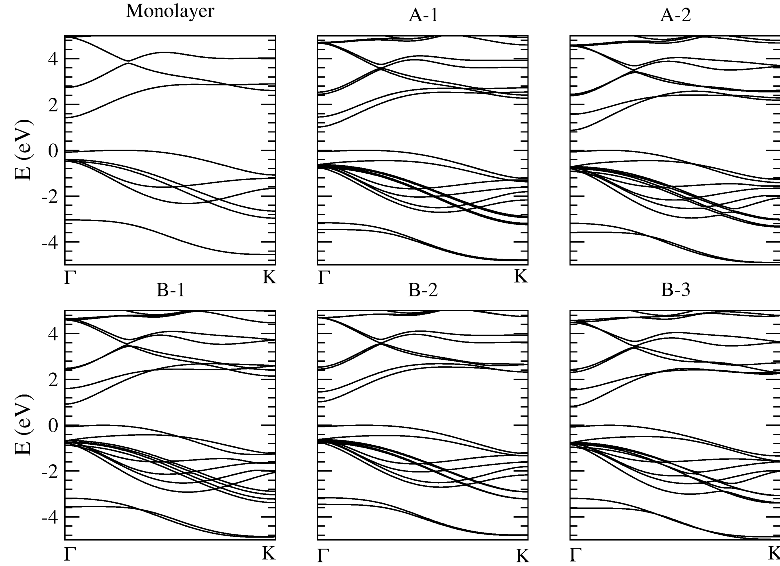

Figure 6.3: Band structures of InSe monolayer and InSe bilayers with different stacking configurations.

Figure 6.4 shows the projected band structures, while table 6.2 and table 6.3 show the PDOS of VBM and CBM at different kpoints for InSe monolayer. The orbital contributions are the same for the same type of atom in InSe monolayer due to the symmetry of the structure. The p_z orbitals (blue) of Se atoms predominate the VBM from Γ to 0.74 Γ-**K**. The p_z orbitals of In atoms predominate for the rest of the kpoint path. In addition, the *s* orbitals (black) of In atoms predominate the CBM. Previous studies have also shown similar projected band structures along Γ to **K**, however, without discussing the details along the path [205, 218]. The contributions from the p_z orbitals of Se atoms for the VBM and CBM decrease on approaching **K**. This leads to the separations between the two valence bands and between the two conduction bands near the Fermi level decrease as approaching toward **K** (figure 6.3). The contributions from p_z orbitals of Se atoms are zero at **K** in table 6.2. It is worth noting that the orbital contributions from p_x and p_y are equivalent due to the symmetry of the structure. The projected band structure of InSe bilayers with different stacking configurations are also displayed in figure 6.5. It looks similar to the projected band structure of InSe monolayer.

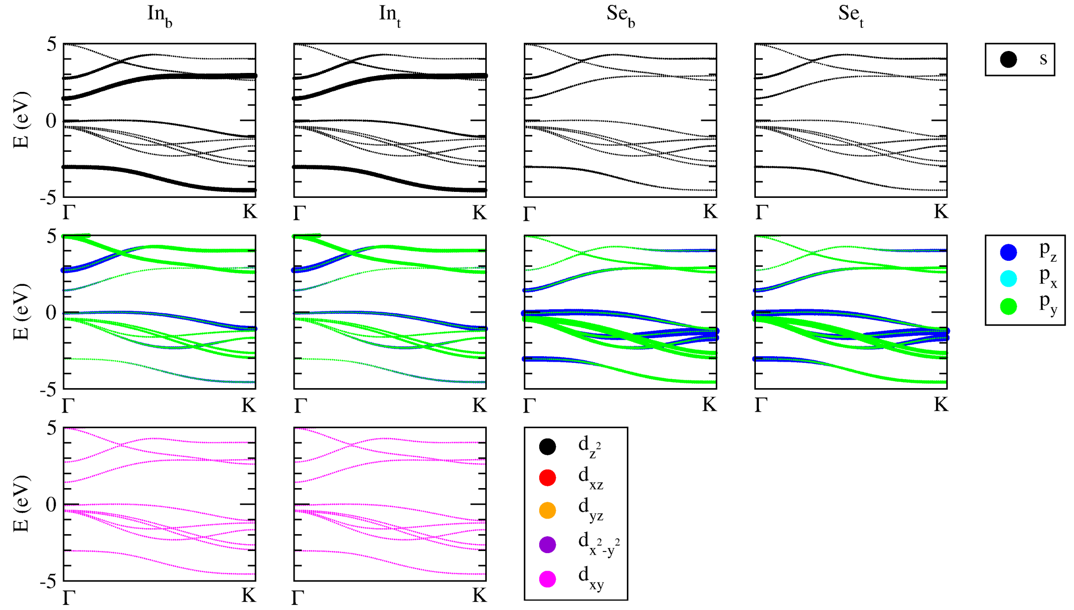

Figure 6.4: Projected band structures for InSe monolayer. In$_t$ and Se$_t$ refer to In and Se atoms in the top layer, respectively. In$_b$ and Se$_b$ refer to In and Se atoms in the bottom layer, respectively.

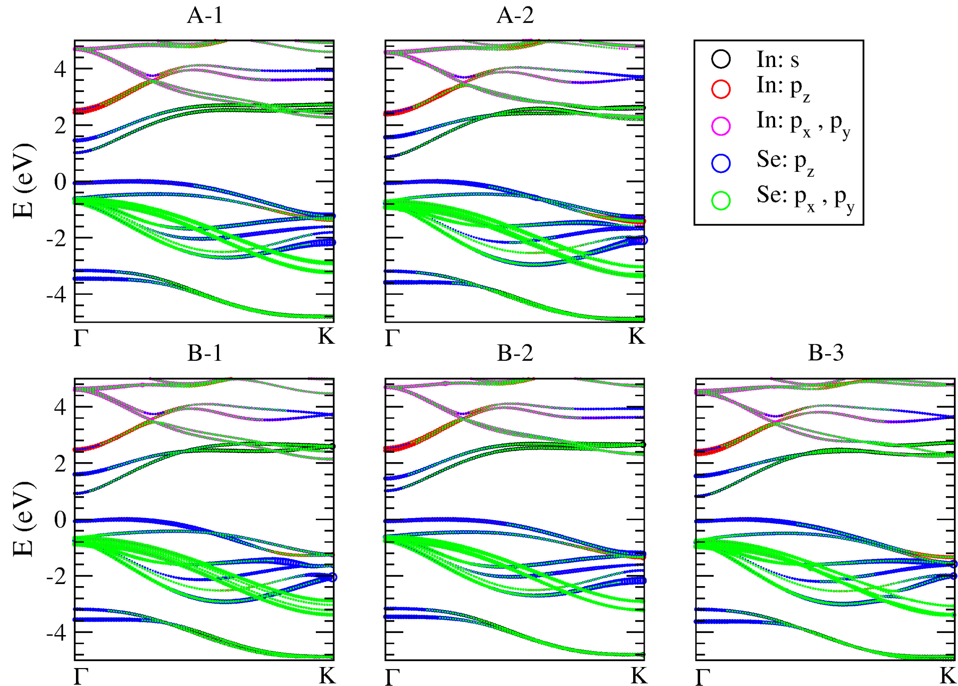

Figure 6.5: Projected band structures for InSe bilayers with different stacking configurations. Black, red and magenta refer to the s, p_z and p_y (or p_x) orbitals of In atoms, whereas blue and green refer to the p_z, p_y (or p_x) orbitals of Se atoms.

K-length	In	Se
Γ	s: 0.048, p_z: 0.062, d_{z^2}: 0.003	p_z: 0.375
0.1	s: 0.040, p_z: 0.077, d_{z^2}: 0.003	p_z:0.344, p_x: 0.012, p_y: 0.012
0.2	s: 0.035, p_z: 0.097, d_{z^2}: 0.003	s: 0.001, p_z: 0.329, p_x: 0.013, p_y: 0.013
0.3	s: 0.035, p_z: 0.110, d_{z^2}: 0.003	s: 0.002, p_z: 0.317, p_x: 0.013, p_y: 0.013
0.4	s: 0.036, p_z: 0.121, d_{z^2}: 0.002	s: 0.003, p_z: 0.298, p_x: 0.016, p_y: 0.016
0.5	s: 0.039, p_z: 0.131, p_x: 0.003, p_y: 0.003, d_{z^2}: 0.002	s: 0.004, p_z: 0.268, p_x: 0.022, p_y: 0.022
0.6	s: 0.042, p_z: 0.143, p_x: 0.006, p_y: 0.006, d_{z^2}: 0.002	s: 0.005, p_z: 0.230, p_x: 0.031, p_y: 0.031
0.7	s: 0.045, p_z: 0.160, p_x: 0.009, p_y: 0.009, d_{z^2}: 0.001	s: 0.006, p_z: 0.186, p_x: 0.040, p_y: 0.040
0.8	s: 0.049, p_z: 0.188, p_x: 0.010, p_y: 0.010, d_{z^2}: 0.001	s: 0.005, p_z: 0.131, p_x: 0.052, p_y: 0.052
0.9	s: 0.057, p_z: 0.236, p_x: 0.005, p_y: 0.005, d_{z^2}: 0.001	s: 0.002, p_z: 0.053, p_x: 0.069, p_y: 0.069
K	s: 0.064, p_z: 0.271, d_{z^2}: 0.001	p_x: 0.081, p_y: 0.081

Table 6.2: Projected density of states (PDOS) for the VBM in InSe monolayer at different kpoints along Γ to **K**.

The contributions from p_z orbitals of each Se atom for the VBM in InSe bilayers with different stacking configurations are shown in figure 6.6, where each Se atom is shown according to its vertical position (from Se_{tt} to Se_{bb}). This can also be classified into two groups: these are group I for the A-1 and B-2 and group II for the A-2 and B-1. The B-3 is similar to both groups if not considering the fluctuation around the band-crossing kpoint in the A-2 and B-1 as well as the rapid rise in the A-1 and B-2. This classification is consistent with the classification according to the band intersection discussed above. The curve of Se_{tt} (black) is the same as Se_{bb} (blue), whereas the curve of Se_{bt} (red) is the same as Se_{tb} (green) for the A-1, B-2 and B-3. The changes of p_z orbitals along Γ to **K** are different for the outermost

K-length	In	Se
Γ	s: 0.196, p_z: 0.049	s: 0.043, p_z: 0.193
0.1	s: 0.191, p_z: 0.038, p_x: 0.002, p_y: 0.002	s: 0.037, p_z: 0.172, p_x: 0.019, p_y: 0.019
0.2	s: 0.194, p_z: 0.022, p_x: 0.005, p_y: 0.005	s: 0.029, p_z: 0.147, p_x: 0.040, p_y: 0.040
0.3	s: 0.208, p_z: 0.009, p_x: 0.006, p_y: 0.006	s: 0.021, p_z: 0.129, p_x: 0.052, p_y: 0.052
0.4	s: 0.229, p_z: 0.002, p_x: 0.004, p_y: 0.004	s: 0.014, p_z: 0.110, p_x: 0.062, p_y: 0.062
0.5	s: 0.249, p_x: 0.001, p_y: 0.001	s: 0.007, p_z: 0.086, p_x: 0.072, p_y: 0.072
0.6	s: 0.262, p_z: 0.002	s: 0.003, p_z: 0.059, p_x: 0.080, p_y: 0.080
0.7	s: 0.271, p_z: 0.006	s: 0.001, p_z: 0.034, p_x: 0.086, p_y: 0.086
0.8	s: 0.278, p_z: 0.011	p_z: 0.015, p_x: 0.089, p_y: 0.089
0.9	s: 0.283, p_z: 0.015	p_z: 0.003, p_x: 0.091, p_y: 0.091
K	s: 0.285, p_z: 0.016	p_x: 0.091, p_y: 0.091

Table 6.3: Projected density of states (PDOS) for the CBM in InSe monolayer at different kpoints along Γ to **K**.

(Se_{tt} (black) and Se_{bb} (blue)) and the innermost (Se_{bt} (red) and Se_{tb} (green)) Se atoms. The contributions from p_z orbitals of the innermost Se atoms are larger than the outermost Se atoms except near the Γ and **K** points. The contributions from p_z orbitals of one of the innermost Se atoms are also smaller than one of the outermost Se atoms around the band intersection for the VBM in the group II. Basically, the contributions from p_z orbitals of the outermost Se atoms decrease as approaching toward **K**, similar to InSe monolayer. However, they are significantly different from InSe monolayer around **K** in the group I. The contributions from p_z orbitals are zero for the VBM at **K** for InSe monolayer, however, they rise rapidly for the cases in the group I. This is due to the interband coupling between the two bands just below the VBM (denoted as VBM-1 and VBM-2) around **K** as we can see these two bands have close energies around **K** in figure 6.3. Thus, the contributions from p_z orbitals for the VBM are then affected due to its interlayer coupling with the VBM-1. It is seen that the contributions from p_z orbitals for the VBM-1 and VBM-2 are approaching zero as approaching toward **K** for the cases in the group I (not shown), whereas they are about 0.4 for InSe monolayer at **K**. This is also true for the B-1

but only related to the interband coupling between the VBM and VBM-1 (figure 6.3), which are contributed by Se atoms in the bottom InSe layer (Se_{tb} and Se_{bb}) (figure 6.6).

Furthermore, the contributions from p_z orbitals of the innermost Se atoms increase to around 0.3 Γ-**K** and 0.4 Γ-**K**, then further decrease as approaching **K** in the group I and (the group II and B-3), respectively. There are abrupt increase and decrease in the orbital contributions from p_z of Se atoms in the bottom and the top InSe layers around the band intersection of the two valence bands near the Fermi level in the A-2, respectively. This phenomenon can also be seen in the B-1, however, the abrupt increase and decrease in the contributions from p_z orbitals in the bottom and the top InSe layers are opposite to the A-2. The B-3 has a similar curve to the group I and group II without the abrupt increase and decrease in the contributions from p_z orbitals around **K** and band intersection. It is worth noting that the abrupt increase and decrease in the contributions from p_z orbitals of Se atoms for the VBM are opposite to the contributions from p_z orbitals of In atoms for the VBM and the contributions from p_z orbitals of Se atoms for the VBM-1. This is as expected, the two valence bands which originate from the two VBMs of the two InSe monolayers couple to each other around the band intersection. It is suggested that the ordering of interaction between the atoms in the two different layers is Se-Se (group I) $>$ Se-In (group II) $>$ In-In (B-3). It is worth noting that the contribution from p_z orbitals of each Se atom changes more rapidly for InSe bilayers with a smaller interlayer distance due to the larger interaction.

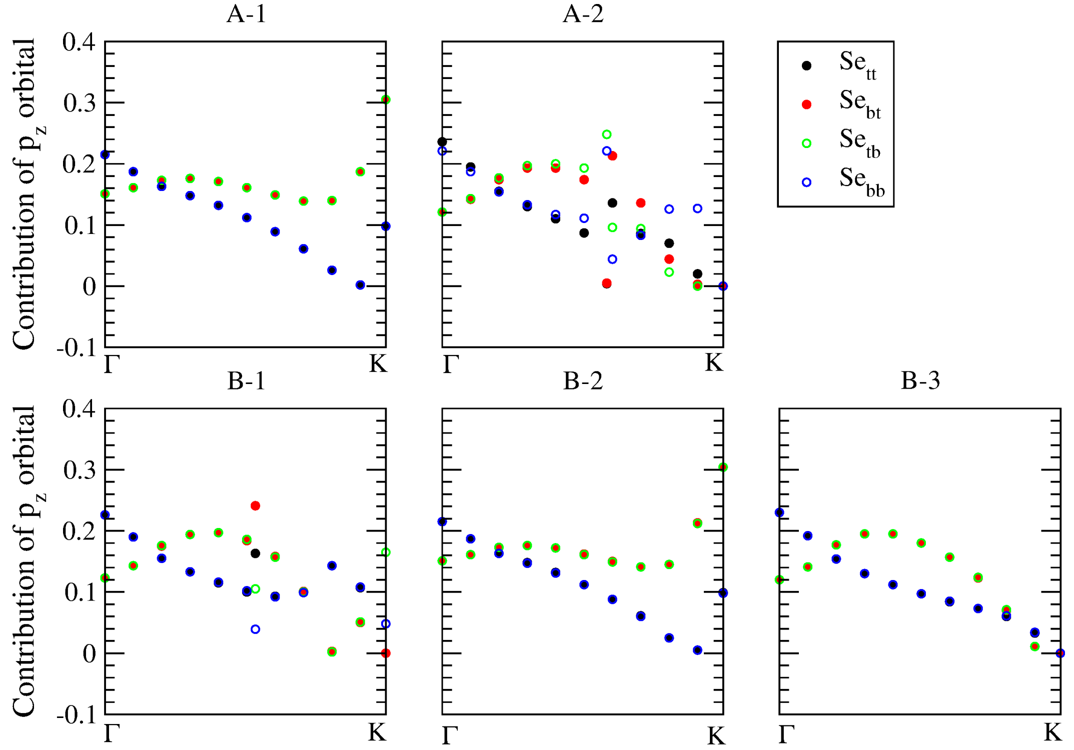

Figure 6.6: The contribution from p_z orbitals of each Se atom for the VBM in InSe bilayers with different stacking configurations.

Furthermore, figure 6.7 shows the band structure of InSe monolayer with the twist angle changes from 0° to 50°. It seems like the VBM and VBM-1 are not affected significantly by the twist angle from Γ to the highest energy point of the VBM although the variations of other bands with the twist angles are larger. Since we are only interested in the band parameters which are related to the bands near the Fermi level, it is suggested that the band gap (the energy difference between the CBM at Γ and the highest energy point of the VBM) and effective mass for holes (inversely proportional to the curvature of the VBM at the highest energy point) approximately remain at a constant with the twist angle.

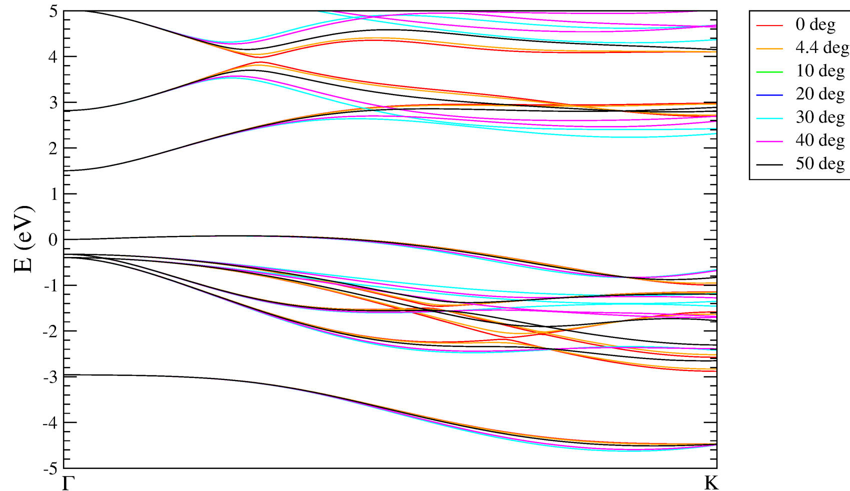

Figure 6.7: Band structures of InSe monolayer with different twist angles (0°, 4.4^o, 10°, 20°, 30°, 40° and 50°) along Γ to **K** of an untwisted (0°) InSe monolayer.

6.3.2 Residual force in twisted InSe bilayer

After the discussion of InSe monolayer and bilayers within primitive cell through traditional DFT, we focus on the twisted InSe bilayers within large supercell calculated by using LS-DFT in this section.

The out-of-plane corrugation originates from the different regions of twisted InSe bilayer corresponding to the different stacking configurations (figure 6.2) with different interlayer distances (table 6.1). The following equation defines the averaged corrugation based on the previous literature [78],

$$\text{Averaged corrugation} = \frac{1}{4}\sum_{n=1}^{4}|d^n - d|, \tag{6.7}$$

where d^n is the averaged interlayer distance calculated from each sublayer (two In and two Se sublayers) in the top layer to the same sublayer in the bottom layer when considering out-of-plane corrugation and d is the optimised interlayer distance without considering out-of-plane corrugation. Figure 6.8 shows the total energy as a function of interlayer distance (without considering the out-of-plane corrugation) and the total energy as a function of the averaged corrugation for the A-type twisted InSe bilayer (twist angle = 4.4^o). Without the out-of-plane corrugation, the optimised interlayer distance is 8.89 Å. For corrugation of $\sim$ 0.1 Å, the lowest total energy is at d = 8.88 Å and d = 8.89 Å, whereas a corrugation of $\sim$ 0.3 Å corresponds to the lowest total energy at d = 9.05 Å and d = 9.25 Å. It is suggested that the out-of-plane corrugation is small ($\simeq$ 0.1 Å) around the optimised interlayer

distance, whereas the corrugation is larger not at the optimised interlayer distance.

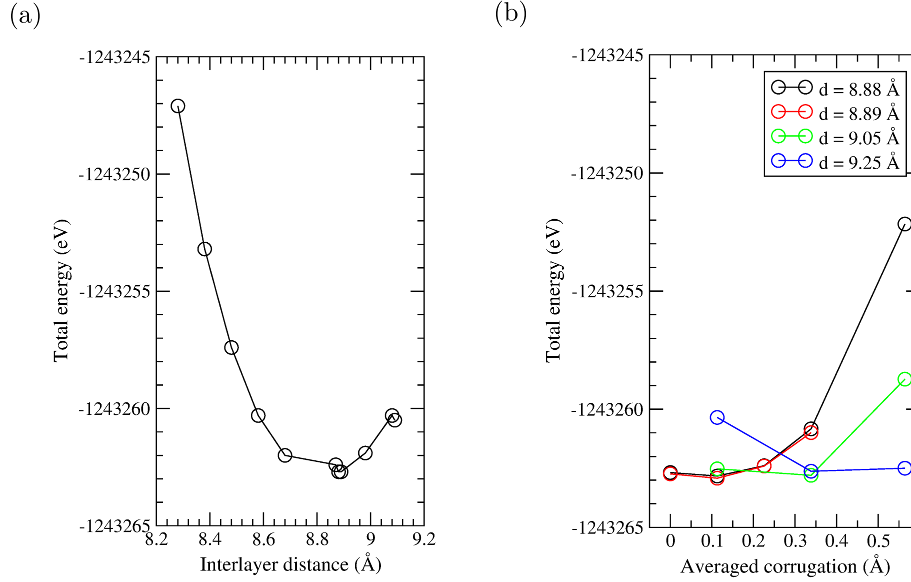

Figure 6.8: Total energy as a function of (a) interlayer distance without considering the out-of-plane corrugation (b) averaged corrugation for the A-type twisted InSe bilayer ($\theta = 4.4^{\circ}$).

To reduce the computational cost and time in the calculations of the structural relaxation for the large-scale twisted InSe bilayer system, an initial z position of each atom was approximately set for smaller twist angles according to the interlayer distances of the InSe bilayers with different stacking configurations (see table 6.1) and considering a corrugation $\sim$ 0.1 Å (figure 6.8(b)). The generation of the relevant atomic structure is based on the FFT and the resulting z positions of atoms are then shifted by the negative and positive corrugation values for the top and bottom InSe layers, respectively. The distribution of the corrugation of each atom with considering the interlayer distance in each region is shown in figure 6.9. The interlayer distances with considering the corrugation are larger around the corners of the supercell where correspond to the A-1 and smaller around the central region of the supercell where correspond to the A-2 (figure 6.2(a)).

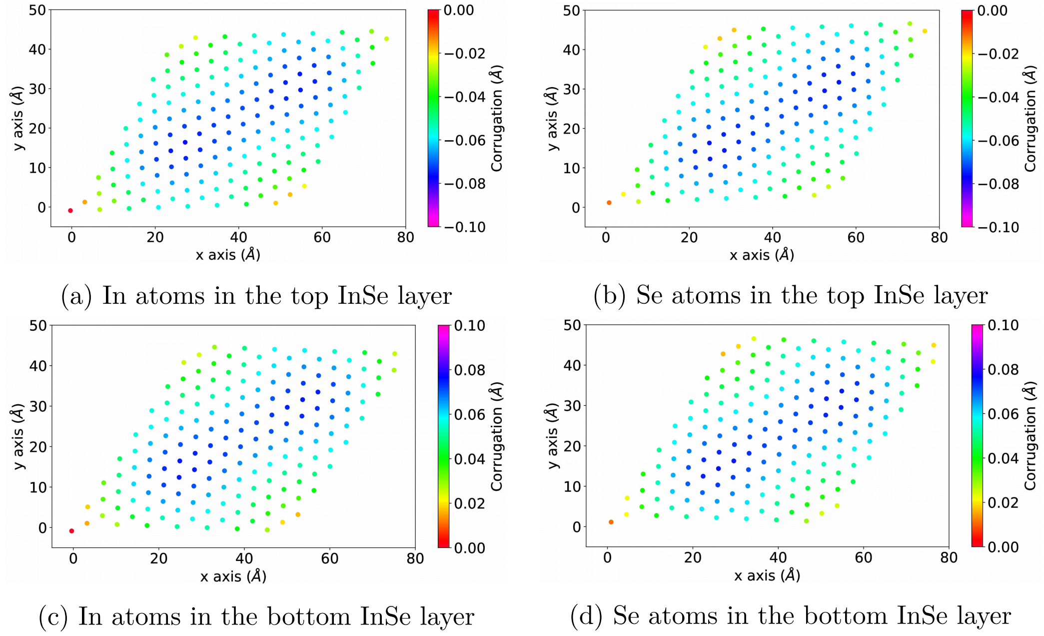

(a) In atoms in the top InSe layer

(b) Se atoms in the top InSe layer

(c) In atoms in the bottom InSe layer

(d) Se atoms in the bottom InSe layer

Figure 6.9: Distribution of the corrugation of each atom with considering the inter-layer distance in each region for the A-type twisted InSe bilayer ($\theta = 4.4^{o}$). The x and y axes refer to the atomic position in x and y direction.

Due to the high computational effort of doing geometry optimisation in this large-scale system, there are residual forces (within the convergence tolerance) after the geometry optimisation. The study of residual force can tell us the direction of the genuine movements of atoms if the atomic structure is fully relaxed. The distribution of the residual total force for the atomic structure when considering the averaged corrugation ($\simeq$ 0.1 Å) (see figure 6.8(b)) is shown in figure 6.10. Before the structural relaxation, the bottom Se atoms in the top layer (Se_{bt}) and the top Se atoms in the bottom layer (Se_{tb}) show distributions of the residual total force similar to the distribution of the corrugation of each atom (figure 6.9) in figure 6.10(b) and (d). After the structural relaxation, similar distributions of the residual total force can be seen in figure 6.10(f) and (h), however, the magnitudes of residual total forces become smaller. In addition, In atoms (In_{bt} and In_{tb}) also show distributions of the residual total force similar to the adjacent Se atoms (Se_{bt} and Se_{tb}) in figure 6.10(e) and (g). This is not seen in the distribution of the residual total force of In atoms before the structural relaxation in figure 6.10(a) and (c). This phenomenon is also not seen for the outermost In (In_{tt} and In_{bb}) and Se atoms (Se_{tt} and Se_{bb}). The outermost atoms have smaller residual forces than the innermost atoms because the interactions between the innermost atoms are larger owing to the smaller distances of innermost atoms between two InSe layers. This may also be the

reason why innermost Se atoms have larger residual force than innermost In atoms. It is suggested this is an intrinsic phenomenon in twisted bilayer system.

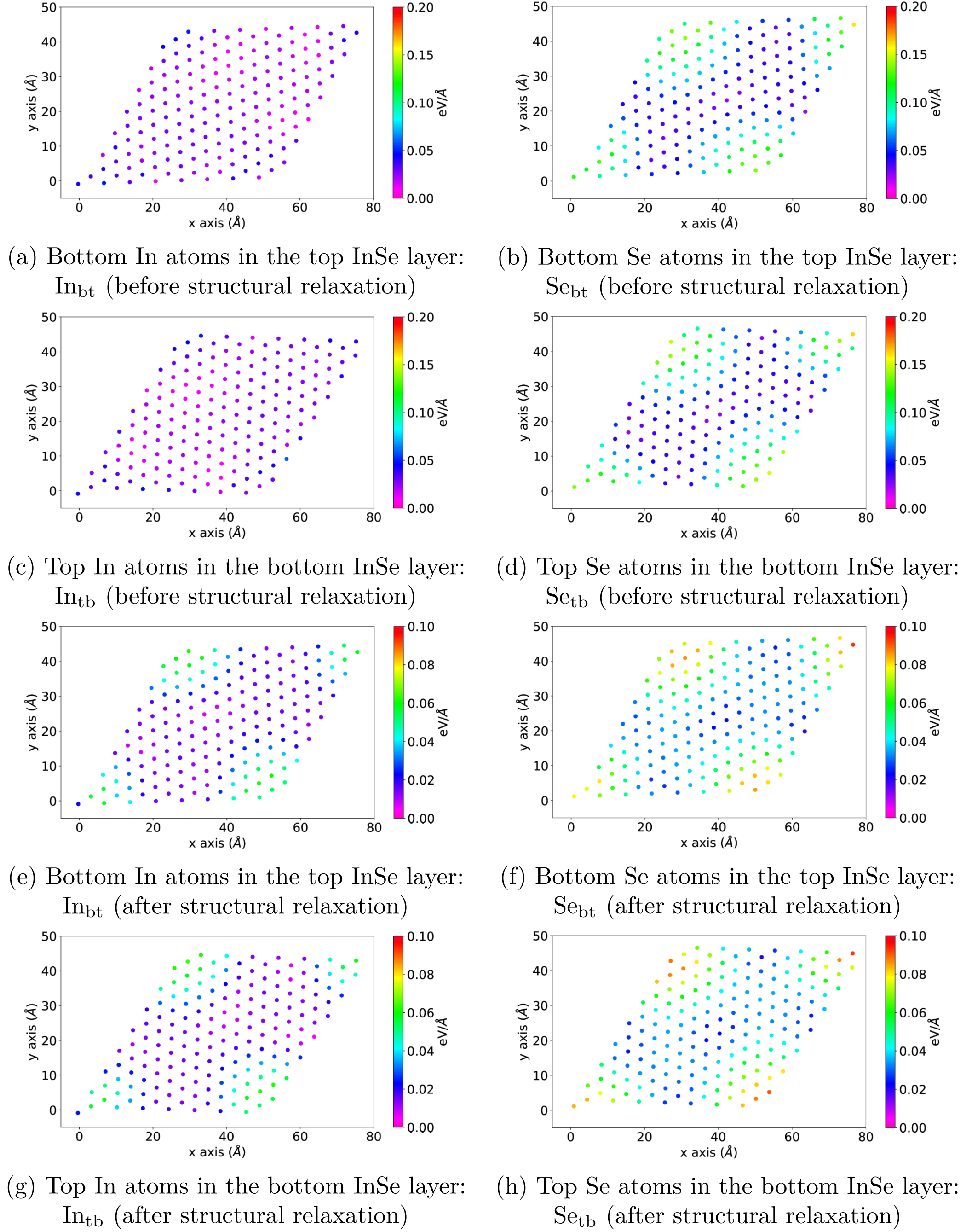

(a) Bottom In atoms in the top InSe layer: In_{bt} (before structural relaxation)

(b) Bottom Se atoms in the top InSe layer: Se_{bt} (before structural relaxation)

(c) Top In atoms in the bottom InSe layer: In_{tb} (before structural relaxation)

(d) Top Se atoms in the bottom InSe layer: Se_{tb} (before structural relaxation)

(e) Bottom In atoms in the top InSe layer: In_{bt} (after structural relaxation)

(f) Bottom Se atoms in the top InSe layer: Se_{bt} (after structural relaxation)

(g) Top In atoms in the bottom InSe layer: In_{tb} (after structural relaxation)

(h) Top Se atoms in the bottom InSe layer: Se_{tb} (after structural relaxation)

Figure 6.10: Distribution of the residual total force for the A-type twisted InSe bilayer ($\theta = 4.4^{o}$, $d = 8.89$ Å , corrugation $\simeq 0.1$ Å). (a)-(d) Before the structural relaxation (e)-(h) After the structural relaxation. The x and y axes refer to the atomic position in x and y direction.

The distribution of the residual force along the z direction is similar to the residual total force. The z directions of the residual forces are opposite in the top and the bottom layers (comparing figure 6.11(a) with (c) or figure 6.11(b) with (d)). The residual forces for In atoms (figure 6.11(a) and (c)) are smaller than the adjacent Se atoms (figure 6.11(b) and (d)). The distribution of the residual force in xy plane (figure 6.11(e)-(h)) is also similar to the residual total force. By comparing the magnitudes of residual forces in figure 6.11(a)-(d) with figure 6.11(e)-(h), it shows that the residual total forces are predominated by the residual forces along the z direction, which means the atoms mainly rearrange their vertical position when forming a twisted bilayer with (at least) the similar length scale of the moiré pattern. The atoms in the top and bottom InSe layers also display opposite directions of the residual forces along x and y directions. Although the distributions of the residual forces along x and y directions are not obvious for In atoms because the residual forces are small, the distributions are still approximately consistent with the distribution of the residual force for the adjacent Se atoms. Overall, this tells us that the residual forces in the top and the bottom InSe layers for all directions are just in reverse.

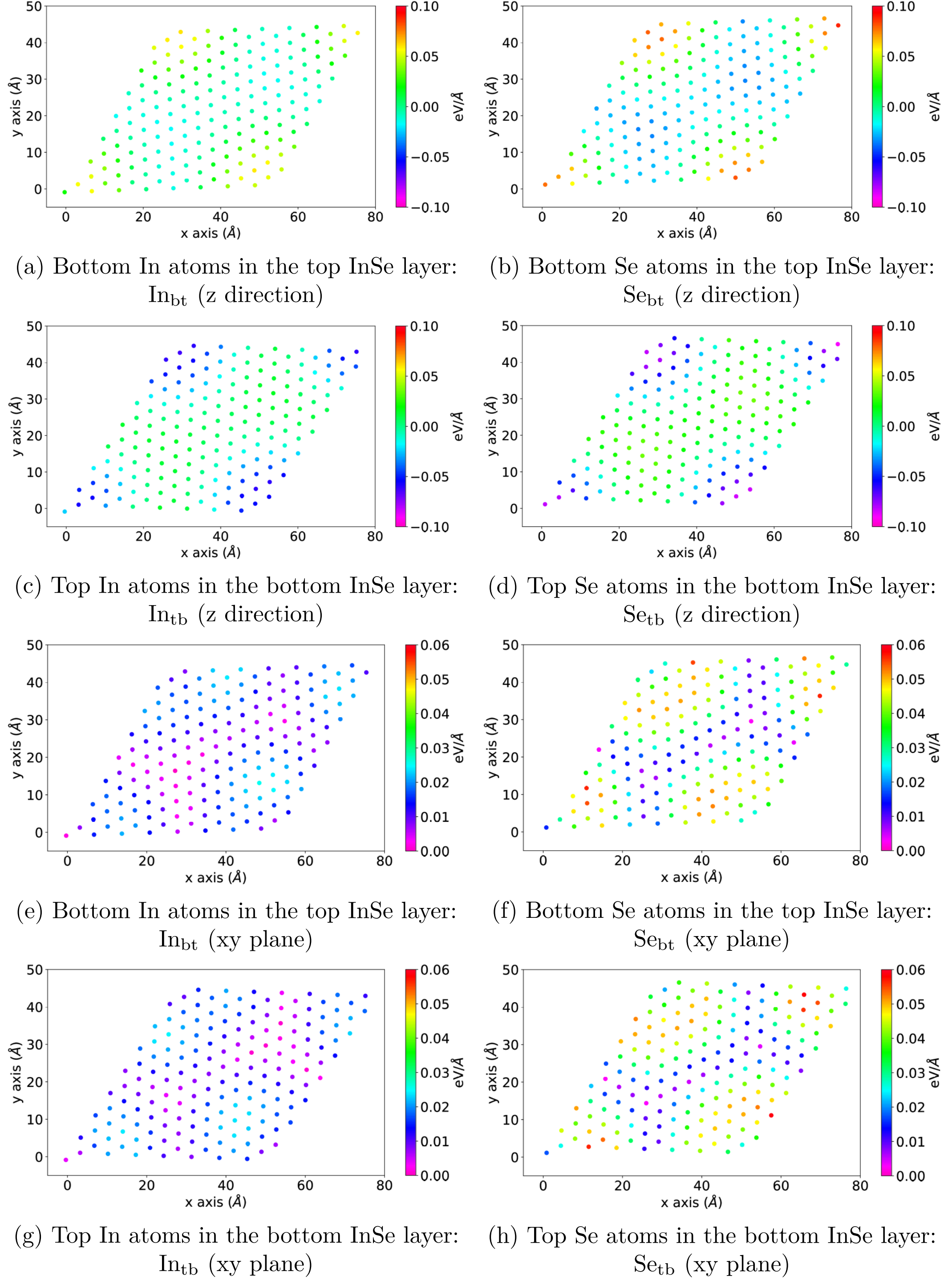

(a) Bottom In atoms in the top InSe layer: In_{bt} (z direction)

(b) Bottom Se atoms in the top InSe layer: Se_{bt} (z direction)

(c) Top In atoms in the bottom InSe layer: In_{tb} (z direction)

(d) Top Se atoms in the bottom InSe layer: Se_{tb} (z direction)

(e) Bottom In atoms in the top InSe layer: In_{bt} (xy plane)

(f) Bottom Se atoms in the top InSe layer: Se_{bt} (xy plane)

(g) Top In atoms in the bottom InSe layer: In_{tb} (xy plane)

(h) Top Se atoms in the bottom InSe layer: Se_{tb} (xy plane)

Figure 6.11: Distribution of the residual force for the A-type twisted InSe bilayer ($\theta = 4.4^{o}$, $d = 8.89$ Å, corrugation $\simeq 0.1$ Å) after the structural relaxation. (a)-(d) Residual forces along z direction (e)-(h) Residual forces in xy plane. The x and y axes refer to the atomic position in x and y direction.

6.3.3 Electronic structure of twisted InSe bilayer

The effective band structure of InSe monolayer, the A-type twisted InSe bilayer and the A-type InSe/hBN/InSe heterostructure are shown in figure 6.12. In figure 6.12(a), InSe monolayer possesses an indirect band gap, where the VBM is at a kpoint between Γ and **K**, whereas the CBM is located at Γ. The spin-orbit coupling (SOC) does not alter significantly the VBM and CBM: the VBM splits near **K** and the CBM splits from intermediate kpoint path to **K** (compare figure 6.12(a) with (b)). This can also be seen in the A-type twisted InSe bilayer (compare figure 6.12(c) with (d)). Thus, the band gap and effective mass for holes are not affected significantly by the spin-orbit coupling. It is worth noting that the SOC leads to the crossing of bands around 4 eV for all structures, whereas it is an avoided crossing of bands for the structures without considering SOC. From the comparison of the effective band structures between considering and without considering SOC, this convinces us that the effective band structure without considering SOC (with less computational effort) is sufficient to provide the information of the electronic properties such as band gap and effective mass for holes of InSe bilayers with different twist angles. It is still an indirect band gap in the A-type twisted InSe bilayer and twisted InSe/hBN/InSe heterostructure. The number of bands in twisted InSe bilayer is as twice as in InSe monolayer. The VBM and VBM-1 merges after intermediate kpoint path (figure 6.12(c)), different from the band structures of the A-1 and A-2 (figure 6.3). The similar effective band structure of the B-type twisted InSe bilayers with different twist angles can be seen in figure 6.13.

The purpose of putting the hBN layer into the twisted InSe bilayer is to flatten the VBM for getting larger effective mass for holes. When the hBN layer is used as a spacer layer between the layers of the A-type twisted InSe bilayer, many neighbouring bands approach each other. For example, the separation between the VBM and VBM-1 becomes smaller (figure 6.12(e)). The twist angle between InSe and hBN has no significant effect on the effective band structure, backing up a previous study which has shown that the band structure is not affected by the stacking arrangement between InSe and hBN layers [219]. The curvature of the VBM in twisted InSe bilayer changes when the hBN layer is encapsulated, thus leading to the changes in the effective mass for holes. Furthermore, there are band anti-crossings near **K** for the valence bands in an energy range between -2.0 eV and -1.0 eV.

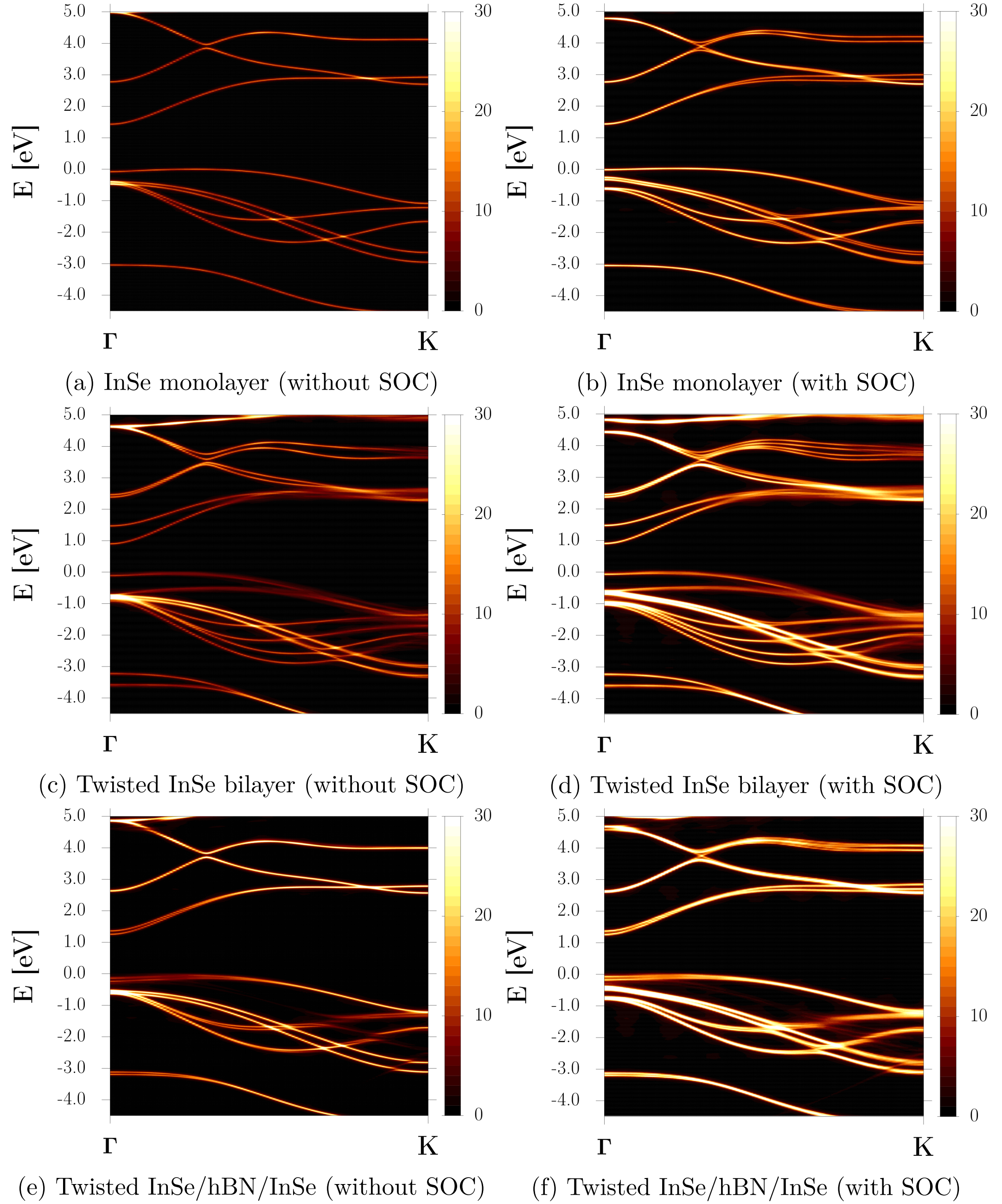

(a) InSe monolayer (without SOC) (b) InSe monolayer (with SOC)

(c) Twisted InSe bilayer (without SOC) (d) Twisted InSe bilayer (with SOC)

(e) Twisted InSe/hBN/InSe (without SOC) (f) Twisted InSe/hBN/InSe (with SOC)

Figure 6.12: Effective band structure along Γ to **K** of (a) InSe monolayer (without SOC) (b) InSe monolayer (with SOC) (c) A-type twisted InSe bilayer (without SOC) (d) A-type twisted InSe bilayer (with SOC) (e) A-type twisted InSe/hBN/InSe heterostructure (without SOC) (f) A-type twisted InSe/hBN/InSe heterostructure (with SOC). A Lorentzian broadening of 0.02 eV was employed in the effective band structures.

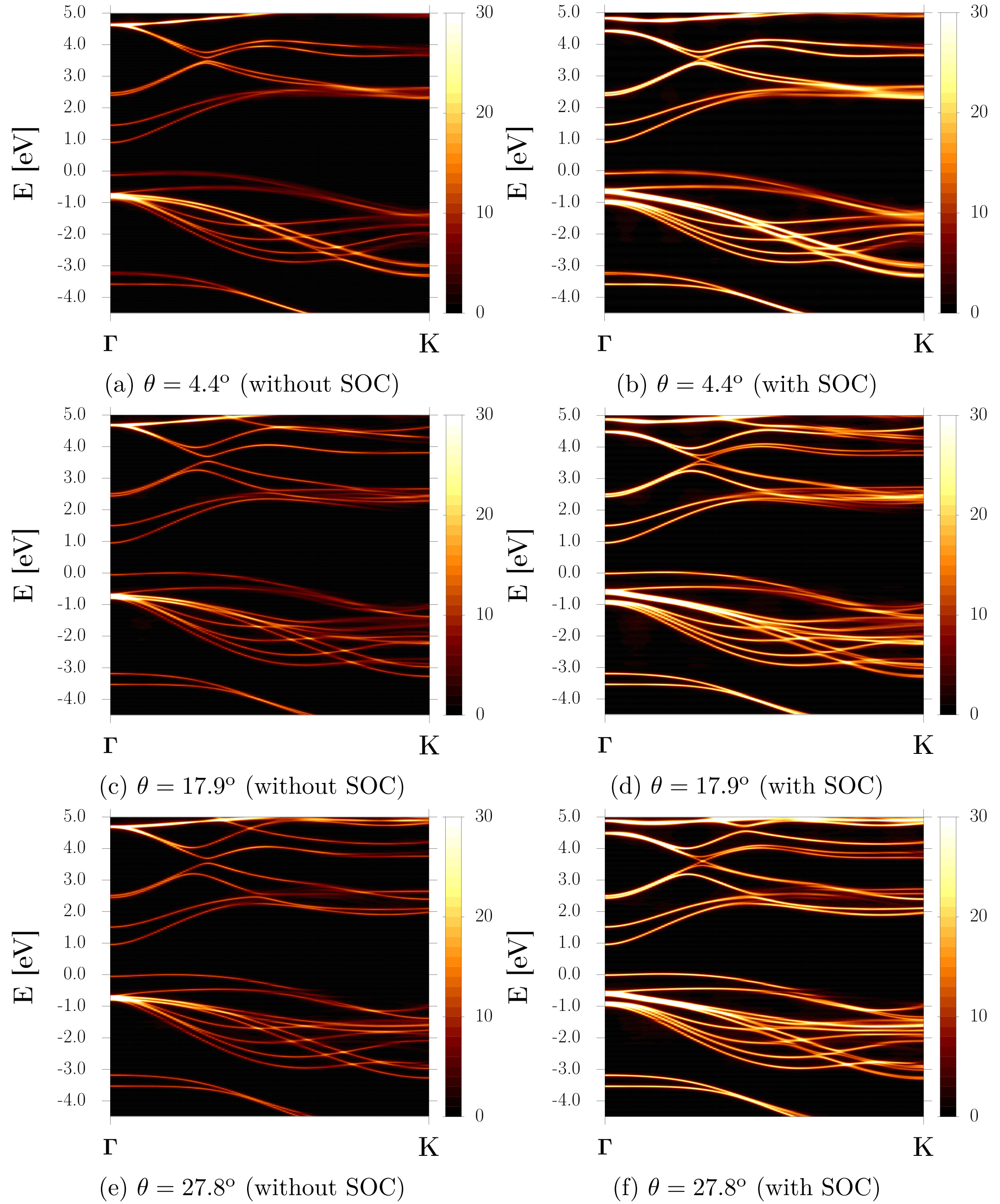

(a) $\theta = 4.4^{o}$ (without SOC)

(b) $\theta = 4.4^{o}$ (with SOC)

(c) $\theta = 17.9^{o}$ (without SOC)

(d) $\theta = 17.9^{o}$ (with SOC)

(e) $\theta = 27.8^{o}$ (without SOC)

(f) $\theta = 27.8^{o}$ (with SOC)

Figure 6.13: Effective band structure along Γ to **K** of the B-type twisted InSe bilayer with a twist angle of (a) 4.4^{o} (without SOC) (b) 4.4^{o} (with SOC) (c) 17.9^{o} (without SOC) (d) 17.9^{o} (with SOC) (e) 27.8^{o} (without SOC) (f) 27.8^{o} (with SOC). A Lorentzian broadening of 0.02 eV was employed in the effective band structures.

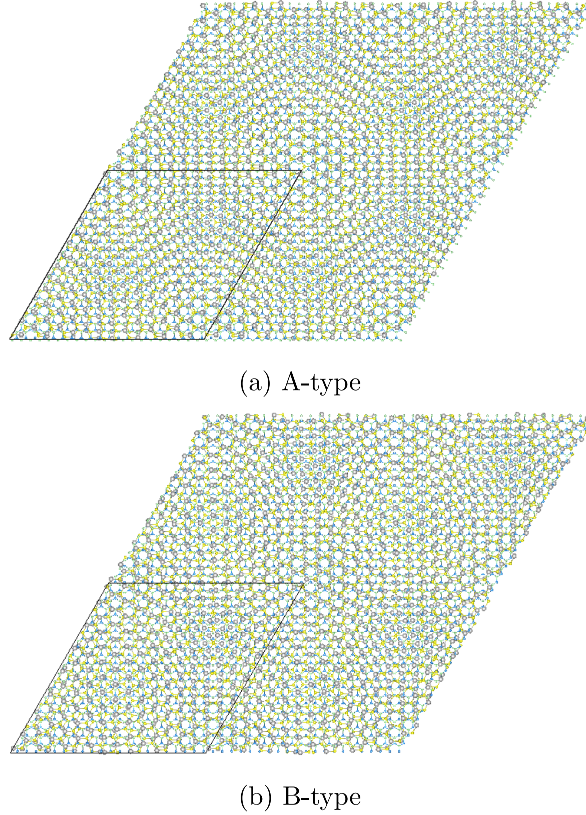

(a) A-type

(b) B-type

Figure 6.14: Top view of the (a) A-type (b) B-type twisted InSe/hBN/InSe heterostructure with a twist angle of $\theta = 4.4^{\text{o}}$. $\phi = 32.2^{\text{o}}$ is the twist angle between InSe and hBN layers. Grey: In, yellow: Se, blue: B and green: N. The moiré pattern can be clearly seen when repeating the unit cell.

In the hBN-encapsulated twisted InSe bilayer (figure 6.14), the valence bands contributed by the hBN layer are more than 1.5 eV below the Fermi level (shifted to be the highest energy of the VBM) (see figure 6.15(a)). This can also be seen in figure 6.15(b), where the largest orbital contributions (p_{z}) for the valence bands are from nitrogen at about 1.5 eV below the Fermi level. Thus, the hBN layer is regarded as a spacer to decrease the interlayer coupling between two InSe layers (separate these two InSe layers). This is similar to the BP/hBN/BP heterostructure in a previous study [220]. Therefore, the effective band structure of this heterostructure is roughly regarded as the superposition of the effective band structure of two InSe monolayers. Although the avoided band-crossings within an energy range between -2.0 eV and -1.0 eV are induced by the hBN, the near-band-edge states are not affected because these anti-crossing bands are far away from these states.

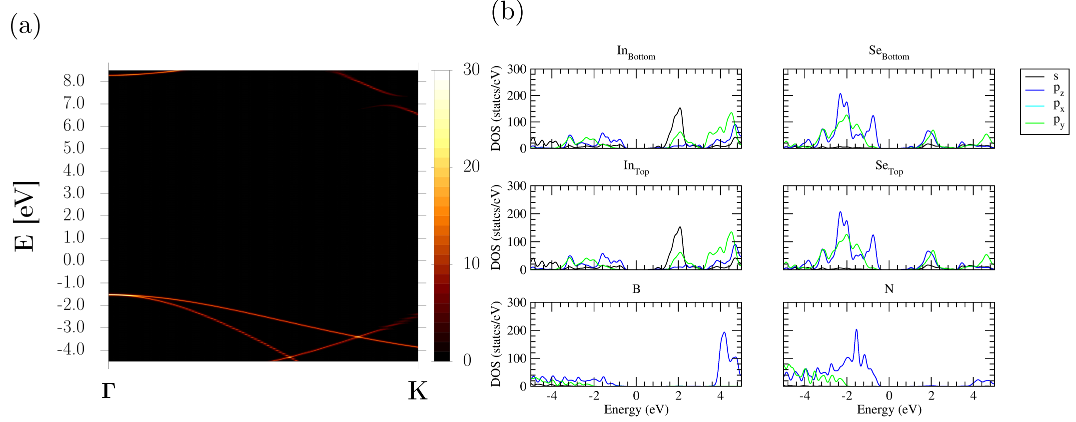

Figure 6.15: (a) Effective band structure along Γ to **K** of the A-type twisted InSe/hBN/InSe heterostructure with a twist angle of 4.4° projected on the hBN layer. A Lorentzian broadening of 0.02 eV was employed in the effective band structures. (b) Projected density of states of the A-type twisted InSe/hBN/InSe heterostructure. In_{Bottom} and In_{Top} refer to In atoms in the bottom and the top InSe layers, respectively. Se_{Bottom} and Se_{Top} refer to Se atoms in the bottom and the top InSe layers, respectively. SOC was not included in the calculations.

In figure 6.16, the corrugation only enlarges slightly the separation between two adjacent bands, such as the VBM and VBM-1. Therefore, the band structure does not change obviously when considering the corrugation (similar to $MoTe_2/MoS_2$ heterostructure in [221]). Previous studies about twisted hBN bilayer [198] has also shown that the appearance of flat bands are not affected by structural relaxation. The band structure of the twisted InSe bilayer is mainly influenced by the interlayer distance (or the stacking configuration). The comparison of the band structure between two different interlayer distances can also be seen in [217]. In this work, the interlayer distance of twisted InSe bilayer varies as the twist angle varies. Its value is expected to be between the largest and the smallest interlayer distance of the same type of stacking configuration (A or B types). For example, the interlayer distance of the B-type twisted InSe bilayer is between 8.389 (B-3) and 9.178 (B-2) in this work (table 6.1).

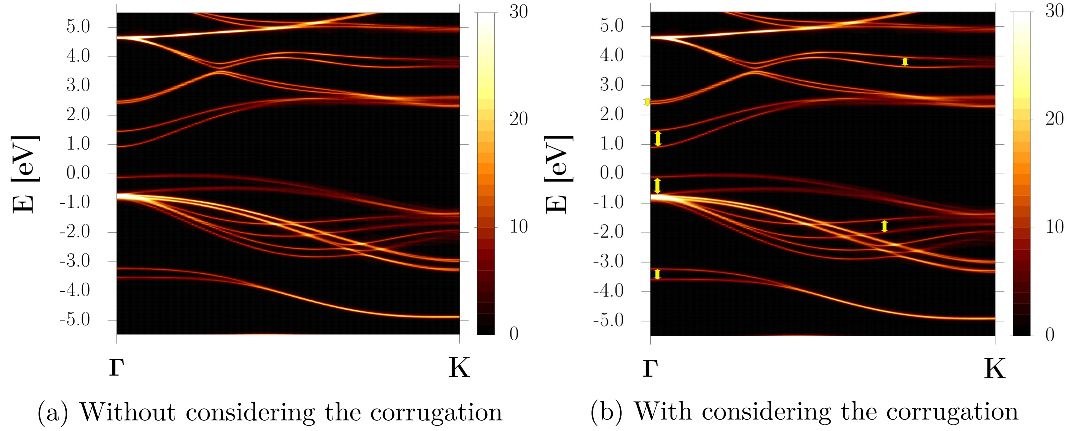

(a) Without considering the corrugation

(b) With considering the corrugation

Figure 6.16: Effective band structure of the A-type twisted InSe bilayer ($\theta = 4.4^{o}$) (a) without (b) with considering the corrugation. A Lorentzian broadening of 0.02 eV was employed in the effective band structures. Some increases of the separations between neighbouring bands are indicated by the double-headed arrows. SOC was not included in the band structure calculations.

In addition, the projection of the effective band structure on the top and the bottom InSe layers for the A-type twisted InSe bilayer ($\theta = 4.4^{o}$) without spin-orbit coupling are shown in figure 6.17(a) and (b). Similar effective band structures for the A-type twisted InSe/hBN/InSe heterostructure ($\theta = 4.4^{o}$) without spin-orbit coupling are also shown in figure 6.17(e) and (f). The effective band structures projected on the bottom layer look very similar to the projection on the top layer for both structures. However, the difference becomes larger at a larger twist angle, such as in figure 6.17(c) and (d) for $\theta = 17.9^{o}$. Similar arguments apply to the B-type twisted InSe bilayers in figure 6.18.

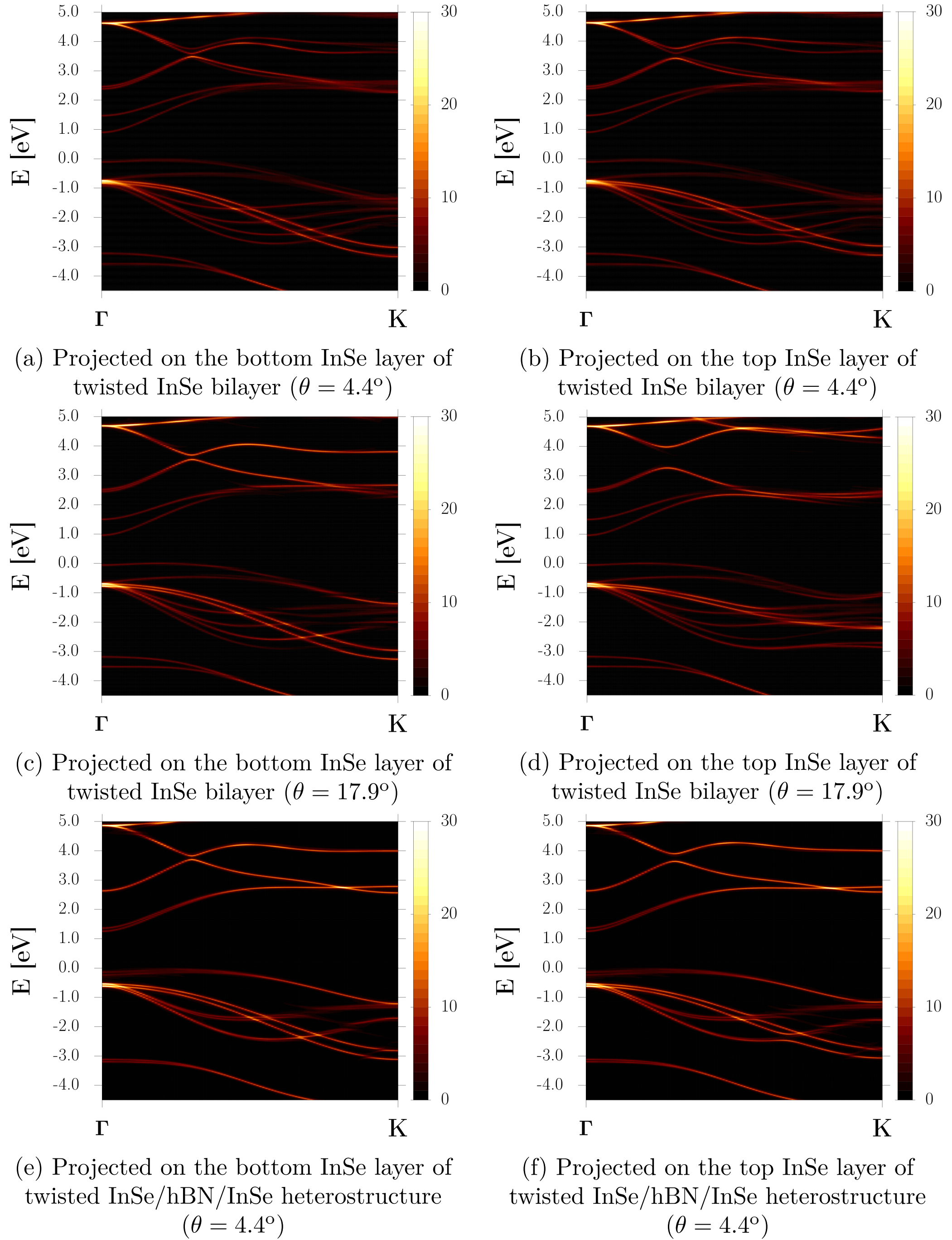

(a) Projected on the bottom InSe layer of twisted InSe bilayer ($\theta = 4.4^o$)

(b) Projected on the top InSe layer of twisted InSe bilayer ($\theta = 4.4^o$)

(c) Projected on the bottom InSe layer of twisted InSe bilayer ($\theta = 17.9^o$)

(d) Projected on the top InSe layer of twisted InSe bilayer ($\theta = 17.9^o$)

(e) Projected on the bottom InSe layer of twisted InSe/hBN/InSe heterostructure ($\theta = 4.4^o$)

(f) Projected on the top InSe layer of twisted InSe/hBN/InSe heterostructure ($\theta = 4.4^o$)

Figure 6.17: Effective band structure along Γ to $\mathbf{K}$ of the A-type twisted InSe bilayer projected on the (a)(c) bottom (b)(d) top InSe layer with a twist angle of (a)(b) $\theta = 4.4^o$ (c)(d) $\theta = 17.9^o$. Effective band structure of the A-type twisted InSe/hBN/InSe heterostructure projected on the (e) bottom (f) top InSe layer with a twist angle of $\theta = 4.4^o$. A Lorentzian broadening of 0.02 eV was employed in the effective band structures. SOC was not included in the band structure calculations.

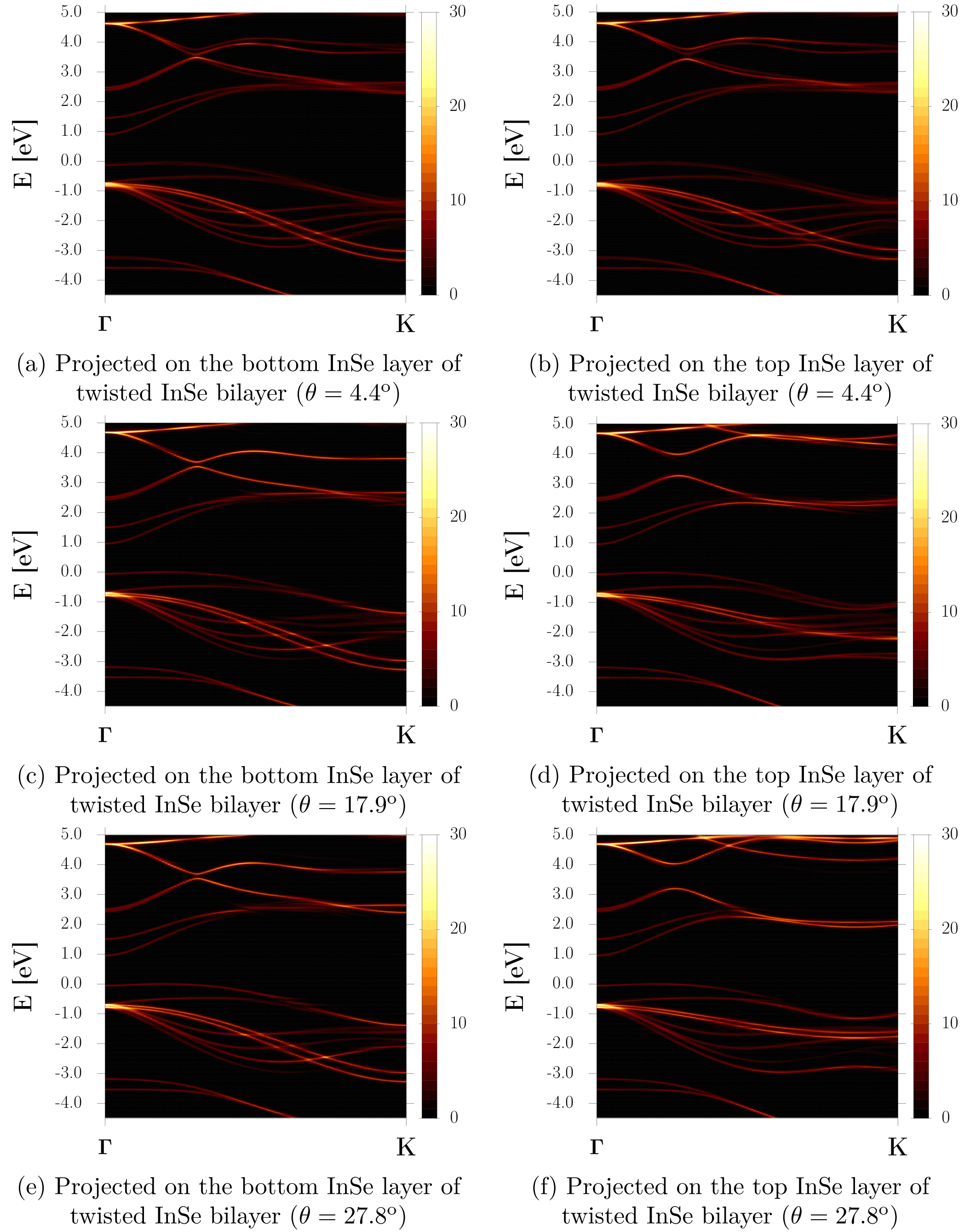

(a) Projected on the bottom InSe layer of twisted InSe bilayer ($\theta = 4.4^o$)

(b) Projected on the top InSe layer of twisted InSe bilayer ($\theta = 4.4^o$)

(c) Projected on the bottom InSe layer of twisted InSe bilayer ($\theta = 17.9^o$)

(d) Projected on the top InSe layer of twisted InSe bilayer ($\theta = 17.9^o$)

(e) Projected on the bottom InSe layer of twisted InSe bilayer ($\theta = 27.8^o$)

(f) Projected on the top InSe layer of twisted InSe bilayer ($\theta = 27.8^o$)

Figure 6.18: Effective band structure along Γ to **K** of the B-type twisted InSe bilayer projected on the (a)(c)(e) bottom (b)(d)(f) top InSe layer with a twist angle of (a)(b) $\theta = 4.4^o$ (c)(d) $\theta = 17.9^o$ (e)(f) $\theta = 27.8^o$. A Lorentzian broadening of 0.02 eV was employed in the effective band structures. SOC was not included in the band structure calculations.

The observation of the appearances of different stacking configurations in some regions of twisted InSe bilayer motivates us to study the effects of these stacking configurations on the electronic structure of twisted InSe bilayer. In figure 6.19(a), the effective band structure of twisted InSe bilayer with a twist angle of 4.4^{o} is shown, superimposed by the bands of the A-1 (green curves) and A-2 (blue curves) calculated by Quantum Espresso within the primitive cell with the same interlayer distance as twisted InSe bilayer. The two superimposed curves match well with the bands in the effective band structure. A similarly close mapping can be seen when including SOC in the band structure calculation in figure 6.19(b). Figure 6.19(c) and (d) show the localisations of the charge densities corresponding to the A-1 and A-2 in some regions of twisted InSe bilayer without including SOC. The combination of A-1 and A-2 also contribute the VBM, based on the analysis of the isosurfaces of the charge densities. Similar results can be seen in figure 6.20 for the A-type and B-type twisted InSe bilayers with different twist angles. The localisation of charge density obtained here is slightly different from twisted hBN bilayer in [198] (with similar stacking configurations to InSe bilayer) and twisted InSe bilayer in the work of Kang et al [78] with smaller twist angles, where the charge density was seen to be localised in the A-1 and A-2 regions for the VBM, respectively. The unfolded VBM in the effective band structure within primitive cell in this work has finite width and the contribution originate from both the A-1 and A-2. The localisation of the charge density for the VBM is possibly contributed by the A-2 as in [78] if further decreasing the twist angles.

The bands from both layers along the same kpoint path within the primitive cell calculated by Quantum Espresso need to be considered to describe well the effective band structure of twisted InSe bilayer (figure 6.20(c)-(f)) because the difference of the effective band structure between the bottom and top InSe layers becomes obvious at larger twist angles. It is seen that the length from Γ to the lowest energy point of the VBM in figure 6.20(d) is 0.886× for $\theta = 17.9^{o}$ (0.867× for $\theta = 27.8^{o}$ in figure 6.20(f)) of the whole kpoint path, consistent with the ratio of the kpoint path of the top InSe layer to the bottom InSe layer in the first Brillouin zone. Similar ratio can also be seen in the band structure of the InSe monolayer with different twist angles in figure 6.7. In addition, the effective band structure of the A-type twisted system looks similar to the B-type twisted system at the same twist angle in figure 6.20, indicating the insensitivity of the band structure to the system considered. This may be due to the similarity of band structure between A-1 and B-2, as well as the band structure between A-2 and B-1 (figure 6.3). Similar phenomenon can be seen in [222].

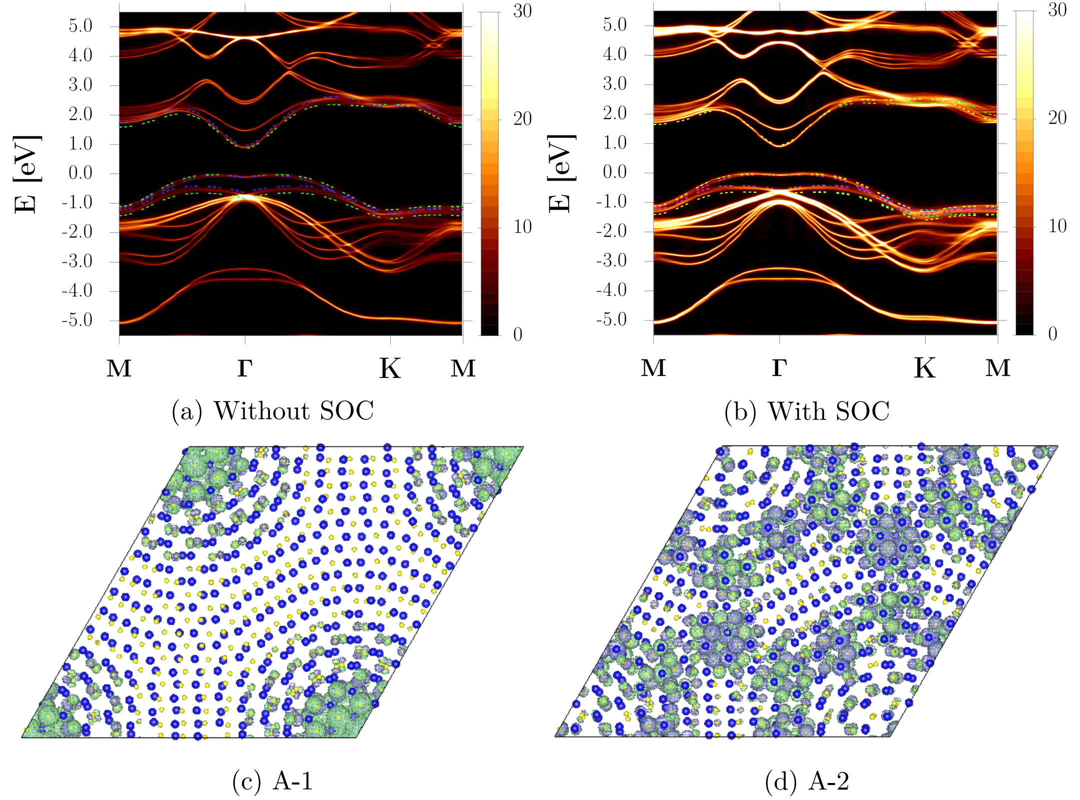

(a) Without SOC (b) With SOC

(c) A-1 (d) A-2

Figure 6.19: (a) Effective band structure along Γ to **K** of the A-type twisted InSe bilayer with a twist angle of 4.4°. (a) Without SOC (b) With SOC. The green and yellow curves refer to the two different spin states for the same band in the A-1, whereas the blue and pink curves refer to the two different spin states for the same band in the A-2. These bands were all calculated by Quantum Espresso in the primitive cells with the same interlayer distance as twisted InSe bilayer. A Lorentzian broadening of 0.02 eV was employed in the effective band structures. Isosurface of the charge density corresponds to the (c) A-1 around an energy range of [-0.03, 0.00] eV (d) A-2 around an energy range of [-0.20, -0.17] eV without considering SOC. The charge densities were calculated via ONETEP by setting the parameter "homo_plot" to the number of bands below the Fermi level desired to plot.

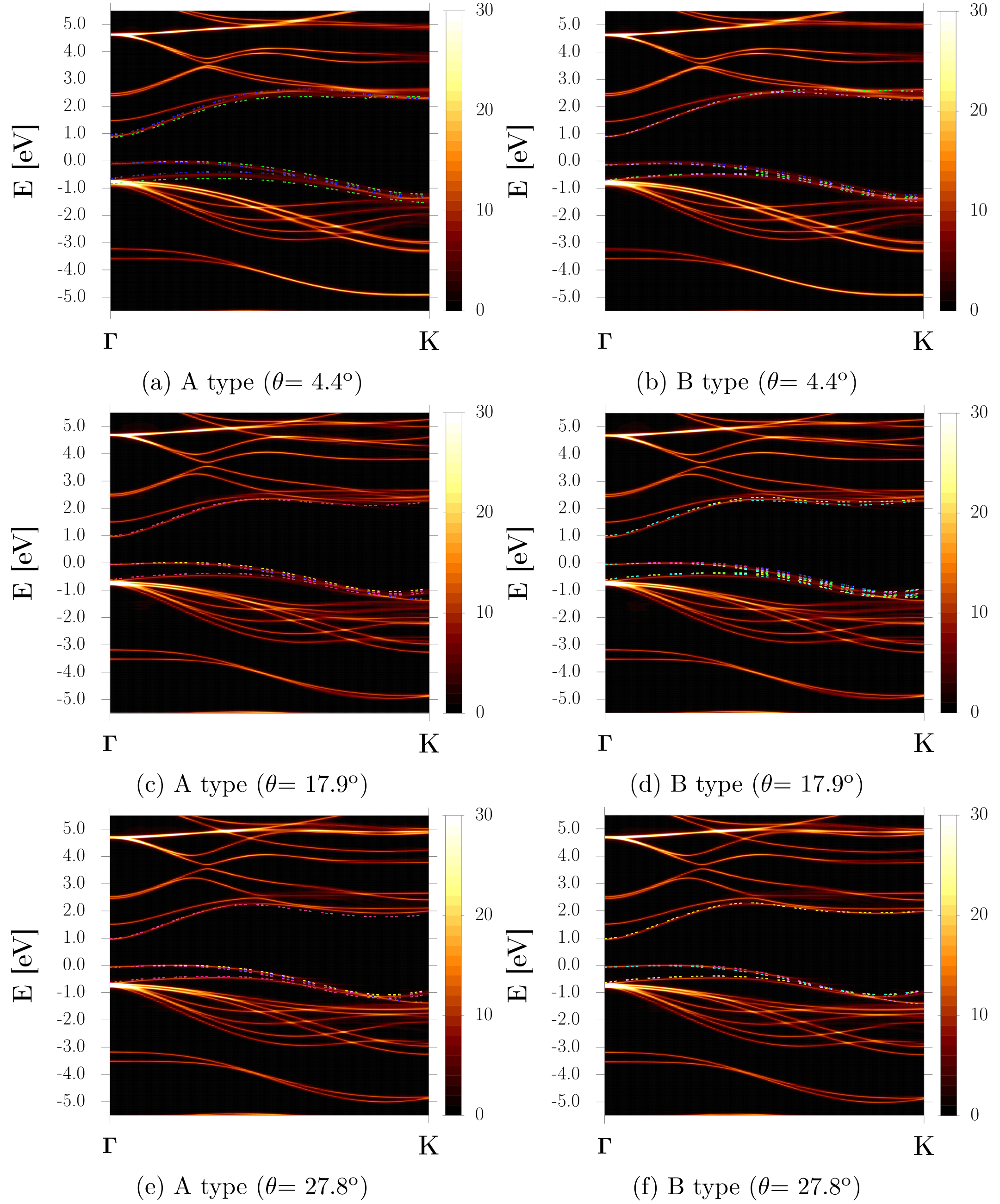

(a) A type (θ= 4.4°) (b) B type (θ= 4.4°)

(c) A type (θ= 17.9°) (d) B type (θ= 17.9°)

(e) A type (θ= 27.8°) (f) B type (θ= 27.8°)

Figure 6.20: Effective band structure along Γ to **K** of the A-type and B-type twisted InSe bilayers with different twist angles. (a) A type with θ= 4.4° (b) B type with θ= 4.4° (c) A type with θ= 17.9° (d) B type with θ= 17.9° (e) A type with θ= 27.8° (f) B type with θ=27.8°. Green (A-1 or B-1), blue (A-2 or B-2) and purple (B-3) curves are the bands corresponding to the bottom InSe layer, whereas yellow (A-1 or B-1), pink (A-2 or B-2) and cyan (B-3) are the bands corresponding to the top InSe layer. All these colour curves were calculated by Quantum Espresso in the primitive cells with the same interlayer distance as twisted InSe bilayers. A Lorentzian broadening of 0.02 eV was employed in the effective band structures. SOC was not included in the band structure calculations.

Although the lattice constant of InSe monolayer (a = 4.059 Å) was used as the lattice constant of twisted InSe bilayer, it does not affect significantly the bands of InSe bilayer if a stacking configuration deviates from this lattice constant (figure 6.21(a)). Figure 6.21(b) shows that the effective mass for holes becomes larger (the VBM becomes flatter) with a larger interlayer distance (red curves) for InSe bilayer with different stacking configurations. It is worth noting that the separation between the VBM and VBM-1 with a larger interlayer distance is smaller due to the repulsion between these two bands being weaker for a larger interlayer distance.

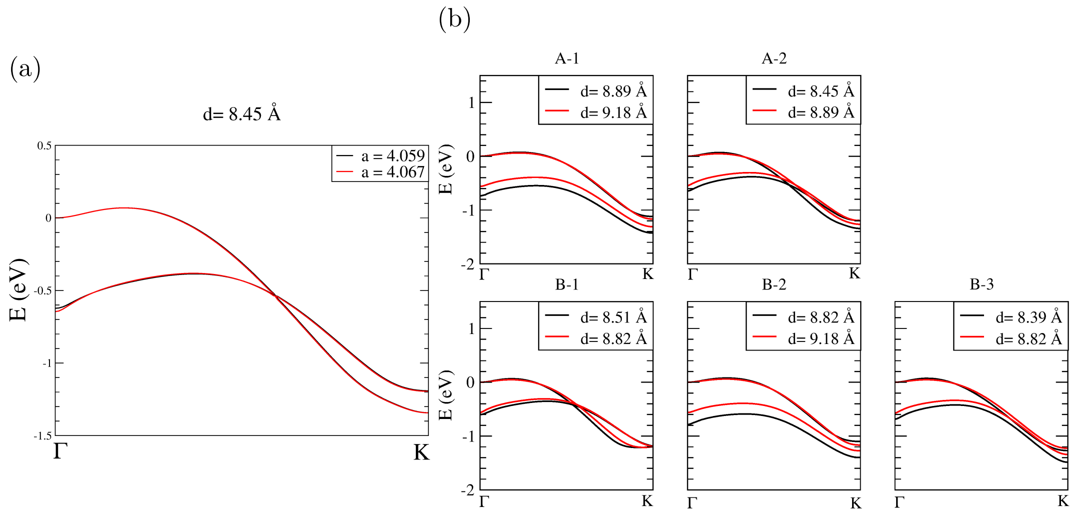

Figure 6.21: (a) Topmost valence band and the band below it along Γ to **K** for the A-2 at two different lattice constants. Black: 4.059 Å (lattice constant of InSe monolayer and twisted InSe bilayer), red: 4.067 Å (lattice constant of the A-2). (b) Topmost valence band and the band below it for InSe bilayers with different stacking configurations at two different interlayer distances. 8.89 Å and 8.82 Å are the optimised interlayer distances (without considering the corrugation) for the A-type and B-type twisted InSe bilayers with a twist angle of 4.4°, respectively. Another interlayer distance in each stacking configuration is the optimised interlayer distance of InSe bilayer with each stacking configuration (see table 6.1).

The bands of InSe monolayer calculated by Quantum Espresso within the primitive cell can also be used to describe the effective band structure of both the A-type and B-type twisted InSe/hBN/InSe heterostructures (figure 6.22).

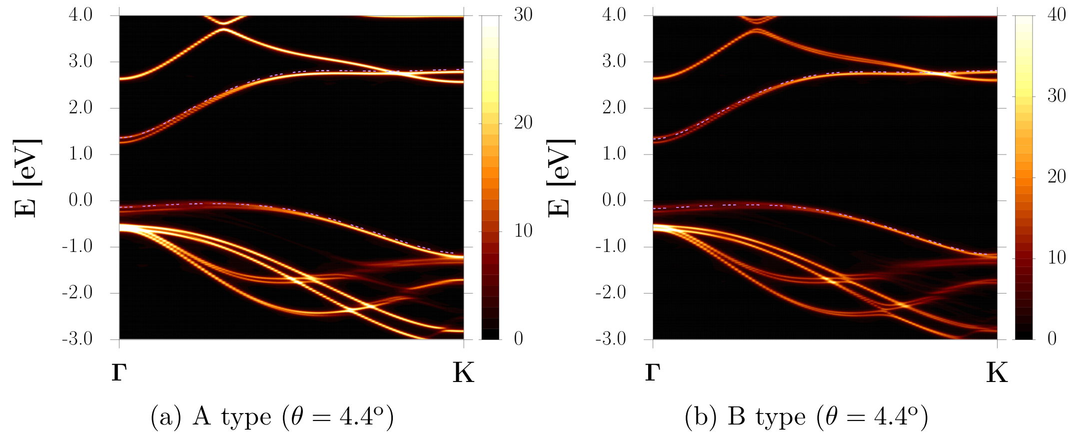

(a) A type ($\theta = 4.4^o$) (b) B type ($\theta = 4.4^o$)

Figure 6.22: Effective band structure along Γ to **K** of the (a) A-type (b) B-type InSe/hBN/InSe heterostructure with a twist angle of 4.4°. Bands of InSe monolayer calculated by Quantum Espresso in the primitive cells was shown in purple colours. A Lorentzian broadening of 0.02 eV was employed in the effective band structures.

Figure 6.23 shows the relation between the interlayer distance and twist angle for the A-type (black) and B-type (red) twisted InSe bilayer. Except for the twist angle of 4.4° with relatively large difference compared to other twist angles (but it is still small), the interlayer distances for the A-type twisted InSe bilayer with twist angles of 3.4°, 6°, 17.9° and 27.8° are similar (difference among these twist angles is not larger than 0.02 Å). The interlayer distance of the B-type twisted InSe bilayer with twist angles of 4.4°, 17.9° and 27.8° are also similar (difference among these twist angles is not larger than 0.02 Å). Overall, the interlayer distance is about 8.85 ± 0.04 Å when considering both types of twisted InSe bilayers with the twist angles considered in this work (a similar small difference of interlayer distance ($\leq$ 0.12 Å) among twist angles of 13.2°, 21.8° and 32.2° can be seen in [222]). It seems like the proportions of different stacking configurations corresponding to the regions in both the A-type and B-type twisted InSe bilayers roughly remain at a constant because the difference of interlayer distance among different twist angles is very small.

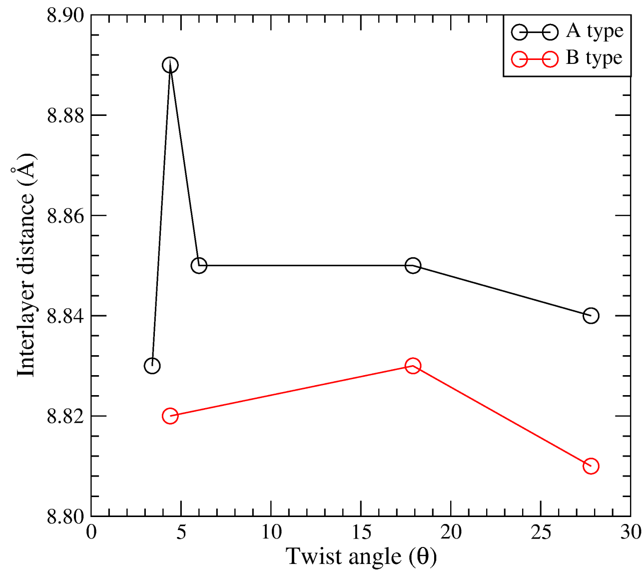

Figure 6.23: Interlayer distance as a function of twist angle for the A-type (black) and B-type (red) twisted InSe bilayers. Corrugation was not considered here.

Figure 6.24 shows the VBM and VBM-1 for InSe bilayer with different stacking configurations at different twist angles and interlayer distances. The difference of bands increases as the twist angle increases. The difference between bands corresponding to the bottom (solid curves) and top (dashed curves) InSe layers increases as the twist angle increases. There are concave curves near **K** for the top InSe layers in each stacking configuration. The flatness of the VBM is expected to increase as the twist angle decreases in the folding band structure of supercell, as it can be seen in [78]. This is not because the VBM changes with the twist angle, but rather because of the different band foldings with the twist angle (the first Brillouin zone decreases as the twist angle decreases); However, the effective mass for holes approximately remains at a constant ($1.57 \pm 0.18\ m_0$). The band gap also approximately remains at a constant for both A-type and B-type twisted InSe bilayers with different twist angles (0.95 ± 0.03 eV), consistent with the results in [222]. At sufficiently small twist angles (not the magic angles), the defect states within the energy range of band gap resulting from the localisation of charge densities in a particular stacking configuration, is suggested leading to the flat bands in a polar 2D semiconductor because their couplings with other electronic states are weak [198]. Naik et al. [223] have also proposed that the inhomogeneous interlayer hybridisation and the local strain cause the formation of ultraflat bands, from the study of twisted MoS_2 bilayer. All the origins mentioned above may lead to the appearance of flat bands in twisted InSe bilayer at sufficiently small twist angles.

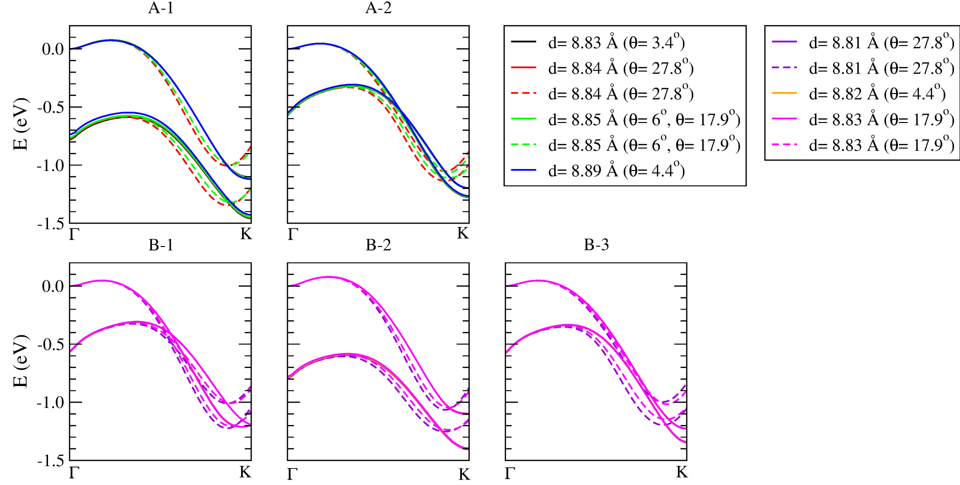

Figure 6.24: Topmost valence band and the band below it along Γ to **K** for InSe bilayers with different stacking configurations at different twist angles and interlayer distances. Solid and dashed curves refer to the bands for the bottom InSe layer and top InSe layer, respectively. The kpoint path (Γ to **K**) shown here is according to the kpoint path of the bottom InSe layer.

6.3.4 Exciton binding energy of twisted InSe bilayer and twisted InSe/hBN/InSe heterostructure

The exciton binding energy can be calculated by substituting the effective mass for holes obtained here to equations in [209, 210, 211] because it has been shown in the previous literature that the effective mass for holes obtained via GGA-PBE is sufficiently consistent with the GW calculation [224]. The intralayer and interlayer exciton binding energies are shown in table 6.4, table 6.5 and figure 6.25 for the environments of vacuum and hBN. The A1s intralayer exciton binding energy is $\sim$ 2.2-2.4X larger than interlayer exciton binding energy in the vacuum and hBN environments. The differences between intralayer and interlayer exciton binding energies decreases rapidly from A2s to A5s. The ratios of intralayer and interlayer exciton binding energies in the environment of vacuum to hBN for A1s to A5s are similar. For intralayer exciton binding energy, the ratios are [A1s = 3.7, A2s = 7.3, A3s = 10.0, A4s = 12.4, A5s = 14.6], whereas for the interlayer exciton binding energy, the ratios are [A1s = 3.4, A2s = 6.5, A3s = 9.3, A4s = 11.6, A5s = 13.7].

	A1s	A2s	A3s	A4s	A5s
Intralayer exciton (meV)	441.1±0.9	169.6±0.5	97.5±0.3	66.1±3.2	48.7±5.7
Interlayer exciton (meV)	183.2±0.1	110.1±0.2	73.4±0.2	52.8±1.7	40.4±4.1

Table 6.4: Intralayer and interlayer exciton binding energies of twisted InSe bilayer in the environment of vacuum. The parameter settings are effective mass for electrons $m_e = 0.16\ m_0$ from InSe bilayer in [224], screening length $r_* = 7.7 * \epsilon_{\text{hBN}} \simeq 38.9$ Å (where $\epsilon_{\text{hBN}} = \sqrt{\epsilon_\parallel * \epsilon_\perp} = \sqrt{6.9 * 3.7} \simeq 5.1$ [225]) [226, 227, 228], effective dielectric constant $\tilde{\epsilon} = \epsilon_{\text{vacuum}} = 1$. The effective mass for holes and interlayer distances obtained in this work are used, $m_h = [1.39, 1.75]\ m_0$ and $d = [8.81, 8.89]$ Å.

	A1s	A2s	A3s	A4s	A5s
Intralayer exciton (meV)	119.1±0.4	23.2±0.1	9.7±0.0	5.3±0.0	3.3±0.0
Interlayer exciton (meV)	54.5±0.1	16.8±0.1	7.9±0.0	4.6±0.0	3.0±0.0

Table 6.5: Intralayer and interlayer exciton binding energies of twisted InSe bilayer in the environment of hBN. The parameter settings are effective mass for electrons $m_e = 0.16\ m_0$ from InSe bilayer in [224], screening length $r_* = 7.7$ Å [226, 227, 228], effective dielectric constant $\tilde{\epsilon} = \epsilon_{\text{hBN}} = \sqrt{\epsilon_\parallel * \epsilon_\perp} = \sqrt{6.9 * 3.7} \simeq 5.1$ [225]. The effective mass for holes and interlayer distances obtained in this work are used, $m_h = [1.39, 1.75]\ m_0$ and $d = [8.81, 8.89]$ Å.

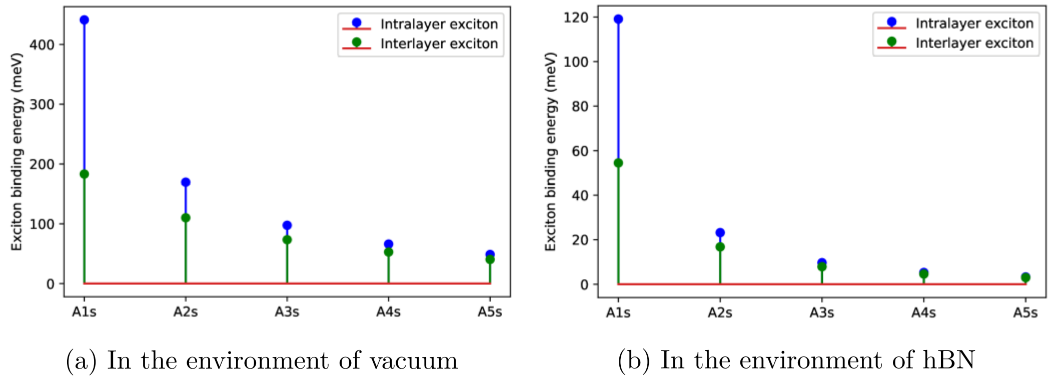

(a) In the environment of vacuum

(b) In the environment of hBN

Figure 6.25: Intralayer and interlayer exciton binding energies of twisted InSe bilayer in the environment of (a) vacuum corresponding to table 6.4 (b) hBN corresponding to table 6.5.

Similarly, the exciton binding energy for the twisted InSe/hBN/InSe heterostructure in the environments of vacuum and hBN are shown in table 6.6 with the effective mass for holes of InSe monolayer as input. Note that the Coulomb potential for calculating the intralayer exciton in monolayer form in [209, 210, 211] was used because the InSe layer can be regarded as monolayer form in this heterostructure. The ratios of intralayer exciton binding energy between the environments of vacuum and hBN are [A1s = 1.7, A2s = 2.2, A3s = 2.4, A4s = 2.5, A5s = 2.5].

	A1s	A2s	A3s	A4s	A5s
Intralayer exciton (meV) (vacuum)	232.9	60.9	27.4	15.5	9.9
Intralayer exciton (meV) (hBN)	138.8	27.8	11.5	6.2	3.9

Table 6.6: Intralayer exciton binding energies of twisted InSe/hBN/InSe heterostructure. The parameter settings are effective mass for electrons $m_{\mathrm{e}} = 0.18\, m_0$ from InSe monolayer in [224], screening length $r_* = 7.7{*}\epsilon_{\mathrm{hBN}}/\tilde{\epsilon} \simeq 12.86$ Å [225, 226, 227, 228], where $\epsilon_{\mathrm{hBN}} = \sqrt{\epsilon_{\parallel} * \epsilon_{\perp}} = \sqrt{6.9 * 3.7} \simeq 5.1$ [225], effective dielectric constant $\tilde{\epsilon} = (\epsilon_{\mathrm{vacuum}} + \epsilon_{\mathrm{hBN}})/2 = (1.0 + 5.1)/2 \simeq 3.0$ for the environment of vacuum and $\tilde{\epsilon} = \epsilon_{\mathrm{hBN}}$ for the environment of hBN. The effective mass for holes of InSe monolayer obtained in this work is used: $m_{\mathrm{h}} = 2.22\, m_0$.

6.4 Conclusions

In this chapter, the atomic and electronic structures of InSe bilayers with different stacking configurations and twisted InSe bilayer were studied. For InSe bilayer with different stacking configurations, there is a trend shows that the binding energy and band gap decreases, whereas the effective mass for holes generally decreases, as the interlayer distance decreases. The VBM and CBM of InSe monolayer are predominated by the p_{z} orbitals of Se atoms and s orbitals of In atoms, respectively. The orbital contributions in InSe bilayer are not exactly the same as InSe monolayer. The classification according to the band intersection near the VBM in the band structure for different stacking configurations can be explained by their p_{z} orbital contribution and atomic alignments. Interlayer coupling is stronger for two neighbouring bands. For example, the interlayer coupling is stronger around the band intersections between the VBM and VBM-1 for the A-2 and B-1.

The choice of twist angle and inclusion of spin-orbit coupling do not significantly change the band structure of InSe monolayer and twisted InSe bilayer from Γ to the highest energy point of the VBM, thus it is expected not to change significantly the band gap and effective mass for holes. Furthermore, the corrugation is small for twisted InSe bilayer at the optimised interlayer distance. The inclusion of the corrugation only enlarges slightly the separation between two adjacent bands. The stacking configurations in each type of InSe bilayer can still be seen in some regions of the same type of twisted InSe bilayer. The innermost In and Se atoms show a distribution of the residual force similar to the distribution of each region corresponding to different stacking configurations in twisted InSe bilayer. The residual forces along z direction are the largest, implying the rearrangement of vertical positions of innermost atoms are larger than their in-plane positions for at least the length scale of the moiré pattern considered in this work.

The effective band structure of the A-type twisted InSe bilayer looks similar to the B-type twisted InSe bilayer, implying the insensitivity of the band structure to the system considered. The difference of the effective band structure along the same kpoint path between the bottom and top InSe layers increases as the twist angle increases. The bands from each stacking configuration calculated within the primitive cell can be used to describe well the effective band structure of the same type of twisted InSe bilayer. It is worth noting that twisted InSe bilayer with a larger interlayer distance gives a larger effective mass for holes, roughly similar to InSe bilayer. However, the interlayer distances are about 8.85 ± 0.04 Å for both types of twisted InSe bilayers, thus the effective mass for holes ($1.57 \pm 0.18\ m_0$) and band gap (0.95 ± 0.03 eV) are similar for different twist angles considered in this work. This leads to the A1s intralayer and interlayer exciton binding energies are $\sim$ 441.1 meV and $\sim$ 183.2 meV in the vacuum, respectively. If twisted InSe bilayer is in the environment of hBN, the A1s intralayer and interlayer exciton binding energies are $\sim$ 119.1 meV and $\sim$ 54.5 meV, respectively.

The hBN layer shown to act appropriately to provide a spacer to separate two InSe monolayers, because the valence bands of the hBN layer are at least 1.5 eV below the VBM of twisted InSe bilayer. The effective band structure of twisted InSe/hBN/InSe heterostructure can also be described well by the bands of InSe monolayer calculated within the primitive cell. The corresponding A1s intralayer exciton binding energies for this heterostructure were calculated to be 232.9 meV in the environment of vacuum and 138.8 meV in the environment of hBN by using the effective mass for holes of InSe monolayer.

Chapter 7

Conclusions

The two transition metal dichalcogenide alloys studied in this thesis exhibit completely different dopant distributions. The W dopant atoms are shown to be randomly distributed in MoS_2 monolayer from the Monte Carlo simulations based on the interaction energy calculated through the plane wave DFT and the statistical analysis of the ADF-STEM images of the as-grown crystal synthesised through CVT.

Furthermore, the electronic properties of $Mo_{1-x}W_xS_2$ monolayer such as the bandwidth, effective mass and band splitting due to spin-orbit coupling near the VBM at **K** calculated through the LS-DFT within large supercells were shown to give more consistent results with the ARPES measurements, compared with the DFT based on the VCA calculations within the primitive cell. When x increases from 0 (MoS_2) to 1 (WS_2), a linear increase of the bandwidth and the band splitting near the VBM can be seen. In contrast, the effective mass for holes reduces linearly with the W composition x. In addition, the spatially localised changes are larger than the band splitting near the CBM in a range between $x = 0.125$ and $x = 0.428$. The calculated band gap suffers from the underestimation of the band gap based on the DFT, the absence of excitonic effect and the existence of intrinsic charge carriers and defects (can cause band gap renormalisation) in the as-grown crystal. Therefore, the theoretical and experimental band gaps cannot be compared. Furthermore, the significant circular dichroism seen in the $Mo_{0.5}W_{0.5}S_2$ monolayer via polarisation-resolved PL measurements proves that spin-valley locking is maintained in these alloys.

Contrastingly, a highly anisotropic dopant distribution with a clear striped pattern was observed experimentally in the as-grown $W_{0.9}Nb_{0.1}S_2$ monolayer. The binding energies of various dopant distributions within small supercells were com-

pared and analysed. It is suggested that the observed dopant distribution in the as-grown $W_{0.9}Nb_{0.1}S_2$ monolayer is the result of the combination of the kinetic effects and the energetics. There are flat bands appearing above the Fermi level in the effective band structure of this alloy. The anisotropy can also be seen in the calculated conductivity based on the semiclassical Boltzmann equations. It is suggested that the degree of anisotropy of conductivity can be increased by increasing the lengths of line segments and spacing between line segments. This provides directions for growing these alloys in the future.

The atomic and electronic structures of InSe monolayer, InSe bilayer with different stacking configurations, twisted InSe bilayer, twisted InSe/hBN/InSe heterostructure were discussed. The InSe bilayer with a smaller interlayer distance (corresponding to a smaller repulsion between atoms in two InSe layers) possesses a smaller binding energy, band gap and effective mass for holes. The contributions from p_z orbitals of Se atom and s orbitals of In atom predominate the VBM and CBM in InSe monolayer, respectively. InSe bilayers with different stacking configurations can be classified into two groups according to the band intersection near the VBM. The interlayer coupling is stronger near the band intersection.

Furthermore, only small corrugation needs to be considered at the optimised interlayer distance of twisted InSe bilayer. The distribution of residual force is similar to the atomic distribution corresponding to different stacking configurations in twisted InSe bilayer. The residual forces applied on the innermost In and Se atoms are larger than the outermost In and Se atoms, while the force applied on Se atom is larger than In atom because Se atoms are at the edges in the top and bottom layers. The force is mainly oriented along the z direction, implying the rearrangement of atoms in the vertical position is larger than the xy-plane when forming twisted InSe bilayer with at least the length scale of moiré pattern considered in this work, though the directions of movement of atoms could change at smaller twist angles with larger moiré patterns.

As the twist angle increases, the difference between the effective band structures of twisted InSe bilayer projected on the bottom and top InSe layers increases. The mapping between the VBM of twisted InSe bilayer from supercell calculation and InSe bilayer from the primitive cell calculation is good. The effective mass for holes for twisted InSe bilayer will increase if the interlayer distance increases, however, the interlayer distances for twisted InSe bilayers with different twist angles (3.4°, 4.4°, 6.0°, 17.9° and 27.8°) considered in this work are generally similar (8.5 ± 0.4 Å). This implies the proportion of each stacking configuration in the twisted InSe bilayer remains roughly at a constant within the range of twist angles

considered in this work. The variation of the VBM with different twist angles mainly originates from the difference of the interlayer distance (or stacking configuration) and slightly affected by the twist angle itself (leading to a different kpoint path for the other InSe layer) and the corrugation. The change of the flatness of the VBM is due to different band foldings within different sizes of Brillouin zone, and approximately not owing to the variation of the VBM with different twist angles (if the twist angle is not very small). The effective mass for holes in twisted InSe bilayer approximately remains at a constant and gives $\sim$ 441.1 meV and $\sim$ 183.2 meV in the environment of vacuum, whereas they are $\sim$ 119.1 meV and $\sim$ 54.5 meV in the enviromnent of hBN, for the A1s intralayer and interlayer exciton binding energies, respectively. The encapsulated hBN layer in twisted InSe bilayer is regarded as a spacer to weaken the interaction between two InSe layers. The effective band structure of twisted InSe/hBN/InSe heterostructure can also be well-described by InSe monolayer from the primitive cell calculation. The A1s intralayer exciton binding energy for this heterostructure is $\sim$ 232.9 meV in the environment of vacuum and $\sim$ 138.8 meV in the environment of hBN, with the effective mass for holes of InSe monolayer as input in the theoretical model.

In this thesis, the fundamental properties of these materials have been revealed from the combination of theory and experiment. This helps theorists and experimentalists expand knowledge of this continuously growing research field of 2D materials, then further developing appropriate technological tools to study other similar 2D materials.

Bibliography

[1] Q. H. Wang, K. Kalantar-Zadeh, A. Kis, J. N. Coleman, and M. S. Strano. Electronics and optoelectronics of two-dimensional transition metal dichalcogenides. *Nature Nanotech.*, 7:699–712, 2012. https://doi.org/10.1038/nnano.2012.193. (Cited on page 1.)

[2] A. Splendiani, L. Sun, Y. Zhang, T. Li, J. Kim, C.-Y. Chim, G. Galli, and F. Wang. Emerging photoluminescence in monolayer MoS_2. *Nano Lett.*, 10:1271–1275, 2010. https://doi.org/10.1021/nl903868w. (Cited on page 1.)

[3] Y. Zhang, T.-R. Chang, B. Zhou, Y.-T. Cui, H. Yan, Z. Liu, F. Schmitt, J. Lee, R. Moore, Y. Chen, H. Lin, H.-T. Jeng, S.-K. Mo, Z. Hussain, A. Bansil, and Z.-X. Shen. Direct observation of the transition from indirect to direct bandgap in atomically thin epitaxial $MoSe_2$. *Nature Nanotech.*, 9:111–115, 2014. https://doi.org/10.1038/nnano.2013.277. (Cited on page 1.)

[4] M. Bernardi, C. Ataca, M. Palummo, and J. C. Grossman. Optical and electronic properties of two-dimensional layered materials. *Nanophotonics*, 6:479–493, 2017. https://doi.org/10.1515/nanoph-2015-0030. (Cited on page 1.)

[5] D. Wickramaratne, L. Weston, and C. G. Van de Walle. Monolayer to bulk properties of hexagonal boron nitride. *J. Phys. Chem. C*, 122:25524–25529, 2018. https://doi.org/10.1021/acs.jpcc.8b09087. (Cited on page 1.)

[6] K. S. Novoselov, A. K. Geim, S. V. Morozov, D. Jiang, Y. Zhang, S. V. Dubonos, I. V. Grigorieva, and A. A. Firsov. Electric field effect in atomically thin carbon films. *Science*, 306:666–669, 2004. https://doi.org/10.1126/science.1102896. (Cited on page 1.)

[7] A. K. Geim and K. S. Novoselov. The rise of graphene. *Nature Mater.*, 6:183–191, 2007. https://doi.org/10.1038/nmat1849. (Cited on page 1.)

[8] K. I. Bolotin, K. J. Sikes, Z. Jiang, M. Klima, G. Fudenberg, J. Hone, P. Kim, and H. L. Stormer. Ultrahigh electron mobility in suspended graphene. *Solid State Commun.*, 146:351–355, 2008. https://doi.org/10.1016/j.ssc.2008.02.024. (Cited on page 1.)

[9] J. Chen, C. Jang, S. Xiao, M. Ishigami, and M. S. Fuhrer. Intrinsic and extrinsic performance limits of graphene devices on SiO_2. *Nature Nanotech.*, 3:206–209, 2008. https://doi.org/10.1038/nnano.2008.58. (Cited on page 1.)

[10] A. K. Geim. Graphene: Status and prospects. *Science*, 324:1530–1534, 2009. https://doi.org/10.1126/science.1158877. (Cited on page 1.)

[11] A. A. Balandin. Thermal properties of graphene and nanostructured carbon materials. *Nature Mater.*, 10:569–581, 2011. https://doi.org/10.1038/nmat3064. (Cited on page 1.)

[12] K. S. Novoselov, A. K. Geim, S. V. Morozov, D. Jiang, M. I. Katsnelson, I. V. Grigorieva, S. V. Dubonos, and A. A. Firsov. Two-dimensional gas of massless Dirac fermions in graphene. *Nature*, 438:197–200, 2005. https://doi.org/10.1038/nature04233. (Cited on page 1.)

[13] K. Kim, J.-Y. Choi, T. Kim, S.-H. Cho, and H.-J. Chung. A role for graphene in silicon-based semiconductor devices. *Nature*, 479:338–344, 2011. https://doi.org/10.1038/nature10680. (Cited on page 1.)

[14] P. Avouris and C. Dimitrakopoulos. Graphene: synthesis and applications. *Mater. Today*, 15:86–97, 2012. https://doi.org/10.1016/S1369-7021(12)70044-5. (Cited on page 1.)

[15] S. P. S. Arya and A. D'Amico. Preparation, properties and applications of boron nitride thin films. *Thin Solid Films*, 157:267–282, 1988. https://doi.org/10.1016/0040-6090(88)90008-9. (Cited on page 1.)

[16] K. K. Kim, A. Hsu, X. Jia, S. M. Kim, Y. Shi, M. Hofmann, D. Nezich, J. F. Rodriguez-Nieva, M. Dresselhaus, T. Palacios, and J. Kong. Synthesis of monolayer hexagonal boron nitride on Cu foil using chemical vapor deposition. *Nano Lett.*, 12:161–166, 2012. https://doi.org/10.1021/nl203249a. (Cited on page 1.)

[17] A. Morita. Semiconducting black phosphorus. *Appl. Phys. A*, 39:227–242, 1986. https://doi.org/10.1007/BF00617267. (Cited on page 1.)

[18] S. Appalakondaiah, G. Vaitheeswaran, S. Lebègue, N. E. Christensen, and A. Svane. Effect of van der Waals interactions on the structural and elastic properties of black phosphorus. *Phys. Rev. B*, 86:035105, 2012. https://doi.org/10.1103/PhysRevB.86.035105. (Cited on page 1.)

[19] F. A. Rasmussen and K. S. Thygesen. Computational 2D materials database: Electronic structure of transition-metal dichalcogenides and oxides. *J. Phys. Chem. C*, 119:13169–13183, 2015. https://doi.org/10.1021/acs.jpcc.5b02950. (Cited on page 1.)

[20] A. K. Singh and R. G. Hennig. Computational prediction of two-dimensional group-IV monochalcogenides. *Appl. Phys. Lett.*, 105:042103, 2014. https://doi.org/10.1063/1.4891230. (Cited on page 1.)

[21] S. Demirci, N. Avazli, E. Durgun, and S. Cahangirov. Structural and electronic properties of monolayer group III monochalcogenides. *Phys. Rev. B*, 95:115409, 2017. https://doi.org/10.1103/PhysRevB.95.115409. (Cited on page 1.)

[22] O. Lopez-Sanchez, D. Lembke, M. Kayci, A. Radenovic, and A. Kis. Ultrasensitive photodetectors based on monolayer MoS_2. *Nature Nanotech.*, 8:497–501, 2013. https://doi.org/10.1038/nnano.2013.100. (Cited on pages 1 and 35).

[23] J. Xia, X. Huang, L.-Z. Liu, M. Wang, L. Wang, B. Huang, D.-D. Zhu, J.-J. Li, C.-Z. Gu, and X.-M. Meng. CVD synthesis of large-area, highly crystalline $MoSe_2$ atomic layers on diverse substrates and application to photodetectors. *Nanoscale*, 6:8949–8955, 2014. https://doi.org/10.1039/C4NR02311K. (Cited on page 1.)

[24] K. Watanabe, T. Taniguchi, and H. Kanda. Direct-bandgap properties and evidence for ultraviolet lasing of hexagonal boron nitride single crystal. *Nature Mater.*, 3:404–409, 2004. https://doi.org/10.1038/nmat1134. (Cited on page 1.)

[25] G. W. Mudd, S. A. Svatek, T. Ren, A. Patanè, O. Makarovsky, L. Eaves, P. H. Beton, Z. D. Kovalyuk, G. V. Lashkarev, Z. R. Kudrynskyi, and A. I. Dmitriev. Tuning the bandgap of exfoliated InSe nanosheets by quantum confinement. *Adv. Mater.*, 25:5714–5718, 2013. https://doi.org/10.1002/adma.201302616. (Cited on page 1.)

[26] J. Miao, L. Zhang, and C. Wang. Black phosphorus electronic and optoelectronic devices. *2D Mater.*, 6:032003, 2019. https://doi.org/10.1088/2053-1583/ab1ebd. (Cited on page 1.)

[27] K. F. Mak, C. Lee, J. Hone, J. Shan, and T. F. Heinz. Atomically thin MoS_2: A new direct-gap semiconductor. *Phys. Rev. Lett.*, 105:136805, 2010. https://doi.org/10.1103/PhysRevLett.105.136805. (Cited on pages 1, 2, and 35).

[28] B. Radisavljevic, A. Radenovic, J. Brivio, V. Giacometti, and A. Kis. Single-layer MoS_2 transistors. *Nature Nanotech.*, 6:147–150, 2011. https://doi.org/10.1038/nnano.2010.279. (Cited on pages 1 and 2).

[29] W. Feng, W. Zheng, W. Cao, and P. Hu. Back gated multilayer InSe transistors with enhanced carrier mobilities via the suppression of carrier scattering from a dielectric interface. *Adv. Mater.*, 26:6587–6593, 2014. https://doi.org/10.1002/adma.201402427. (Cited on page 1.)

[30] M. Asadi, K. Kim, C. Liu, A. V. Addepalli, P. Abbasi, P. Yasaei, P. Phillips, A. Behranginia, J. M. Cerrato, R. Haasch, P. Zapol, B. Kumar, R. F. Klie, J. Abiade, L. A. Curtiss, and A. Salehi-Khojin. Nanostructured transition metal dichalcogenide electrocatalysts for CO_2 reduction in ionic liquid. *Science*, 353:467–470, 2016. https://doi.org/10.1126/science.aaf4767. (Cited on page 1.)

[31] M. M. Ugeda, A. J. Bradley, Y. Zhang, S. Onishi, Y. Chen, W. Ruan, C. Ojeda-Aristizabal, H. Ryu, M. T. Edmonds, H.-Z. Tsai, A. Riss, S.-K. Mo, D. Lee, A. Zettl, Z. Hussain, Z.-X. Shen, and M. F. Crommie. Characterization of collective ground states in single-layer $NbSe_2$. *Nature Phys.*, 12:92–97, 2016. https://doi.org/10.1038/nphys3527. (Cited on page 1.)

[32] Y. Cao, A. Mishchenko, G. L. Yu, E. Khestanova, A. P. Rooney, E. Prestat, A. V. Kretinin, P. Blake, M. B. Shalom, C. Woods, J. Chapman, G. Balakrishnan, I. V. Grigorieva, K. S. Novoselov, B. A. Piot, M. Potemski, K. Watanabe, T. Taniguchi, S. J. Haigh, A. K. Geim, and R. V. Gorbachev. Quality heterostructures from two-dimensional crystals unstable in air by their assembly in inert atmosphere. *Nano Lett.*, 15:4914–4921, 2015. https://doi.org/10.1021/acs.nanolett.5b00648. (Cited on page 1.)

[33] I. N. Yakovkin. Dirac cones in graphene, interlayer interaction in layered materials, and the band gap in MoS_2. *Crystals*, 6:143, 2016. https://doi.org/10.3390/cryst6110143. (Cited on page 2.)

[34] O. V. Yazyev and A. Kis. MoS_2 and semiconductors in the flatland. *Materials Today*, 18:20–30, 2015. https://doi.org/10.1016/j.mattod.2014.07.005. (Cited on pages 2 and 35).

[35] T. Cheiwchanchamnangij and W. R. L. Lambrecht. Quasiparticle band structure calculation of monolayer, bilayer, and bulk MoS_2. *Phys. Rev. B*, 85:205302, 2012. https://doi.org/10.1103/PhysRevB.85.205302. (Cited on page 2.)

[36] K. K. Kam and B. A. Parkinson. Detailed photocurrent spectroscopy of the semiconducting group VIB transition metal dichalcogenides. *J. Phys. Chem.*, 86:463–467, 1982. https://doi.org/10.1021/j100393a010. (Cited on page 2.)

[37] K. Dileep, R. Sahu, S. Sarkar, S. C. Peter, and R. Datta. Layer specific optical band gap measurement at nanoscale in MoS_2 and ReS_2 van der waals compounds by high resolution electron energy loss spectroscopy. *J. Appl. Phys.*, 119:114309, 2016. https://doi.org/10.1063/1.4944431. (Cited on page 2.)

[38] E. E. Salpeter and H. A. Bethe. A relativistic equation for bound-state problems. *Phys. Rev.*, 84:1232, 1951. https://doi.org/10.1103/PhysRev.84.1232. (Cited on page 2.)

[39] L. J. Sham and T. M. Rice. Many-particle derivation of the effective-mass equation for the Wannier exciton. *Phys. Rev.*, 144:708, 1966. https://doi.org/10.1103/PhysRev.144.708. (Cited on page 2.)

[40] A. Ramasubramaniam. Large excitonic effects in monolayers of molybdenum and tungsten dichalcogenides. *Phys. Rev. B*, 86:115409, 2012. https://doi.org/10.1103/PhysRevB.86.115409. (Cited on page 2.)

[41] Z. Y. Zhu, Y. C. Cheng, and U. Schwingenschlögl. Giant spin-orbit-induced spin splitting in two-dimensional transition-metal dichalcogenide semiconductors. *Phys. Rev. B*, 84:153402, 2011. https://doi.org/10.1103/PhysRevB.84.153402. (Cited on page 2.)

[42] Y. Chen, J. Xi, D. O. Dumcenco, Z. Liu, K. Suenaga, D. Wang, Z. Shuai, Y.-S. Huang, and L. Xie. Tunable band gap photoluminescence from atomically thin transition-metal dichalcogenide alloys. *ACS Nano*, 7:4610–4616, 2013. https://doi.org/10.1021/nn401420h. (Cited on pages 2, 3, 36, 37, and 52).

[43] D. W. Latzke, W. Zhang, A. Suslu, T.-R. Chang, H. Lin, H.-T. Jeng, S. Tongay, J. Wu, A. Bansil, and A. Lanzara. Electronic structure, spin-orbit coupling, and interlayer interaction in bulk MoS_2 and WS_2. *Phys. Rev. B*, 91:235202, 2015. https://doi.org/10.1103/PhysRevB.91.235202. (Cited on page 2.)

[44] S. Roy and P. Bermel. Electronic and optical properties of ultra-thin 2D tungsten disulfide for photovoltaic applications. *Solar Energy Materials and Solar Cells*, 174:370–379, 2018. https://doi.org/10.1016/j.solmat.2017.09.011. (Cited on page 2.)

[45] C. Yelgel, Ö. C. Yelgel, and O. Gülseren. Structural and electronic properties of MoS_2, WS_2, and WS_2/MoS_2 heterostructures encapsulated with hexagonal boron nitride monolayers. *J. Appl. Phys.*, 122:065303, 2017. https://doi.org/10.1063/1.4998522. (Cited on page 2.)

[46] D. Ovchinnikov, A. Allain, Y.-S. Huang, D. Dumcenco, and A. Kis. Electrical transport properties of single-layer WS_2. *ACS Nano*, 8:8174–8181, 2014. https://doi.org/10.1021/nn502362b. (Cited on pages 2 and 35).

[47] Z. Wang, P. Liu, Y. Ito, S. Ning, Y. Tan, T. Fujita, A. Hirata, and M. Chen. Chemical vapor deposition of monolayer $Mo_{1-x}W_xS_2$ crystals with tunable band gaps. *Sci. Rep.*, 6:21536, 2016. https://doi.org/10.1038/srep21536. (Cited on pages 2 and 36).

[48] X. Zhang, S. Xiao, L. Shi, H. Nan, X. Wan, X. Gu, Z. Ni, and K. K. Ostrikov. Large-size $Mo_{1-x}W_xS_2$ and $W_{1-x}Mo_xS_2$ (x = 0-0.5) monolayers by confined-space chemical vapor deposition. *Appl. Surf. Sci.*, 457:591–597, 2018. https://doi.org/10.1016/j.apsusc.2018.06.299. (Cited on page 2.)

[49] H. Liu, K. K. A. Antwi, S. Chua, and D. Chi. Vapor-phase growth and characterization of $Mo_{1-x}W_xS_2$ ($0 \leq x \leq 1$) atomic layers on 2-inch sapphire substrates. *Nanoscale*, 6:624–629, 2014. https://doi.org/10.1039/C3NR04515C. (Cited on page 2.)

[50] W. Zhang, X. Li, T. Jiang, J. Song, Y. Lin, L. Zhu, and X. Xu. CVD synthesis of $Mo_{(1-x)}W_xS_2$ and $MoS_{2(1-x)}Se_{2x}$ alloy monolayers aimed at tuning the

bandgap of molybdenum disulfide. *Nanoscale*, 7:13554–13560, 2015. https://doi.org/10.1039/C5NR02515J. (Cited on pages 2 and 36).

[51] F. Shao, Z. Tian, P. Qin, K. Bu, W. Zhao, L. Xu, D. Wang, and F. Huang. 2H-NbS_2 film as a novel counter electrode for meso-structured perovskite solar cells. *Sci. Rep.*, 8:7033, 2018. https://doi.org/10.1038/s41598-018-25449-x. (Cited on page 2.)

[52] A. S. de R. Neto and L. Seixas. Toward a two-dimensional NbS_2-based electrode for lithium–ion batteries. *Int. J. Quantum Chem.*, 121:e26603, 2021. https://doi.org/10.1002/qua.26603. (Cited on page 2.)

[53] R. Yan, G. Khalsa, B. T. Schaefer, A. Jarjour, S. Rouvimov, K. C. Nowack, H. G. Xing, and D. Jena. Thickness dependence of superconductivity in ultrathin NbS_2. *Appl. Phys. Express*, 12:023008, 2019. https://doi.org/10.7567/1882-0786/aaff89. (Cited on page 2.)

[54] S. Lei, L. Ge, S. Najmaei, A. George, R. Kappera, J. Lou, M. Chhowalla, H. Yamaguchi, G. Gupta, R. Vajtai, A. D. Mohite, and P. M. Ajayan. Evolution of the electronic band structure and efficient photo-detection in atomic layers of InSe. *ACS Nano*, 8:1263–1272, 2014. https://doi.org/10.1021/nn405036u. (Cited on page 3.)

[55] K. Yuan, R. Yin, X. Li, Y. Han, M. Wu, S. Chen, S. Liu, X. Xu, K. Watanabe, T. Taniguchi, D. A. Muller, J. Shi, P. Gao, X. Wu, Y. Ye, and L. Dai. Realization of quantum Hall effect in chemically synthesized InSe. *Adv. Funct. Mater.*, 29:1904032, 2019. https://doi.org/10.1002/adfm.201904032. (Cited on page 3.)

[56] P. D. Haynes, C.-K. Skylaris, A. A. Mostofi, and M. C. Payne. Onetep: linear-scaling density-functional theory with plane waves. *Psi-k Newsletter*, 72:78–91, 2005. https://psi-k.net/download/highlights/Highlight_72.pdf. (Cited on pages 3, 22, 23, 24, 25, 26, 27, 28, and 29).

[57] E. Hernández, M. J. Gillan, and C. M. Goringe. Linear-scaling density-functional-theory technique: The density-matrix approach. *Phys. Rev. B*, 53:7147, 1996. https://doi.org/10.1103/PhysRevB.53.7147. (Cited on page 3.)

[58] S. Mohr, L. E. Ratcliff, L. Genovese, D. Caliste, P. Boulanger, S. Goedecker, and T. Deutsch. Accurate and efficient linear scaling DFT calculations with

universal applicability. *Phys. Chem. Chem. Phys.*, 17:31360–31370, 2015. https://doi.org/10.1039/C5CP00437C. (Cited on page 3.)

[59] J. C. A. Prentice, J. Aarons, J. C. Womack, A. E. A. Allen, L. Andrinopoulos, L. Anton, R. A. Bell, A. Bhandari, G. A. Bramley, R. J. Charlton, R. J. Clements, D. J. Cole, G. Constantinescu, F. Corsetti, S. M.-M. Dubois, K. K. B. Duff, J. M. Escartín, A. Greco, Q. Hill, L. P. Lee, E. Linscott, D. D. O'Regan, M. J. S. Phipps, L. E. Ratcliff, Á. Ruiz Serrano, E. W. Tait, G. Teobaldi, V. Vitale, N. Yeung, T. J. Zuehlsdorff, J. Dziedzic, P. D. Haynes, N. D. M. Hine, A. A. Mostofi, M. C. Payne, and C.-K. Skylaris. The ONETEP linear-scaling density functional theory program. *J. Chem. Phys.*, 152:174111, 2020. https://doi.org/10.1063/5.0004445. (Cited on pages 3, 22, 38, 62, and 82).

[60] S. J. Clark, M. D. Segall, C. J. Pickard, P. J. Hasnip, M. I. J. Probert, K. Refson, and M. C. Payne. First principles methods using CASTEP. *Z. Kristallogr.*, 220:567–570, 2005. https://doi.org/10.1524/zkri.220.5.567.65075. (Cited on pages 3, 38, and 62).

[61] P. Giannozzi, S. Baroni, N. Bonini, M. Calandra, R. Car, C. Cavazzoni, D. Ceresoli, G. L. Chiarotti, M. Cococcioni, I. Dabo, A. D. Corso, S. de Dironcoli, S. Fabris, G. Fratesi, R. Gebauer, U. Gerstmann, C. Gougoussis, A. Kokalj, M. Lazzeri, L. Martin-Samos, N. Marzari, F. Mauri, R. Mazzarello, S. Paolini, A. Pasquarello, L. Paulatto, C. Sbraccia, S. Scandolo, G. Sclauzero, A. P. Seitsonen, A. Smogunov, P. Umari, and R. M. Wentzcovitch. QUANTUM ESPRESSO: a modular and open-source software project for quantum simulations of materials. *J. Phys.: Condens. Matter*, 21:395502, 2009. https://doi.org/10.1088/0953-8984/21/39/395502. (Cited on pages vi, 3, 36, 39, and 82).

[62] P. Giannozzi, O. Andreussi, T. Brumme, O. Bunau, M. B. Nardelli, M. Calandra, R. Car, C. Cavazzoni, D. Ceresoli, M. Cococcioni, N. Colonna, I. Carnimeo, A. D. Corso, S. de Gironcoli, P. Delugas, R. A. DiStasio Jr, A. Ferretti, A. Floris, G. Fratesi, G. Fugallo, R. Gebauer, U. Gerstmann, F. Giustino, T. Gorni, J. Jia, M. Kawamura, H.-Y. Ko, A. Kokalj, E. Küçükbenli, M. Lazzeri, M. Marsili, N. Marzari, F. Mauri, N. L. Nguyen, H.-V. Nguyen, A. Otero-de-la-Roza, L. Paulatto, S. Poncé, D. Rocca, R. Sabatini, B. Santra, M. Schlipf, A. P. Seitsonen, A. Smogunov, I. Timrov, T. Thonhauser, P. Umari, N. Vast, X. Wu, and S. Baroni. Advanced capabilities for

materials modelling with Quantum ESPRESSO. *J. Phys.: Condens. Matter*, 29:465901, 2017. https://doi.org/10.1088/1361-648X/aa8f79. (Cited on pages vi, 3, 36, 39, and 82).

[63] C.-K. Skylaris, P. D. Haynes, A. A. Mostofi, and M. C. Payne. Introducing ONETEP: Linear-scaling density functional simulations on parallel computers. *J. Chem. Phys.*, 122:084119, 2005. https://doi.org/10.1063/1.1839852. (Cited on pages 3, 22, 23, 26, 38, 62, and 82).

[64] C.-K. Skylaris, P. D. Haynes, A. A. Mostofi, and M. C. Payne. Using ONETEP for accurate and efficient *O(N)* density functional calculations. *J. Phys.: Condens. Matter*, 17:5757, 2005. https://doi.org/10.1088/0953-8984/17/37/012. (Cited on pages 3 and 26).

[65] V. Popescu and A. Zunger. Extracting E versus $\vec{k}$ effective band structure from supercell calculations on alloys and impurities. *Phys. Rev. B*, 85:085201, 2012. https://doi.org/10.1103/PhysRevB.85.085201. (Cited on pages 3, 31, 32, and 33).

[66] G. C. Constantinescu and N. D. M. Hine. Energy landscape and band-structure tuning in realistic $MoS_2/MoSe_2$ heterostructures. *Phys. Rev. B*, 91:195416, 2015. https://doi.org/10.1103/PhysRevB.91.195416. (Cited on pages 3, 33, and 39).

[67] The code of Monte Carlo simulation in this work was adapted from a code provided by Prof. David Quigley (University of Warwick). (Cited on pages 3 and 38).

[68] G. K. H. Madsen and D. J. Singh. Boltztrap. A code for calculating band-structure dependent quantities. *Comput. Phys. Commun.*, 175:67–71, 2006. https://doi.org/10.1016/j.cpc.2006.03.007. (Cited on pages 3, 4, and 63).

[69] D. O. Dumcenco, H. Kobayashi, Z. Liu, Y.-S. Huang, and K. Suenaga. Visualization and quantification of transition metal atomic mixing in $Mo_{1-x}W_xS_2$ single layers. *Nat. Commun.*, 4:1351, 2013. https://doi.org/10.1038/ncomms2351. (Cited on pages 3, 36, and 47).

[70] A. Kuc and T. Heine. On the stability and electronic structure of transition-metal dichalcogenide monolayer alloys $Mo_{1-x}X_xS_{2-y}Se_y$ with X = W, Nb. *Electronics*, 5:1, 2016. https://doi.org/10.3390/electronics5010001. (Cited on page 4.)

[71] G. Tarnopolsky, A. J. Kruchkov, and A. Vishwanath. Origin of magic angles in twisted bilayer graphene. *Phys. Rev. Lett.*, 122:106405, 2019. https://doi.org/10.1103/PhysRevLett.122.106405. (Cited on pages 4 and 79).

[72] H. C. Po, L. Zou, A. Vishwanath, and T. Senthil. Origin of Mott insulating behavior and superconductivity in twisted bilayer graphene. *Phys. Rev. X*, 8:031089, 2018. https://doi.org/10.1103/PhysRevX.8.031089. (Cited on pages 4 and 79).

[73] J. M. B. Lopes dos Santos, N. M. R. Peres, and A. H. Castro Neto. Continuum model of the twisted graphene bilayer. *Phys. Rev. B*, 86:155449, 2012. https://doi.org/10.1103/PhysRevB.86.155449. (Cited on page 4.)

[74] L. Zou, H. C. Po, A. Vishwanath, and T. Senthil. Band structure of twisted bilayer graphene: Emergent symmetries, commensurate approximants, and Wannier obstructions. *Phys. Rev. B*, 98:085435, 2018. https://doi.org/10.1103/PhysRevB.98.085435. (Cited on page 4.)

[75] R. Bistritzer and A. H. MacDonald. Moiré bands in twisted double-layer graphene. *PNAS*, 108:12233–12237, 2011. https://doi.org/10.1073/pnas.1108174108. (Cited on page 4.)

[76] M. Yankowitz, S. Chen, H. Polshyn, Y. Zhang, K. Watanabe, T. Taniguchi, D. Graf, A. F. Young, and C. R. Dean. Tuning superconductivity in twisted bilayer graphene. *Science*, 363:1059–1064, 2019. https://doi.org/10.1126/science.aav1910. (Cited on pages 4 and 79).

[77] L. Xian, D. M. Kennes, N. Tancogne-Dejean, M. Altarelli, and A. Rubio. Multiflat bands and strong correlations in twisted bilayer boron nitride: Doping-induced correlated insulator and superconductor. *Nano Lett.*, 19:4934–4940, 2019. https://doi.org/10.1021/acs.nanolett.9b00986. (Cited on page 4.)

[78] P. Kang. Indirect-to-direct bandgap transition in bilayer InSe: roles of twistronics. *2D Mater.*, 7:021002, 2020. https://doi.org/10.1088/2053-1583/ab6707. (Cited on pages 4, 80, 81, 83, 85, 93, 107, and 112).

[79] R. M. Martin. *Electronic structure : basic theory and practical methods*. Cambridge University Press, Cambridge, UK ; New York, 2004. (Cited on pages 6, 7, 8, 9, 10, 12, 13, 14, 16, 17, 18, 19, 20, and 21).

[80] M. Born and R. Oppenheimer. Zur Quantentheorie der Molekeln. *Ann. Physik.*, 389:457–484, 1927. https://doi.org/10.1002/andp.19273892002. (Cited on page 7.)

[81] D. R. Hartree. The wave mechanics of an atom with a non-Coulomb central field. Part I. Theory and methods. *Proc. Camb. Phil. Soc.*, 24:89–110, 1928. https://doi.org/10.1017/S0305004100011919. (Cited on page 7.)

[82] J. C. Slater. The theory of complex spectra. *Phys. Rev.*, 34:1293, 1929. https://doi.org/10.1103/PhysRev.34.1293. (Cited on page 8.)

[83] N. W. Ashcroft and N. D. Mermin. *Solid State Physics*. Saunders College, Philadelphia, 1976. (Cited on page 8.)

[84] V. Fock. Näherungsmethode zur Lösung des quantenmechanischen Mehrkörperproblems. *Z. Physik*, 61:126–148, 1930. https://doi.org/10.1007/BF01340294. (Cited on page 9.)

[85] P. Hohenberg and W. Kohn. Inhomogeneous electron gas. *Phys. Rev.*, 136:B864, 1964. https://doi.org/10.1103/PhysRev.136.B864. (Cited on pages 9 and 10).

[86] W. Kohn and L. J. Sham. Self-consistent equations including exchange and correlation effects. *Phys. Rev.*, 140:A1133, 1965. https://doi.org/10.1103/PhysRev.140.A1133. (Cited on pages 11, 12, and 13).

[87] R. G. Parr and W. Yang. *Density-functional theory of atoms and molecules*. Oxford University Press, New York, 1989. (Cited on page 13.)

[88] E. Wigner. On the interaction of electrons in metals. *Phys. Rev.*, 46:1002, 1934. https://doi.org/10.1103/PhysRev.46.1002. (Cited on page 14.)

[89] E. Wigner. Effects of the electron interaction on the energy levels of electrons in metals. *Trans. Faraday Soc.*, 34:678–685, 1938. https://doi.org/10.1039/TF9383400678. (Cited on page 14.)

[90] M. Gell-Mann and K. A. Brueckner. Correlation energy of an electron gas at high density. *Phys. Rev.*, 106:364, 1957. https://doi.org/10.1103/PhysRev.106.364. (Cited on page 14.)

[91] J. P. Perdew and K. Burke. Comparison shopping for a gradient-corrected density functional. *Int. J. Quant. Chem.*, 57:309–319,

1996. https://doi.org/10.1002/(SICI)1097-461X(1996)57:3<309::AID-QUA4>3.0.CO;2-1. (Cited on page 14.)

[92] A. D. Becke. Density-functional exchange-energy approximation with correct asymptotic behavior. *Phys. Rev. A*, 38:3098, 1988. https://doi.org/10.1103/PhysRevA.38.3098. (Cited on page 14.)

[93] J. P. Perdew and Y. Wang. Accurate and simple analytic representation of the electron-gas correlation energy. *Phys. Rev. B*, 45:13244, 1992. https://doi.org/10.1103/PhysRevB.45.13244. (Cited on page 14.)

[94] J. P. Perdew, K. Burke, and M. Ernzerhof. Generalized gradient approximation made simple. *Phys. Rev. Lett.*, 77:3865, 1996. https://doi.org/10.1103/PhysRevLett.77.3865. (Cited on pages 14, 38, and 62).

[95] K. Müller-Dethlefs and P. Hobza. Noncovalent interactions: A challenge for experiment and theory. *Chem. Rev.*, 100:143–168, 2000. https://doi.org/10.1021/cr9900331. (Cited on page 14.)

[96] H. Rydberg, M. Dion, N. Jacobson, E. Schröder, P. Hyldgaard, S. I. Simak, D. C. Langreth, and B. I. Lundqvist. Van der Waals density functional for layered structures. *Phys. Rev. Lett.*, 91:126402, 2003. https://doi.org/10.1103/PhysRevLett.91.126402. (Cited on pages 14 and 15).

[97] M. Dion, H. Rydberg, E. Schröder, D. C. Langreth, and B. I. Lundqvist. Van der Waals density functional for general geometries. *Phys. Rev. Lett.*, 92:246401, 2004. https://doi.org/10.1103/PhysRevLett.92.246401. (Cited on page 14.)

[98] G. Román-Pérez and J. M. Soler. Efficient implementation of a van der Waals density functional: application to double-wall carbon nanotubes. *Phys. Rev. Lett.*, 103:096102, 2009. https://doi.org/10.1103/PhysRevLett.103.096102. (Cited on page 15.)

[99] J. Klimeš, D. R. Bowler, and A. Michaelides. Chemical accuracy for the van der Waals density functional. *J. Phys.: Condens. Matter*, 22:022201, 2009. https://doi.org/10.1088/0953-8984/22/2/022201. (Cited on pages 15 and 82).

[100] D. R. Hamann, M. Schlüter, and C. Chiang. Norm-conserving pseudopotentials. *Phys. Rev. Lett.*, 43:1494, 1979. https://doi.org/10.1103/PhysRevLett.43.1494. (Cited on page 17.)

[101] W. E. Pickett. Pseudopotential methods in condensed matter applications. *Comput. Phys. Rep.*, 9:115–197, 1989. https://doi.org/10.1016/0167-7977(89)90002-6. (Cited on page 17.)

[102] G. B. Bachelet, D. R. Hamann, and M. Schlüter. Pseudopotentials that work: From H to Pu. *Phys. Rev. B*, 26:4199, 1982. https://doi.org/10.1103/PhysRevB.26.4199. (Cited on page 17.)

[103] D. Vanderbilt. Soft self-consistent pseudopotentials in a generalized eigenvalue formalism. *Phys. Rev. B*, 41:7892(R), 1990. https://doi.org/10.1103/PhysRevB.41.7892. (Cited on pages 17, 38, and 62).

[104] P. E. Blöchl. Projector augmented-wave method. *Phys. Rev. B*, 50:17953, 1994. https://doi.org/10.1103/PhysRevB.50.17953. (Cited on pages 17, 18, 39, 62, and 82).

[105] G. Kresse and D. Joubert. From ultrasoft pseudopotentials to the projector augmented-wave method. *Phys. Rev. B*, 59:1758, 1999. https://doi.org/10.1103/PhysRevB.59.1758. (Cited on pages 17, 39, 62, and 82).

[106] N. A. W. Holzwarth, G. E. Matthews, R. B. Dunning, A. R. Tackett, and Y. Zeng. Comparison of the projector augmented-wave, pseudopotential, and linearized augmented-plane-wave formalisms for density-functional calculations of solids. *Phys. Rev. B*, 55:2005, 1997. https://doi.org/10.1103/PhysRevB.55.2005. (Cited on page 17.)

[107] C. Kittel. *Introduction to solid state physics.* Wiley, Hoboken, NJ, 2005. (Cited on page 19.)

[108] H. Hellmann. *Einführung in die Quantenchemie.* Franz Dueticke, Leipzig und Wien, 1937. (Cited on page 20.)

[109] R. P. Feynman. Forces in molecules. *Phys. Rev.*, 56:340, 1939. https://doi.org/10.1103/PhysRev.56.340. (Cited on page 20.)

[110] P. Pulay. *Ab initio* calculation of force constants and equilibrium geometries in polyatomic molecules. *Mol. Phys.*, 17:197–204, 1969. https://doi.org/10.1080/00268976900100941. (Cited on page 21.)

[111] C.-K. Skylaris, A. A. Mostofi, P. D. Haynes, O. Diéguez, and M. C. Payne. Nonorthogonal generalized Wannier function pseudopotential plane-wave method. *Phys. Rev. B*, 66:035119, 2002. https://doi.org/10.1103/PhysRevB.66.035119. (Cited on pages 22 and 24).

[112] W. Kohn. Density functional and density matrix method scaling linearly with the number of atoms. *Phys. Rev. Lett.*, 76:3168, 1996. https://doi.org/10.1103/PhysRevLett.76.3168. (Cited on page 23.)

[113] E. Prodan and W. Kohn. Nearsightedness of electronic matter. *PNAS*, 102:11635–11638, 2005. https://doi.org/10.1073/pnas.0505436102. (Cited on page 23.)

[114] W. Kohn. Analytic properties of Bloch waves and Wannier functions. *Phys. Rev.*, 115:809, 1959. https://doi.org/10.1103/PhysRev.115.809. (Cited on page 24.)

[115] J. D. Cloizeaux. Energy bands and projection operators in a crystal: analytic and asymptotic properties. *Phys. Rev.*, 135:A685, 1964. doi: https://doi.org/10.1103/PhysRev.135.A685. (Cited on page 24.)

[116] J. D. Cloizeaux. Analytical properties of n-dimensional energy bands and Wannier functions. *Phys. Rev.*, 135:A698, 1964. https://doi.org/10.1103/PhysRev.135.A698. (Cited on page 24.)

[117] S. Ismail-Beigi and T. A. Arias. Locality of the density matrix in metals, semiconductors, and insulators. *Phys. Rev. Lett.*, 82:2127, 1999. https://doi.org/10.1103/PhysRevLett.82.2127. (Cited on page 24.)

[118] E. Hernández and M. J. Gillan. Self-consistent first-principles technique with linear scaling. *Phys. Rev. B*, 51:10157, 1995. https://doi.org/10.1103/PhysRevB.51.10157. (Cited on page 24.)

[119] Á. Ruiz-Serrano and C.-K. Skylaris. Variationally localized search direction method for constrained optimization of non-orthogonal, localized orbitals in electronic structure calculations. *J. Chem. Phys.*, 139:164110, 2013. https://doi.org/10.1063/1.4826164. (Cited on pages 24 and 25).

[120] R. McWeeny. Some recent advances in density matrix theory. *Rev. Mod. Phys.*, 32:335, 1960. https://doi.org/10.1103/RevModPhys.32.335. (Cited on pages 24 and 27).

[121] C.-K. Skylaris, A. A. Mostofi, P. D. Haynes, O. Diéguez, and M. C. Payne. Nonorthogonal generalized Wannier function pseudopotential plane-wave method. *Phys. Rev. B*, 66:035119, 2002. https://doi.org/10.1103/PhysRevB.66.035119. (Cited on page 25.)

[122] A. A. Mostofi, C.-K. Skylaris, P. D. Haynes, and M. C. Payne. Total-energy calculations on a real space grid with localized functions and a plane-wave basis. *Comput. Phys. Commun.*, 147:788–802, 2002. https://doi.org/10.1016/S0010-4655(02)00461-7. (Cited on pages 25 and 26).

[123] A. A. Mostofi, P. D. Haynes, C.-K. Skylaris, and M. C. Payne. Preconditioned iterative minimization for linear-scaling electronic structure calculations. *J. Chem. Phys.*, 119:8842, 2003. https://doi.org/10.1063/1.1613633. (Cited on pages 25 and 28).

[124] N. D. M. Hine, P. D. Hayne, A. A. Mostofi, C.-K. Skylaris, and M. C. Payne. Linear-scaling density-functional theory with tens of thousands of atoms: Expanding the scope and scale of calculations with ONETEP. *Comput. Phys. Commun.*, 180:1041–1053, 2009. https://doi.org/10.1016/j.cpc.2008.12.023. (Cited on pages 27 and 31).

[125] Á. Ruiz-Serrano, N. D. M. Hine, and C.-K. Skylaris. Pulay forces from localized orbitals optimized *in situ* using a psinc basis set. *J. Chem. Phys.*, 136:234101, 2012. https://doi.org/10.1063/1.4728026. (Cited on page 27.)

[126] P. D. Haynes and M. C. Payne. Corrected penalty-functional method for linear-scaling calculations within density-functional theory. *Phys. Rev. B*, 59:12173, 1999. https://doi.org/10.1103/PhysRevB.59.12173. (Cited on page 27.)

[127] X.-P. Li, R. W. Nunes, and David Vanderbilt. Density-matrix electronic-structure method with linear system-size scaling. *Phys. Rev. B*, 47:10891, 1993. https://doi.org/10.1103/PhysRevB.47.10891. (Cited on page 27.)

[128] P. D. Haynes, C.-K. Skylaris, A. A. Mostofi, and M. C. Payne. Density kernel optimization in the ONETEP code. *J. Phys.: Condens. Matter*, 20:294207, 2008. https://doi.org/10.1088/0953-8984/20/29/294207. (Cited on pages 27 and 28).

[129] C.-K. Skylaris, A. A. Mostofi, P. D. Haynes, C. J. Pickard, and M. C. Payne. Accurate kinetic energy evaluation in electronic structure calculations with localized functions on real space grids. *Comput. Phys. Commun.*, 140:315–322, 2001. https://doi.org/10.1016/S0010-4655(01)00248-X. (Cited on page 29.)

[130] N. D. M. Hine. Linear-scaling density functional theory using the projector augmented wave method. *J. Phys.: Condens. Matter*, 29:024001, 2017. https://doi.org/10.1088/0953-8984/29/2/024001. (Cited on pages 29, 30, 31, 39, 62, and 82).

[131] N. D. M. Hine, P. D. Haynes, A. A. Mostofi, and M. C. Payne. Linear-scaling density-functional simulations of charged point defects in Al_2O_3 using hierarchical sparse matrix algebra. *J. Chem. Phys.*, 133:114111, 2010. https://doi.org/10.1063/1.3492379. (Cited on page 31.)

[132] T. G. Dargam, R. B. Capaz, and Belita Koiller. Disorder and size effects in the envelope-function approximation. *Phys. Rev. B*, 56:9625, 1997. https://doi.org/10.1103/PhysRevB.56.9625. (Cited on pages 31 and 32).

[133] L.-W. Wang, L. Bellaiche, S.-H. Wei, and A. Zunger. "Majority representation" of alloy electronic states. *Phys. Rev. Lett.*, 80:4725, 1998. https://doi.org/10.1103/PhysRevLett.80.4725. (Cited on pages 31 and 32).

[134] T. B. Boykin, N. Kharche, G. Klimeck, and M. Korkusinski. Approximate bandstructures of semiconductor alloys from tight-binding supercell calculations. *J. Phys.: Condens. Matter*, 19:036203, 2007. https://doi.org/10.1088/0953-8984/19/3/036203. (Cited on pages 31 and 33).

[135] W. Ku, T. Berlijn, and C.-C. Lee. Unfolding first-principles band structures. *Phys. Rev. Lett.*, 104:216401, 2010. https://doi.org/10.1103/PhysRevLett.104.216401. (Cited on page 31.)

[136] Y. Zhang and L.-W. Wang. Global electronic structure of semiconductor alloys through direct large-scale computations for III-V alloys $Ga_xIn_{1-x}P$. *Phys. Rev. B*, 83:165208, 2011. https://doi.org/10.1103/PhysRevB.83.165208. (Cited on page 31.)

[137] A.-B. Chen and A. Sher. *Semiconductor alloys: physics and materials engineering*. Plenum Press, New York, 1995. (Cited on page 31.)

[138] J. S. Faulkner and G. M. Stocks. Calculating properties with the coherent-potential approximation. *Phys. Rev. B*, 21:3222, 1980. https://doi.org/10.1103/PhysRevB.21.3222. (Cited on page 31.)

[139] H Ebert, D Ködderitzsch, and J Minár. Calculating condensed matter properties using the KKR-Green's function method—recent developments and ap-

plications. *Rep. Prog. Phys.*, 74:096501, 2011. https://doi.org/10.1088/0034-4885/74/9/096501. (Cited on page 31.)

[140] L. Bellaiche, S.-H. Wei, and A. Zunger. Composition dependence of interband transition intensities in GaPN, GaAsN, and GaPAs alloys. *Phys. Rev. B*, 56:10233, 1997. https://doi.org/10.1103/PhysRevB.56.10233. (Cited on page 32.)

[141] C.-C. Lee, Y. Yamada-Takamura, and T. Ozaki. Unfolding method for first-principles LCAO electronic structure calculations. *J. Phys.: Condens. Matter*, 25:345501, 2013. https://doi.org/10.1088/0953-8984/25/34/345501. (Cited on page 33.)

[142] X. Xia, S. M. Loh, J. Viner, N. C. Teutsch, A. J. Graham, V. Kandyba, A. Barinov, A. M. Sanchez, D. C. Smith, N. D. M. Hine, and N. R. Wilson. Atomic and electronic structure of two-dimensional $Mo_{(1-x)}W_xS_2$ alloys. *J. Phys. Mater.*, 4:025004, 2021. https://doi.org/10.1088/2515-7639/abdc6e. (Cited on pages vii, viii, ix, 35, 46, 51, 58, 62, and 78).

[143] S. Jo, N. Ubrig, H. Berger, A. B. Kuzmenko, and A. F. Morpurgo. Mono- and bilayer WS_2 light-emitting transistors. *Nano Lett.*, 14:2019–2025, 2014. https://doi.org/10.1021/nl500171v. (Cited on page 35.)

[144] A. Azizi, Y. Wang, Z. Lin, K. Wang, A. L. Elias, M. Terrones, V. H. Crespi, and N. Alem. Spontaneous formation of atomically thin stripes in transition metal dichalcogenide monolayers. *Nano Lett.*, 16:6982–6987, 2016. https://doi.org/10.1021/acs.nanolett.6b03075. (Cited on pages 36, 47, 61, 71, and 78).

[145] W. Tan, Z. Wei, X. Liu, J. Liu, X. Fang, D. Fang, X. Wang, D. Wang, J. Tang, and X. Fan. Ordered and disordered phases in $Mo_{1-x}W_xS_2$ monolayer. *Sci. Rep.*, 7:15124, 2017. https://doi.org/10.1038/s41598-017-15286-9. (Cited on pages 36, 37, and 56).

[146] J. E. Bernard and A. Zunger. Electronic structure of ZnS, ZnSe, ZnTe, and their pseudobinary alloys. *Phys. Rev. B*, 36:3199, 1987. https://doi.org/10.1103/PhysRevB.36.3199. (Cited on page 37.)

[147] J. Kang, S. Tongay, J. Li, and J. Wu. Monolayer semiconducting transition metal dichalcogenide alloys: stability and band bowing. *J. Appl. Phys.*, 113:143703, 2013. https://doi.org/10.1063/1.4799126. (Cited on page 37.)

[148] L. Vegard. Die Konstitution der Mischkristalle und die Raumfüllung der Atome. *Z. Physik*, 5:17–26, 1921. https://doi.org/10.1007/BF01349680. (Cited on page 37.)

[149] L. Nørdheim. Zur Elektronentheorie der Metalle. I. *I. Ann. Phys.*, 401:607–640, 1931. https://doi.org/10.1002/andp.19314010507. (Cited on pages 37 and 39).

[150] R. Vaidya, M. Dave, S. S. Patel, S. G. Patel, and A. R. Jani. Growth of molybdenum disulphide using iodine as transport material. *Pramana -J Phys*, 63:611–616, 2004. https://doi.org/10.1007/BF02704487. (Cited on page 37.)

[151] E. Ising. Beitrag zur Theorie des Ferromagnetismus. *Z. Physik*, 31:253–258, 1925. https://doi.org/10.1007/BF02980577. (Cited on page 38.)

[152] F. Jollet, M. Torrent, and N. Holzwarth. Generation of projector augmented-wave atomic data: a 71 element validated table in the XML format. *Comput. Phys. Commun.*, 185:1246–1254, 2014. https://doi.org/10.1016/j.cpc.2013.12.023. (Cited on page 39.)

[153] D. R. Hamann. Optimized norm-conserving Vanderbilt pseudopotentials. *Phys. Rev. B*, 88:085117, 2013. https://doi.org/10.1103/PhysRevB.88.085117. (Cited on pages 39 and 82).

[154] M. J. van Setten, M. Giantomassi, E. Bousquet, M. J. Verstraete, D. R. Hamann, X. Gonze, and G.-M. Rignanese. The PSEUDODOJO: Training and grading a 85 element optimized norm-conserving pseudopotential table. *Comput. Phys. Commun.*, 226:39–54, 2018. https://doi.org/10.1016/j.cpc.2018.01.012. (Cited on pages 39 and 82).

[155] A. D. Corso. Projector augmented wave method with spin-orbit coupling: Applications to simple solids and zincblende-type semiconductors. *Phys. Rev. B*, 86:085135, 2012. https://doi.org/10.1103/PhysRevB.86.085135. (Cited on page 39.)

[156] A. D. Corso and A. M. Conte. Spin-orbit coupling with ultrasoft pseudopotentials: application to Au and Pt. *Phys. Rev. B*, 71:115106, 2005. https://doi.org/10.1103/PhysRevB.71.115106. (Cited on pages 39 and 63).

[157] A. D. Corso. Projector augmented-wave method: Application to relativistic spin-density functional theory. *Phys. Rev. B*, 82:075116, 2010. https://doi.org/10.1103/PhysRevB.82.075116. (Cited on page 39.)

[158] Ph. Ghosez, D. Desquesnes, X. Gonze, and K. M. Rabe. First-principles study of lattice instabilities in $Ba_xSr_{1-x}TiO_3$. *AIP Conf. Proc*, 535:102–110, 2000. https://doi.org/10.1063/1.1324445. (Cited on page 39.)

[159] A. H. Larsen, J. J. Mortensen, J. Blomqvist, I. E. Castelli, R. Christensen, M. Dułak, J. Friis, M. N. Groves, B. Hammer, C. Hargus, E. D. Hermes, P. C. Jennings, P. B. Jensen, J. Kermode, J. R. Kitchin, E. L. Kolsbjerg, J. Kubal, K. Kaasbjerg, S. Lysgaard, J. B. Maronsson, T. Maxson, T. Olsen, L. Pastewka, A. Peterson, C. Rostgaard, J. Schiøtz, O. Schütt, M. Strange, K. S. Thygesen, T. Vegge, L. Vilhelmsen, M. Walter, Z. Zeng, and K. W. Jacobsen. The atomic simulation environment—a Python library for working with atoms. *J. Phys.: Condens. Matter*, 29:273002, 2017. https://doi.org/10.1088/1361-648X/aa680e. (Cited on pages 40, 63, 82, and 84).

[160] C. R. Harris, K. J. Millman, S. J. van der Walt, R. Gommers, P. Virtanen, D. Cournapeau, E. Wieser, J. Taylor, S. Berg, N. J. Smith, R. Kern, M. Picus, S. Hoyer, M. H. van Kerkwijk, M. Brett, A. Haldane, J. Fernández del Río, M. Wiebe, P. Peterson, P. Gérard-Marchant, K. Sheppard, T. Reddy, W. Weckesser, H. Abbasi, C. Gohlke, and T. E. Oliphant. Array programming with NumPy. *Nature*, 585:357–362, 2020. https://doi.org/10.1038/s41586-020-2649-2. (Cited on pages 40, 64, and 84).

[161] K. Momma and F. Izumi. VESTA 3 for three-dimensional visualization of crystal, volumetric and morphology data. *J. Appl. Cryst.*, 44:1272–1276, 2011. https://doi.org/10.1107/S0021889811038970. (Cited on pages 40, 64, and 84).

[162] A. Kormányos, G. Burkard, M. Gmitra, J. Fabian, V. Zólyomi, N. D. Drummond, and V. Fal'ko. $\mathbf{k}\cdot\mathbf{p}$ theory for two-dimensional transition metal dichalcogenide semiconductors. *2D Mater.*, 2:022001, 2015. https://doi.org/10.1088/2053-1583/2/2/022001. (Cited on page 40.)

[163] S. B. Zhang and J. E. Northrup. Chemical potential dependence of defect formation energies in GaAs: Application to Ga self-diffusion. *Phys. Rev. Lett.*, 67:2339, 1991. https://doi.org/10.1103/PhysRevLett.67.2339. (Cited on page 41.)

[164] P. Mori-Sánchez, A. J. Cohen, and W. Yang. Localization and delocalization errors in density functional theory and implications for band-gap prediction. *Phys. Rev. Lett.*, 100:146401, 2008. https://doi.org/10.1103/PhysRevLett.100.146401. (Cited on page 52.)

[165] L. J. Sham and M. Schlüter. Density-functional theory of the energy gap. *Phys. Rev. Lett.*, 51:1888, 1983. https://doi.org/10.1103/PhysRevLett.51.1888. (Cited on page 52.)

[166] J. P. Perdew. Density functional theory and the band gap problem. *Int. J. Quantum Chem.*, 28:497–523, 1985. https://doi.org/10.1002/qua.560280846. (Cited on page 52.)

[167] J. P. Perdew and M. Levy. Physical content of the exact Kohn-Sham orbital energies: Band gaps and derivative discontinuities. *Phys. Rev. Lett.*, 51:1884, 1983. https://doi.org/10.1103/PhysRevLett.51.1884. (Cited on page 52.)

[168] E. J. Baerends, O. V. Gritsenko, and R. van Meer. The Kohn–Sham gap, the fundamental gap and the optical gap: The physical meaning of occupied and virtual Kohn–Sham orbital energies. *Phys. Chem. Chem. Phys.*, 15:16408–16425, 2013. https://doi.org/10.1039/c3cp52547c. (Cited on page 52.)

[169] J.-L. Bredas. Mind the gap! *Mater. Horiz.*, 1:17–19, 2014. https://doi.org/10.1039/C3MH00098B. (Cited on page 52.)

[170] P. V. Nguyen, N. C. Teutsch, N. P. Wilson, J. Kahn, X. Xia, A. J. Graham, V. Kandyba, A. Giampietri, A. Barinov, G. C. Constantinescu, N. Yeung, N. D. M. Hine, X. Xu, D. H. Cobden, and N. R. Wilson. Visualizing electrostatic gating effects in two-dimensional heterostructures. *Nature*, 572:220–223, 2019. https://doi.org/10.1038/s41586-019-1402-1. (Cited on page 53.)

[171] J. Xi, T. Zhao, D. Wang, and Z. Shuai. Tunable electronic properties of two-dimensional transition metal dichalcogenide alloys: A first-principles prediction. *J. Phys. Chem. Lett.*, 5:285–291, 2014. https://doi.org/10.1021/jz402375s. (Cited on pages 53 and 54).

[172] K. D. Bronsema, J. L. De Boer, and F. Jellinek. On the structure of molybdenum diselenide and disulfide. *Z. anorg. allg. Chem.*, 540:15–17, 1986. https://doi.org/10.1002/zaac.19865400904. (Cited on page 53.)

[173] W. J. Schutte, J. L. De Boer, and F. Jellinek. Crystal structures of tungsten disulfide and diselenide. *J. Solid State Chem.*, 70:207–209, 1987. https://doi.org/10.1016/0022-4596(87)90057-0. (Cited on page 53.)

[174] F. Cadiz, E. Courtade, C. Robert, G. Wang, Y. Shen, H. Cai, T. Taniguchi, K. Watanabe, H. Carrere, D. Lagarde, M. Manca, T. Amand, P. Renucci, S. Tongay, X. Marie, and B. Urbaszek. Excitonic linewidth approaching the homogeneous limit in MoS_2-based van der Waals heterostructures. *Phys. Rev. X*, 7:021026, 2017. https://doi.org/10.1103/PhysRevX.7.021026. (Cited on page 57.)

[175] A. Chernikov, T. C. Berkelbach, H. M. Hill, A. Rigosi, Y. Li, O. B. Aslan, D. R. Reichman, M. S. Hybertsen, and T. F. Heinz. Exciton binding energy and non-hydrogenic Rydberg series in monolayer WS_2. *Phys. Rev. Lett.*, 113:076802, 2014. https://doi.org/10.1103/PhysRevLett.113.076802. (Cited on page 57.)

[176] K. F. Mak, K. He, J. Shan, and T. F. Heinz. Control of valley polarization in monolayer MoS_2 by optical helicity. *Nature Nanotech.*, 7:494–498, 2012. https://doi.org/10.1038/nnano.2012.96. (Cited on page 57.)

[177] H. Zeng, J. Dai, W. Yao, D. Xiao, and X. Cui. Valley polarization in MoS_2 monolayers by optical pumping. *Nature Nanotech.*, 7:490–493, 2012. https://doi.org/10.1038/nnano.2012.95. (Cited on page 57.)

[178] T. Cao, G. Wang, W. Han, H. Ye, C. Zhu, J. Shi, Q. Niu, P. Tan, E. Wang, B. Liu, and J. Feng. Valley-selective circular dichroism of monolayer molybdenum disulphide. *Nat. Commun.*, 3:887, 2012. https://doi.org/10.1038/ncomms1882. (Cited on page 57.)

[179] G. Aivazian, Z. Gong, A. M. Jones, R.-L. Chu, J. Yan, D. G. Mandrus, C. Zhang, D. Cobden, W. Yao, and X. Xu. Magnetic control of valley pseudospin in monolayer WSe_2. *Nature Phys.*, 11:148–152, 2015. https://doi.org/10.1038/nphys3201. (Cited on page 57.)

[180] S. M. Loh, X. Xia, N. R. Wilson, and N. D. M. Hine. Strong in-plane anisotropy in the electronic properties of doped transition metal dichalcogenides exhibited in $W_{1-x}Nb_xS_2$. *Phys. Rev. B*, 103:245410, 2021. https://doi.org/10.1103/PhysRevB.103.245410. (Cited on pages ix, 60, and 64).

[181] M. Leroux, M. Le Tacon, M. Calandra, L. Cario, M-A. Méasson, P. Diener, E. Borrissenko, A. Bosak, and P. Rodière. Anharmonic suppression of charge

density waves in 2H-NbS_2. *Phys. Rev. B*, 86:155125, 2012. https://doi.org/10.1103/PhysRevB.86.155125. (Cited on page 60.)

[182] F. Güller, V. L. Vildosola, and A. M. Llois. Spin density wave instabilities in the NbS_2 monolayer. *Phys. Rev. B*, 93:094434, 2016. https://doi.org/10.1103/PhysRevB.93.094434. (Cited on pages 60 and 61).

[183] X. Ding, S. Zhang, M. Zhao, Y. Xiang, K. H. L. Zhang, X. Zu, S. Li, and L. Qiao. NbS_2: A promising *p*-type Ohmic contact for two-dimensional materials. *Phys. Rev. Applied*, 12:064061, 2019. https://doi.org/10.1103/PhysRevApplied.12.064061. (Cited on page 61.)

[184] Y. Jin, Z. Zeng, Z. Xu, Y.-C. Lin, K. Bi, G. Shao, T. S. Hu, S. Wang, S. Li, K. Suenaga, H. Duan, Y. Feng, and S. Liu. Synthesis and transport properties of degenerate p-type Nb-doped WS_2 monolayers. *Chem. Mater.*, 31:3534–3541, 2019. https://doi.org/10.1021/acs.chemmater.9b00913. (Cited on pages 61 and 65).

[185] S. Sasaki, Y. Kobayashi, Z. Liu, K. Suenaga, Y. Maniwa, Y. Miyauchi, and Y. Miyata. Growth and optical properties of Nb-doped WS_2 monolayers. *Appl. Phys. Express*, 9:071201, 2016. https://doi.org/10.7567/APEX.9.071201. (Cited on page 61.)

[186] L. Feng, W. Jiang, J. Su, L. Zhou, and Z. Liu. Performance of field-effect transistors based on $Nb_xW_{1-x}S_2$ monolayers. *Nanoscale*, 8:6507–6513, 2016. https://doi.org/10.1039/C6NR00380J. (Cited on pages 61 and 74).

[187] Y. Nie, C. Liang, P.-R. Cha, L. Colombo, R. M. Wallace, and K. Cho. A kinetic Monte Carlo simulation method of van der Waals epitaxy for atomistic nucleation-growth processes of transition metal dichalcogenides. *Sci. Rep.*, 7:2977, 2017. https://doi.org/10.1038/s41598-017-02919-2. (Cited on pages 61 and 71).

[188] Y. Nie, C. Liang, K. Zhang, R. Zhao, S. M. Eichfeld, P.-R. Cha, L. Colombo, J. A. Robinson, R. M. Wallace, and K. Cho. First principles kinetic Monte Carlo study on the growth patterns of WSe_2 monolayer. *2D Mater.*, 3:025029, 2016. https://doi.org/10.1088/2053-1583/3/2/025029. (Cited on pages 61 and 71).

[189] G. S. Bales and D. C. Chrzan. Transition from compact to fractal islands during submonolayer epitaxial growth. *Phys. Rev. Lett.*, 74:4879, 1995. https://doi.org/10.1103/PhysRevLett.74.4879. (Cited on pages 61 and 71).

[190] A. I. Romanenko, G. E. Yakovlena, V. E. Fedorov, A. Yu. Ledneva, V. A. Kuznetsov, A. V. Sotnikov, A. R. Tsygankova, and B. M. Kuchumov. Electron transport properties of thermoelectrics based on layered substituted transition metal dichalcogenides. *J. Struct. Chem.*, 58:893–900, 2017. https://doi.org/10.1134/S0022476617050067. (Cited on page 62.)

[191] A. Kuc, N. Zibouche, and T. Heine. Influence of quantum confinement on the electronic structure of the transition metal sulfide TS_2. *Phys. Rev. B*, 83:245213, 2011. https://doi.org/10.1103/PhysRevB.83.245213. (Cited on page 62.)

[192] J. A. Wilson and A. D. Yoffe. The transition metal dichalcogenides discussion and interpretation of the observed optical, electrical and structural properties. *Adv. Phys.*, 18:193–335, 1969. https://doi.org/10.1080/00018736900101307. (Cited on page 62.)

[193] K. F. Garrity, J. W. Bennett, K. M. Rabe, and D. Vanderbilt. Pseudopotentials for high-throughput DFT calculations. *Comput. Mater. Sci.*, 81:446–452, 2014. https://doi.org/10.1016/j.commatsci.2013.08.053. (Cited on pages 62 and 82).

[194] A. Azizi, M. Dogan, J. D. Cain, R. Eskandari, X. Yu, E. C. Glazer, M. L. Cohen, and A. Zettl. Frustration and atomic ordering in a monolayer semiconductor alloy. *Phys. Rev. Lett.*, 124:096101, 2020. https://doi.org/10.1103/PhysRevLett.124.096101. (Cited on page 64.)

[195] J. Gao, Y. D. Kim, L. Liang, J. C. Idrobo, P. Chow, J. Tan, B. Li, L. Li, B. G. Sumpter, T.-M. Lu, V. Meunier, J. Hone, and N. Koratkar. Transition-metal substitution doping in synthetic atomically thin semiconductors. *Adv. Mater.*, 28:9735–9743, 2016. https://doi.org/10.1002/adma.201601104. (Cited on pages 72 and 73).

[196] G. T. de Laissardière, D. Mayou, and L. Magaud. Localization of Dirac electrons in rotated graphene bilayers. *Nano Lett.*, 10:804–808, 2010. https://doi.org/10.1021/nl902948m. (Cited on page 79.)

[197] S. Venkateswarlu, A. Honecker, and G. T. de Laissardière. Electronic localization in twisted bilayer MoS_2 with small rotation angle. *Phys. Rev. B*, 102:081103(R), 2020. https://doi.org/10.1103/PhysRevB.102.081103. (Cited on page 79.)

[198] X.-J. Zhao, Y. Yang, D.-B. Zhang, and S.-H Wei. Formation of Bloch flat bands in polar twisted bilayers without magic angles. *Phys. Rev. Lett.*, 124:086401, 2020. https://doi.org/10.1103/PhysRevLett.124.086401. (Cited on pages 79, 103, 107, and 112).

[199] Z. Zhan, Y. Zhang, P. Lv, H. Zhong, G. Yu, F. Guinea, J. Á. Silva-Guillén, and S. Yuan. Tunability of multiple ultraflat bands and effect of spin-orbit coupling in twisted bilayer transition metal dichalcogenides. *Phys. Rev. B*, 102:241106(R), 2020. https://doi.org/10.1103/PhysRevB.102.241106. (Cited on page 79.)

[200] F. Wu, T. Lovorn, and A. H. MacDonald. Topological exciton bands in moiré heterojunctions. *Phys. Rev. Lett.*, 118:147401, 2017. https://doi.org/10.1103/PhysRevLett.118.147401. (Cited on page 80.)

[201] N. Liu, J. Zhang, S. Zhou, and J. Zhao. Tuning the electronic properties of bilayer black phosphorene with the twist angle. *J. Mater. Chem. C*, 8:6264–6272, 2020. https://doi.org/10.1039/D0TC00062K. (Cited on page 80.)

[202] M. R. Rosenberger, H.-J. Chuang, M. Phillips, V. P. Oleshko, K. M. McCreary, S. V. Sivaram, C. S. Hellberg, and B. T. Jonker. Twist angle-dependent atomic reconstruction and moiré patterns in transition metal dichalcogenide heterostructures. *ACS Nano*, 14:4550–4558, 2020. https://doi.org/10.1021/acsnano.0c00088. (Cited on page 80.)

[203] D. A. Bandurin, A. V. Tyurnina, G. L. Yu, A. Mishchenko, V. Zólyomi, S. V. Morozov, R. K. Kumar, R. V. Gorbachev, Z. R. Kudrynskyi, S. Pezzini, Z. D. Kovalyuk, U. Zeitler, K. S. Novoselov, A. Patanè, L. Eaves, I. V. Grigorieva, V. I. Fal'ko, A. K. Geim, and Y. Cao. High electron mobility, quantum Hall effect and anomalous optical response in atomically thin InSe. *Nature Nanotech.*, 12:223–227, 2017. https://doi.org/10.1038/nnano.2016.242. (Cited on page 80.)

[204] W. Feng, W. Zheng, W. Cao, and P. Hu. Back gated multilayer InSe transistors with enhanced carrier mobilities via the suppression of carrier scattering from a dielectric interface. *Adv. Mater.*, 26:6587–6593, 2014. https://doi.org/10.1002/adma.201402427. (Cited on page 80.)

[205] X. Yang, B. Sa, H. Zhan, and Z. Sun. Electric field-modulated data storage in bilayer InSe. *J. Mater. Chem. C*, 5:12228–12234, 2017. https://doi.org/10.1039/C7TC03698A. (Cited on pages 80, 85, and 87).

[206] H. J. Monkhorst and J. D. Pack. Special points for Brillouin-zone integrations. *Phys. Rev. B*, 13:5188, 1976. https://doi.org/10.1103/PhysRevB.13.5188. (Cited on page 82.)

[207] D. Stradi, L. Jelver, S. Smidtrup, and K. Stokbro. Method for determining optimal supercell representation of interfaces. *J. Phys.: Condens. Matter*, 29:185901, 2017. https://doi.org/10.1088/1361-648X/aa66f3. (Cited on pages 82 and 83).

[208] N. D. M. Hine. https://bitbucket.org/ndmhine/2dm-toolkit/. (Cited on page 83.)

[209] J. J. S. Viner, L. P. McDonnell, D. A. Ruiz-Tijerina, P. Rivera, X. Xu, V. I. Fal'ko, and D. C. Smith. Excited Rydberg states in $MoSe_2/WSe_2$ heterostructures. *2D Mater.*, 8:035047, 2021. https://doi.org/10.1088/2053-1583/ac0296. (Cited on pages 84, 113, and 115).

[210] M. Danovich, D. A. Ruiz-Tijerina, R. J. Hunt, M. Szyniszewski, N. D. Drummond, and V. I. Fal'ko. Localized interlayer complexes in heterobilayer transition metal dichalcogenides. *Phys. Rev. B*, 97:195452, 2018. https://doi.org/10.1103/PhysRevB.97.195452. (Cited on pages 84, 113, and 115).

[211] D. A. Ruiz-Tijerina, I. Soltero, and F Mireles. Theory of moiré localized excitons in transition metal dichalcogenide heterobilayers. *Phys. Rev. B*, 102:195403, 2020. https://doi.org/10.1103/PhysRevB.102.195403. (Cited on pages 84, 113, and 115).

[212] P. Virtanen, R. Gommers, T. E. Oliphant, M. Haberland, T. Reddy, D. Cournapeau, E. Burovski, P. Peterson, W. Weckesser, J. Bright, S. J. van der Walt, M. Brett, J. Wilson, K. J. Millman, N. Mayorov, A. R. J. Nelson, E. Jones, R. Kern, E. Larson, C. J. Carey, İ. Polat, Y. Feng, E. W. Moore, J. VanderPlas, D. Laxalde, J. Perktold, R. Cimrman, I. Henriksen, E. A. Quintero, C. R. Harris, A. M. Archibald, A. H. Ribeiro, F. Pedregosa, P. van Mulbregt, and SciPy 1.0 Contributors. SciPy 1.0: Fundamental algorithms for scientific computing in Python. *Nat. Methods*, 17:261–272, 2020. https://doi.org/10.1038/s41592-019-0686-2. (Cited on page 84.)

[213] J. D. Hunter. Matplotlib: A 2D graphics environment. *Computing in Science & Engineering*, 9:90–95, 2007. https://doi.org/10.1109/MCSE.2007.55. (Cited on page 84.)

[214] Y. Ding, J. Shi, C. Xia, M. Zhang, J. Du, P. Huang, M. Wu, H. Wang, Y. Cen, and S. Pan. Enhancement of hole mobility in InSe monolayer via an InSe and black phosphorus heterostructure. *Nanoscale*, 9:14682–14689, 2017. https://doi.org/10.1039/C7NR02725G. (Cited on page 85.)

[215] S. Gopalan, G. Gaddemane, M. L. Van de Put, and M. V. Fischetti. Monte Carlo study of electronic transport in monolayer InSe. *Materials*, 12:4210, 2019. https://doi.org/10.3390/ma12244210. (Cited on page 85.)

[216] G. W. Mudd, M. R. Molas, X. Chen, V. Zólyomi, K. Nogajewski, Z. R. Kudrynskyi, Z. D. Kovalyuk, G. Yusa, O. Makarovsky, L. Eaves, M. Potemski, V. I. Fal'ko, and A. Patanè. The direct-to-indirect band gap crossover in two-dimensional van der Waals indium selenide crystals. *Sci. Rep.*, 6:39619, 2016. https://doi.org/10.1038/srep39619. (Cited on pages 85 and 86).

[217] J. Shang, L. Pan, X. Wang, J. Li, and Z. Wei. Tunable electric properties of bilayer InSe with different interlayer distances and external electric field. *Semicond. Sci. Technol.*, 33:034002, 2018. https://doi.org/10.1088/1361-6641/aaaad2. (Cited on pages 85 and 103).

[218] L. Guan, X. Cheng, and J. Tao. Strain effect on electronic structure of two-dimensional γ-InSe nanosheets. *Appl. Phys. Express*, 10:125202, 2017. https://doi.org/10.7567/APEX.10.125202. (Cited on page 87.)

[219] N. Shen, X. Yang, X. Wang, G. Wang, and J. Wan. Two-dimensional van der Waals heterostructure of indium selenide/hexagonal boron nitride with strong interlayer coupling. *Chem. Phys. Lett.*, 749:137430, 2020. https://doi.org/10.1016/j.cplett.2020.137430. (Cited on page 99.)

[220] G. C. Constantinescu and N. D. M. Hine. Multipurpose black-phosphorus/hBN heterostructures. *Nano Lett.*, 16:2586–2594, 2016. https://doi.org/10.1021/acs.nanolett.6b00154. (Cited on page 102.)

[221] W. T. Geng, V. Wang, Y. C. Liu, T. Ohno, and J. Nara. Moiré potential, lattice corrugation, and band gap spatial variation in a twist-free $MoTe_2/MoS_2$ heterobilayer. *J. Phys. Chem. Lett.*, 11:2637–2646, 2020. https://doi.org/10.1021/acs.jpclett.0c00605. (Cited on page 103.)

[222] X. Yao and X. Zhang. Electronic structures of twisted bilayer InSe/InSe and heterobilayer graphene/InSe. *ACS Omega*, 6:13426–13432, 2021. https://doi.org/10.1021/acsomega.1c01562. (Cited on pages 107, 111, and 112).

[223] M. H. Naik, S. Kundu, I. Maity, and M. Jain. Origin and evolution of ultraflat bands in twisted bilayer transition metal dichalcogenides: Realization of triangular quantum dots. *Phys. Rev. B*, 102:075413, 2020. https://doi.org/10.1103/PhysRevB.102.075413. (Cited on page 112.)

[224] M. Wu, J.-J. Shi, M. Zhang, Y.-M. Ding, H. Wang, Y.-L. Cen, and J. Lu. Enhancement of photoluminescence and hole mobility in 1- to 5-layer InSe due to the top valence-band inversion: Strain effect. *Nanoscale*, 10:11441–11451, 2018. https://doi.org/10.1039/C8NR03172J. (Cited on pages v, 113, 114, and 115).

[225] A. Laturia, M. L. Van de Put, and W. G. Vandenberghe. Dielectric properties of hexagonal boron nitride and transition metal dichalcogenides: From monolayer to bulk. *npj 2D Mater. Appl.*, 2:6, 2018. https://doi.org/10.1038/s41699-018-0050-x. (Cited on pages v, 114, and 115).

[226] A. Ceferino, K. W. Song, S. J. Magorrian, V. Zólyomi, and V. I. Fal'ko. Crossover from weakly indirect to direct excitons in atomically thin films of InSe. *Phys. Rev. B*, 101:245432, 2020. https://doi.org/10.1103/PhysRevB.101.245432. (Cited on pages v, 114, and 115).

[227] P. Cudazzo, I. V. Tokatly, and A. Rubio. Dielectric screening in two-dimensional insulators: Implications for excitonic and impurity states in graphane. *Phys. Rev. B*, 84:085406, 2011. https://doi.org/10.1103/PhysRevB.84.085406. (Cited on pages v, 114, and 115).

[228] J. Rigoult, A. Rimsky, and A. Kuhn. Refinement of the 3R γ-indium monoselenide structure type. *Acta Cryst.*, B36:916–918, 1980. https://doi.org/10.1107/S0567740880004840. (Cited on pages v, 114, and 115).